industriales
etsii

Escuela Técnica Superior de Ingeniería Industrial

UNIVERSIDAD POLITÉCNICA DE CARTAGENA

Escuela Técnica Superior de Ingeniería Industrial

Analysis of Metal Matrix Composites (MMC) by FEM

TRABAJO FIN DE MÁSTER

MÁSTER EN INGENIERÍA INDUSTRIAL

Autor: **José Antonio López Garrido**
Director: José Andrés Moreno Nicolás

Cartagena, 4 de febrero de 2019

Universidad Politécnica de Cartagena

EXECUTIVE SUMMARY

Introduction:

This work is based on a real process used at IFKB which works with thixo-forging. This is a metal matrix composites manufacturing.

In this work we have simulated the chilling of a simple metal plate.

Aim of the task:

The basic aim of the present work is the application of FEM in order to evaluate the MMC design.

Method:

To obtain the results of this work we are simulated the chilling of a metal plate using finite element method software for different cases including radiation or convection, and different interface materials.

Main results:

We can observe the results of the work in the graphics of section 5.

Main conclusions:

The results remark the influence of the chilling process on the thermal stress.

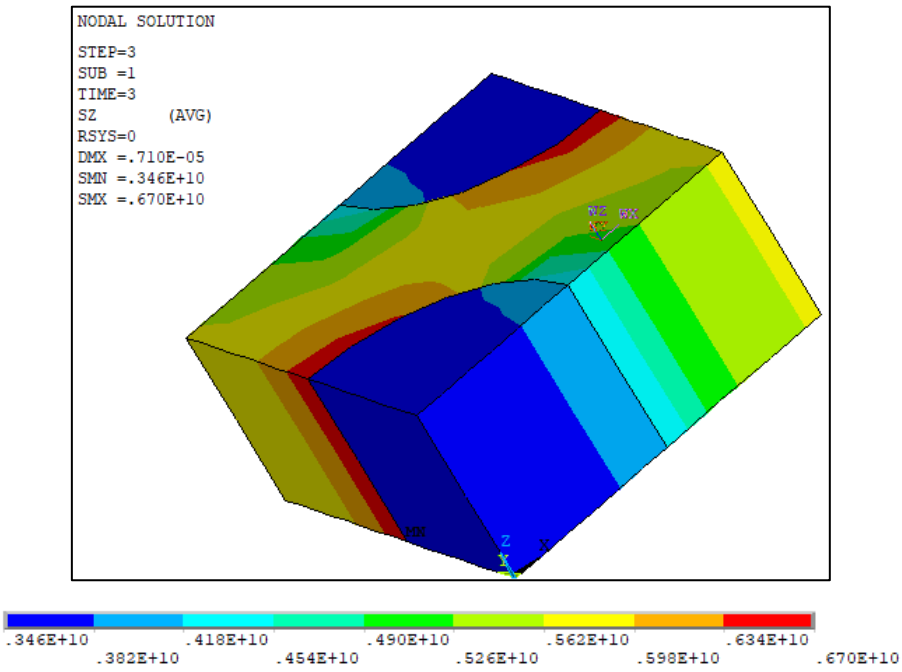

TABLE OF CONTENS

1 INTRODUCTION

1.1 Introduction

The union of two or more materials combined on a macroscopic scale forms a composite material, which usually exhibit the best qualities of their components. The manufacturing of these materials presents several problems that conventional manufacturing cannot solve. These can be resolved using a process which is called thixo-forging.

To predict the elastic properties of the composite in terms of the elastic properties of the constituents is used homogenization techniques.

One of the tasks proposed in this work is the simulation with the purpose of studying the temperatures distribution and the stresses in the plate during a chilling process, simulation software is nowadays widely used to simulate complex processes. In order to study the nonlinear material behaviour of composites with periodic microstructure, the finite element method is employed.

The predecessor work is referred to thermal and mechanical analysis of one thixo-forged of aluminium and carbon fibre by ABAQUS where radiation is not used.

At the end of this chapter we stand out the literature more important.

1.2 Stade of the art

1.2.1 Metal Matrix Composites (MMC)

The union of two or more materials, that are combined on a macroscopic scale, forms a useful third material which is called composite material. The components manufactured with this material can be distinguished by the naked eye from other combined on a microscopic scale, like alloying materials, because the resulting material is macroscopically homogeneous. Moreover, composite materials usually exhibit the best qualities of their components or constituents and some qualities that the constituents do not present separately. Some of those properties that can be improved by forming a composite material are: strength, fatigue life, stiffness, temperature-dependent behaviour, corrosion resistance, thermal insulation, wear resistance, thermal conductivity, attractiveness, acoustical insulation, weight [Robert M. Jones, 1999].

However, some of the properties are in conflict each other. Thus, the objective is to design a material that has only the characteristics needed to perform the design task [Robert M. Jones, 1999].

Four commonly accepted types of composite materials are:

- Fibrous composite materials that consist of fibres in a matrix. This work is focused on this case.
- Laminated composite materials that consist of layers of various materials.
- Particulate composite materials that are composed of particles in a matrix.
- Combinations of some or all of the first three types.

About fibrous composite materials that consist of fibres in a matrix, long fibres in various forms are inherently much stiffer and stronger than the same material in bulk form. In fibres, the crystals are aligned along the fibre axis. Moreover, there are fewer internal defects in fibres than in bulk material [Robert M. Jones, 1999].

Graphite or carbon fibres are of high interest in today's composite structures. Both are made from polyacrylonitrile (PAN) precursor fibres that are heated in an inert atmosphere to about 1700 °C to carbonize the fibres, being a key processing parameter the fibre tension. Moreover, as the processing temperature is increased, the fibre modulus increases, but the strength often decreases. Generally, the fibres are much thinner than human hairs and they can be bent quite easily, thus, carbon or graphite fibres can be woven into fabric.

An alternative to fibres can be the whiskers. These have essentially the same near-crystal-sized diameter as a fibre, but generally is very short and stubby, although the length-to-diameter ratio can be in the hundreds. A whisker is even more perfect than a fibre and therefore exhibits even higher properties because whiskers are obtained by crystallization on a very small scale resulting in a nearly perfect alignment of crystals [Robert M. Jones, 1999].

Fibres, generally, exhibit linear-elastic behaviour, although reinforcing steel bars in concrete are more nearly elastic-perfectly plastic. Aluminium, as well as many polymers, and some composite materials exhibit elastic-plastic behaviour that is really nonlinear elastic behaviour if there is no unloading. Fibre-reinforced composite materials are usually treated as linear elastic materials because the essentially linear elastic fibres provide the majority of the strength and stiffness. Refinement of that approximation requires consideration of some form of plasticity, viscoelasticity, or both (viscoplasticity) [Robert M. Jones, 1999].

Obviously, fibres and whiskers are of little use unless they are bonded together to take the form of a structural element that can carry loads. The binder material is called matrix and this has several functions among which the following are stood out: support of the fibres or whiskers, protection of the fibres or whiskers and stress transfer between broken fibres or whiskers.

The latter function is especially important if a fibre breaks as in Fig. 1.1. There, load from one portion of a broken fibre is transferred to the matrix and, subsequently, to the other portion of the broken fibre as well as to adjacent fibres. The mechanism for load transfer is the shearing stress developed in the matrix, which avoids the pulling out of the broken fibre [Robert M. Jones, 1999].

Typically, the matrix is of considerably lower density, stiffness, and strength than the fibres or whiskers. However, the combination of fibres or whiskers and a matrix can have very high strength and stiffness, yet still have low density. Matrix materials can be polymers, metals, ceramics or carbon. These can be made to flow around an in-place fibre system by diffusion bonding or by heating and vacuum infiltration. Common examples include aluminium, titanium, and nickel-chromium alloys. The cost of each matrix escalates in that order as does the temperature resistance [Robert M. Jones, 1999].

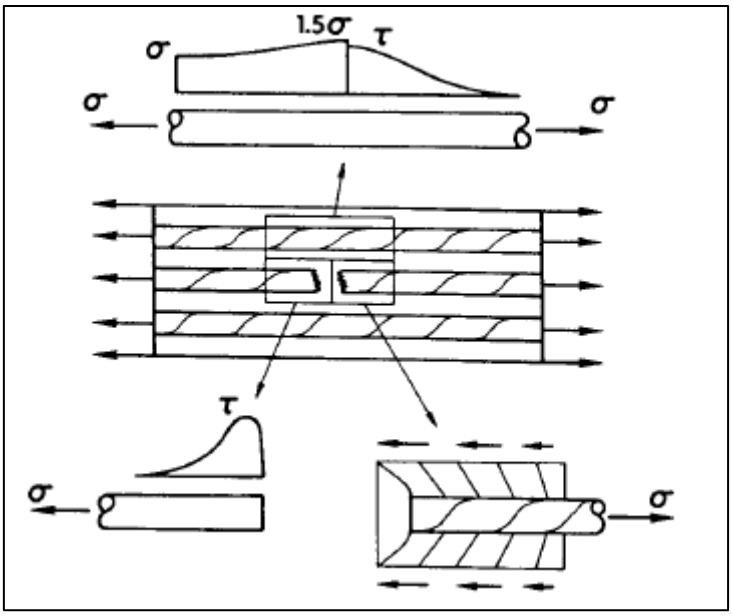

Figure 1.1 Effect of broken fibre on matrix and fibre stresses [Robert M. Jones, 1999]

The MMC stand out in the composite materials, and, in this category, aluminium matrix composites are interesting lightweight materials for special applications, for example, in automotive and aerospace applications where these require high mechanical properties (fatigue behaviour, wear resistance, stiffness and absolute strength) and low density. The inclusion of ceramic fibre materials like carbon fibres as reinforcement phase in order to form a metal matrix composite leads to an increase in mechanical properties of light metals, and furthermore, can also lead to a decrease of material density in case of carbon fibres, thus, the necessities can be solved [Gadow, 2010].

Metal matrix composites have many mechanical behaviour characteristics that are different from those of more conventional engineering materials. Unlike conventional materials, these composites are often heterogeneous and nonisotropic, orthotropic or anisotropic.

MMC with discontinuous reinforcement in the form of particles, whiskers or short fibres can be attractive alternatives to continuously reinforced material, because they show more isotropic material properties as well as, generally, lower production and process cost. Thereby, the properties of short fibre reinforced MMC are in-between continuous fibre and particle reinforced MMC [Gadow, 2010].

Because of the inherently heterogeneous nature of composite materials, they are studied from two points of view: micromechanics and macromechanics [Robert M. Jones, 1999].

Micromechanics is the study of MMC behaviour wherein the interaction of the constituent materials is examined on a microscopic scale to determine their effect on the properties of the composite material. Micromechanics will be investigated in order to gain an appreciation for how the constituents of composite materials can be proportioned and arranged to achieve certain specified strengths and stiffnesses.

Macromechanics is the study of MMC behaviour wherein the material is presumed homogeneous and the effects of the constituent materials are detected only as averaged

apparent macroscopic properties of the composite material. It is the most appreciated of the two and the more important topic in structural design analysis.

Use of the two concepts of macromechanics and micromechanics allows the tailoring of a composite material to meet a particular structural requirement with little waste of material capability. The ability to tailor a MMC to its job is one of the most significant advantages of a composite material over an ordinary material. Perfect tailoring of a composite material yields only the stiffness and strength required in each direction, no more. In contrast, an isotropic material is, by definition, constrained to have excess strength and stiffness in any direction other than that of the largest required strength or stiffness [Robert M. Jones, 1999].

Thus, there is a very close relation between the manufacture of a composite material and its end use [Robert M. Jones, 1999]. Presently, it has been possible to obtain long fibre reinforced MMC with excellent physical and thermal properties like specific strength and stiffness, reduced thermal deformation and improved wear resistance. Nevertheless, the design of this type of composites is highly challenging compared to the standard fibre-reinforced polymers and some critical factors must be carefully controlled [M. Jiménez et al, 2017].

The basic building block of a laminate is a lamina which is a flat, sometimes curved as in a shell, arrangement of unidirectional fibres or woven fibres in a matrix. Two typical flat laminae along with their principal material axes that are parallel and perpendicular to the fibre direction are shown in Fig. 1.2.

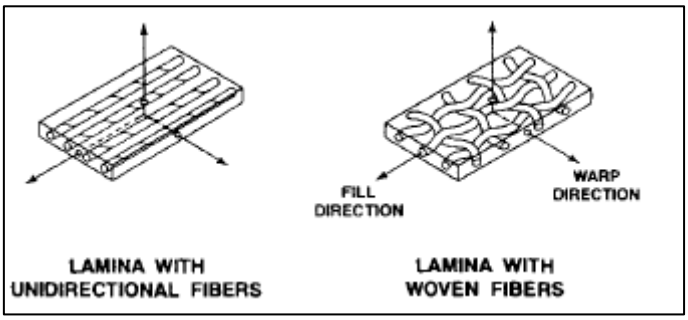

Figure 1.2 Two principal types of laminae [Robert M. Jones, 1999]

Then, a laminate is a bonded stack of laminae with various orientations of principal material directions in the laminae as in Fig. 1.3. The layers of a laminate are usually bonded together by the same matrix material that is used in the individual laminae. Laminates can be composed of plates of different materials or, in the present context, layers of fibre-reinforced laminae [Robert M. Jones, 1999].

Fibre reinforced aluminium is a kind of material that has unique properties, like high specific strength and stiffness, if the characteristics of composites are considered during the manufacturing process, e. g. accurate fibre orientation, control of residual stresses, or the properties of the fibre/matrix interface. However, industrial cost targets can only be achieved by the application of carbon fibres, which have good mechanical properties but yet reasonable costs as compared to alumina or SiC fibres. Carbon fibres also lead to further reduction of the composite's density, and thus increase of the specific material properties [Gadow, 2010].

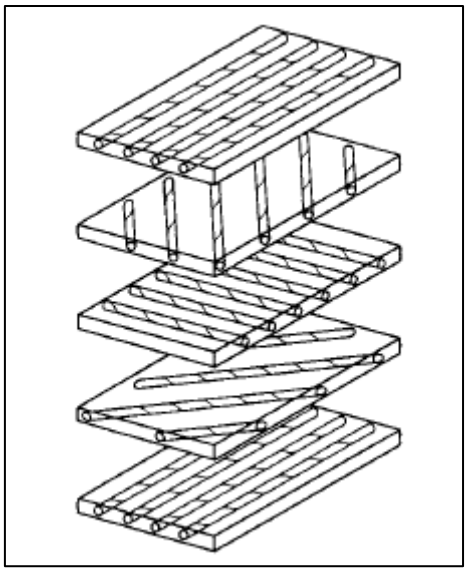

Figure 1.3 Unbonded view of laminate construction [Robert M. Jones, 1999]

But carbon fibres are sensitive to oxidation at high temperatures and chemical reaction if getting in contact with aluminium melts. Therefore, in order to avoid fibre damage during matrix infiltration, protective fibre coatings have to be applied in an additional process, or the process temperature and process time (duration of fibre/melt contact) have to be reduced. This approach would at the same time lead to a reduction of residual stresses and lower processing costs because of reduced cycle times and wear of the tools and equipment [Gadow, 2010].

On the one hand, the solid-phase techniques avoid fibre damage by chemical reactions, but the design of the component is strongly limited to extruded or rolled geometries. More complex geometries can be realized with liquid metal infiltrations, but the preform positioning problems in the die and the need for high pressure resistance of the preform still limit the possible geometries. On the other hand, the main disadvantage of these liquid-phase techniques are the relatively long contact of the fibre with the melt resulting in significant fibre damage by chemical reaction at the interface [Konstantin von Niessen, 2006].

This problem can be solved using the laminates, consisting of metal sheets and woven fibre layers, in combination with semisolid forming, called thixo-forging.

Thixo-forming is a method of forming technology, where a semisolid slug is formed to a near-net-shape part. Thixo-forming process can be divided in two variant, thixo-casting and thixo-forging [J.T. Álvarez, 2005].

Thixo-casting is done on slightly modified die casting machines. The inductively reheated and partly molten billet is set into the shot sleeve. The semisolid material is pressed into the closed die by the shot arm [J.T. Álvarez, 2005].

In thixo-casting process, a solid billet, with a fine grained equiaxed microstructure, is partially remelted to the semisolid state. The billet is then transferred to the shot chamber of a die cast machine and injected into a die. Billets produced by rheocasting reheated

into the mushy state and forged (procedure also called semisolid forging) [J.T. Álvarez, 2005].

Thixo-forging is done on hydraulic forging presses. The reheated billet is taken into the opening forging die. While closing the die, the work piece is formed [J.T. Álvarez, 2005].

Thixo-forging in closed dies can be realized using double action presses. The slurry is taken into the open die. After, the die is closed, the work piece is formed by the press piston. On single action presses is necessary a closing tool to perform this forming variation [J.T. Álvarez, 2005].

In Fig. 1.4 and 1.5 we observe different forms of thixo-forming.

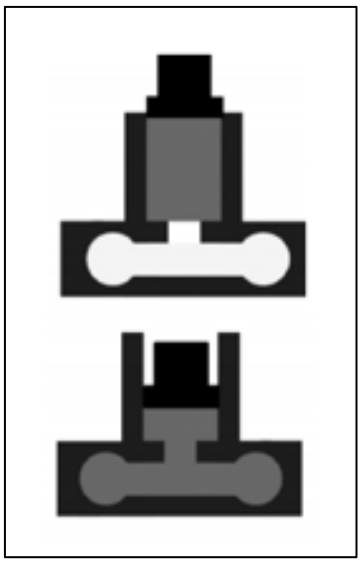

Figure 1.4 Thixo-casting [Hirt, 2009]

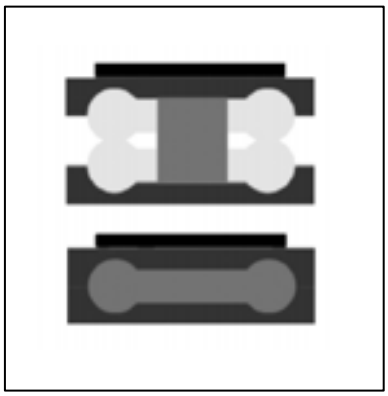

Figure 1.5 Thixo-forging [Hirt, 2009]

1.2.2 Thixo-forging

Thixo-forging of MMC in the semisolid state of the matrix alloy is an approach to a new processing route that considers lower process temperatures, reduced aluminium melt content, and lower cycle times. However, semisolid forging requires a globular microstructure of the metal, and due to the partially solid matrix alloy during infiltration, the flow paths need to be short.

A suitable microstructure can be obtained by thermal spray deposition of metals, leading to fine, globular-like grains within the thermal spray splats. Additionally, the temperature of the substrate, which consists of the reinforcement fibres, can be controlled during thermal spraying, and the spray coated material is already impregnating into the topmost fibre layers [Gadow, 2010].

The semisolid state of the metal and the short forming times prevent chemical interaction with the fibres [Konstantin von Niessen, 2006]. Moreover, this method offers a reduction of the mechanical stress on the fibres, as, in the thixotropic state, the viscosity of the alloy decreases abruptly with the application of shear forces [M. Jiménez et al, 2017]. Through this process we can obtain a plate as we can see in the Fig. 1.6.

Figure 1.6 Thixo-forged, woven carbon fibre reinforced MMC with AlSi6 matrix, 214 x 124 mm [Gadow, 2010]

When the mould is reused, the process is called permanent mould casting, and if the mould is not reused, the process is called expendable mould casting. Thus, we can distinguish two kind of shape-casting processes [J.T. Álvarez, 2005]:

- Expendable mould.
- Permanent mould.

With a mix of the characteristics of these two pure kinds, we can find the centrifuged mould with the following subclass [J.T. Álvarez, 2005]:

- True centrifugal (outer mould).
- Semicentrifugal (complete mould).
- Centrifuged (complete mould).

The Institut für Fertigungstechnologie keramischer Bauteile (IFKB, Stuttgart) uses the process called thixo-forging and is included in the permanent mould processes, concretely semisolid [J.T. Álvarez, 2005].

Carbon fibre reinforced aluminium cost more than ten times the cost of its constituents (carbon fibre itself is much more expensive than aluminium), thus, MMC's are expensive. The reason of this is due to the intensive labour of its manufacturing process [J.T. Álvarez, 2005]:

- The liquid metal is infiltrated in fibre tows, which are laid up on a platen press.
- There are also aluminium sheets interlaid between one fibre tows and the next.
- Finally, the laminate is consolidated by diffusion bonding.

Thixo-forging process is in which the material is stirred during solidification, producing a partly liquid, partly solid structure that behaves as solid when no external force is applied, or flows as liquid under pressure. We would select an alloy with a wide freezing range so that a significant portion of the solidification process occurs by the growth of dendrites. A hypoeutectic aluminium-silicon alloy might be appropriate. In the thixo-forging process, the dendrites are broken up by stirring during solidification. The billet is later reheated to cause melting of just the eutectic portion of the alloy, and it is then forced into the mould in its semisolid condition at a temperature below the liquidus temperature [J.T. Álvarez, 2005].

Thixo-forging of continuous fibre reinforced components can be divided in 3 phases: prepreg fabrication, prepreg heating and solidification of prepregs by thixo-forging. Its manufacturing route can be seen in Fig. 1.7.

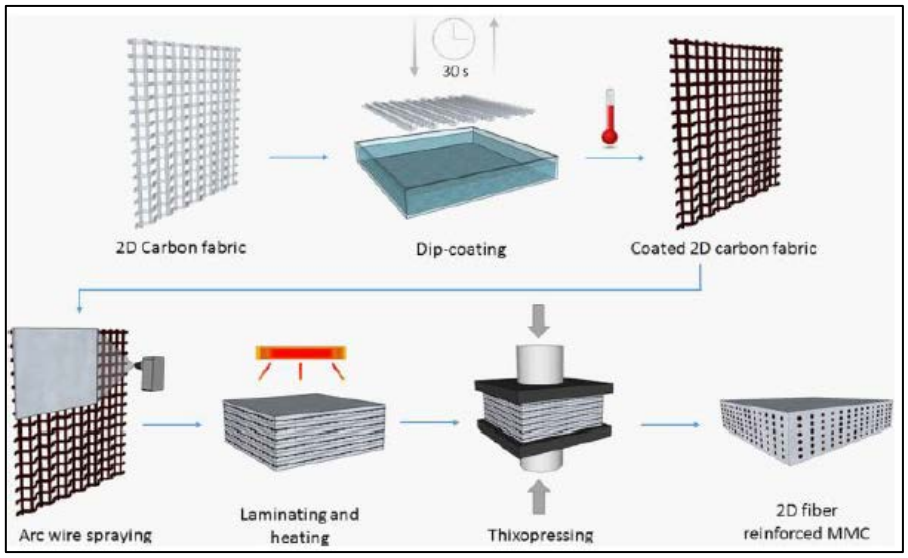

Figure 1.7 Process chain for the manufacturing of fibre reinforced MMC composites from coated carbon fibre fabrics by thermal spraying and semi-solid forming [M. Jiménez et al, 2017]

Prepreg fabrication, which is the production of the composites and consists of two single processes:

- Thin metal sheets of aluminium AlSi6 (Aluminium organization: 319.0, ISO: AlSiCu4) and alternating carbon fibre fabrics are arranged to a laminated prepreg, a kind of mesh with special disposition. Previously, the carbon fibre fabrics were impregnated with a solution, generally a resin, by liquid phase impregnation (LPI) fibre coating with subsequent annealing [M. Jiménez et al, 2017; Konstantin von Niessen, 2006].

- Thermally sprayed coatings on fibre fabrics are used to built-up the metal matrix. The prepregs are heated up to the processing temperature and densified by thixo-forging. The semisolid metal infiltrates the porosity between the fibres. The

resulting metal matrix composite is completely infiltrated and has not residual porosity [M. Jiménez et al, 2017].

An important feature of the thermal spraying technique is the low temperature on the substrate during the coating process and the high deposition rate. Using simultaneous air or liquid CO_2 cooling techniques, the thermal load on the substrate can be held on a moderate temperature level, in the range of 50-150 ºC. In this phase, the ambient temperature is approximated to 450 ºC [M. Jiménez et al, 2017].

Twin wire arc spraying, Fig. 1.8, can be selected to perform this phase because it was selected because it fulfils the goal of deposition rate and thermal load for the substrate. This process is based on a constant electric arc generated between two electrically charged metal wires, which are fed parallel and with equal speed to the contact point, where an electric arc melts the wires and a compressed air flow atomises and accelerates the melt particles towards the substrate the number of passages is optimised to achieve the coating thickness necessary and fabrics were coated on both sides [M. Jiménez et al, 2017].

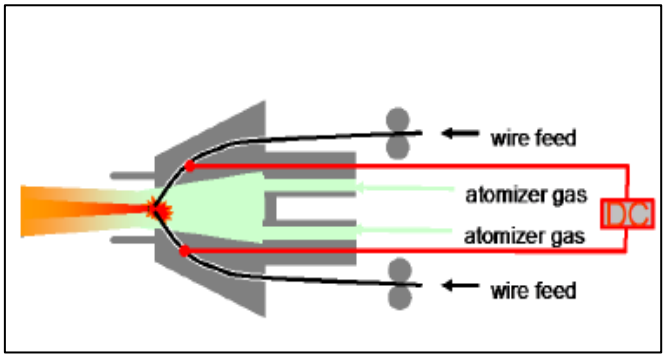

Figure 1.8 Principle sketch of the twin-wire electric arc spraying process [Gadow, 2010]

The spray coated fabrics, from now on called prepregs, is cut into rectangular plates. Some layers of prepregs are laminated and wrapped with a steel foil, to avoid loss of liquid fraction alloy during densification. The reasons to select steel as film material are its higher melting point compared to aluminium alloys and the low adhesion of the foil to the surface of the matrix material [M. Jiménez et al, 2017].

The application of this technique must consider two important difficulties, kinetic and thermal energy of jet of particles may damage the fibres mechanically and chemically. Special winding equipment is designed for give solution to this problem (roll to roll) [J.T. Álvarez, 2005].

After laminating, the prepregs are reheated to thixo-forging temperature by means of convection inside an oven with nitrogen atmosphere. An alternative heating process, for reduce heating time and fibre damage, is using a short wave infrared radiator. This is developed by the IFKB [M. Jiménez et al, 2017].

After heating up, prepregs are placed in the heated die. To minimize the thermal shock effects due to temperature difference between the heated prepreg and the die, the die temperatures ranges up to 450 ºC.

Short time of production of thixo-forging process and the semisolid state of the metal matrix make sure the reduction of fibre damage at the interface between the single fibre

and the matrix metal. The high stroke speed ensures the appropriate thixotropic behaviour of matrix material by preventing early solidification due to the heat transfer between the die and the prepreg. The forging process is performed by a modular constructed die that is adapted according to the process and the shape of fibre reinforcement in the component. The semi-solid temperature range is located between 577 ºC and 620 ºC [M. Jiménez et al, 2017].

The production of the MMC's is realized by a thixo-forging unit at the IFU. It consists of a hydraulic high speed press and a 6-axis robot system. The hydraulic press is using a hydraulic accumulator what obtain high punch speed under a defined force-path [J.T. Álvarez, 2005].

The chill process starts at 600 ºC during 10 s in the cavity and after the piece put on a table what we suppose of infinite size. The chill process is constituted by of two differentiates phases because the exterior temperature varies between 450 ºC and 20 ºC according to the temperature value inside the piece [M. Jiménez et al, 2017].

1.2.3 Computational micromechanics

An alternative to predict the elastic properties of the composite in terms of the elastic properties of the constituents (matrix and reinforcements) is to use homogenization techniques [Barbero, 2014]. Since homogenization models are based on more or less accurate modelling of the microstructure, these models are also called micromechanics models, and the techniques used to obtain approximate values of the composite's properties are called micromechanics methods or techniques.

Many analytical techniques of homogenization are based on the equivalent eigenstrain method [Eshelby, 1957, 1959], which considers the problem of a single ellipsoidal inclusion embedded in an infinite elastic medium. Homogenization of composites with periodic microstructure has been accomplished by using various techniques including an extension of the Eshelby inclusion problem, the Fourier series technique, and variational principles.

The analytical procedures mentioned so far yield approximate estimates of the exact solution of the micromechanics problem. Several variational principles were developed to evaluate bounds on the homogenized elastic properties of macroscopically isotropic heterogeneous materials [Hashin and Shtrikman, 1963]. These bounds depend only on the volume fractions and the physical properties of the constituents.

In order to study the nonlinear material behaviour of composites with periodic microstructure, numerical methods, mainly the finite element method, are employed.

1.2.4 Analytical homogenization

Simple analytical models yield formulas for the stiffness C and compliance S tensors of the composite [Aboudi, 1991], such as

$$C = \sum V_i \cdot C^i \cdot A^i \qquad ; \qquad \sum V_i \cdot A^i = I$$

$$S = \sum V_i \cdot S^i \cdot B^i \qquad ; \qquad \sum V_i \cdot B^i = I \tag{1.1}$$

where V_i, C^i, S^i, are the volume fraction, stiffness, and compliance tensors (in contracted notation, four-order tensors) of the i-th phase in the composite, respectively, and I is the 6×6 identity matrix. Furthermore, A^i, B^i, are the strain and stress concentration tensors (in contracted notation) of the i-th phase [Aboudi, 1991]. For fibre reinforced composites, i = f, m, represent the fibre and matrix phases, respectively.

Fourth-order tensors with minor symmetry are represented by a 6×6 matrix taking advantage of contracted notation.

The Reuss model (rule of mixtures, ROM) assumes that the strain tensors in the fibre, matrix, and composite are the same $\varepsilon = \varepsilon^f = \varepsilon^m$, so, the strain concentration tensors are all equal to the 6×6 matrix $A^i = I$. The rule of mixtures formulas for E_1 and ν_{12} are derived and computed in this way.

If the composite has a periodic microstructure, or if it can be approximated as having such a microstructure, then the Fourier series can be used to estimate all the components of the stiffness tensor of a composite. Explicit formulas for a composite reinforced by isotropic, circular-cylindrical fibres, which are periodically arranged in a square array, Fig. 1.9, were developed by Luciano and Barbero [Luciano and Barbero, 1995].

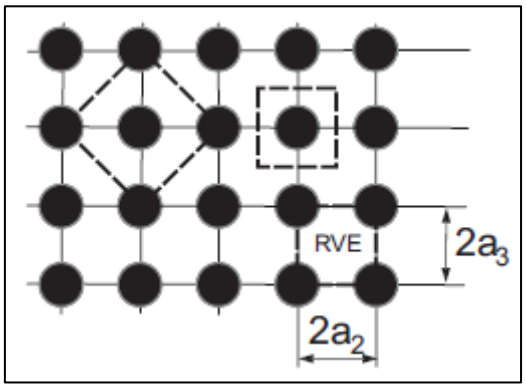

Figure 1.9 Three possible representative volume elements (RVE) for a composite material with a periodic, square fibre array

The fibres are aligned with the x_1 axis, and they are equally spaced ($2 \cdot a_2 = 2 \cdot a_3$). If the fibres are randomly distributed in the cross-section, the resulting composite has transversely isotropic properties.

Because the microstructure has a square symmetry, the stiffness tensor has six unique coefficients given by

$$C_{11}{}^* = \lambda_m + 2 \cdot \mu_m - \frac{V_f}{D} \cdot \left[\frac{S_3{}^2}{\mu_m{}^2} - \frac{2 \cdot S_6 \cdot S_3}{\mu_m{}^2 \cdot g} - \frac{a \cdot S_3}{\mu_m \cdot c} + \frac{S_6{}^2 - S_7{}^2}{\mu_m{}^2 \cdot g^2} + \frac{a \cdot S_6 + b \cdot S_7}{\mu_m \cdot g \cdot c} + \frac{a^2 - b^2}{4 \cdot c^2} \right]$$

$$C_{12}{}^* = \lambda_m + \frac{V_f}{D} \cdot b \cdot \left[\frac{S_3}{2 \cdot c \cdot \mu_m} - \frac{S_6 - S_7}{2 \cdot c \cdot \mu_m \cdot g} - \frac{a + b}{4 \cdot c^2} \right]$$

$$C_{23}{}^{*} = \lambda_m + \frac{V_f}{D} \cdot \left[\frac{a \cdot S_7}{2 \cdot \mu_m \cdot g \cdot c} - \frac{b \cdot a + b^2}{4 \cdot c^2} \right]$$

$$C_{22}{}^{*} = \lambda_m + 2 \cdot \mu_m - \frac{V_f}{D} \cdot \left[-\frac{a \cdot S_3}{2 \cdot \mu_m \cdot c} + \frac{a \cdot S_6}{2 \cdot \mu_m \cdot g \cdot c} + \frac{a^2 - b^2}{4 \cdot c^2} \right]$$

$$C_{44}{}^{*} = \mu_m - V_f \cdot \left[-\frac{2 \cdot S_3}{\mu_m} + (\mu_m - \mu_f)^{-1} + \frac{4 \cdot S_7}{\mu_m \cdot (2 - 2 \cdot \nu_m)} \right]^{-1}$$

$$C_{66}{}^{*} = \mu_m - V_f \cdot \left[-\frac{S_3}{\mu_m} + (\mu_m - \mu_f)^{-1} \right]^{-1} \tag{1.2}$$

Where

$$D = \frac{a \cdot S_3{}^2}{2 \cdot \mu_m{}^2 \cdot c} - \frac{a \cdot S_6 \cdot S_3}{\mu_m{}^2 \cdot g \cdot c} + \frac{a \cdot \left(S_6{}^2 - S_7{}^2 \right)}{2 \cdot \mu_m{}^2 \cdot g^2 \cdot c} + \frac{S_3{}^2 \cdot (b^2 - a^2)}{2 \cdot \mu_m \cdot c^2} + \frac{S_6 \cdot (a^2 - b^2) + S_7 \cdot (a \cdot b + b^2)}{2 \cdot \mu_m \cdot g \cdot c^2} + \frac{(a^3 - 2 \cdot b^3 - 3 \cdot a \cdot b^2)}{8 \cdot c^3}$$

(1.3)

And

$$a = \mu_f - \mu_m - 2 \cdot \mu_f \cdot \nu_m + 2 \cdot \mu_m \cdot \nu_f$$

$$b = -\mu_m \cdot \nu_m + \mu_f \cdot \nu_f + 2 \cdot \mu_m \cdot \nu_m \cdot \nu_f - 2 \cdot \mu_1 \cdot \nu_m \cdot \nu_f$$

$$c = (\mu_m - \mu_f) \cdot (\mu_f - \mu_m + \mu_f \cdot \nu_f - \mu_m \cdot \nu_m + 2 \cdot \mu_m \cdot \nu_f - 2 \cdot \mu_f \cdot \nu_m + 2 \cdot \mu_m \cdot \nu_m \cdot \nu_f - 2 \cdot \mu_f \cdot \nu_m \cdot \nu_f)$$

$$g = (2 - 2 \cdot \nu_m) \tag{1.4}$$

The subscripts m and f refer to matrix and fibre, respectively. Assuming the fibre and matrix are both isotropic, Lamé constants of both materials are obtained by using

$$\lambda = \frac{E \cdot \nu}{(1+\nu) \cdot (1-2 \cdot \nu)} \tag{1.5}$$

and $\mu = G$, in terms of the Young's modulus E, the Poisson's ratio ν, and the shear modulus G.

For a composite reinforced by long circular cylindrical fibres, periodically arranged in a square array, Fig. 1.9, aligned with x_1-axis, with $a_2 = a_3$, the constants S_3, S_6, and S_7 are given as follows [Luciano and Barbero, 1995]

$$S_3 = 0.49247 - 0.47603 \cdot V_f - 0.02748 \cdot V_f{}^2$$

$$S_6 = 0.36844 - 0.14944 \cdot V_f - 0.27152 \cdot V_f{}^2$$

$$S_7 = 0.12346 - 0.32035 \cdot V_f + 0.23517 \cdot V_f{}^2 \tag{1.6}$$

The resulting tensor C* has a square symmetry (not transverse isotropy) due to the microstructural periodic arrangement in the form of a square array. The tensor C* is therefore described by six constants. However, most composites have random

arrangement of the fibres, Fig. 1.10, resulting in a transversely isotropic stiffness tensor, with only five independent constants. Therefore, the tensor C for a transversely isotropic material can be derived from the tensor C*.

In order to obtain a transversely isotropic stiffness tensor, equivalent in the average sense to the stiffness tensor with square symmetry, the following averaging procedure is used. A rotation θ of the tensor C* about the x_1-axis produces

$$B(\theta) = \overline{T}^{T}(\theta) \cdot C \cdot \overline{T}(\theta) \tag{1.7}$$

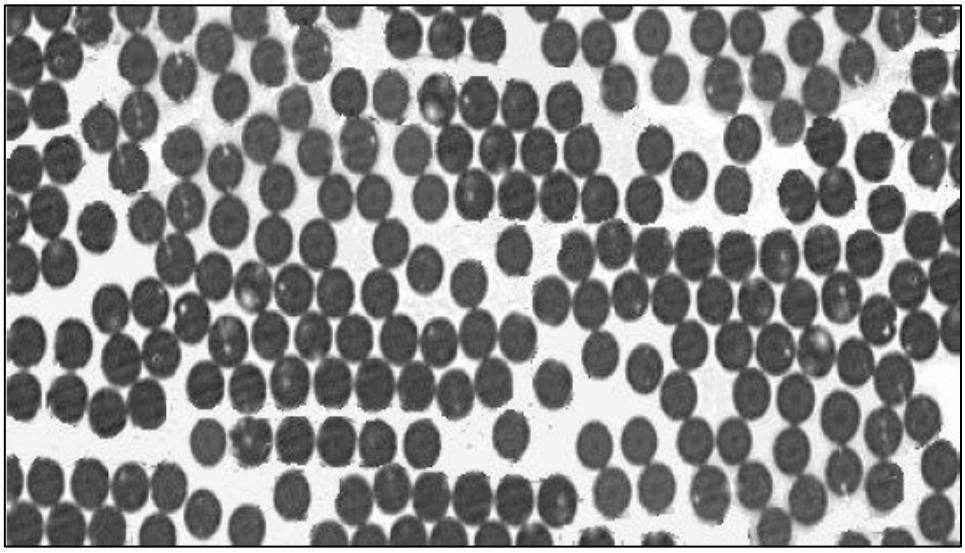

Figure 1.10 Randomly distributed E-glass fibres with 200X magnification

where $\overline{T}(\theta)$ is the coordinate transformation matrix. Then the equivalent transversely isotropic tensor is obtained by averaging as follows

$$\overline{B} = \frac{1}{\pi} \cdot \int_0^{\pi} B(\theta) d\theta \tag{1.8}$$

Then, using the relations between the engineering constants and the components of the $\overline{B}$ tensor, the following expressions are obtained explicitly in terms of the coefficients in Eqs. 1.2 to 1.6 of the tensor C*.

$$E_1 = {C_{11}}^{*} - \frac{2 \cdot {C_{12}}^{*2}}{{C_{22}}^{*} + {C_{23}}^{*}}$$

$$E_2 = \frac{\left(2 \cdot {C_{11}}^{*} \cdot {C_{22}}^{*} + 2 \cdot {C_{11}}^{*} \cdot {C_{23}}^{*} - 4 \cdot {C_{12}}^{*2}\right) \cdot \left({C_{22}}^{*} - {C_{23}}^{*} - 2 \cdot {C_{44}}^{*}\right)}{3 \cdot {C_{11}}^{*} \cdot {C_{22}}^{*} + {C_{11}}^{*} \cdot {C_{23}}^{*} + 2 \cdot {C_{11}}^{*} \cdot {C_{44}}^{*} - 4 \cdot {C_{12}}^{*2}}$$

$$G_{12} = G_{13} = {C_{66}}^{*}$$

$$\nu_{12} = \nu_{13} = \frac{{C_{12}}^{*}}{{C_{22}}^{*} + {C_{23}}^{*}}$$

$$\nu_{23} = \frac{{C_{11}}^{*} \cdot {C_{22}}^{*} + 3 \cdot {C_{11}}^{*} \cdot {C_{23}}^{*} - 2 \cdot {C_{11}}^{*} \cdot {C_{44}}^{*} - 4 \cdot {C_{12}}^{*2}}{3 \cdot {C_{11}}^{*} \cdot {C_{22}}^{*} + {C_{11}}^{*} \cdot {C_{23}}^{*} + 2 \cdot {C_{11}}^{*} \cdot {C_{44}}^{*} - 4 \cdot {C_{12}}^{*2}} \tag{1.9}$$

In paragraph A.1, there is an application of this averaging (Enclosure A).

1.2.5 Numerical homogenization

In general, composites reinforced with parallel fibres display orthotropic material properties at the mesoscale (lamina level). In special cases, such as the hexagonal array shown in Figs. 1.11 and 1.12, the properties become transversely isotropic.

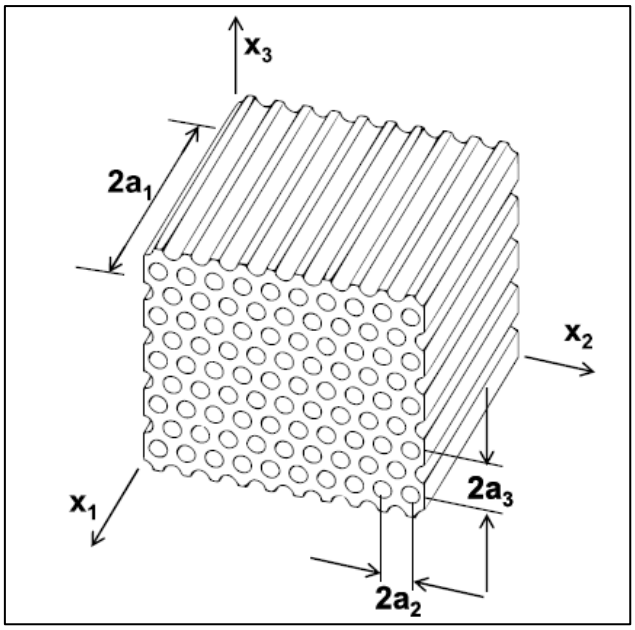

Figure 1.11 Composite material with hexagonal array

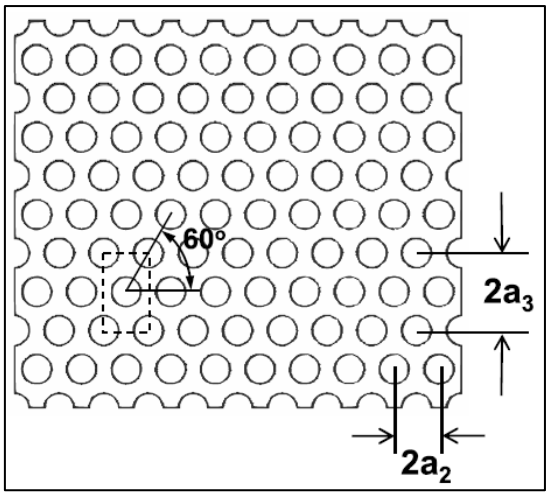

Figure 1.12 Cross-section of the composite material

In most commercially fabricated composites, it is impossible to control the placement of the fibres so precisely and most of the time the resulting microstructure is random. A random microstructure results in transversely isotropic properties at the mesoscale. The analysis of composites with random microstructure still can be done using a fictitious periodic microstructure, such as that shown in Fig. 1.9, then averaging the stiffness tensor C as shown before to obtain the stiffness tensor of a transversely isotropic material. A simpler alternative is to assume that the random microstructure is well approximated by the hexagonal microstructure displayed in Fig. 1.11 and 1.12. Analysis of such

microstructure directly yields a transversely isotropic stiffness tensor, represented by Eq. B.14 (enclosure B).

Once the components of the transversely isotropic tensor C are known, the five elastic properties of the homogenized material can be computed by

$$E_1 = C_{11} - 2 \cdot {C_{12}}^2/(C_{22} + C_{23})$$

$$\nu_{12} = C_{12}/(C_{22} + C_{23})$$

$$E_2 = \left[C_{11} \cdot (C_{22} + C_{23}) - 2 \cdot {C_{12}}^2\right] \cdot (C_{22} - C_{23})/\left(C_{11} \cdot C_{22} - {C_{12}}^2\right)$$

$$\nu_{23} = \left[C_{11} \cdot C_{23} - {C_{12}}^2\right]/\left(C_{11} \cdot C_{22} - {C_{12}}^2\right)$$

$$G_{12} = C_{66} \tag{1.10}$$

The shear modulus G_{23} in the transversal plane can be obtained by the classical relation

$$G = \frac{E}{2 \cdot (1+\nu)} \tag{1.11}$$

or directly as follows

$$G_{23} = C_{44} = \frac{1}{2} \cdot (C_{22} - C_{23}) = \frac{E_2}{2 \cdot (1+\nu_{23})} \tag{1.12}$$

In order to evaluate the overall elastic matrix C of the composite, the RVE is subjected to an average strain $\bar{\epsilon}_\beta$.The six components of strain ${\varepsilon^0}_{ij}$ are applied by enforcing the following boundary conditions on the displacement components

$$-a_2 \le x_2 \le a_2$$

$$u_i(a_1, x_2, x_3) - u_i(-a_1, x_2, x_3) = 2 \cdot a_1 \cdot {\varepsilon_{i1}}^0$$

$$-a_3 \le x_3 \le a_3 \tag{1.13}$$

$$-a_1 \le x_1 \le a_1$$

$$u_i(x_1, a_2, x_3) - u_i(x_1, -a_2, x_3) = 2 \cdot a_2 \cdot {\varepsilon_{i2}}^0$$

$$-a_3 \le x_3 \le a_3 \tag{1.14}$$

$$-a_1 \le x_1 \le a_1$$

$$u_i(x_1, x_2, a_3) - u_i(x_1, x_2, -a_3) = 2 \cdot a_3 \cdot {\varepsilon_{i3}}^0$$

$$-a_2 \le x_2 \le a_2 \tag{1.15}$$

The tensor components of strain, defined in Eq. B.2, are used in Eqs. 1.13 to 1.15. A superscript 0 indicates an applied strain, while a bar indicates a volume average.

Furthermore, $2a_j \cdot \varepsilon^0_{ij}$ is the displacement necessary to enforce a strain ε^0_{ij} over a distance $2 \cdot a_j$ Fig. 1.13.

The strain ε^0_{ij} applied on the boundary by using Eqs. 1.13 to 1.15 results in a complex state of strain inside the RVE. However, the volume average of the strain in the RVE equals the applied strain, as long as there are no discontinuities, such as voids or cracks, inside the RVE, i.e.,

$$\bar{\varepsilon}_{ij} = \frac{1}{V}\int_V \varepsilon_{ij} dV = \varepsilon_{ij}{}^0 \tag{1.16}$$

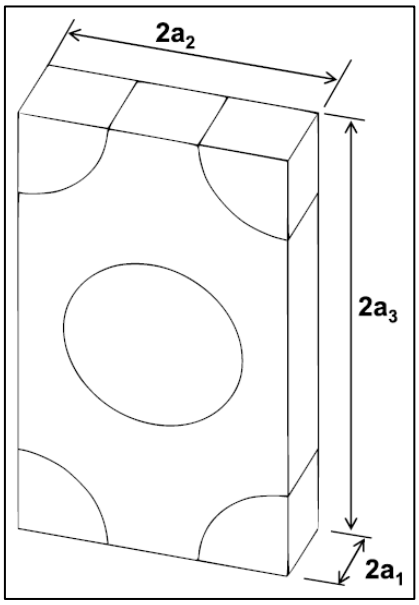

Figure 1.13 Representative volume element (RVE)

For the homogeneous composite material, the relationship between average stress and strain is

$$\bar{\sigma}_\alpha = C_{\alpha\beta}\bar{\epsilon}\beta \tag{1.17}$$

where the relationship between i, j = 1…3 and β = 1…6 is given by the definition of (Voigt) contracted notation

$$\begin{aligned} \alpha &= i \qquad \text{if } i = j \\ \alpha &= 9 - i - j \qquad \text{if } i \neq j \end{aligned} \tag{1.18}$$

Thus, the components of the tensor C are determined solving six elastic models of the RVE subjected to the boundary conditions, Eqs. 1.13 to 1.15, where only one component of the strain ε^0_β is different from zero for each of the six problems.

By choosing a unit value of applied strain, and once the problem defined by the boundary conditions, Eqs. 1.13 to 1.15, is solved, it is possible to compute the stress field σ_α, whose average gives the required components of the elastic matrix, one column at a time, as

$$C_{\alpha\beta} = \bar{\sigma}_\alpha = \frac{1}{V}\int_V \sigma_\alpha(x_1, x_2, x_3) dV \tag{1.19}$$

with $\varepsilon^0_\beta = 1$ and $\alpha, \beta = 1 \ldots 6$. The integrals in Eq. 1.19 are evaluated within each finite element using the Gauss-Legendre quadrature. Commercial programs, such as ANSYS, have the capability to compute the average stress and volume, element by element.

The coefficients in C are found by setting a different problem for each column in Eq. 1.10, as follows.

In order to determine the components C_{i1}, with i = 1, 2, 3, the following strain is applied to stretch the RVE in the fibre direction (x_1-direction)

$$\epsilon_1{}^0 = 1; \qquad \epsilon_2{}^0 = \epsilon_3{}^0 = \gamma_4{}^0 = \gamma_5{}^0 = \gamma_6{}^0 = 0 \tag{1.20}$$

Thus, the displacement boundary conditions, Eqs. 1.13 to 1.15, for the RVE in Figure 1.13 become

$$\begin{aligned}
&u_1(a_1, x_2, x_3) - u_1(-a_1, x_2, x_3) = 2 \cdot a_1 \\
&\qquad\qquad -a_2 \le x_2 \le a_2 \\
&u_2(a_1, x_2, x_3) - u_2(-a_1, x_2, x_3) = 0 \\
&\qquad\qquad -a_3 \le x_3 \le a_3 \\
&u_3(a_1, x_2, x_3) - u_3(-a_1, x_2, x_3) = 0 \\
&\qquad\qquad -a_1 \le x_1 \le a_1 \\
&u_i(x_1, a_2, x_3) - u_i(x_1, -a_2, x_3) = 0 \\
&\qquad\qquad -a_3 \le x_3 \le a_3 \\
&\qquad\qquad -a_1 \le x_1 \le a_1 \\
&u_i(x_1, x_2, a_3) - u_i(x_1, x_2, -a_3) = 0 \\
&\qquad\qquad -a_2 \le x_2 \le a_2
\end{aligned} \tag{1.21}$$

The conditions in Eq. 1.21 are constraints on the relative displacements between opposite faces of the RVE. Because of the symmetries of the RVE and symmetry of the constraints, Eq. 1.21, only one-eighth of the RVE needs to be modelled in finite element analysis (FEA). Assuming the top-right-front portion is modelled, Fig. 1.14, the following equivalent external boundary conditions, i.e., boundary conditions on components of displacements and stresses, can be used

$$\begin{aligned}
u_1(a_1, x_2, x_3) &= a_1 \\
u_1(0, x_2, x_3) &= 0 \\
\sigma_{12}(a_1, x_2, x_3) &= 0 \quad 0 \le x_2 \le a_2 \\
\sigma_{12}(0, x_2, x_3) &= 0 \quad 0 \le x_3 \le a_3
\end{aligned}$$

$$\sigma_{13}(a_1, x_2, x_3) = 0$$
$$\sigma_{13}(0, x_2, x_3) = 0$$

$$u_2(x_1, a_2, x_3) = 0$$
$$u_2(x_1, 0, x_3) = 0$$
$$\sigma_{21}(x_1, a_2, x_3) = 0 \quad 0 \le x_1 \le a_1$$
$$\sigma_{21}(x_1, 0, x_3) = 0 \quad 0 \le x_3 \le a_3$$
$$\sigma_{23}(x_1, a_2, x_3) = 0$$
$$\sigma_{23}(x_1, 0, x_3) = 0$$

$$u_3(x_1, x_2, a_3) = 0$$
$$u_3(x_1, x_2, 0) = 0$$
$$\sigma_{31}(x_1, x_2, a_3) = 0 \quad 0 \le x_1 \le a_1$$
$$\sigma_{31}(x_1, x_2, 0) = 0 \quad 0 \le x_2 \le a_2$$
$$\sigma_{32}(x_1, x_2, a_3) = 0$$
$$\sigma_{32}(x_1, x_2, 0) = 0$$

(1.22)

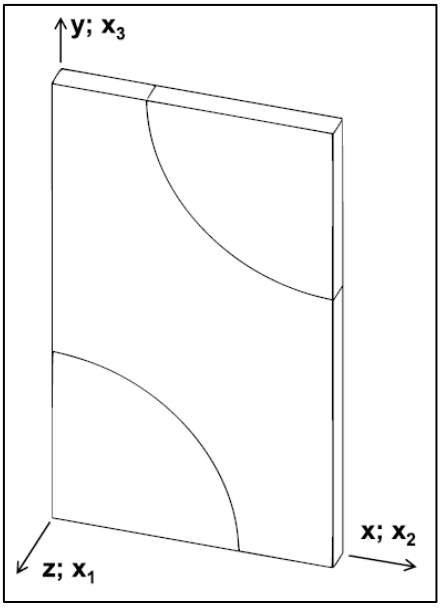

Figure 1.14 One-eighth model of the RVE, with the fibre along the z-axis, which corresponds to the x1-direction in the equations

Symmetry boundary conditions are applied on the planes $x_1 = 0$, $x_2 = 0$, $x_3 = 0$. Then, a uniform displacement is applied on the plane $x_1 = a_1$. The stress boundary conditions do not need to be applied explicitly in a displacement-based formulation. The displacement

components in Eq. 1.22 represent strains that are not zero along the x_1-direction and zero along the other two directions. The stress boundary conditions listed in Eq. 1.22 reflect the fact that, in the coordinate system used, the composite material is macroscopically orthotropic and that the constituent materials are orthotropic too. Therefore, there is no coupling between extension and shear strains. This is evidenced by the zero coefficients above the diagonal in columns 4 to 6 in Eq. 1.10.

The coefficients in column one of Eq. 1.10 are found by using Eq. 1.19, as follows

$$C_{\alpha 1} = \overline{\sigma}_{\alpha} = \frac{1}{V}\int_V \sigma_{\alpha}(x_1, x_2, x_3)dV \tag{1.23}$$

The components $C_{\alpha 2}$, with $\alpha = 1, 2, 3$, are determined by setting

$$\epsilon_2{}^0 = 1; \qquad \epsilon_1{}^0 = \epsilon_3{}^0 = \gamma_4{}^0 = \gamma_5{}^0 = \gamma_6{}^0 = 0 \tag{1.24}$$

Thus, the following boundary conditions on displacements can be used

$$\begin{gathered} u_1(a_1, x_2, x_3) = 0 \\ u_1(0, x_2, x_3) = 0 \\ u_2(x_1, a_2, x_3) = a_2 \\ \\ u_2(x_1, 0, x_3) = 0 \\ u_3(x_1, x_2, a_3) = 0 \\ u_3(x_1, x_2, 0) = 0 \end{gathered} \tag{1.25}$$

The trivial stress boundary conditions have not been listed because they are automatically enforced by the displacement-based FEA formulation. Using Eq. 1.19, the stiffness terms in the second column of C are computed as

$$C_{\alpha 2} = \overline{\sigma}_{\alpha} = \frac{1}{V}\int_V \sigma_{\alpha 2}(x_1, x_2, x_3)dV \tag{1.26}$$

Because of the transverse isotropy of the material, Eq. 1.10, the components of the third column of the matrix C can be determined from the first and the second column, so no further computation is required. However, if desired, the components $C_{\alpha 3}$, with $\alpha = 1, 2, 3$, can be found by applying the following strain

$$\varepsilon_3{}^0 = 1; \qquad \varepsilon_1{}^0 = \varepsilon_2{}^0 = \gamma_4{}^0 = \gamma_5{}^0 = \gamma_6{}^0 = 0 \tag{1.27}$$

Thus, the following boundary conditions on displacement can be used

$$\begin{gathered} u_1(a_1, x_2, x_3) = 0 \\ u_1(0, x_2, x_3) = 0 \\ u_2(x_1, a_2, x_3) = 0 \\ \\ u_2(x_1, 0, x_3) = 0 \end{gathered}$$

$$u_3(x_1, x_2, a_3) = a_3$$
$$u_3(x_1, x_2, 0) = 0$$

(1.28)

The required components of C are determined by averaging the stress field as in Eq. 1.19.

In paragraph A.2, there is a calculation of this tensor (Enclosure A).

If the material is orthotropic, a procedure similar to that used for column number six must be used in order to obtain the fourth column of C. But for a transversally isotropic material, only the term C_{44} is nonzero in column 4 of Eq. 1.10 and it can be determined as a function of the other components as

$$C_{44} = \frac{1}{2} \cdot (C_{22} - C_{23}) \tag{1.29}$$

If the material is orthotropic, a procedure similar to that used for column number six must be used in order to obtain the fifth column of C. But for a transversally isotropic material, only the term $C_{55} = C_{66}$ is nonzero in column 5 of Eq. 1.10 and it can be found from column number six.

Because of the lack of symmetry of the loads, for the sixth column it is not possible to use boundary conditions as was done for the first three columns. Thus, the boundary conditions must be enforced by using coupling constraint equations (called CE in most finite element analysis (FEA) commercial packages).

According to Eq. 1.10, only the term C_{66} is different from zero. The components $C_{\alpha 6}$ are determined by setting

$$\gamma_6{}^0 = \varepsilon_{12}{}^0 + \varepsilon_{21}{}^0 = 1; \qquad \epsilon_1{}^0 = \epsilon_2{}^0 = \epsilon_3{}^0 = \gamma_4{}^0 = \gamma_5{}^0 = 0 \tag{1.30}$$

It is important not to forget that $\varepsilon^0_{12} = 1/2$ is applied between $x_1 = \pm a_1$ and another one-half is applied between $x_2 = \pm a_2$. In this case, the CE applied between two periodic faces (except points in the edges and vertices) are given as a particular case of Eqs. 1.13 to 1.15) as follows

$$u_1(a_1, x_2, x_3) - u_1(-a_1, x_2, x_3) = 0$$
$$-a_2 \le x_2 \le a_2$$
$$u_2(a_1, x_2, x_3) - u_2(-a_1, x_2, x_3) = a_1$$
$$-a_3 \le x_3 \le a_3$$
$$u_3(a_1, x_2, x_3) - u_3(-a_1, x_2, x_3) = 0$$

$$u_1(x_1, a_2, x_3) - u_1(x_1, -a_2, x_3) = a_2$$
$$-a_1 \le x_1 \le a_1$$
$$u_2(x_1, a_2, x_3) - u_2(x_1, -a_2, x_3) = 0$$

$$-a_3 \le x_3 \le a_3$$

$$u_3(x_1, a_2, x_3) - u_3(x_1, -a_2, x_3) = 0$$

$$u_1(x_1, x_2, a_3) - u_1(x_1, x_2, -a_3) = 0$$

$$-a_1 \le x_1 \le a_1$$

$$u_2(x_1, x_2, a_3) - u_2(x_1, x_2, -a_3) = 0$$

$$-a_2 \le x_2 \le a_2$$

$$u_3(x_1, x_2, a_3) - u_3(x_1, x_2, -a_3) = 0 \tag{1.31}$$

Equally, it is remarkable that the components of Eq. 1.31 are applied between opposite points on the faces of the RVE but not on edges and vertices. In FEA, CE are applied between degrees of freedom (DOF). Once a DOF has been used in a CE, it cannot be used in another CE. For example, the first component of Eq. 1.31 for $x_2 = a_2$ becomes

$$u_1(a_1, a_2, x_3) - u_1(-a_1, a_2, x_3) = 0 \tag{1.32}$$

The DOF associated to $u_1(a_1,a_2,x_3)$ (for all $-a_3 < x_3 < a_3$) are eliminated because they are identical to $u_1(-a_1, a_2,x_3)$, as required by Eq. 1.32 and enforced by a CE based on the same. Once the DOF are eliminated, they cannot be used in another CE. For example, the fourth of Eq. 1.32 at $x_1 = a_1$ is

$$u_1(a_1, a_2, x_3) - u_1(a_1, -a_2, x_3) = 0 \tag{1.33}$$

but this CE cannot be enforced because the DOF associated to $u_1(a_1,a_2,x_3)$ have been eliminated by the CE associated to Eq. 1.32. As a corollary, CE on the edges and vertices of the RVE must be written separately from Eq. 1.31. Furthermore, only three equations, one for each component of displacement u_i can be written between a pair of edges or pair of vertices. Simply put, there are only three displacements that can be used to enforce periodicity conditions.

For pairs of edges, the task at hand is to reduce the first six equations of Eq. 1.31 to three equations that can be applied between pairs of edges for the interval $-a_3 < x_3 < a_3$. Again, the new equations will not be applied at $x_3 = \pm a_3$ because those are vertices, which will be dealt with separately. Therefore, the last three equations of Eq. 1.31 are inconsequential at this point.

The only way to reduce six equations to three, in terms of six unique DOF, is to add the equations for diagonally opposite edges. Figure 1.15 is a top view of the RVE looking from the positive x_3 axis. Point A in Fig. 1.15 represents the edge formed by the planes $x_1 = a_1$ and $x_2 = a_2$. This location is constrained by the first of Eq. 1.31 at that location, which is precisely Eq. 1.32. Point C in Fig. 1.15 represents the edge formed by the planes $x_1 = -a_1$ and $x_2 = -a_2$. This location is constrained by the fourth of Eq. 1.31, which at that location reduces to

$$u_1(-a_1, a_2, x_3) - u_1(-a_1, -a_2, x_3) = a_2 \tag{1.34}$$

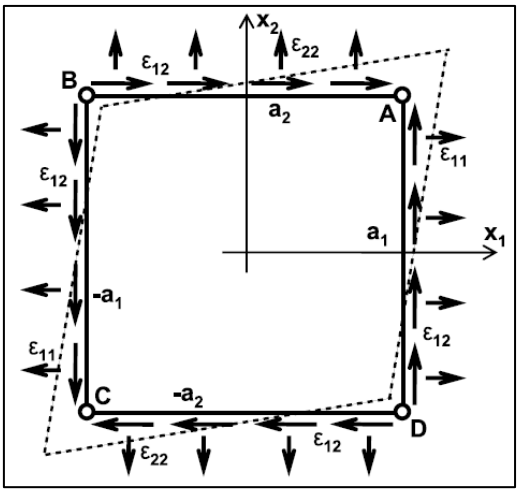

Figure 1.15 Top view of the RVE showing that two displacements must be applied at edges to impose shear strain

Adding Eq. 1.32 and Eq. 1.34 yields a single equation as follows

$$u_1(a_1, a_2, x_3) - u_1(-a_1, -a_2, x_3) = a_2 \tag{1.35}$$

Repeating the procedure for the components u_2 and u_3, and grouping the resulting equations with Eq. 1.35 results in

$$\begin{aligned} u_1(a_1, a_2, x_3) - u_1(-a_1, -a_2, x_3) &= a_2 \\ u_2(a_1, a_2, x_3) - u_2(-a_1, -a_2, x_3) &= a_1 \qquad -a_3 \le x_3 \le a_3 \\ u_3(a_1, a_2, x_3) - u_3(-a_1, -a_2, x_3) &= 0 \end{aligned} \tag{1.36}$$

Considering Eq. 1.31 between edges B and D in Fig. 1.15 results in

$$\begin{aligned} u_1(a_1, -a_2, x_3) - u_1(-a_1, a_2, x_3) &= -a_2 \\ u_2(a_1, -a_2, x_3) - u_2(-a_1, a_2, x_3) &= a_1 \qquad -a_3 \le x_3 \le a_3 \\ u_3(a_1, -a_2, x_3) - u_3(-a_1, a_2, x_3) &= 0 \end{aligned} \tag{1.37}$$

The planes $x_1 = \pm a_1$ and $x_3 = \pm a_3$ define two pairs of edges restrained by the following six CE

$$\begin{aligned} u_1(a_1, x_2, a_3) - u_1(-a_1, x_2, -a_3) &= 0 \\ u_2(a_1, x_2, a_3) - u_2(-a_1, x_2, -a_3) &= a_1 \qquad -a_2 \le x_2 \le a_2 \\ u_3(a_1, x_2, a_3) - u_3(-a_1, x_2, -a_3) &= 0 \end{aligned}$$

$$\begin{aligned} u_1(a_1, x_2, -a_3) - u_1(-a_1, x_2, a_3) &= 0 \\ u_2(a_1, x_2, -a_3) - u_2(-a_1, x_2, a_3) &= a_1 \qquad -a_2 \le x_2 \le a_2 \end{aligned}$$

$$u_3(a_1, x_2, -a_3) - u_3(-a_1, x_2, a_3) = 0 \tag{1.38}$$

The six CE for the two pairs of edges defined by the planes $x_2 = \pm a_2$ and $x_3 = \pm a3$ are

$$\begin{aligned} u_1(x_1, a_2, a_3) - u_1(x_1, -a_2, -a_3) &= a_2 \\ u_2(x_1, a_2, a_3) - u_2(x_1, -a_2, -a_3) &= 0 \qquad -a_1 \le x_1 \le a_1 \\ u_3(x_1, a_2, a_3) - u_3(x_1, -a_2, -a_3) &= 0 \end{aligned}$$

$$\begin{aligned} u_1(x_1, a_2, -a_3) - u_1(x_1, -a_2, a_3) &= a_2 \\ u_2(x_1, a_2, -a_3) - u_2(x_1, -a_2, a_3) &= 0 \qquad -a_1 \le x_1 \le a_1 \\ u_3(x_1, a_2, -a_3) - u_3(x_1, -a_2, a_3) &= 0 \end{aligned} \tag{1.39}$$

Eqs. 1.36 to 1.39 are not applied at the vertices because redundant CE would appear among pairs of vertices that are located symmetrically with respect to the centre of the RVE's volume. Therefore, each of the four pairs of vertices need to be constrained one at a time. The resulting CE are as follows

$$\begin{aligned} u_1(a_1, a_2, a_3) - u_1(-a_1, -a_2, -a_3) &= a_2 \\ u_2(a_1, a_2, a_3) - u_2(-a_1, -a_2, -a_3) &= a_1 \\ u_3(a_1, a_2, a_3) - u_3(-a_1, -a_2, -a_3) &= 0 \end{aligned}$$

$$\begin{aligned} u_1(a_1, a_2, -a_3) - u_1(-a_1, -a_2, a_3) &= a_2 \\ u_2(a_1, a_2, -a_3) - u_2(-a_1, -a_2, a_3) &= a_1 \\ u_3(a_1, a_2, -a_3) - u_3(-a_1, -a_2, a_3) &= 0 \end{aligned}$$

$$\begin{aligned} u_1(-a_1, a_2, a_3) - u_1(a_1, -a_2, -a_3) &= a_2 \\ u_2(-a_1, a_2, a_3) - u_2(a_1, -a_2, -a_3) &= -a_1 \\ u_3(-a_1, a_2, a_3) - u_3(a_1, -a_2, -a_3) &= 0 \end{aligned}$$

$$\begin{aligned} u_1(a_1, -a_2, a_3) - u_1(-a_1, a_2, -a_3) &= -a_2 \\ u_2(a_1, -a_2, a_3) - u_2(-a_1, a_2, -a_3) &= a_1 \\ u_3(a_1, -a_2, a_3) - u_3(-a_1, a_2, -a_3) &= 0 \end{aligned} \tag{1.40}$$

Eqs. 1.31 and 1.40 constrain the volume of the RVE with a unit strain given by Eq 1.30. The FEA of this model yields all the component of stress. As discussed previously, element by element averages of these components of stress are available from the FEA or they can be easily computed by post-processing. Therefore, the coefficient C_{66}, for this case is found using Eq. 1.19 written as

$$C_{66} = \overline{\sigma}_6 = \frac{1}{V}\int_V \sigma_6(x_1, x_2, x_3)dV \tag{1.41}$$

with $\gamma^0_6 = 1$.

1.2.6 Global-local analysis

In global-local analysis, Fig. 1.16, an RVE is used to perform a refined computation at each Gauss integration point of the global model. The global model is used to compute the displacements and resulting strains, assuming that the material is homogeneous. The local model takes the inhomogeneities into account by modelling them with an RVE and thus providing a better computation of stress, state variables, as well as secant and tangent constitutive tensors. In a way, the local analysis is a surrogate for a constitutive equation that might be unknown due to the complexity of the material behaviour inside the RVE. Also, the computational cost may be too high to model the entire structure with the refinement that can be afforded inside the RVE.

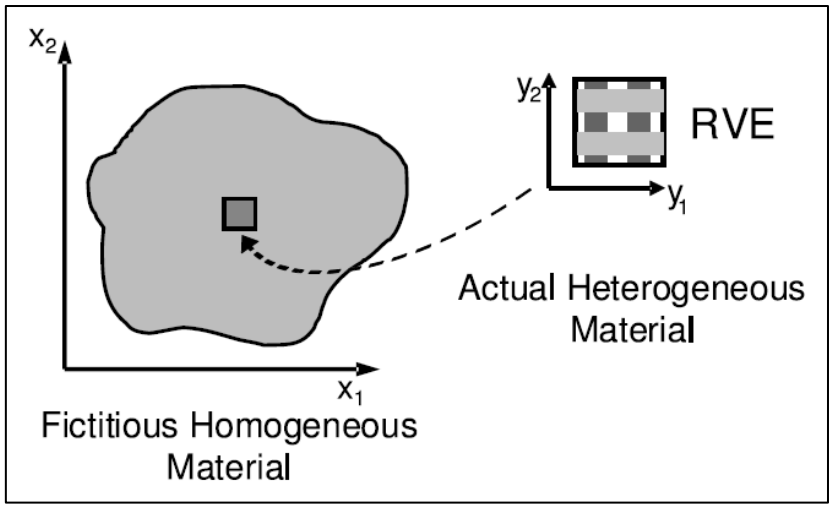

Figure 1.16 Global-local analysis using RVE

Eqs. 1.13 to 1.15 are used in numerical homogenization to enforce one component of strain at a time, with the objective of finding the equivalent elastic properties of the material. These equations are still valid for a general state of strain applied to the RVE but care must be taken with the specification of periodic boundary conditions at the edges and vertices, as discussed before. Eqs. 1.13 to 1.15 are nine constraint equations that can be imposed between all the pairs of periodic points on the faces of the RVE except on the edges and vertices.

On the faces $x_1 = \pm a_1$, u_1 is used to impose ε^0_{11}, u_2 is used to impose $\varepsilon^0_{21} = \gamma_6/2$, and u_3 is used to impose $\varepsilon^0_{31} = \gamma_5/2$. To achieve this, Eq. 1.13 is expanded into its three components, using tensor notation for strains, as follows

$$u_1(a_1, x_2, x_3) - u_1(-a_1, x_2, x_3) = 2 \cdot a_1 \cdot {\varepsilon_{11}}^0$$

$$u_2(a_1, x_2, x_3) - u_2(-a_1, x_2, x_3) = 2 \cdot a_1 \cdot {\varepsilon_{21}}^0$$

$$u_3(a_1, x_2, x_3) - u_3(-a_1, x_2, x_3) = 2 \cdot a_1 \cdot {\varepsilon_{31}}^0 \quad (1.42)$$

On the faces $x_2 = \pm a_2$, u_1 is used to impose ${\varepsilon^0}_{12} = \gamma_6/2$, u_2 is used to impose ${\varepsilon^0}_{22}$, and u_3 is used to impose ${\varepsilon^0}_{32} = \gamma_4/2$. Therefore, Eq. 1.14 is expanded into its three components, using tensor notation for strains, as follows

$$\begin{aligned} u_1(x_1, a_2, x_3) - u_1(x_1, -a_2, x_3) &= 2 \cdot a_2 \cdot \varepsilon_{12} \\ u_2(x_1, a_2, x_3) - u_2(x_1, -a_2, x_3) &= 2 \cdot a_2 \cdot \varepsilon_{22} \\ u_3(x_1, a_2, x_3) - u_3(x_1, -a_2, x_3) &= 2 \cdot a_2 \cdot \varepsilon_{32} \end{aligned} \quad (1.43)$$

On the faces $x_3 = \pm a_3$, u_1 is used to impose ${\varepsilon^0}_{13} = \gamma_5/2$, u_2 is used to impose ${\varepsilon^0}_{23} = \gamma_4/2$, and u_3 is used to impose ${\varepsilon^0}_{33}$. Therefore, Eq. 1.15 is expanded into its three components, using tensor notation for strains, as follows

$$\begin{aligned} u_1(x_1, x_2, a_3) - u_1(x_1, x_2, -a_3) &= 2 \cdot a_3 \cdot \varepsilon_{13} \\ u_2(x_1, x_2, a_3) - u_2(x_1, x_2, -a_3) &= 2 \cdot a_3 \cdot \varepsilon_{23} \\ u_3(x_1, x_2, a_3) - u_3(x_1, x_2, -a_3) &= 2 \cdot a_3 \cdot \varepsilon_{33} \end{aligned} \quad (1.44)$$

The planes $x_1 = \pm a_1$ and $x_2 = \pm a_2$ define two pairs of edges, for which Eqs. 1.42 to 1.44 reduce to the following six equations (with i = 1,2,3), as follows

$$\begin{aligned} u_i(a_1, a_2, x_3) - u_i(-a_1, -a_2, x_3) - 2 \cdot a_1 \cdot \varepsilon_{i1} - 2 \cdot a_2 \cdot \varepsilon_{i2} &= 0 \\ u_i(a_1, -a_2, x_3) - u_i(-a_1, a_2, x_3) - 2 \cdot a_1 \cdot \varepsilon_{i1} + 2 \cdot a_2 \cdot \varepsilon_{i2} &= 0 \end{aligned} \quad (1.45)$$

The planes $x_1 = \pm a_1$ and $x_3 = \pm a_3$ define two pairs of edges, for which Eqs. 1.42 to 1.44 reduce to the following six equations (with i = 1,2,3), as follows

$$\begin{aligned} u_i(a_1, x_2, a_3) - u_i(-a_1, x_2, -a_3) - 2 \cdot a_1 \cdot \varepsilon_{i1} - 2 \cdot a_3 \cdot \varepsilon_{i3} &= 0 \\ u_i(a_1, x_2, -a_3) - u_i(-a_1, x_2, a_3) - 2 \cdot a_1 \cdot \varepsilon_{i1} + 2 \cdot a_3 \cdot \varepsilon_{i3} &= 0 \end{aligned} \quad (1.46)$$

The planes $x_2 = \pm a_2$ and $x_3 = \pm a_3$ define two pairs of edges, for which Eqs. 1.42 to 1.44 reduce to the following six equations (with i = 1,2,3), as follows

$$\begin{aligned} u_i(x_1, a_2, a_3) - u_i(x_1, -a_2, -a_3) - 2 \cdot a_2 \cdot \varepsilon_{i2} - 2 \cdot a_3 \cdot \varepsilon_{i3} &= 0 \\ u_i(x_1, a_2, -a_3) - u_i(x_1, -a_2, a_3) - 2 \cdot a_2 \cdot \varepsilon_{i2} + 2 \cdot a_3 \cdot \varepsilon_{i3} &= 0 \end{aligned} \quad (1.47)$$

Four pairs of corners need to be analysed one at a time. For each pair, the corners are located symmetrically with respect to the centre of the RVE located at coordinates (0,0,0). The resulting CE are as follows

$$\begin{aligned} u_i(a_1, a_2, a_3) - u_i(-a_1, -a_2, -a_3) - 2 \cdot a_1 \cdot \varepsilon_{i1} - 2 \cdot a_2 \cdot \varepsilon_{i2} - 2 \cdot a_3 \cdot \varepsilon_{i3} &= 0 \\ u_i(a_1, a_2, -a_3) - u_i(-a_1, -a_2, a_3) - 2 \cdot a_1 \cdot \varepsilon_{i1} - 2 \cdot a_2 \cdot \varepsilon_{i2} + 2 \cdot a_3 \cdot \varepsilon_{i3} &= 0 \\ u_i(-a_1, a_2, a_3) - u_i(a_1, -a_2, -a_3) + 2 \cdot a_1 \cdot \varepsilon_{i1} - 2 \cdot a_2 \cdot \varepsilon_{i2} - 2 \cdot a_3 \cdot \varepsilon_{i3} &= 0 \\ u_i(a_1, -a_2, a_3) - u_i(-a_1, a_2, -a_3) - 2 \cdot a_1 \cdot \varepsilon_{i1} + 2 \cdot a_2 \cdot \varepsilon_{i2} - 2 \cdot a_3 \cdot \varepsilon_{i3} &= 0 \end{aligned} \quad (1.48)$$

A similar procedure to that used to obtain the RVE at the microscale can be used to analyse laminates on the mesoscale. In this case the RVE represents a laminate.

1.2.7 Numerical Simulation: Heat transfer

One of the tasks proposed in this work is the simulation with the purpose of studying the temperatures distribution and the stresses in the piece during a chilling process.

Simulation software are nowadays widely used to simulate complex processes, where the interests is to know beforehand what will happen. For example, in the area of MMC, ABAQUS, ANSYS and others software are used. These softwares handle the laws which control the heat transfer.

The basic energy balance is:

$$\int_V \rho \cdot \dot{U} \cdot dV = \int_S q_S \cdot dS + \int_V q_V \cdot dV \tag{1.49}$$

Where V is a volume of solid material, with surface area S, ρ is the density of the material, $\dot{U}$ is the material time rate of the internal energy, q_S is the heat flux per unit area of the body and q_V is the heat supplied externally into the body per unit volume.

The equation of heat flow balance inside a body in Cartesian coordinates is:

$$-\frac{\partial}{\partial x}\left(k_x \cdot \frac{\partial T}{\partial x}\right) - \frac{\partial}{\partial y}\left(k_y \cdot \frac{\partial T}{\partial y}\right) - \frac{\partial}{\partial z}\left(k_z \cdot \frac{\partial T}{\partial z}\right) + q_V = \rho \cdot C \cdot \frac{\partial T}{\partial t} \tag{1.50}$$

Where k is the thermal conductivity, T is the temperature and C is the specific heat of material.

Except in the phase changes, the internal energy can be related with the specific heat, by means of the following equation:

$$C(T) = \frac{dU}{dT} \tag{1.51}$$

The phase change supposes the appearance of a latent heat, added to the effect of the specific heat (see Fig. 1.17 and 1.18). For many cases it is reasonable to assume that the phase change occurs within a known temperature range and the process is modelled with just a generation of heat for unit of mass. However, in some cases, it may be necessary to include a kinetic theory for the phase change to model the effect accurately.

The equation of flow balance is:

$$\rho \cdot \frac{\partial U}{\partial t} + \frac{\partial}{\partial x}\left(k_x \cdot \frac{\partial T}{\partial x}\right) + \frac{\partial}{\partial y}\left(k_y \cdot \frac{\partial T}{\partial y}\right) + \frac{\partial}{\partial z}\left(k_z \cdot \frac{\partial T}{\partial z}\right) - q_V = 0 \tag{1.52}$$

The convection and radiation processes take place at the surface of the solid and they can be defined by different laws.

The heat convection process is governed by

$$q_{SC} = h \cdot (T - T^0) \tag{1.53}$$

Where h = h(x,t) is the film coefficient, $T^0 = T^0(x,t)$ is the sink temperature and $q_{SC} = q_{SC}(x,T)$ is the surface heat flux per area.

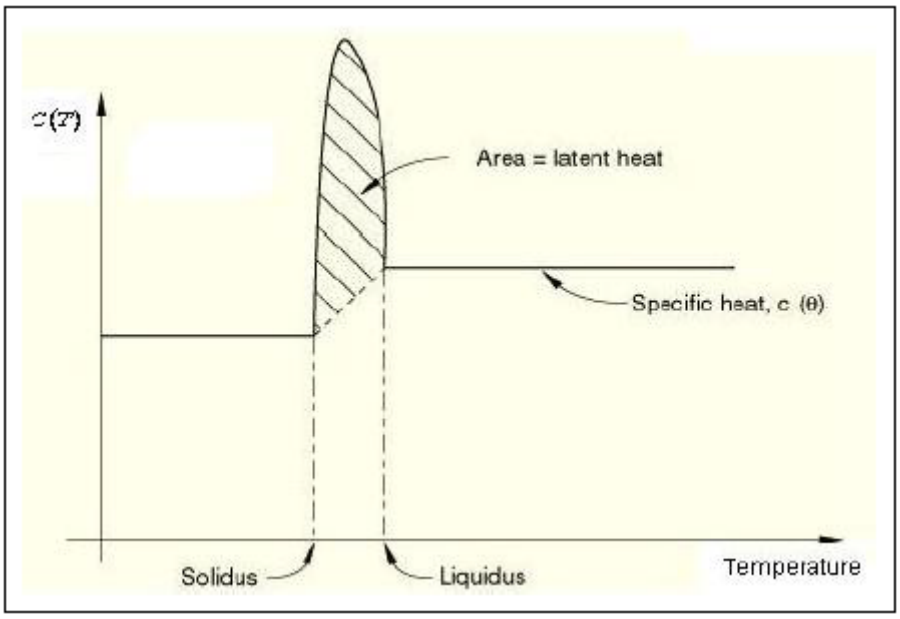

Figure 1.17 Relationship between specific heat and temperature

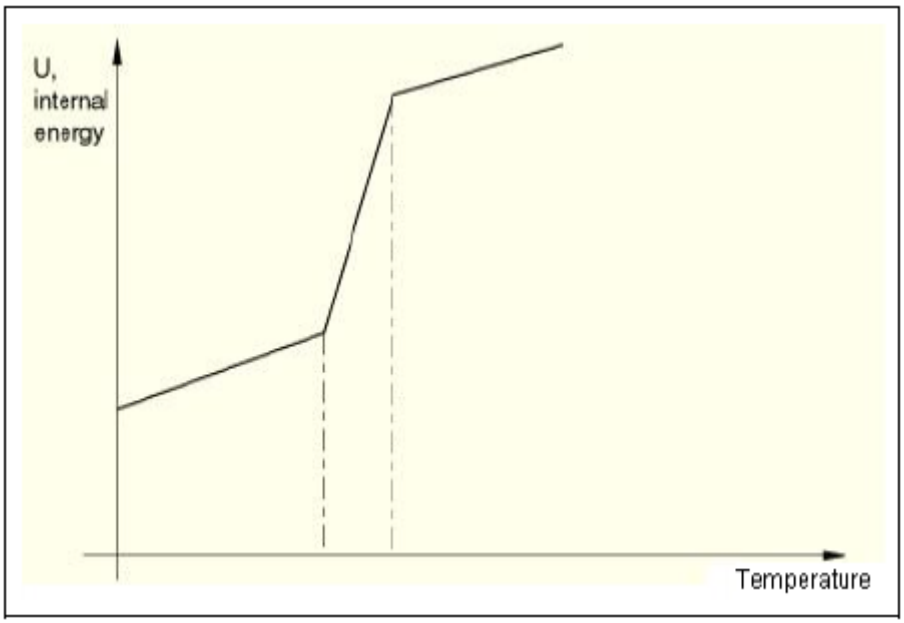

Figure 1.18 Relationship between internal energy and temperature

The heat radiation process is the transfer of energy via electromagnetic waves. The waves travel at the speed of light, and energy transfer requires no medium. Thermal radiation is just a small band on the electromagnetic spectrum. Because the heat flow that radiation causes varies with the fourth power of the body's absolute temperature, radiation analyses are highly nonlinear.

$$q_{SR} = A[(T - T^z)^4 - (T^0 - T^z)^4] \tag{1.54}$$

Where A is the radiation constant, emissivity (C.1 in enclosure C) times the Stefan-Boltzmann constant, and T^z is the absolute zero on the temperature scale used.

The ANSYS program provides four methods for radiation analysis, each one for a different situation:

- The radiation link element, LINK31, for simple problems involving radiation between two points or several pairs of points.
- The surface effect elements, SURF151 and SURF152, for radiation between a surface and a point.
- Radiation Matrix method, AUX12, for more generalized radiation problems involving two or more surfaces.
- Radiosity Solver method for more generalized radiation problems in 3-D/2-D involving two or more surfaces.

The Radiosity Solver method accounts for the heat exchange between radiating bodies by solving for the outgoing radiative flux for each surface, when the surface temperatures for all surfaces are known. The surface fluxes provide boundary conditions to the finite element model for the conduction process analysis. When new surface temperatures are computed, due to either a new time step or iteration cycle, new surface flux conditions are found by repeating the process. The surface temperatures used in the computation must be uniform over each surface facet to satisfy the conditions of the radiation model.

In the radiation matrix method, for a system of two radiating surfaces, Eq. C.16 in enclosure C can be expanded as:

$$Q_i = \sigma \cdot \varepsilon_i \cdot F_{ij} \cdot A_i \cdot \left(T_i{}^2 + T_j{}^2\right) \cdot \left(T_i + T_j\right) \cdot \left(T_i - T_j\right) \tag{1.55}$$

or

$$Q_i = K' \cdot \left(T_i - T_j\right) \tag{1.56}$$

where:

$$K' = \sigma \cdot \varepsilon_i \cdot F_{ij} \cdot A_i \cdot \left(T_i{}^2 + T_j{}^2\right) \cdot \left(T_i + T_j\right) \tag{1.57}$$

K' cannot be calculated directly since it is a function of the unknowns T_i and T_j. The temperatures from previous iterations are used to calculate K' and the solution is computed iteratively.

For a more general case, Eq. C.13 in enclosure C can be used to construct a single row in the following matrix equation:

$$[C]\{Q\} = [D]\{T^4\} \tag{1.58}$$

such that:

$$\text{each row j in } [C] = \left(\frac{\delta_{ji}}{\varepsilon_i} - F_{ji} \cdot \frac{1-\varepsilon_i}{\varepsilon_i}\right) \cdot \frac{1}{A_i}, \quad i = 1,2 \dots N \tag{1.59}$$

$$\text{each row j in } [D] = \left(\delta_{ji} - F_{ji}\right) \cdot \sigma, \quad i = 1,2 \dots N \tag{1.60}$$

Solving for $\{Q\}$:

$$\{Q\} = [K^{ts}] \cdot \{T^4\} \tag{1.61}$$

and therefore:

$$[K^{ts}] = [C]^{-1} \cdot [D] \tag{1.62}$$

Eq. 1.61 is analogous to Eq. C.13 in enclosure C and can be set up for standard matrix equation solution by the process similar to the steps shown in Eqs. 1.55 and 1.56.

$$\{Q\} = [K'] \cdot \{T\} \tag{1.63}$$

$[K']$ now includes T^3 terms and is calculated in the same manner as in Eq. 1.56. MATRIX50 (the substructure element) has an option that implements the solution phase to calculate $[K']$. The AUX12 utility is used to create the substructure radiation matrix. AUX12 calculates the effective conductivity matrix, $[K^{ts}]$, in Eq. 1.61, as well as the view factors required for finding $[K^{ts}]$. The user defines flat surfaces to be used in AUX12 by overlaying nodes and elements on the radiating edge of a 2-D model or the radiating face of a 3-D model.

Two methods are available in the radiation matrix method to calculate the view factors, the non-hidden method and the hidden method (C.3 in enclosure C).

Radiosity (radiation heat flux) solver method is supported by all 3-D/2-D elements having a temperature degree of freedom.

PLANE55 is one of the elements supported for the radiosity method include.

The radiosity solver method consists of five steps:

- Define the radiating surfaces.
- Define Solution options.
- Define View Factor options.
- Calculate and query view factors.
- Define load options.

The radiating surfaces are defined by performing the following tasks:

- For the radiosity solution method radiating surfaces are faces of a 3-D model or sides of a 2-D model. In the Radiosity Solver Method, you can have up to ten enclosures, with surfaces radiating to each other.

- Flag the radiation surfaces for a given emissivity and enclosure number using the SF, SFA, SFE, or SFL command. For all surface or line facets radiating to each other, issue the same enclosure number.

For the radiosity solver method, radiation is calculated as a heat flow rate vector. Recall that, as a simplified viewpoint, radiation heat flow rate between two surfaces i and j is defined as Eq. C.16 in enclosure C:

$$Q_i = A_i \cdot \varepsilon_i \cdot F_{ij}{}' \cdot \sigma \cdot \left(T_i{}^4 - T_j{}^4\right)$$

Assuming that the temperatures at the radiation surfaces are known, the radiation heat flux (radiosity) can be calculated. The radiation heat flux can then be applied to the thermal system as a load vector:

$$[K] \cdot \{T\} = \{Q\} + \{Q_{rad}\}$$

This is the basics of the radiosity solution method. Since the surface temperatures and the radiative fluxes are not necessarily known in advance, the radiosity equation and the conduction equation above are solved in a segregated, iterative way until convergence is achieved.

In the radiosity solver method for the analysis of grey diffuse radiation between N surfaces, Eq. C.13 in enclosure C is solved in conjunction with the basic conduction problem.

For the purpose of computation, it is convenient to rearrange Eq. C.13 in enclosure C into the following series of equations:

$$\sum_{j=1}^{N}\left(\delta_{ij} - (1-\varepsilon_i)\cdot F_{ij}\right)\cdot {q_j}^0 = \varepsilon \cdot \sigma \cdot T^4 \tag{1.64}$$

and

$$q_i = {q_i}^0 - \sum_{j=1}^{N} F_{ij} \cdot {q_j}^0 \tag{1.65}$$

Eqs. C.22 in enclosure C and 1.64 are expressed in terms of the outgoing radiative fluxes (radiosity) for each surface, ${q_j}^0$, and the net flux from each surface q_i. For known surface temperatures, T_i, in the enclosure, Eq. 1.64 forms a set of linear algebraic equations for the unknown, outgoing radiative flux at each surface. Eq. 1.64 can be written as

$$[A] \cdot \{q^0\} = \{D\} \tag{1.66}$$

Where:

$A_{ij} = \delta_{ij} - (1-\varepsilon_i)\cdot F_{ij}$

${q_j}^0$ = radiosity flux for surface i.

$D_i = \varepsilon_i \cdot \sigma \cdot {T_i}^4$

[A] is a full matrix due to the surface to surface coupling represented by the view factors and is a function of temperature due to the possible dependence of surface emissivities on temperature. Eq. 1.66 is solved using a Newton-Raphson procedure for the radiosity flux $\{q^0\}$.

When the q^0 values are available, Eq. 1.64 then allows the net flux at each surface to be evaluated. The net flux calculated during each iteration cycle is under-relaxed, before being updated using

$${q_i}^{net} = \Phi \cdot {q_i}^{k+1} + (1-\Phi)\cdot {q_i}^k \tag{1.67}$$

Φ = radiosity flux relaxation factor.
k = iteration number.

The net surface fluxes provide boundary conditions to the finite element model for the conduction process. The radiosity Eq. 1.58 is solved coupled with the conduction Eq. C.13 in enclosure C using a segregated solution procedure until convergence of the radiosity flux and temperature for each time step or load step.

The surface temperatures used in the above computation must be uniform over each surface in order to satisfy conditions of the radiation model. In the finite element model, each surface in the radiation problem corresponds to a face or edge of a finite element. The uniform surface temperatures needed for use in Eq. 1.65 are obtained by averaging the nodal point temperatures on the appropriate element face.

For open enclosure problems using the radiosity method, an ambient temperature needs to be specified using a space temperature or a space node, to account for energy balance between the radiating surfaces and the ambient.

For solution of radiation problems in 3-D, the radiosity method calculates the view factors using the hemicube method instead of the traditional double area integration method for 3-D geometry (C.4 in enclosure C).

1.2.8 Numerical Simulation: Stress calculation

Stress are generated during the chilling process. Starting from the field of temperatures, the coefficient of thermal expansion, α, and a reference temperature, T_0, we can obtain the unitary deformation according to the following equation:

$$\varepsilon = \alpha\left(T, f_\beta\right) \cdot (T - T_0) - \alpha\left(T_1, f_{\beta,1}\right) \cdot (T_1 - T_0) \tag{1.68}$$

Where T is the actual temperature, T_1 is the initial temperature, T_0 is the reference temperature, f_β are actual values of predefined field variables and $f_{\beta,1}$ are initial values of predefined field variables.

Figure 1.19 shows the relationship between the unitary deformation and temperature with α being a function of temperature.

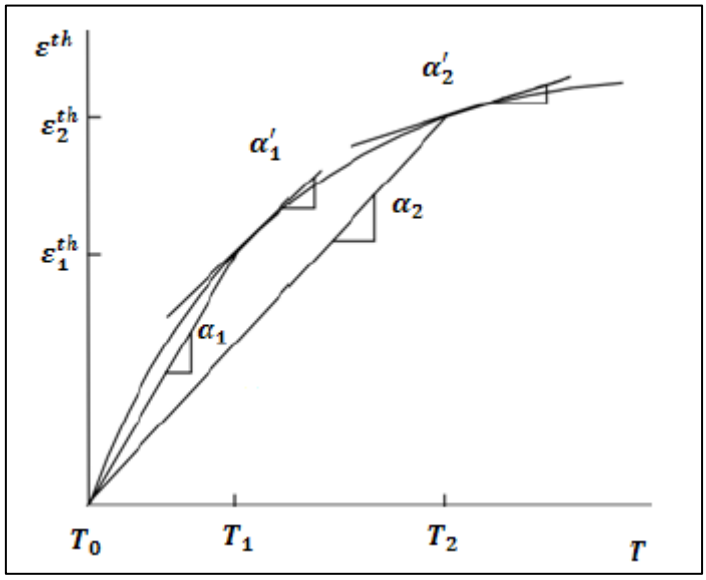

Figure 1.19 Relationship between unitary deform and temperature

The second term of the Eq. 1.68 represents the deformation due to the difference among the reference temperature and initial conditions. If we assume that there is not deformation of thermal origin for the initial conditions, the second adding disappears.

Using the laws that define the mechanical behaviour of the material, it is possible to translate these deformations in tensions. Exactly, in the case of elastic deformations, that is the simplest, the relationship between tensions and deformations it is given by:

$$\sigma = \varepsilon^{th} \cdot E \tag{1.69}$$

1.2.9 Finite element method (FEM)

The actual goal of most heat transfer (modelling) problems is to find the temperature field and heat fluxes in a material domain, given a previous knowledge of the subject like the general partial differential equations (PDE), and a set of particular constraints: boundary conditions (BC), initial conditions (IC), distribution of sources or sinks (loads), etc. [Martínez, 1992].

In a few cases the goal is not in the direct problem (given the PDE+BC+IC, find the T-field) but on the inverse problem: given the T-field and some aspects of PDE+BC+IC, find some missing parameters (identification problem).

To achieve the goal of solving a thermal problem, three steps are usually followed:

- Mathematical modelling of the physical problem.
- Mathematical solution of the mathematical problem.
- Analysis of the results and physical interpretation.

The mathematical modelling is the idealisation of the physical problem to yield a well-defined set of (mathematical) restrictions that serve as a good local approximation (all models are local). This is the most creative engineering part in the whole process of problem solving.

On one side, the geometry is idealised, assuming perfect planar, cylindrical or spherical surfaces, or a set of points and a given interpolation function. Besides the edges or boundaries (that are usually fixed, as in Fig. 1.20, except in some special cases like the Stefan problem of moving phase change), further information is needed to know if the region or domain of interest lies inside, outside, or in between boundaries. The space-time domain is divided in the spatial domain or boundary, D, that may be 1D, 2D or 3D and is usually assumed independent of time in thermal problems, $D(t) = D(t_0)$, and the time domain, that is one-dimensional, with a clear start, $t = t_0$, and a clear bias, $t > t_0$.

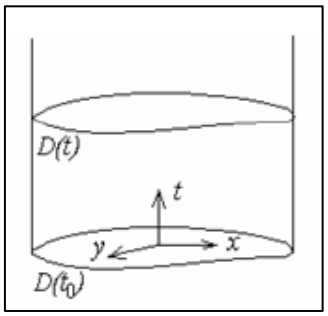

Figure 1.20 The space-time domain is divided in the spatial domain or boundary, D

Additionally, several numerical methods of solution make use of a subdivision of the domain in small sub-domains called elements, and procedures are needed to carry out an

automatic meshing and the associated numbering. Location procedures are also need to know which element a given point belongs, which are the neighbour elements, and so on.

On the other side, the materials properties must be idealised, because density, thermal conductivity, etc. depend on the base materials, their impurity contents, actual temperatures, etc.

Finally, or from the beginning, the differential equation, initial and boundary conditions are idealised, assuming e.g. that radiation terms are negligible, that initial conditions are at equilibrium, that boundary conditions are suddenly changed, or kept constant, or symmetric, etc. Sometimes the idealisation of the PDE is just the first step, and afterwards a regular or singular perturbation approach is followed to better model the real problem. Moreover, instead of solving the PDE, one might try solving the same physical problem but changing the approach; e.g. solving the variational problem of minimising the potential energy in mechanical problems or minimising the generation of entropy in thermal problems.

Real applications may have very complex geometry of different materials. Most of the times, the geometry, material and boundary conditions are such that real 3D problems can be modelled as 2D (e.g. a hexagonal nut heated from the hole) or even 1D.

There are a number of commercial packages for numerical solutions of PDE, applicable in principle to thermal, structural, fluid and electrical problems. However, in practice, the thermal problem may be highly non-linear (particularly if radiation is important) and it may be inconvenient to use the same discretization or even the same problem for thermal and structural analysis (in many cases the number of nodes and elements is 1 to 2 orders of magnitude larger for structural than for thermal analysis).

To use these commercial packages, the user first makes use of a pre-processor to draws the geometry or to import it as a CAD-file, to defines the materials (from a pre-loaded list or entering its properties), and to indicates a mesh type and size, what completes the input to the solver. After solving it, the user needs a post-processor to interpret the results.

The mathematical solution is the bare answer to the mathematical model. Although it is just a mathematical burden, engineers must be aware of the available methods of solution, and their pros and cons, in order to direct the previous idealisation towards feasible, available, affordable, efficient and solvable problems. The available methods to solve a mathematical model may be grouped in analytical and numerical:

a) Analytical solutions:

   Analytical solutions are, in principle, the best approach because the influence of the parameters is explicitly shown in the answer. The general equations for heat transfer are the energy balance and the constitutive equations that relate heat flux to temperature gradients, and they may be applied to a finite or to an infinitesimal system.

   In a strict sense, integral formulations should correspond to the variational problem of finding a function (e.g. T(x,t)) that makes extremum some physical magnitude: minimise the potential energy of the system, the production of entropy, the time

spent by a process, etc. It is worth to remember the basic equivalence in variational calculus (Lagrange equation):

$$I = \int_a^b f(x, y, y')dx = \min \leftrightarrow \frac{\partial f}{\partial y} - \frac{d}{dx}\left(\frac{\partial f}{\partial y'}\right) = 0 \tag{1.70}$$

But some other times, integral formulations usually refer to integro-differential equations obtained from balance equations applied to a control mass in a finite volume, the kind of black-box approach typical of the thermodynamic analysis. The energy balance at constant pressure and the constitutive equation (to be used in the Finite Volume Method below) are:

$$\frac{dH}{dt} = -\int_a \vec{q} \cdot \vec{n} \cdot dA \tag{1.71}$$

With:

$$\vec{q} = -k \cdot \nabla T \quad \text{or} \quad \vec{q} = h \cdot (T_\infty - T) \cdot \vec{n} \quad \text{or} \quad \vec{q} = \varepsilon \cdot \sigma \cdot \left({T_\infty}^4 - T^4\right) \cdot \vec{n}$$

However, this integral formulation only yields analytical solutions in a few degenerated cases, when the enthalpy function and the heat fluxes can be directly related to representative temperatures, as in high conductive system being exposed to low conductance environments (e.g. cooling of a small piece of metal). Thus, the differential formulation is usually preferred.

Differential formulation. For an elementary control volume dV the energy balance (combined with the Fourier constitutive equation) and the constitutive equation are:

$$\frac{DT}{Dt} = a \cdot \nabla^2 T + \frac{\Phi}{\rho \cdot c} \tag{1.72}$$

With:

$$\vec{q} = -k \cdot \nabla T \quad \text{or} \quad \vec{q} = h \cdot (T_\infty - T) \cdot \vec{n} \quad \text{or} \quad \vec{q} = \varepsilon \cdot \sigma \cdot \left({T_\infty}^4 - T^4\right) \cdot \vec{n}$$

where a known source term, f(T,x,t) is introduced to account for other possible enthalpy content other than that due to temperature. It is usually this form of the energy balance that is first solved to find the T-field, and afterwards heat fluxes are computed if necessary. Most of the techniques explained below may be learnt with the simple one-dimensional equation for a plane wall $\frac{\partial T}{\partial t} = a \cdot \frac{\partial^2 T}{\partial x^2}$, and practically all the cases of interest are covered by the bidimensional equation:

$$\frac{1}{r^n} \cdot \frac{\partial}{\partial r}\left(r^n \cdot \frac{\partial T}{\partial r}\right) + \frac{\partial^2 T}{\partial z^2} - \frac{\rho \cdot c \cdot V}{k} \cdot \frac{\partial T}{\partial z} - \frac{hp}{k \cdot A} \cdot (T - T_\infty) + \frac{\Phi(r, z, t)}{k} - \frac{1}{a} \cdot \frac{\partial T}{\partial r} = 0 \tag{1.73}$$

Where n = 0 for planar geometry, n = 1 for cylindrical and n = 2 for spherical. The third term applies when the material is moving at speed V relative to the coordinate system (e.g. a travelling furnace), the forth term applies for one-dimensional bodies with lateral flux like in fins, the fifth term is a generic but explicit source term, and the last one is the local accumulation (thermal inertia).

The heat transfer equation is:

$$\frac{\partial T}{\partial t} = a \cdot \frac{\partial^2 T}{\partial x^2} \qquad (\text{Parabolic} - \text{PDE}) \qquad (1.74)$$

Its solution decays to a steady state with time, although the steady state is:

$$\frac{\partial^2 T}{\partial x^2} + \frac{\partial^2 T}{\partial y^2} = 0 \qquad (\text{Elliptic} - \text{PDE}) \qquad (1.75)$$

Typical wave-like phenomena is:

$$\frac{\partial T}{\partial t} + V \cdot \frac{\partial T}{\partial x} = 0 \qquad (\text{Hyperbolic} - \text{PDE}) \qquad (1.76)$$

For steady states without sources or sinks, the heat equation reduces to:

$$\nabla^2 T = 0 \qquad (\text{Laplace equation}) \qquad (1.77)$$

This equation has the following symmetric solutions:

$$T = A \cdot x + B \qquad (1D)$$

$$T = A \cdot \ln(r) + B \qquad (2D)$$

$$T = \frac{A}{r} + B \qquad (3D)$$

For unsteady states without sources or sinks, the heat equation reduces to:

$$\frac{\partial T}{\partial t} - a \cdot \nabla^2 = 0 \qquad (1.78)$$

This equation has fundamental solutions (symmetric and unbounded to a heat pulse)

$$T(t, r) = \frac{\exp\left(\frac{-r^2}{4 \cdot a \cdot t}\right)}{4 \cdot \pi \cdot a \cdot t^{n-1/2}} \qquad (1.79)$$

With n = 0 for 1D, n = 1 for 2D and n = 2 for 3D.

Although problems with complex boundary or initial conditions can be solved by series expansion or Green's function integrals, they require numerical evaluation anyway for the sums or integrals, and straightforward numerical methods are preferred.

b) Numerical solutions:

Numerical solutions are the only practical approach most of the times, in spite of the handicap that they give only one particular answer to one particular instance of the parameter set, and to realise the influence of each parameter one has to perform a multiparametric sweep of the input and an analytical fitting of the numerical answer, a time-consuming and entangled task. Numerical methods transform the continuous-media problem to a discrete problem with N unknown values to be optimised (approximated to minimise some residue with respect to the continuous problem), what yields a finite system of algebraic equations of the form $K \cdot u = F$, i.e.:

$$[\text{assembled matrix of coefficients}] \cdot [\text{unknown function values}] = \\ = [\text{known applied stimuli}],$$

that is finally solved. Note that the generic variable u, here used and common in generic PDE-analysis represents temperature in thermal problems. Numerical methods differ in the way they yield this system of algebraic equations, but a general baseline exists. The problem may be generally stated as:

$$\mathrm{PDE}\big(u(\vec{x},t)\big) = 0,\ \mathrm{BC}\big(u(\vec{x}_0,t)\big) = 0,\ \mathrm{IC}(u(\vec{x},t_0)) \tag{1.80}$$

where PDE, BC and IC represent functionals related to de partial differential equation, boundary conditions and initial conditions respectively. Numerical methods approximate the infinite-degrees-of-freedom solution by a finite N-degrees-of-freedom solution of the form:

$$u^{\mathrm{approx}}(\vec{x},t) = u^{\mathrm{IBC}}(\vec{x},t) + \sum_{i=1}^{N} u_i(t)\cdot\Phi_i(\vec{x}) \tag{1.81}$$

Where $u^{\mathrm{IBC}}(\vec{x},t)$ is a known function (chosen by the modeller) that must satisfy all the initial and boundary conditions, $u_i(t)$ are unknown coefficients (varying with time for transient problems) to be numerically found, and $\Phi_i(\vec{x})$ are known functions, the base functions the modeller chooses as a function space of the solution. Observe the separation of variables in time and space; in practice, the time-dependence is also discretized, but this is a simpler problem, and we forget it for the moment.

Substituting this approximation in the original differential formulation one gets a residue, R, to be minimised, what can be done in different ways but those most used can be related to a general weighted-residue or multiple-projection spatial cancellation:

$$\mathrm{PDE}\big(\sum_{i=1}^{N} u_i(t)\cdot\Phi_i(\vec{x})\big) = R(\vec{x},t) = \min \tag{1.82}$$

For independent $u_i \rightarrow \quad < w_i(\vec{x}), R(\vec{x},t) \geq 0$

with

$w_i(\vec{x}) = \delta(\vec{x} - \vec{x}_i)$ method of collocation of finite differences (FDM).

$w_i(\vec{x}) = (1 \text{ if } \vec{x} \in \Omega, 0 \text{ otherwise})$ method of finite volumes (FVM).

$w_i(\vec{x}) = \Phi_i(\vec{x})$ method of finite elements of Galerkin (FEM).

$w_i(\vec{x}) = \frac{\partial R}{\partial u_i}$ method of least squares (LSM).

where w_i are the weighting functions and $<w_i,R>$ is the projection or scalar product. In any case, it is wise to start with as few unknowns as feasible, for an efficient feedback.

A main classification of numerical methods, according to how they asymptotically approach the continuous solution, may be in spectral and spatial methods (note that we always refer here to the spatial solution at a given time, although the same is valid for the time evolution).

Spectral methods consider a given domain and try to approximate the function (solution) by increasing the number of modes or parameters in a given space of functions, e.g. approximating $T(x) = \sum a_i \cdot x_i$ and increasing i, or $T(x) = \sum a_n \cdot \sin(n \cdot \pi \cdot x)$, etc. Although any function can be approximated by an infinite series expansion of any kind, if the base functions are orthogonal the coefficients in the series are uncoupled and a lot of work is saved (they can be found independently, and if their number is increased, only the added ones must be computed). Spectral methods usually take the domain globally, but some new methods take a local approach, in combination with spatial methods. The handicap of spectral methods is that for a multiparametric fit of a global base function, unless one succeeds in choosing a 'good' global function, the approximation is usually poor and misleading (e.g. with ripples), and it is better to divide the domain in small elements to be able to use simple fitting functions (spatial methods).

Spatial methods consider simple base function (e.g. piece-wise linear polynomials for second order PDE) and try to approximate the function (solution) by increasing the number of spatial elements (a finer partition of the domain). Different spatial methods have been developed according to different spatial meshing schemes and the kind of weighted residual chosen:

- Finite differences method (FDM). A partition of the domain is made in a regular mesh, e.g. a square mesh of size h in 2D, and derivatives in the PDE are approximated by finite differences in terms of Taylor series based on nodal points. From another point of view, for second order PDE, the T-field is approximated by a piecewise linear (bilinear) function with unknown temperatures at the nodes, and these unknowns are solved by collocation of the differential equation (second derivatives being taken as mean values of the piecewise-constant first derivatives), i.e. by forcing the PDE (cancelling its residue) only at nodal points (internal intersections and boundary intersections), in the form:

$$\nabla^2 T_{ij} \approx \frac{1}{h^2} \cdot \left(T_{i-1,j} + T_{i+1,j} + T_{i,j-1} + T_{i,j+1} - 4 \cdot T_{i,j}\right) \tag{1.83}$$

for standard internal nodes, or

$$\nabla^2 T_{ij} \approx \frac{2}{h^2} \cdot \left(\frac{\frac{1}{f_W}}{f_W + f_E} \cdot T_{i-1,j} + \frac{\frac{1}{f_E}}{f_W + f_E} \cdot T_{i+1,j} + \frac{\frac{1}{f_S}}{f_S + f_N} \cdot T_{i,j-1} + \frac{\frac{1}{f_N}}{f_S + f_N} \cdot T_{i,j+1} - \frac{f_S \cdot f_N + f_W \cdot f_E}{f_S \cdot f_N \cdot f_W \cdot f_E} \cdot 4 \cdot T_{i,j} \right) \tag{1.84}$$

for especial nodes that have only fractions of an h-step in the North-South-East-West neighbour. In any case, if the domain boundary doesn't coincide with a constant coordinate, and although standard (commercial) algorithms exists to mesh any irregular domain, the approximation of second derivatives at a node surrounded by irregularly distributed neighbour-nodes is difficult to handle automatically (e.g. even with a regular mesh in an irregular domain, a mesh refinement doesn't include all previous nodes in the boundary). For regular domains, it is the best numerical approach (the simplest) and the most used in research studies of new thermal problems.

- Finite volumes method (FVM). A partition of the domain is made in a regular mesh, e.g. a square mesh of size h in 2D, and the integro-differential equations of balance, e.g. $\rho \cdot c \cdot V \cdot \frac{dT_i}{dt} = \sum Q_{Ai}$, applied to each element, which is considered to have uniform temperature T_i. The heat exchanges with the neighbours are averaged with a mean thermal conductivity and mean thermal gradient. For simple averaging, the FVM usually yield the same nodal equations as the FDM, the difference been in the strictly mathematical approach in FDM and the more physical one in FVM.

  Lumped network method (LNM). A partition of the domain is made in a few elements manually defined and assumed isothermal (the unknown temperatures). The interactions among them are manually computed, and the set of coupling algebraic equations automatically solved. It is only used for well-conducting sets of pieces (nearly isothermal) with highly non-linear effects (e.g. radiation coupling).

- Finite elements method (FEM, also known as FEA). A partition of the domain is made in a regular or irregular mesh, the latter being most useful for irregular domains and concentrated loads, and, although it is awkward to design automatic meshings for irregular domains, several standard (commercial) algorithms exists that are easy to use. The ability to deal with irregular domains lays in the fact that the approximation of the solution is sought by cancelling some integral (instead of local) residues, and these integrals may be computed (with suitable base functions) locally in each element, without any directionality, instead of by differentiation (that is a directional operation based on all neighbour elements). The task is massive but simple (ideal for computers), thus finite element is the preferred numerical method for (non-singular) engineering problems, particularly for multidisciplinary computations (mechanical, thermal, fluiddynamic, electrical).

- Boundary elements method (BEM). The divergence theorem teaches that, for a linear PDE with constant coefficients, the solution in an interior point can be exactly expressed as an integral function of the solution at the boundary. With this method, first the full solution (function and derivatives) at the boundary points are computed by a kind of finite-element method where the base functions are the fundamental solutions of the PDE at the boundary nodes, then solving a set of algebraic equations at the nodes, and finally, if needed, the value at any internal point is directly computed by a quadrature (without interpolation). The problem with the boundary element method is that the local integration in the boundary are more involved than in the standard FEM because there are singular points that require more elaborated computations. Other handicap is that the BEM only applies to regions of constant properties. The great advantage is that for bulky domains the number of nodes significantly decreases, particularly for infinite domains (what explains its massive use in external fluidmechanics and geomechanics). Incidentally, for infinite domains, besides the BEM, one may also resort to classical FEM with a truncated domain progressively enlarged, or matched to an asymptotic analytical expansion, or stretching the external elements with a log-transformation.

  One-dimensional steady problems give just ordinary differential equations but with boundary values. In this case, besides previous spatial methods, it may be of importance the shooting method, what is the transformation of a boundary-value

problem into an initial-value problem. The ordinary differential equations are integrated with assumed initial conditions to find end-conditions that at first do not verify the data, but give a residue that can be cancelled by iterations in a root-finder approach. The shooting method may be thought also as a local approximation where the coefficients u_i are sequentially found by an Euler or Runge-Kutta forward extrapolation.

For problems with restrictions varying with time, all previous numerical methods become expansive because one must always start at time t = 0 and use a small Dt for accuracy and stability. It is better to approximate the solution function in terms of eigenfunctions, $T(x,t) = \sum \exp(\lambda_i \cdot t) \cdot T_i(x)$ obtained by solving the unloaded system $(K - \lambda \cdot I) \cdot u_i = 0$, where I_i are the eigenvalues and $f_i = \frac{1}{2 \cdot x} \cdot \sqrt{\lambda_i}$ the eigenfrequencies. This is called modal analysis (or eigenvalue method). There are still other problems where the interest is only to find the value of a parameter that produces branching solutions (bifurcation analysis), as in the buckling of bars, onset of Bénard-Marangoni convection, etc.

In any case, the user must signal to the numerical solver which problem must be solved, usually by selection from a list, what instruct the program to select appropriate coefficients to the standard differential equation programmed in the standard package, typically of the form:

$$c_1 \cdot \frac{\partial u}{\partial t} + c_2 \cdot \frac{\partial^2 y}{\partial x^2} + \frac{\partial}{\partial x}\left(a_1(x) \cdot \frac{\partial u}{\partial x}\right) + \frac{\partial}{\partial x}\left(b_1(x) \cdot \frac{\partial^2 y}{\partial x^2}\right) + \frac{\partial}{\partial y}\left(a_2(y) \cdot \frac{\partial u}{\partial y}\right) + \frac{\partial y}{\partial x}\left(b_2(y) \cdot \frac{\partial^2 u}{\partial x^2}\right) + c(x,y) = f(t,x,y) \qquad (1.85)$$

The analysis of the results is the interpretation of the numerical solution, its validity, accuracy and sensitivity to parameter variations. The direct solution usually gives just the set of values of the function at the nodes, what is difficult to grasp for humans in raw format (a list of numbers or, for regular meshes, a matrix). Some basic post-processing tools are needed for:

a) Visualisation of the function by graphic display upon the geometry or at user-selected cuttings. Unfortunately, many commercial routines, besides the obvious geometry overlay, only present the function values as a linear sequence of node values and don't allow the user to select cuts. Additional capabilities as contour mapping and pseudo-colour mapping are most welcome.
b) Computation of function derivatives (and visualisation).
c) Feedback on the meshing, refining it if there are large gradients, or large residues in the overall thermal balance.
d) Precision and sensitivity analysis by running some trivial cases (e.g. relaxing some boundary condition) and by running 'what-if' type of trials, changing some material property, boundary condition and even the geometry.

1.3 Preliminary work

The Institut für Fertingungs technologie keramischer Bauteile (IFKB of University of Stuttgart) and the Mechanical Engineering Department of the Technical University of Cartagena had stablished, since years, a collaboration in the studying of metal matrix composites.

The predecessor work is referred to thermal and mechanical analysis of one thixo-forged of aluminium and carbon fibre by ABAQUS. In this previous model is not used radiation phenomenon, because this is strongly nonlinear and it is very difficult to implement.

However, due to the complex process to obtain a MMC plate, it is necessary to improve the model to know the thermal and mechanical effects of chilling process. In this work, we will make a model including the radiation to study the thermal and mechanical behaviour of an aluminium and carbon fibre plate.

1.4 Only the important literature

Following, we stand out the literature more important:

[5] E. J. Barbero. Finite element analysis of composite materials using ANSYS. CRC Press. 2014.

[7] P. Cézard, V. Favier, R. Bigot, T. Balan, M. Berveiller. Simulation of semi-solid thixoforging using a micro-macro constitutive equation. Computational Materials Science 32. 323–328. 2005.

[15] M. Jiménez, R. Gadow, P. Weichand. Optimisation of fibre-matrix interface in carbon fibre reinforced light metals via liquid phase impregnation coatings. International Journal of Automotive Composites. 3. 101. 10.1504/IJAUTOC.2017.10012482. 2017.

[19] J. A. Moreno, K. von Niessen, R. Gadow. Thermo-mechanical modelling of the cooling process during thixoforging of fibre reinforced light metal composites. Solid State Phenomena Vols. 116-117 pp 596-600. 2006.

2 NATURE OF THE WORK

2.1 Introduction

This section deals with the aims of the study, the useful effects of this work and ultimately the work in the future in relation to this process of manufacture.

2.2 Aims of the task

The basic aim of the present work is the application of FEM in order to evaluate the MMC design.

As result of these calculations, the temperature and stress field of different designs can be compared.

2.3 Useful effects

This work permits to understand the relationship between the carbon fibre distribution and the strength.

2.4 Work in the future

For the following works, we recommend the simulation of stress responds of full model of RVE for a composite material with a periodic, hexagonal fibre array and other loads.

3 ANALYSIS OF LITERATURE

In this section, we are going to describe the literature used in the present work:

[1] ANSYS, Inc. ANSYS Mechanical APDL Element Reference. Release 15.0 November 2013.

This handbook is essential to use correctly this software. To be more precise, this work contains clear explanations about the use of the program elements.

[2] J. Aboudi. Mechanics of composite materials: a unified micromechanical approach. Vol. 29 of Studies in Applied Mechanics. Elsevier, New York. 1991.

This book addresses about the developing of a micromechanical composite model based of the study of the interacting periodic cells and its applications. This model has the capability of analyse elastic as well as nonelastic constituents, forming a unified approach in the prediction of the behaviour of composite materials.

[3] J. T. Álvarez Egea. Thermal and mechanical analysis of one thixoforged piece of 319 aluminium alloy reinforced with carbon fibre. Polytechnic University of Cartagena. Cartagena, Spain. 2005.

This works provides information about thermal and mechanical analysis of one thixo-forged of aluminium and carbon fibre by ABAQUS.

[4] E. J. Barbero. Introduction to Composite Materials Design. Second Edition. CRC Press. Boca Raton. 2010.

This book provides information and several examples about composite materials. Furthermore, it incorporates state of the art advances in knowledge and design methods of these kind of materials.

[5] E. J. Barbero. Finite element analysis of composite materials using ANSYS. CRC Press. 2014.

This book includes an explanation of the concepts involved in the detailed analysis of composites, a sound explanation of the mechanics needed to translate those concepts into a mathematical representation of the physical reality, and a detailed explanation of the solution of the resulting boundary value problems by using commercial Finite Element Analysis software.

[6] F. P. Beer, E. R. Johnston Jr., J. T. DeWolf. Mechanics of Materials, 3rd Edition. McGraw-Hill, Boston, MA. 2001.

This book provides general information about mechanics of materials accompanied of numerous engineering examples.

[7] P. Cézard, V. Favier, R. Bigot, T. Balan, M. Berveiller. Simulation of semi-solid thixoforging using a micro-macro constitutive equation. Computational Materials Science 32, 323–328. 2005.

This article studies the constitutive equation of the isothermal steady-state behaviour of semi-solid materials which is described with a micro-macro modelling. Furthermore, the

influence of the normal and abnormal namely softening stress–strain rate relationship on thixoforging is analysed using compression and extrusion tests simulations.

[8] L. J. Ebert, O. K. Wright. Mechanical aspects of the interface. Interfaces in metal matrix composites. A. G. Metcalfe ed. Academic Press. New York. 1974.

This book includes an explanation about metal matrix composites.

[9] J. D. Eshelby. The determination of the elastic field of an ellipsoidal inclusion and related problems. Proceedings of the Royal Society, A241:376-396. 1957.

In this article it is supposed that a region within an isotropic elastic solid undergoes a spontaneous change of form which, if the surrounding material were absent, would be some prescribed homogeneous deformation. Because of the presence of the surrounding material stresses will be present both inside and outside the region. If the region is an ellipsoid the strain inside it is uniform and may be expressed in terms of tabu-lated elliptic integrals and to know only the relatively simple elastic field inside the ellipsoid.

[10] J. D. Eshelby. The elastic field outside an ellipsoidal inclusion. Acta Metallurgical, A252:561-569. 1959.

This article provides an extension of the results obtained in the paper before.

[11] R. Gadow, M. Speicher. Advanced manufacturing of ceramic matrix composites for disk brake rotors. SAE Techn. Paper No. 2003-01-1178. SAE International. 2003.

This article describes the manufacturing technologies for SiC based compounds that show great promise for the serial production of ceramic brake discs. Different fibre content and architectures are explored to match the properties of these compounds with brake disk applications.

[12] Z. Hashin, S. Shtrikman. A variational approach to the elastic behaviour of multiphase materials. Journal of Mechanics and Physics of Solids, 11:127-140. 1963.

This article provides information about the theory of the elastic behaviour of multiphase materials.

[13] G. Hirt, L. Khizhnyakova, R. Baadjou, F. Knauf, R. Kopp. Semi-solid Forming of Aluminium and Steel–Introduction and Overview. Thixoforming: Semi-solid Metal Processing. Edited by G. Hirt and R. Kopp. Weinheim. 2009.

This book tries to summarize fundamental knowledge and technological applications for semisolid forming and to contribute to a better understanding of the governing relations between the process parameters and the achieved part quality and to present selected technological solutions to overcome existing process challenges.

[14] G. Ibe. Grundlagen der Verstärkung in Metallmatrix-Verbundwerkstoffe. Metallische Verbundwerkstoffe. Ed. K. U. Krainer, DGM Informations gesellschaft. 1994. ISBN 3-88355-201, pp. 3-41. 2004.

This book provides information about metal matrix composites: combination of materials for light metal composites, reinforcement, matrix alloy systems, manufacturing of MMC, applications and recycling.

[15] M. Jiménez, R. Gadow, P. Weichand. Optimisation of fibre-matrix interface in carbon fibre reinforced light metals via liquid phase impregnation coatings. International Journal of Automotive Composites. 3.101.10.1504/IJAUTOC.2017. 10012482. 2017.

Fibre reinforced metals are a potential alternative to replace steel components in the automotive industry due to their enhanced specific strength. In this paper interfaces in carbon fibre reinforced AlSi6 are modified by LPI fibre coatings, improving the strength and strain to failure of composites.

[16] R. M. Jones. Mechanics of composite materials. 2nd ed. Taylor & Francis. ISBN 1-56032-712-X. 1999.

This book provides general information about features, mechanical behaviour and design of composite materials.

[17] R. Luciano, E. J. Barbero. Analytical expressions for the relaxation moduli of linear viscoelastic composites with periodic microstructure. ASME J. Applied Mechanics, 62(3):786-793. 1995.

In this article the viscoelastostatic problem of composite materials with periodic microstructure is studied. The matrix is assumed linear viscoelastic and the fibres elastic. The problem in the Laplace domain is solved by using the Fourier series technique and assuming the Laplace transform of the homogenization eigenstrain piecewise constant in the space. Furthermore, comparisons with experimental results are presented.

[18] I. Martínez. Termodinámica básica y aplicada. Ed. Dossat, 1992, ISBN 84-237-0810-1. 1992.

This book provides general information about basic and applied thermodynamics.

[19] J. A. Moreno, K. von Niessen, R. Gadow. Thermo-mechanical modelling of the cooling process during thixoforging of fibre reinforced light metal composites. Solid State Phenomena Vols. 116-117 pp 596-600. 2006.

This article, which studies the modelling by means of finite elements and numerical simulation, is used in order to study parameter variations during the cooling procedure of a light-metal MMC and to select an optimized process route.

[20] K. Siegert, R. Gadow, K. von Niessen, P. Unseld, M. Speicher. Thixoforging of continuous fibre reinforced AlSi / AlMg – alloys. 8th International Conference “Semisolid Processing”. Limasol, Cyprus. 2004.

This article addresses about the manufacturing technology of MMC and the first experimental results with a special focus on the penetration of the fibre and the infiltration behaviour and, also, on the formation of the fibre matrix interface for fibre damage by mechanical or chemical attack.

[21] J. Vico. Numerical analysis of thermal radiation effect in ceramic coating process by HVOF. Polytechnic University of Cartagena. Cartagena, Spain. 2010.

This paper is based on a real process used at IFKB which uses thermal spraying. In this work the cooling of a simple metal plate is simulated to introduce thermal radiation calculates in a finite elements model.

[22] T. J. Whalen, A. T. Anderson. Wetting of SiC, Si3N4 and carbon by Si and binary Si alloy. Journal of the American Ceramic Society. Vol. 58. The American Ceramic Society. ISSN 0002-7820, pp. 396-398. 1975.

This article provides information about a study of the wetting of several new materials for gas turbine engines, for example, SiC, Si3N4 and C, by Si liquid and Si binary alloys containing Cu, Fe and B was determined by the sessile drop method.

4 METHODS

4.1 Introduction

In this chapter the following models will be described:

- One-eighth model of composite material with periodic microstructure analysis.
- Full model of RVE for a composite material with a periodic, hexagonal fibre array.
- Thermal analysis of one thixoforged aluminium plate.
- Thermal stress analysis of one thixoforged aluminium plate.

4.2 One-eighth model of composite material with periodic microstructure analysis

This model studies the system represented in Fig. 1.14. The geometry is characterized by the parameters: a_2, equal to 7.071 µm in direction X-axis, a_3, equal to 7.071 µm in direction Y-axis, a_1, equal to a half of a_2 in direction Z-axis, which is orientated along the fibre length and a fibre radius of 3.5 µm. The origin of the framework is in a corner of the parallelepiped with the following length: a_2 in direction X-axis, a_3 in direction Y-axis and a_1 in direction Z-axis.

The selected element is SOLID186 (D.1 in enclosure D). Figure 4.1 represents the mesh of this model. Table 4.1 shows of the values of the mechanical properties.

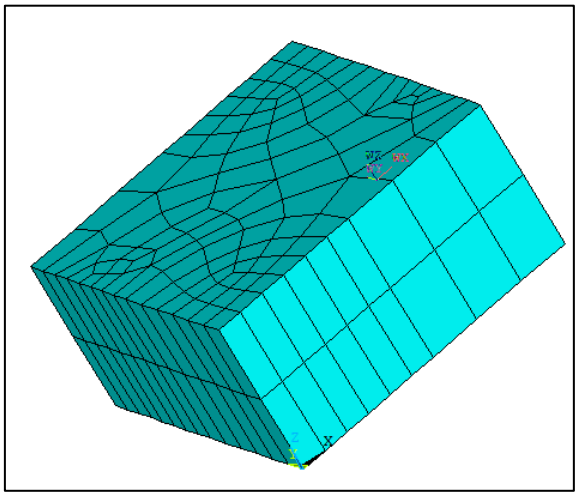

Figure 4.1 Model mesh of one-eighth model

Table 4.1 Mechanical properties of one-eighth and full model.

MECHANICAL PROPERTIES	VALUE
E_X (carbon fibre) [Pa]	0.241e12
Poisson's ratio, µ (carbon fibre)	0.2
E_X (matrix) [Pa]	3.12e9
Poisson's ratio, µ (matrix)	0.38

The boundary conditions consist in constraining displacement in all the faces except in the face defined by z equal to a_1, which has displacement of a_1.

The most interesting ANSYS commands used in this work are summarised in enclosure E. In this enclosure, the most useful postprocessing procedures are also explained.

4.3 Full model of RVE for a composite material with a periodic, hexagonal fibre array

This model studies the system represented in Fig. 1.13. The geometry is characterized by the parameters: a_2, equal to 7.071 µm in direction X-axis, a_3, equal to 7.071 µm in direction Y-axis, a_1, equal to a quarter of a_2 in direction Z-axis, which is orientated along the fibre length and a fibre radius, r_f, of 3.5 µm. The origin of the framework is in the centre of the parallelepiped with the following length: $2 \cdot a_2$ in direction X-axis, $2 \cdot a_3$ in direction Y-axis and $2 \cdot a_1$ in direction Z-axis.

The selected element is SOLID186. Figure 4.2 shows the mesh of this model. The mechanical properties are the same as in paragraph 4.2.

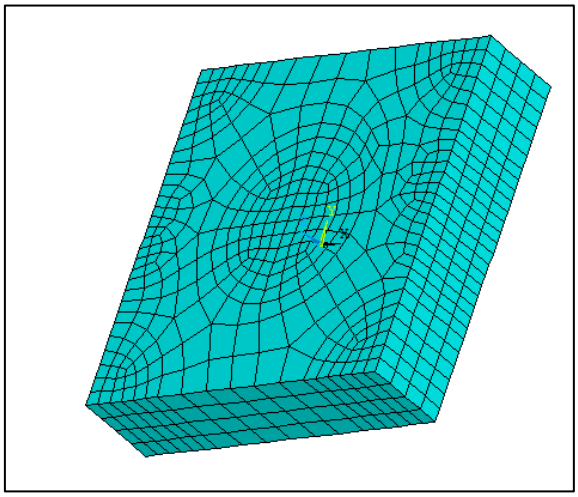

Figure 4.2 Model mesh of full model of RVE

The boundary conditions consist in defining the strain γ_6 equal to 0.5, equivalent to $\varepsilon_{12}/2$. This deformation is represented in Fig. 4.3.

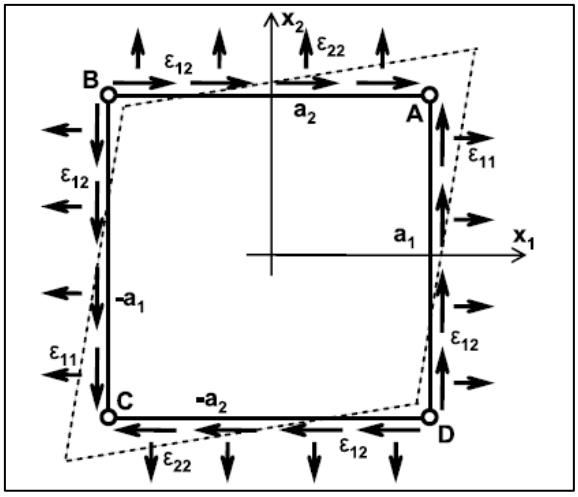

Figure 4.3 Top view of the RVE showing that two displacements (vertical and horizontal) must be applied at edges (points A and C) to impose shear

The model is constraint in the nodes with X-coordinate equal to zero, except the edges corresponding to Y and Z-axis.

Four pairs of corners need to be analysed one at a time. For each pair, the corners are located symmetrically with respect to the centre of the RVE located at coordinates (0,0,0). From Eq. 1.48 and in order to use in ANSYS, we write CE in the following form:

$$2 \cdot a_1 \cdot \varepsilon_{21} + 2 \cdot a_2 \cdot \varepsilon_{22} + 2 \cdot a_3 \cdot \varepsilon_{23} = u_2(a_1, a_2, a_3) - u_2(-a_1, -a_2, -a_3)$$
$$2 \cdot a_1 \cdot \varepsilon_{31} + 2 \cdot a_2 \cdot \varepsilon_{32} + 2 \cdot a_3 \cdot \varepsilon_{33} = u_3(a_1, a_2, a_3) - u_3(-a_1, -a_2, -a_3)$$
$$2 \cdot a_1 \cdot \varepsilon_{11} + 2 \cdot a_2 \cdot \varepsilon_{12} + 2 \cdot a_3 \cdot \varepsilon_{13} = u_1(a_1, a_2, a_3) - u_1(-a_1, -a_2, -a_3)$$

$$2 \cdot a_1 \cdot \varepsilon_{21} + 2 \cdot a_2 \cdot \varepsilon_{22} - 2 \cdot a_3 \cdot \varepsilon_{23} = u_2(a_1, a_2, -a_3) - u_2(-a_1, -a_2, a_3)$$
$$2 \cdot a_1 \cdot \varepsilon_{31} + 2 \cdot a_2 \cdot \varepsilon_{32} - 2 \cdot a_3 \cdot \varepsilon_{33} = u_3(a_1, a_2, -a_3) - u_3(-a_1, -a_2, a_3)$$
$$2 \cdot a_1 \cdot \varepsilon_{11} + 2 \cdot a_2 \cdot \varepsilon_{12} - 2 \cdot a_3 \cdot \varepsilon_{13} = u_1(a_1, a_2, -a_3) - u_1(-a_1, -a_2, a_3)$$

$$2 \cdot a_1 \cdot \varepsilon_{21} - 2 \cdot a_2 \cdot \varepsilon_{22} + 2 \cdot a_3 \cdot \varepsilon_{23} = u_2(a_1, -a_2, a_3) - u_2(-a_1, a_2, -a_3)$$
$$2 \cdot a_1 \cdot \varepsilon_{31} - 2 \cdot a_2 \cdot \varepsilon_{32} + 2 \cdot a_3 \cdot \varepsilon_{33} = u_3(a_1, -a_2, a_3) - u_3(-a_1, a_2, -a_3)$$
$$2 \cdot a_1 \cdot \varepsilon_{11} - 2 \cdot a_2 \cdot \varepsilon_{12} + 2 \cdot a_3 \cdot \varepsilon_{13} = u_1(a_1, -a_2, a_3) - u_1(-a_1, a_2, -a_3)$$

$$2 \cdot a_1 \cdot \varepsilon_{21} - 2 \cdot a_2 \cdot \varepsilon_{22} - 2 \cdot a_3 \cdot \varepsilon_{23} = u_2(a_1, -a_2, -a_3) - u_2(-a_1, a_2, a_3)$$
$$2 \cdot a_1 \cdot \varepsilon_{31} - 2 \cdot a_2 \cdot \varepsilon_{32} - 2 \cdot a_3 \cdot \varepsilon_{33} = u_3(a_1, -a_2, -a_3) - u_3(-a_1, a_2, a_3)$$
$$2 \cdot a_1 \cdot \varepsilon_{11} - 2 \cdot a_2 \cdot \varepsilon_{12} - 2 \cdot a_3 \cdot \varepsilon_{13} = u_1(a_1, -a_2, -a_3) - u_1(-a_1, a_2, a_3)$$

(4.1)

Using contracted notation, the generalized Hooke's law is shown by the Eq. B.11, in which σ_6 is σ_{XZ}. Thus, if γ_6 is equal to 1, C_{66} is equal to σ_{XZ}.

For the calculation of C_{66}, the average in all the volume for the averaged element centroid value of the stress σ_{XZ} is used.

Then,

$$\Sigma_k = \sigma_{Xk} \cdot V_k + \sigma_{Yk} \cdot V_k + \sigma_{Zk} \cdot V_k + \sigma_{XYk} \cdot V_k + \sigma_{XZk} \cdot V_k + \sigma_{YZk} \cdot V_k \quad (4.2)$$

Where $\sigma_{ij,k}$ and V_k are the stress in the i and j direction and the volume in the element k.

The summation of σ_{Xk} for all the elements is:

$$\sigma_{X,Vol} = \sum_k \cdot \sigma_{Xk} \quad (4.3)$$

The summation for the rest of the variables are obtained in an analogous way.

Thus, the following ratio

$$\frac{\sum_k \cdot \sigma_{XZk}}{V}$$

is C_{66}.

From Eq. 1.9, $G_{12} = G_{13} = C_{66}^{*}$.

4.4 Thermal analysis of one thixoforged aluminium plate

The selected element is PLANE55 (D.2 in enclosure D). Table 4.2 shows of the values of the mechanical properties.

Table 4.2 Mechanical properties of MMC plate.

Material	MECHANICAL PROPERTIES	VALUE 1	VALUE 2
Aluminium in plate	Density [kg/m^3]	2.79e3	
	Conductivity [W/m·K]	141	
	Specific heat [J/kg·K]	963	
Carbon fibre in plate	Density [kg/m^3]	1.83e3	
	Conductivity [W/m·K]	17	
	Specific heat [J/kg·K]	60 (at 800 K)	400 (at 1100 K)
Steel/glass in interface	Density [kg/m^3]	7800/2500	
	Conductivity [W/m·K]	50.2/0.8	
	Specific heat [J/kg·K]	460/837	
Steel in support	Density [kg/m^3]	7800	
	Conductivity [W/m·K]	50.2	
	Specific heat [J/kg·K]	460	

The carbon fibre layers are meshed in a set, Figure 4.4. In Figure 4.5, it is shown a zoom.

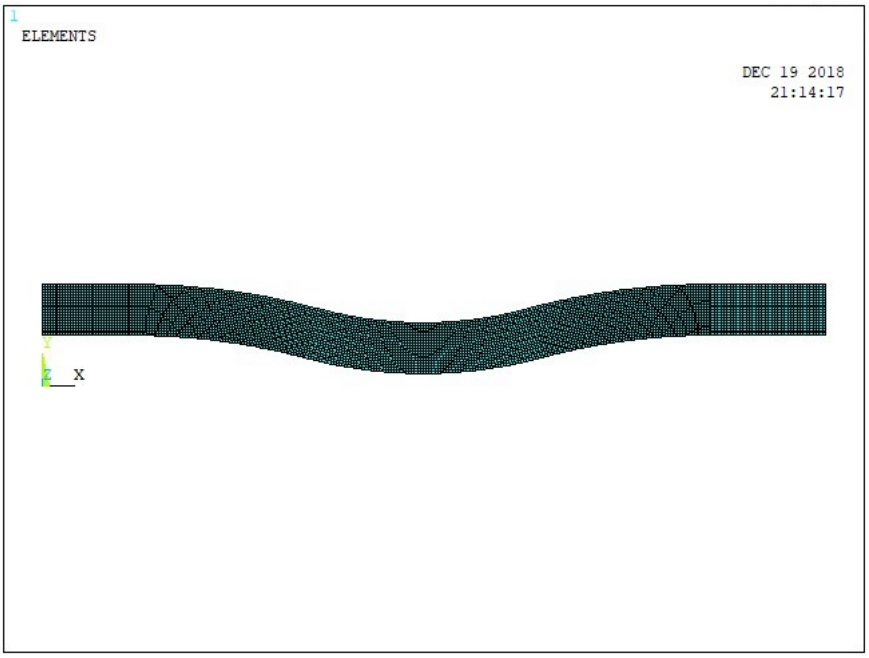

Figure 4.4 Carbon fibre layers mesh

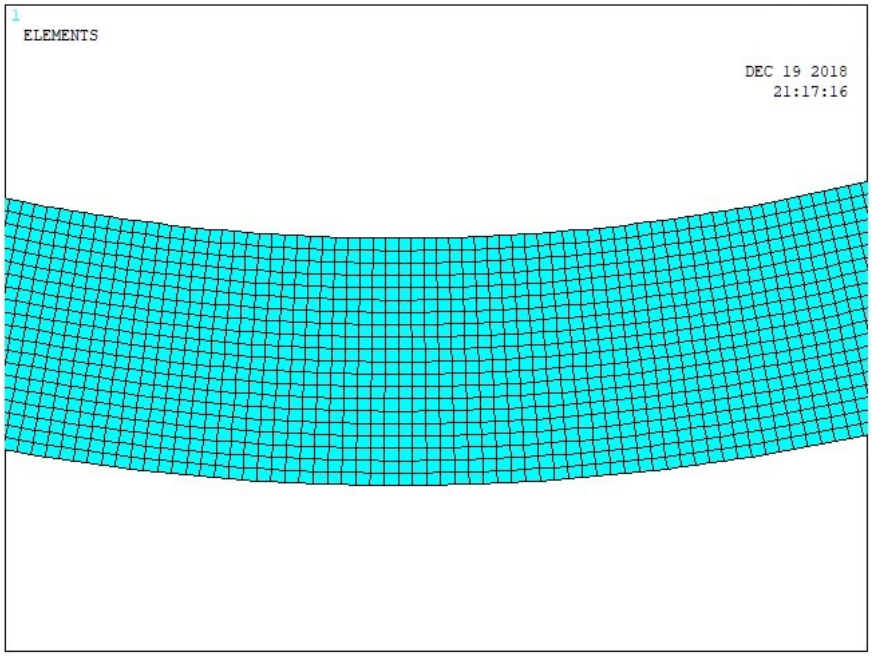

Figure 4.5 Zoom of Fig. 4.4

The aluminium in Figure 4.6 is located over and under the carbon fibre. The upper aluminium is divided in three zones, each one in turn is split up in two, Figures 4.7 to 4.9. The same is made with the bottom zones, Figures 4.10 to 4.12.

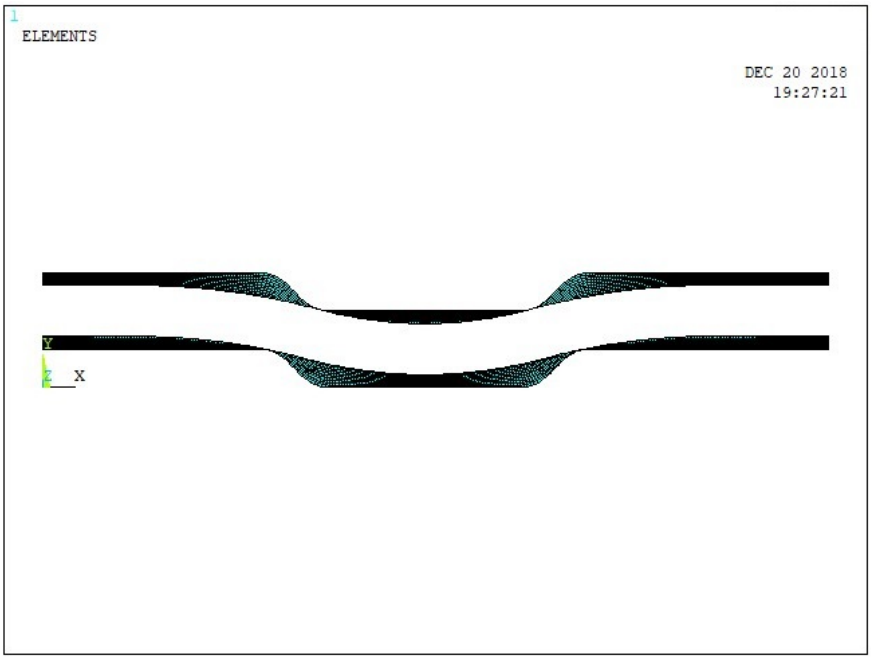

Figure 4.6 Aluminium mesh

Figure 4.13 shows the mesh of the plate and its support.

The initial temperature in all nodes of the plate is 873 K, meanwhile the initial temperature of the support is 293 K. Two kind of interfaces between the plate and the support are considered: steel and glass. The initial temperature of this interface is 293 K.

The temperature calculation considers four situations without radiation: with a convection characterized by a film coefficient of 10 $W/m^2 \cdot K$ and an interface of steel, the same case but with an interface of glass, and two more calculations with a film coefficient of 100 $W/m^2 \cdot K$ and the both mentioned interfaces. In order to compare the results, another calculation considering only the radiation is made.

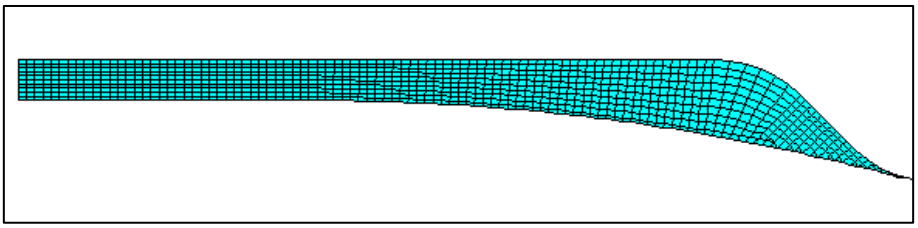

Figure 4.7 Left upper zone of aluminium

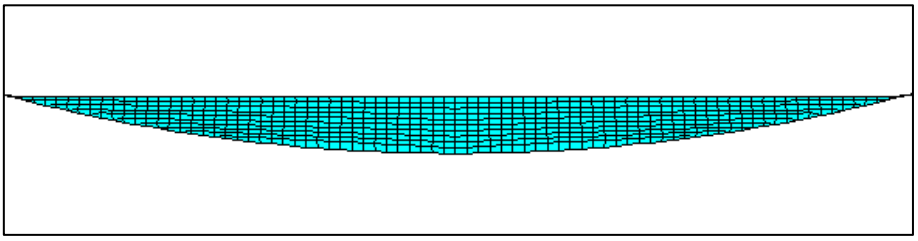

Figure 4.8 Middle upper zone of aluminium

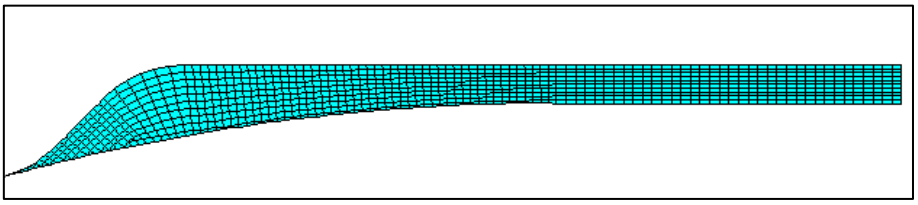

Figure 4.9 Right upper zone of aluminium

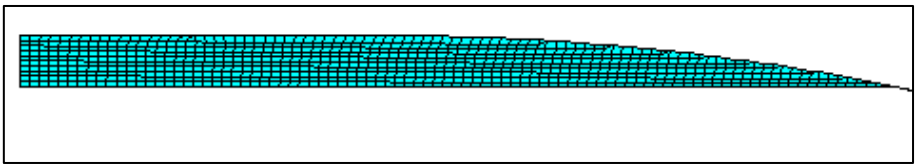

Figure 4.10 Left bottom zone of aluminium

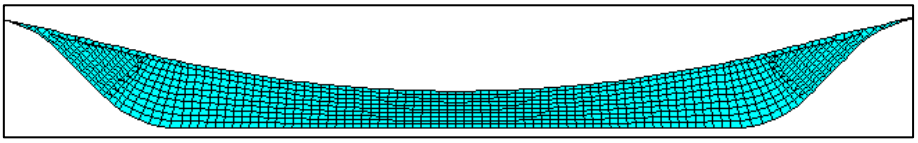

Figure 4.11 Middle bottom zone of aluminium

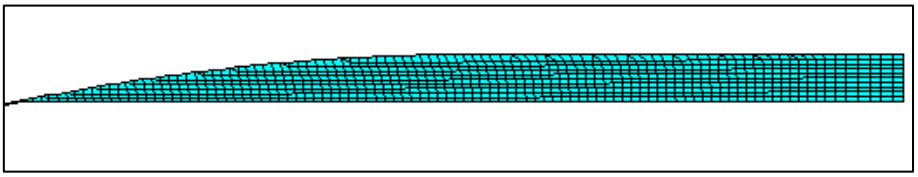

Figure 4.12 Right bottom zone of aluminium

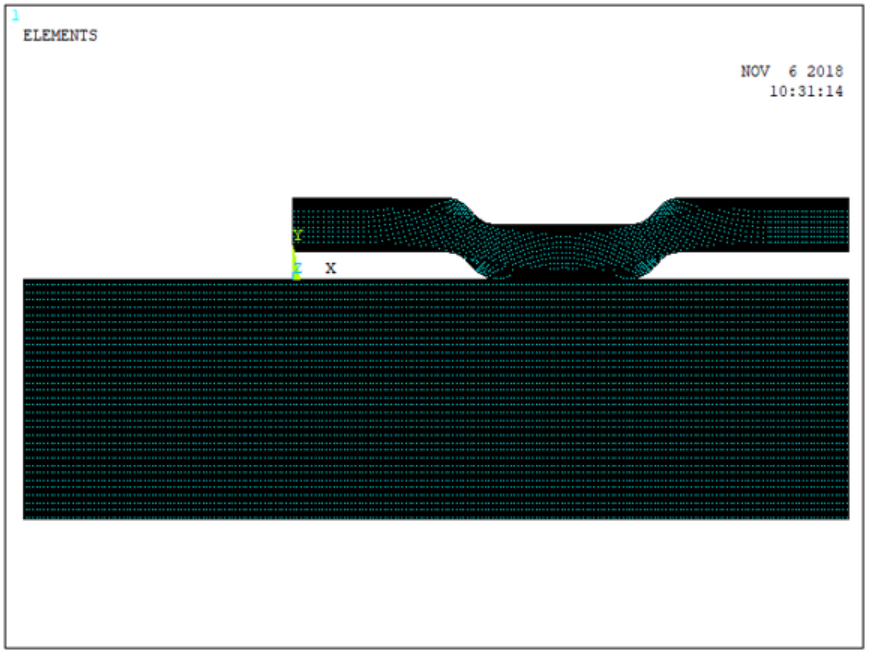

Figure 4.13 Plate of carbon fibre-aluminium and tray of steel

The temperature evolution in several nodes will be represented in order to know the cooling process. Figures 4.14 to 4.16 show the position of some selected nodes.

4.5 Thermal stress analysis of one thixoforged aluminium plate

From the results of temperatures calculation, the stress analysis is fulfilled by Eq. 1.68 and 1.69 for radiation heat transfer.

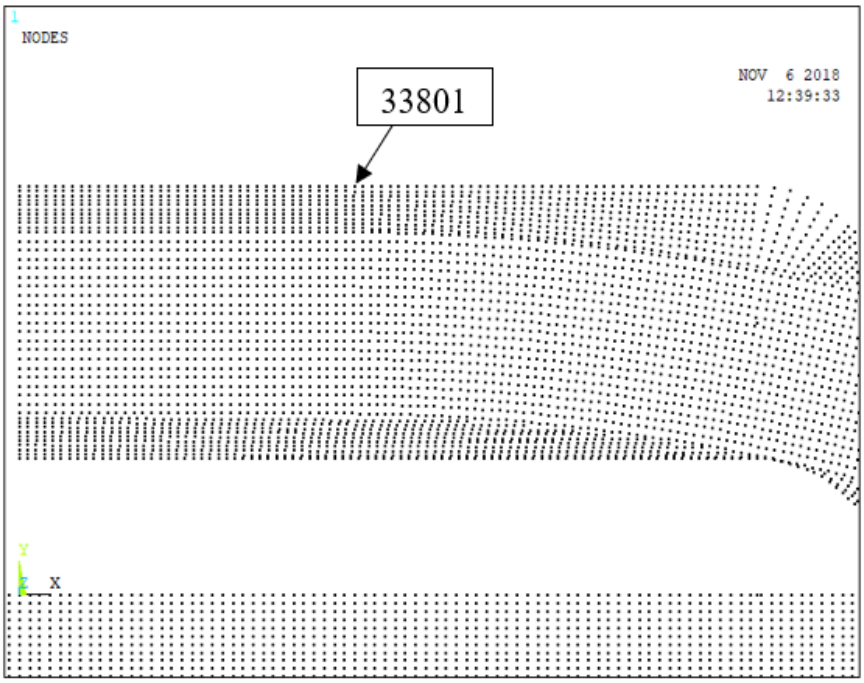

Figure 4.14 Location of node 33801, in its vertical are the remaining points: 33805, 33810, 3801, 3810, 3821, 63910, 63906, 63901 and 121259

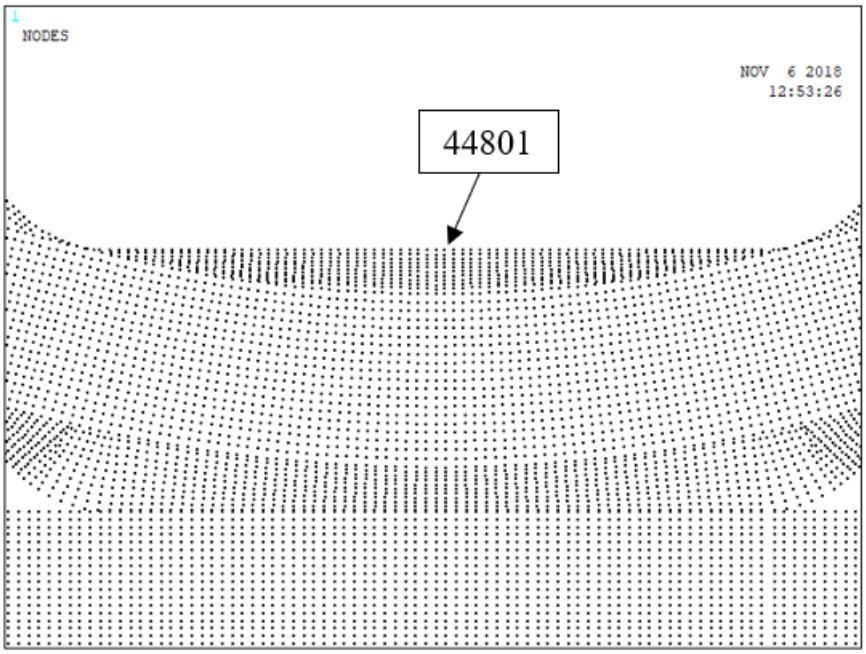

Figure 4.15 Location of node 44801, in its vertical are the remaining points: 44805, 44810, 14901, 14910, 14921, 75210, 75206, 75201 and 121354

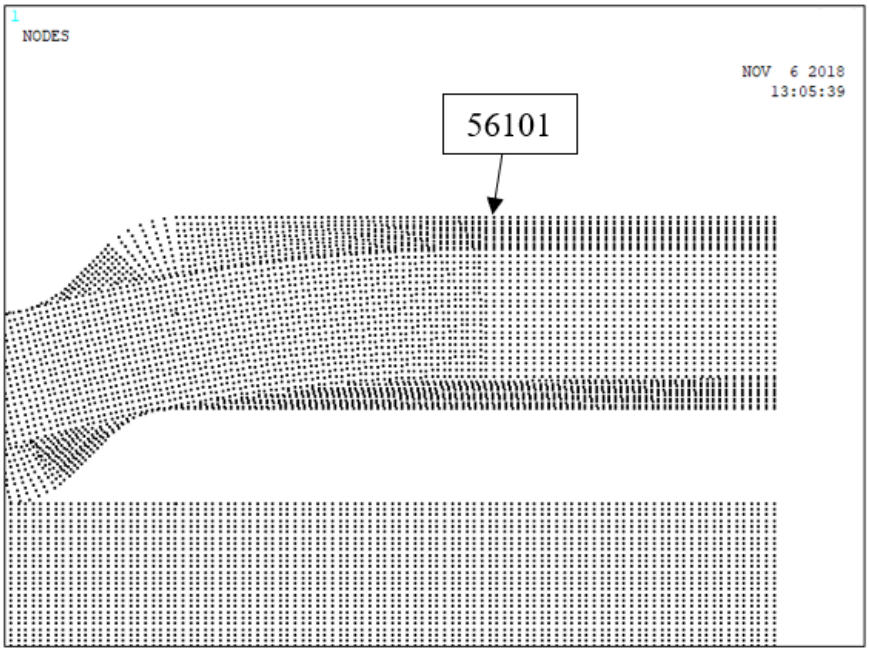

Figure 4.16 Location of node 56101, in its vertical are the remaining points: 56105, 56110, 26301, 26310, 26321, 78910, 78906, 78901 and 407585

5 RESULTS AND DISCUSSIONS

5.1 Introduction

In the following sections the results of the proposal simulations are analysed and the manufacture cost of a plate with 1 m^2 is calculated.

As shown in chapter 4, the simulations are presented in three groups. Firstly, stress analysis of one-eighth model of composite material with periodic microstructure and a full model of RVE for a composite material with a periodic, hexagonal fibre array. Secondly, thermal analysis of one thixoforged aluminium plate considering convection and without considering thermal radiation and vice versa. Thirdly, thermal stress analysis of one thixoforged aluminium plate.

5.2 One-eighth model of composite material with periodic microstructure analysis

Figures 5.1 and 5.2 show the X-stress and Z-stress distributions respectively for the strains mentioned in chapter 4.

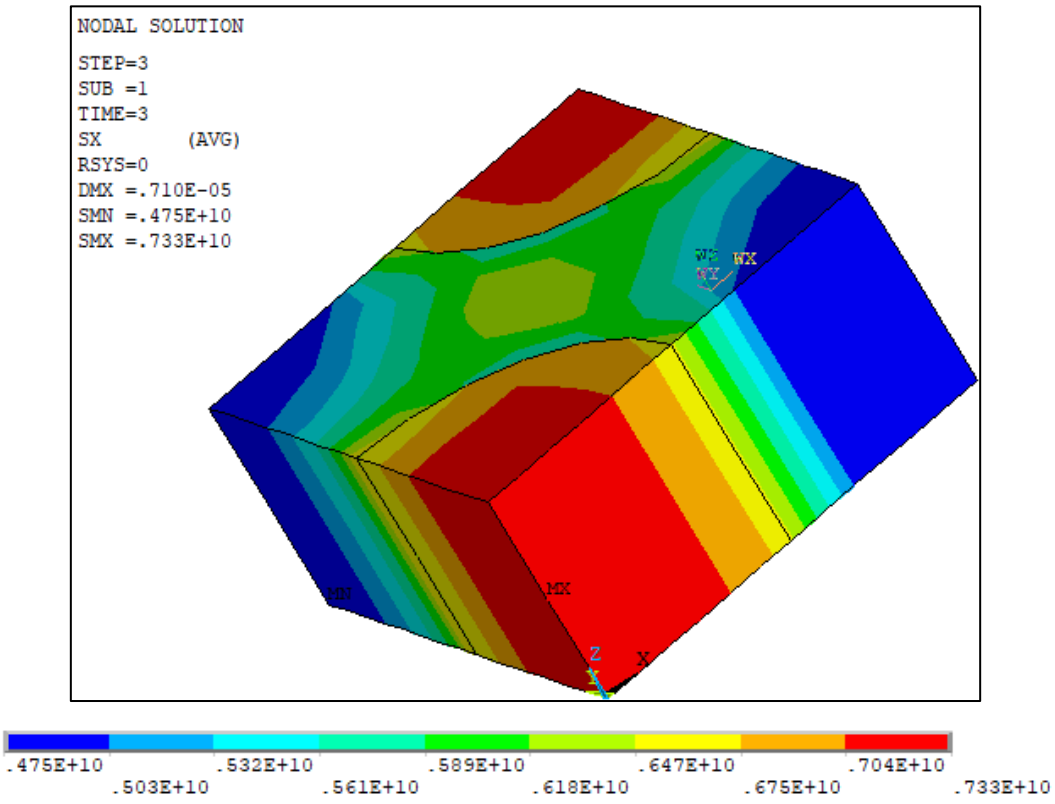

Figure 5.1 X-stress, one-eighth model

5.3 Full model of RVE for a composite material with a periodic, hexagonal fibre array

Figures 5.3 and 5.4 show the X-stress and Z-stress distributions respectively for the strains mentioned in chapter 4.

Barbero obtained G_{12} = 2583 MPa for r_f = 3.5 µm, a_2 = 5.2701 µm, a_3 = 9.1281 µm. With the data used in this work, r_f = 3.5 µm, a_2 = 7.071 µm, a_3 = 7.071 µm, G_{12} = 2507 MPa.

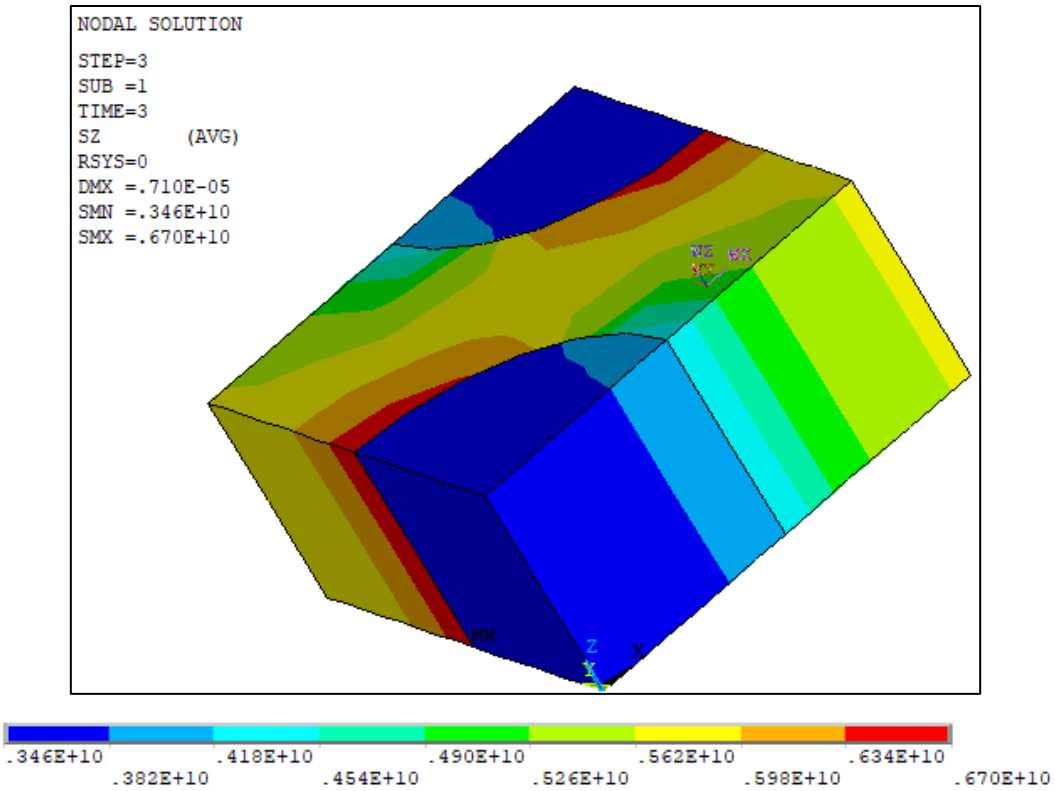

Figure 5.2 Z-stress, one-eighth model

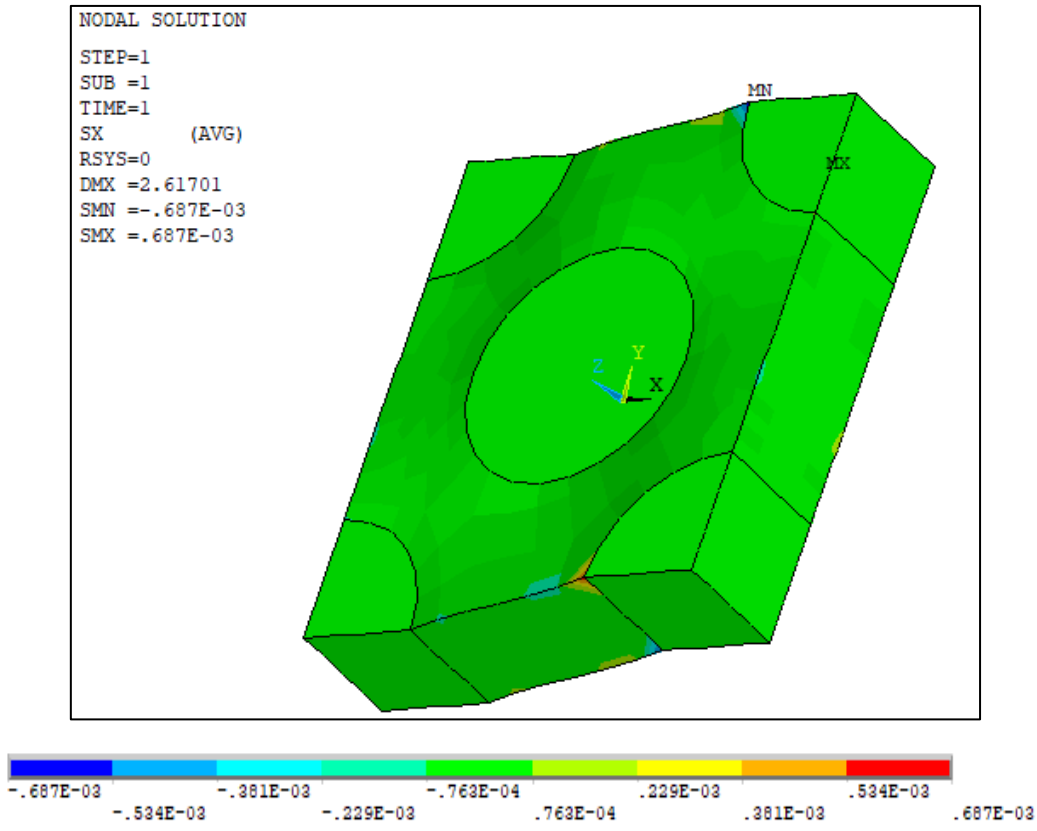

Figure 5.3 X-stress, full model of RVE

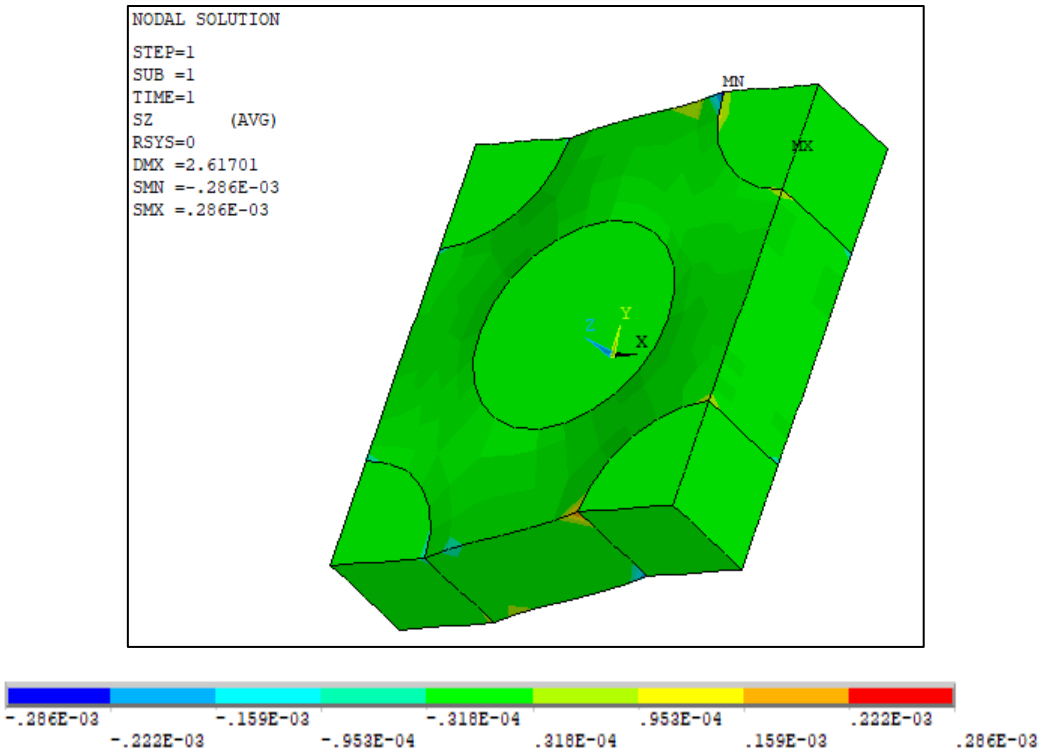

Figure 5.4 Z-stress, full model of RVE

5.4 Thermal analysis of one thixoforged aluminium plate considering convection and without considering thermal radiation

On the one hand, the results of the thermal simulation with an interface conductivity equal to the steel one considering convection and without considering thermal radiation are shown in Figures 5.5 to 5.8 at 20 s, meanwhile Figures 5.9 to 5.12 show the results at the same time considering the conductivity in the interface equal to the glass one. Both simulations are remade with a film coefficient of 10 $W/m^2 \cdot K$, it was described in chapter 4.

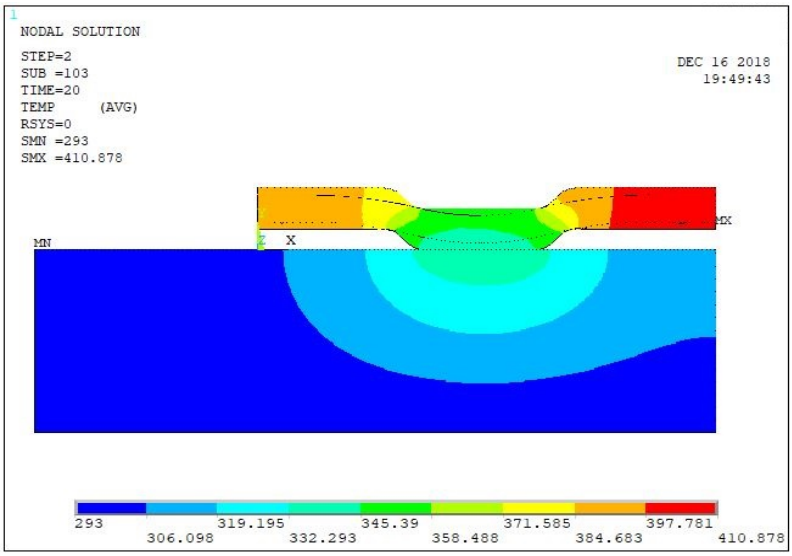

Figure 5.5 Temperature distribution at 20 s with an interface conductivity equal to the steel one, with k = 50.2 W/m·K and considering convection

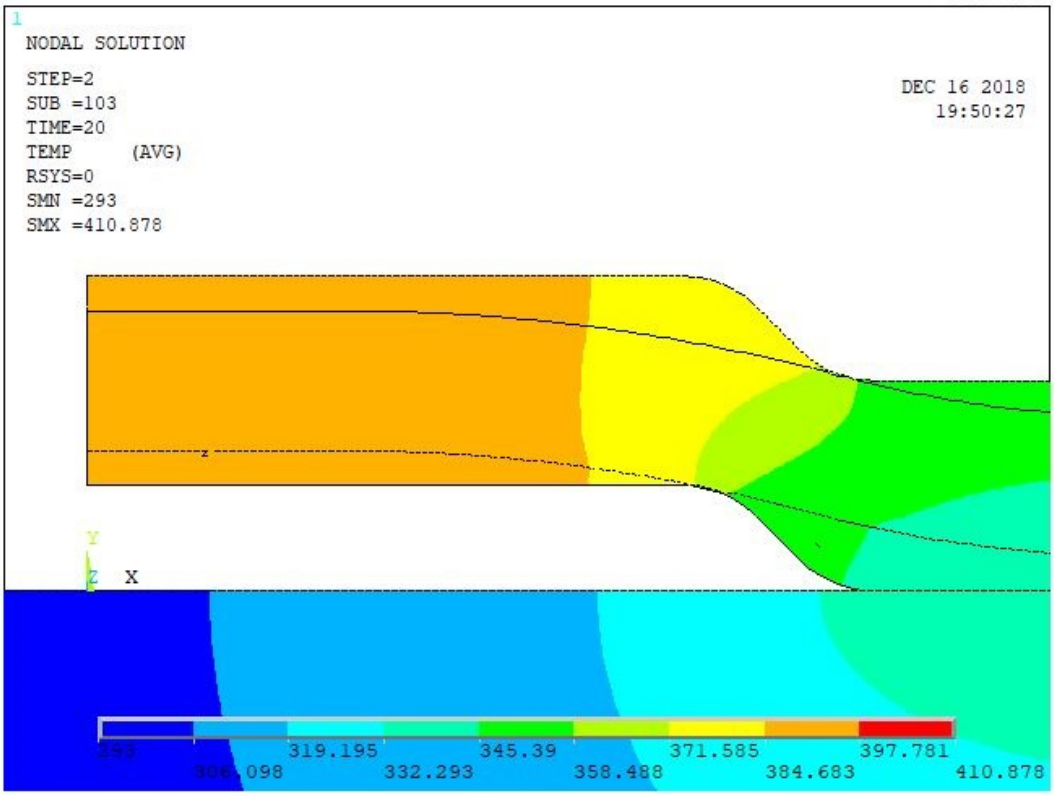

Figure 5.6 Temperature distribution at 20 s with an interface conductivity equal to the steel one, with k = 50.2 W/m·K and considering convection, left part of the plate

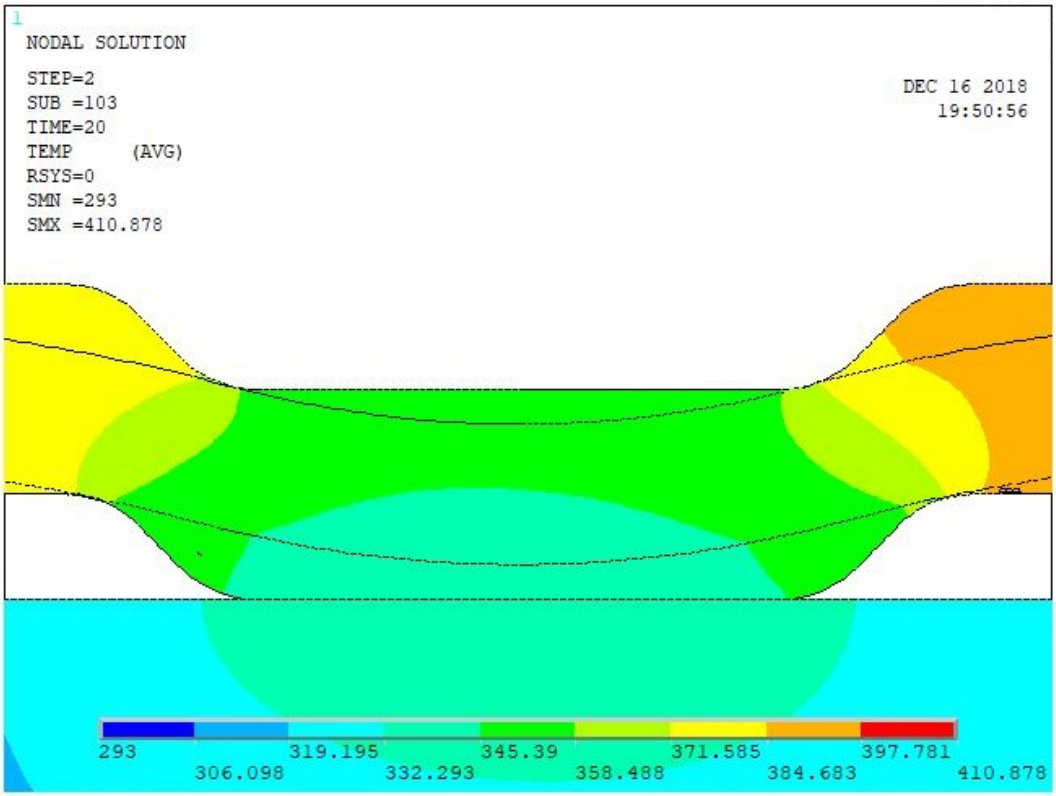

Figure 5.7 Temperature distribution at 20 s with an interface conductivity equal to the steel one, with k = 50.2 W/m·K and considering convection, centre of the plate

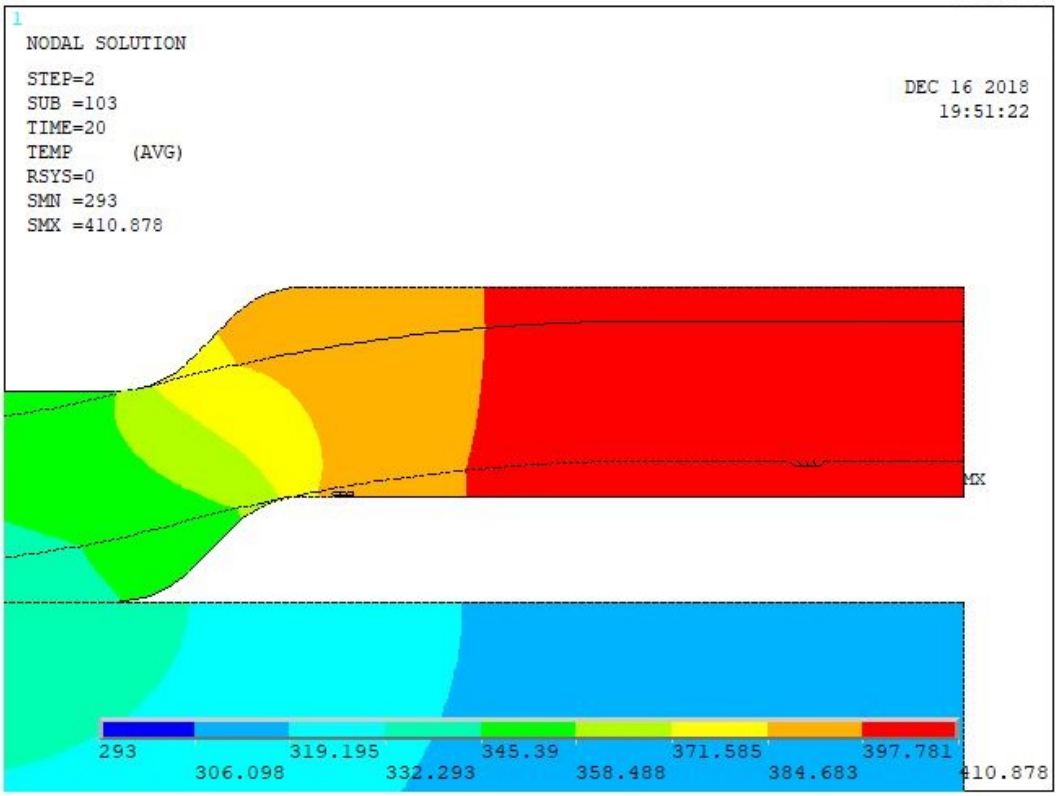

Figure 5.8 Temperature distribution at 20 s with an interface conductivity equal to the steel one, with k = 50.2 W/m·K and considering convection, right part of the plate

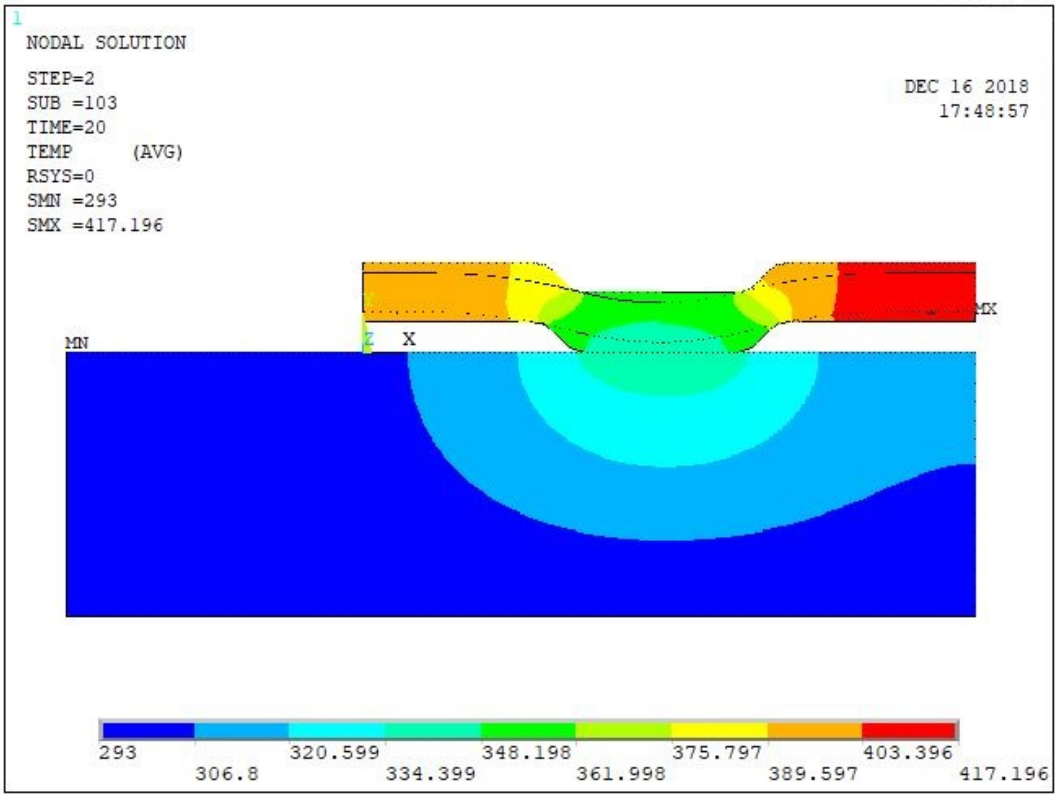

Figure 5.9 Temperature distribution at 20 s with an interface conductivity equal to the glass one, with k = 0.8 W/m·K and considering convection

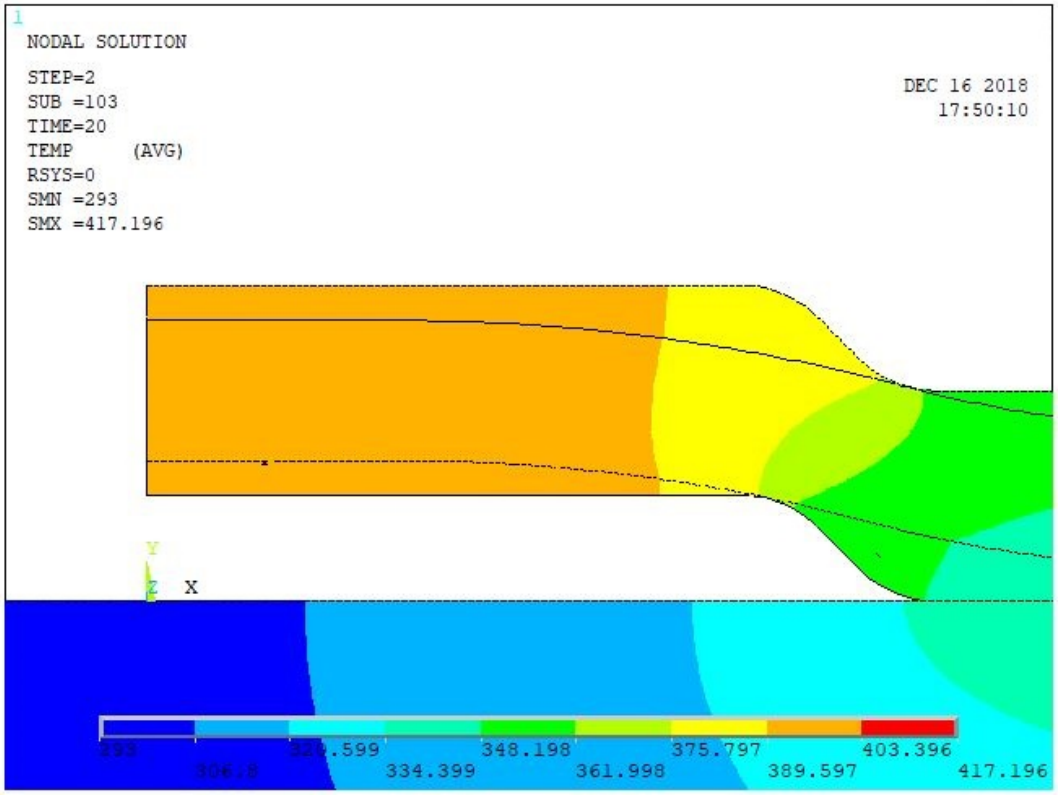

Figure 5.10 Temperature distribution at 20 s with an interface conductivity equal to the glass one, with k = 0.8 W/m·K and considering convection, left part of the plate

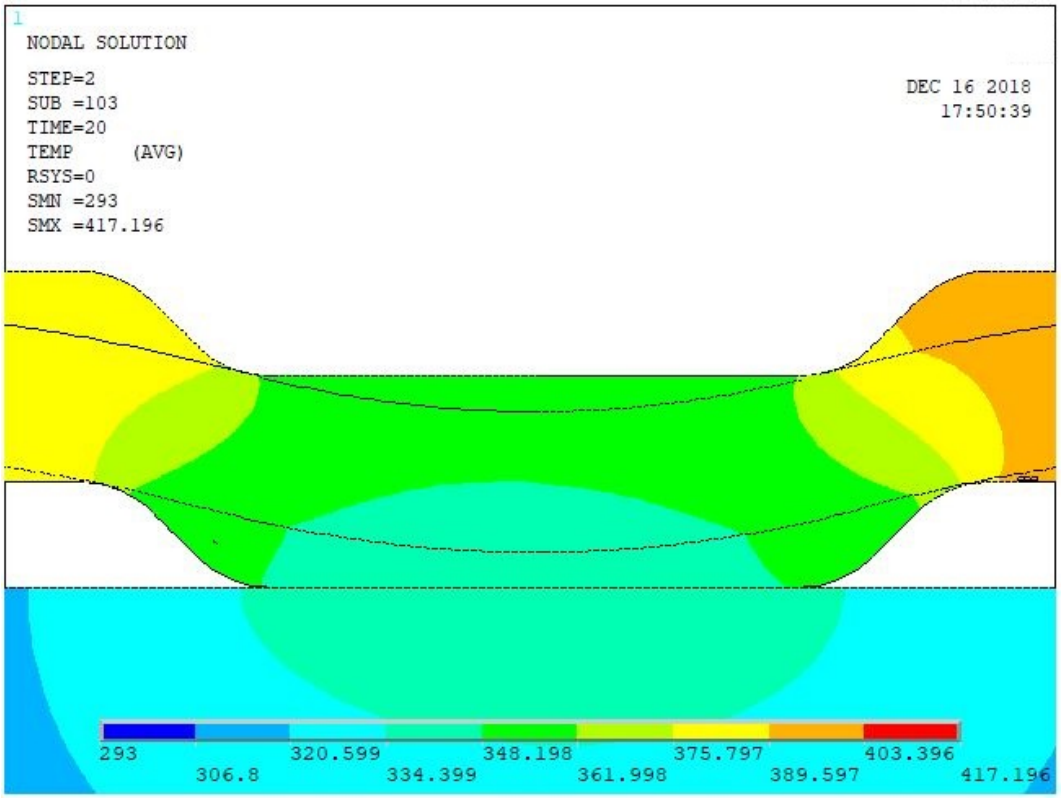

Figure 5.11 Temperature distribution at 20 s with an interface conductivity equal to the glass one, with k = 0.8 W/m·K and considering convection, centre of the plate

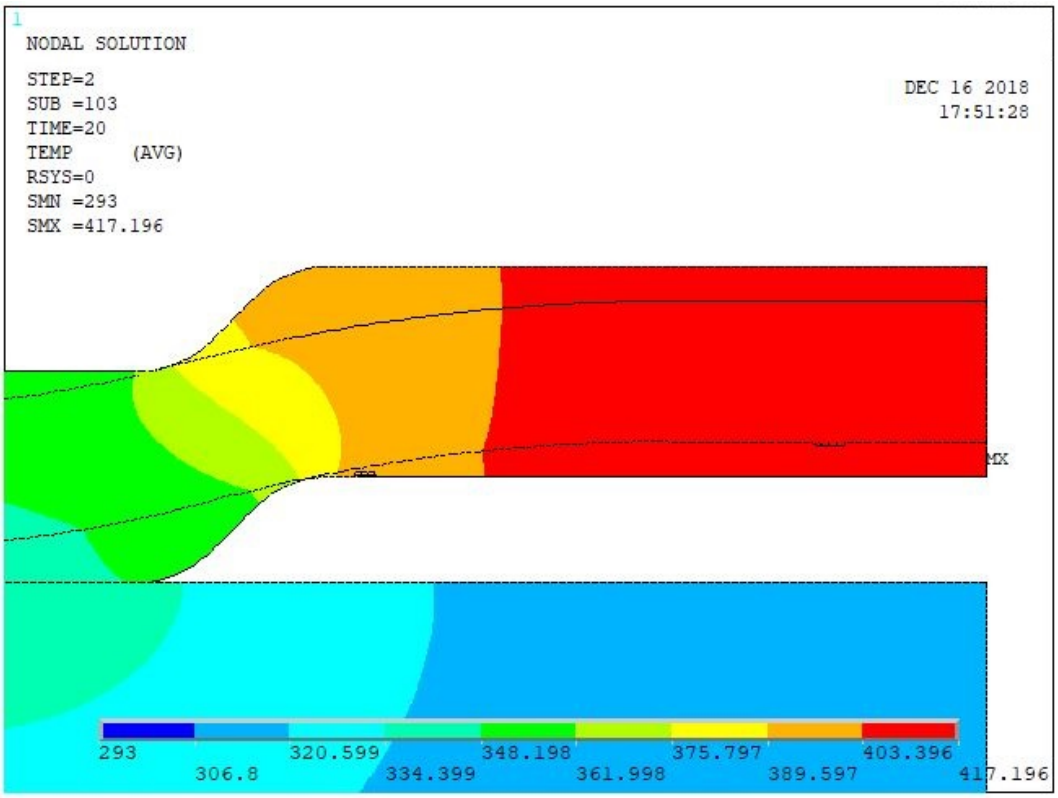

Figure 5.12 Temperature distribution at 20 s with an interface conductivity equal to the glass one, with k = 0.8 W/m·K and considering convection, right part of the plate

On the other hand, the results of the thermal simulation, evolution of the temperature, with interface conductivity equal to the steel one considering convection and without considering thermal radiation in the selected nodes, as shown in chapter 4, are shown in Figures 5.13 to 5.23, meanwhile Figures 5.24 to 5.34 show the results considering the conductivity in the interface equal to the glass one.

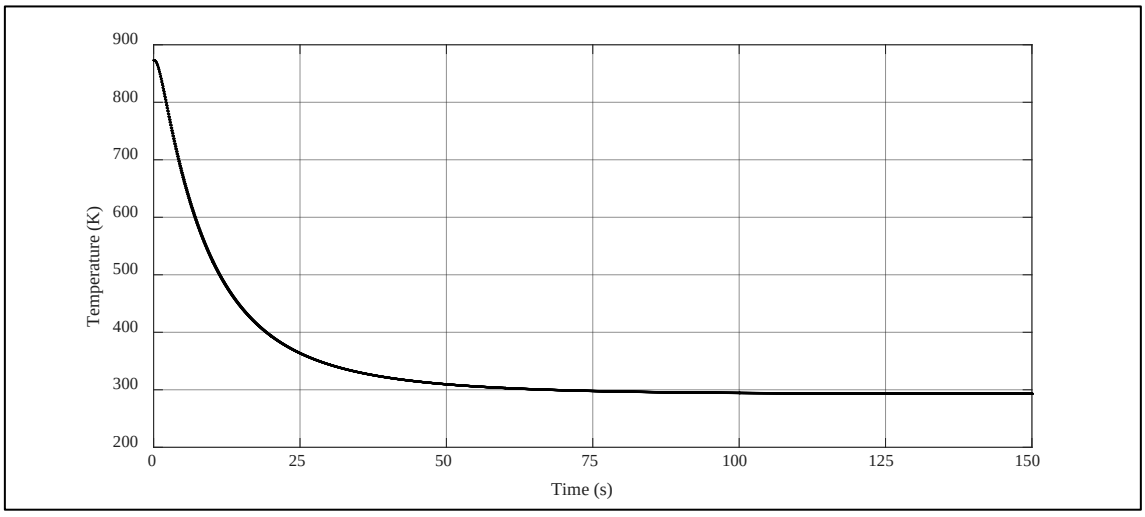

Figure 5.13 Temperature evolution of nodes 33801, 33805, 33810, 63910, 63906 and 63901 with k = 50.2 W/m·K, considering convection

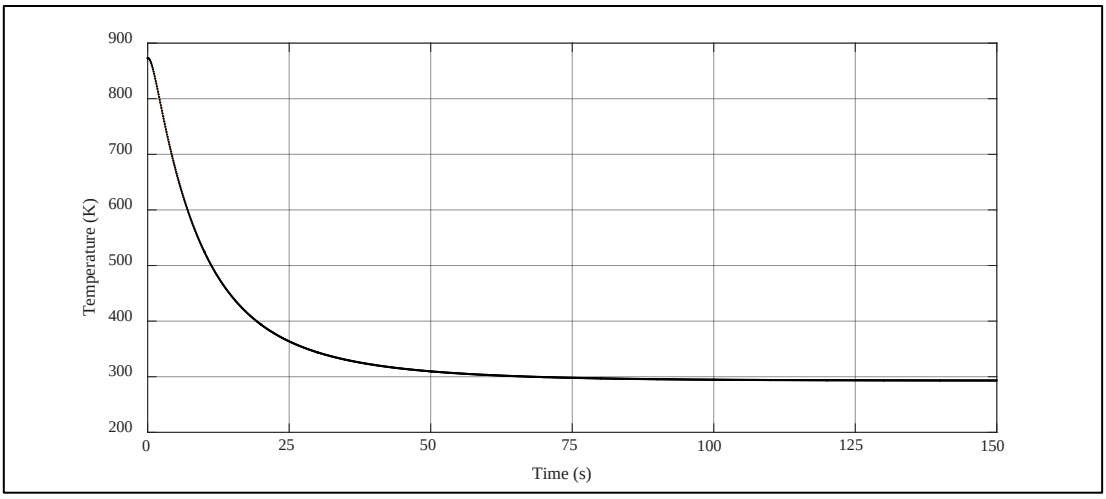

Figure 5.14 Temperature evolution of nodes 3801, 3810 and 3821 with k = 50.2 W/m·K, considering convection

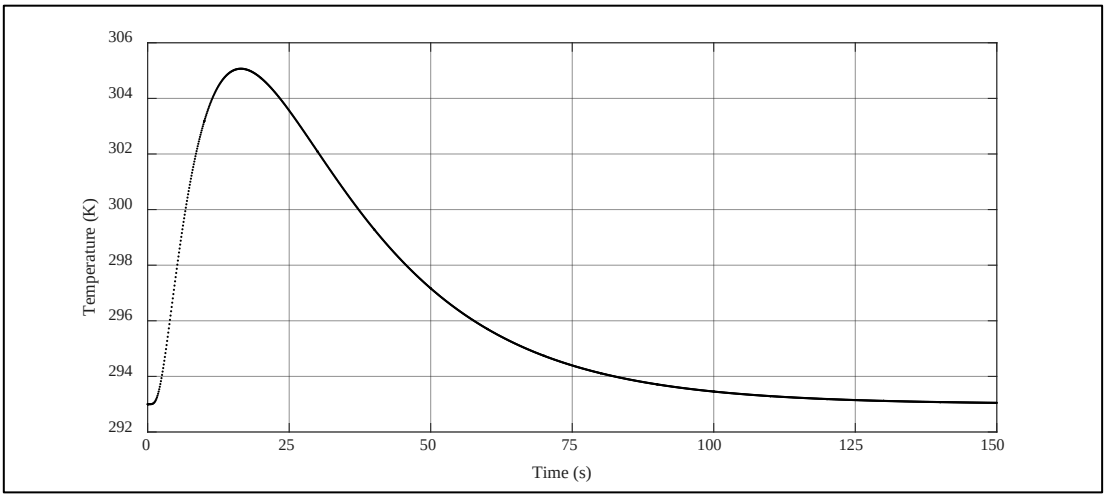

Figure 5.15 Temperature evolution of node 121259 with k = 50.2 W/m·K, considering convection

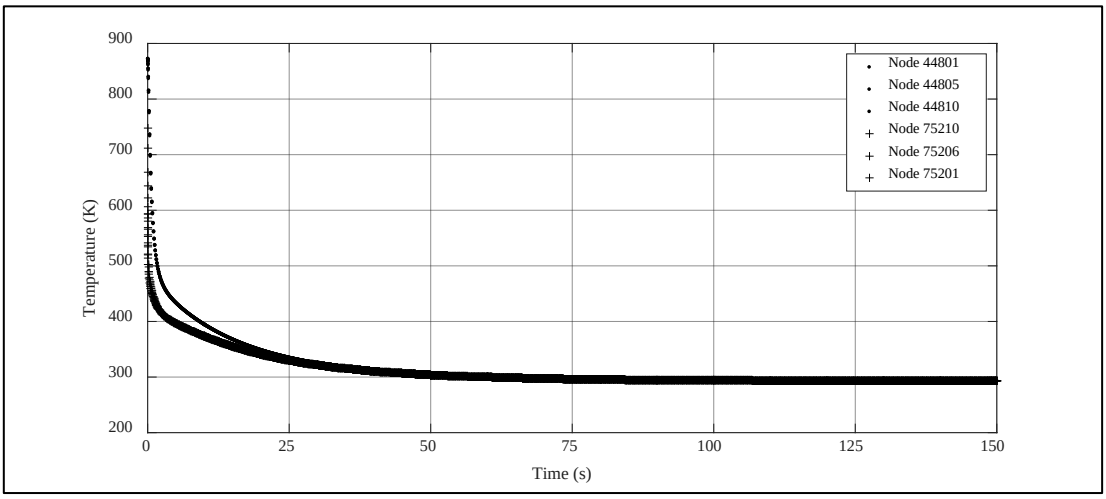

Figure 5.16 Temperature evolution of nodes 44801, 44805, 44810, 75210, 75206 and 75201 with k = 50.2 W/m·K, considering convection

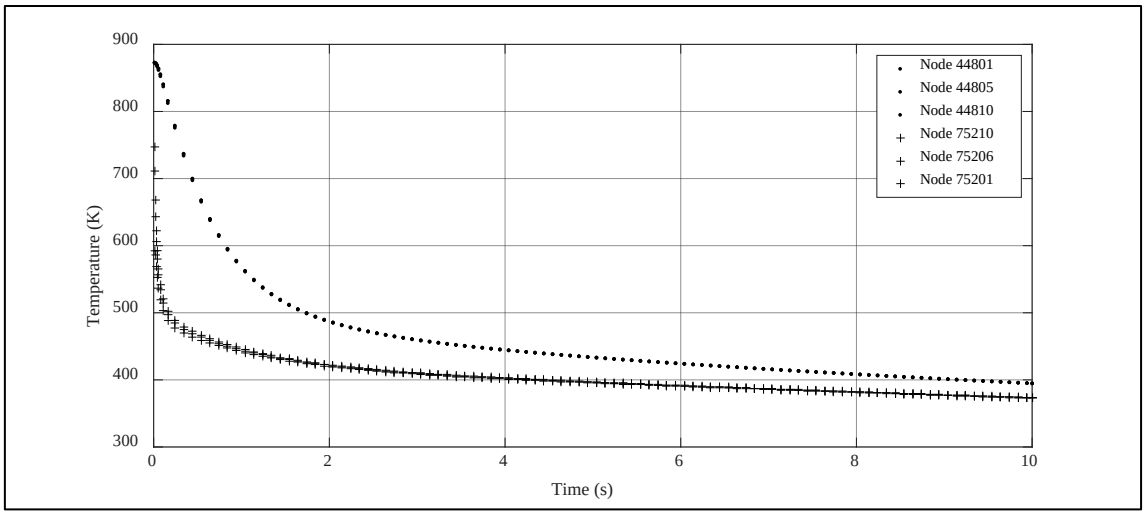

Figure 5.17 Zoom of figure 5.16

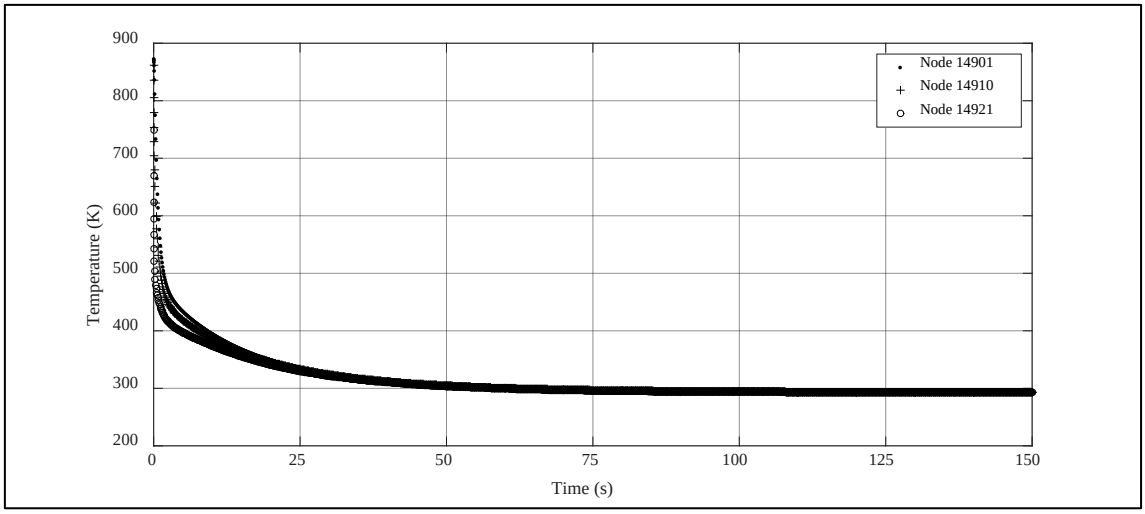

Figure 5.18 Temperature evolution of nodes 14901, 14910 and 14921 with k = 50.2 W/m·K, considering convection

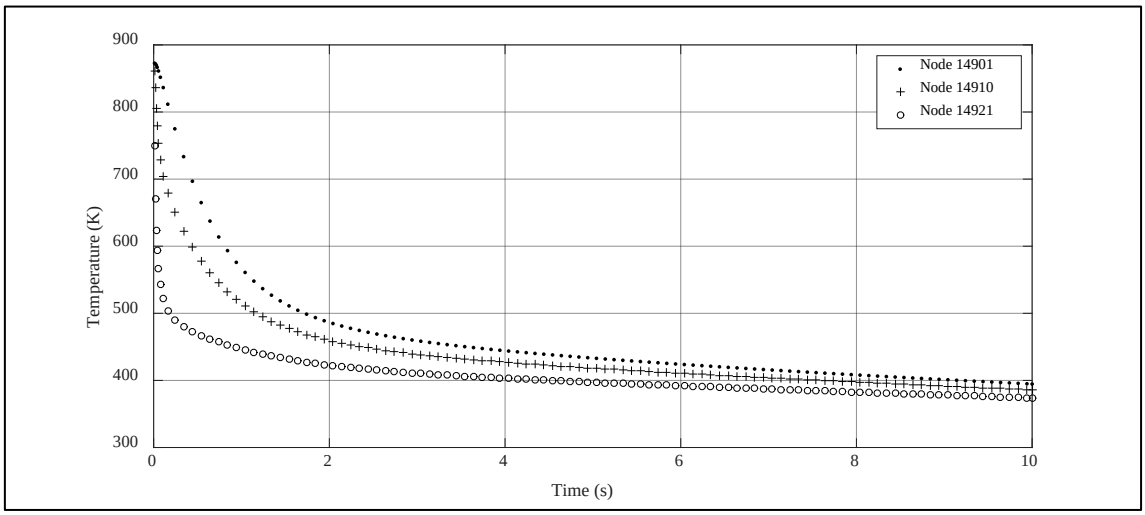

Figure 5.19 Zoom of figure 5.18

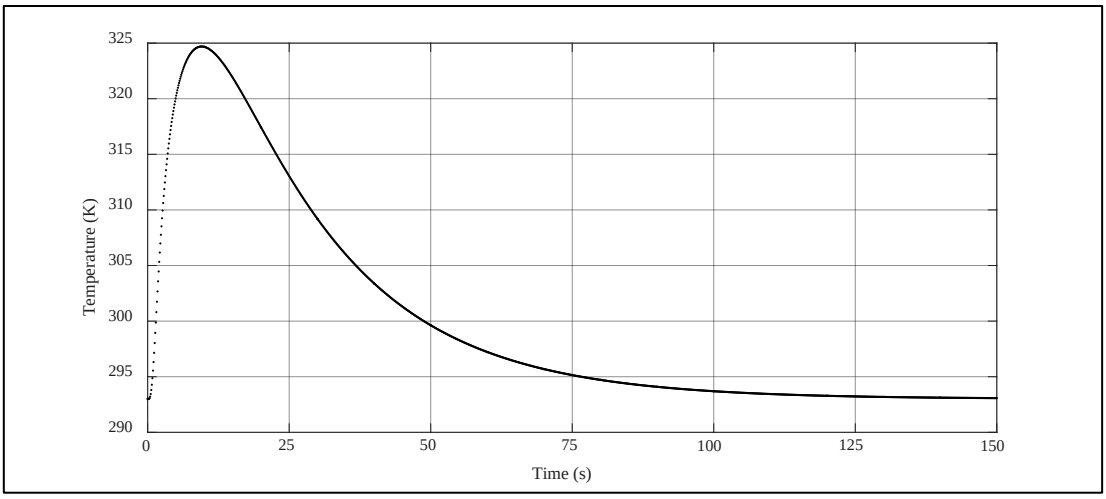

Figure 5.20 Temperature evolution of node 121354 with k = 50.2 W/m·K, considering convection

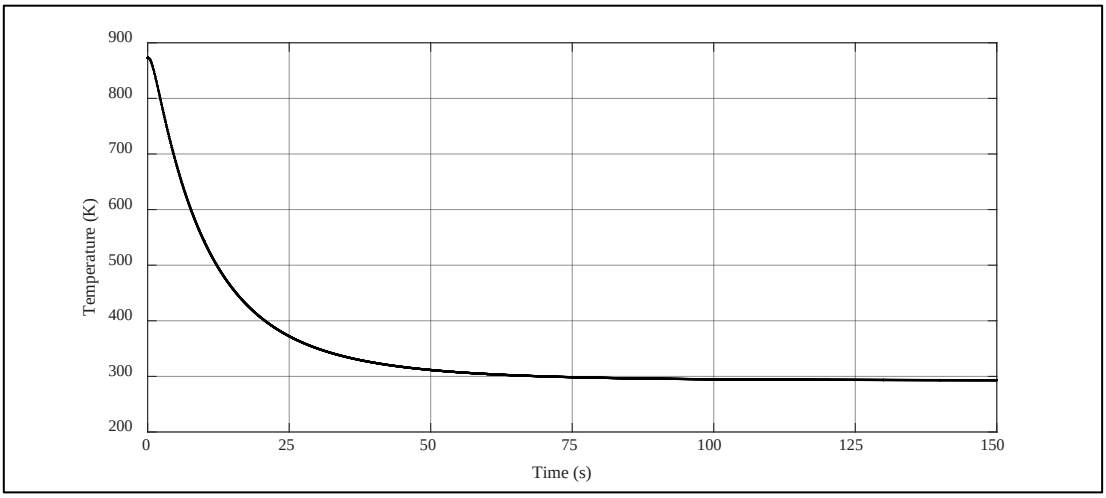

Figure 5.21 Temperature evolution of nodes 56101, 56105, 56110, 78910, 78906 and 78901 with k = 50.2 W/m·K, considering convection

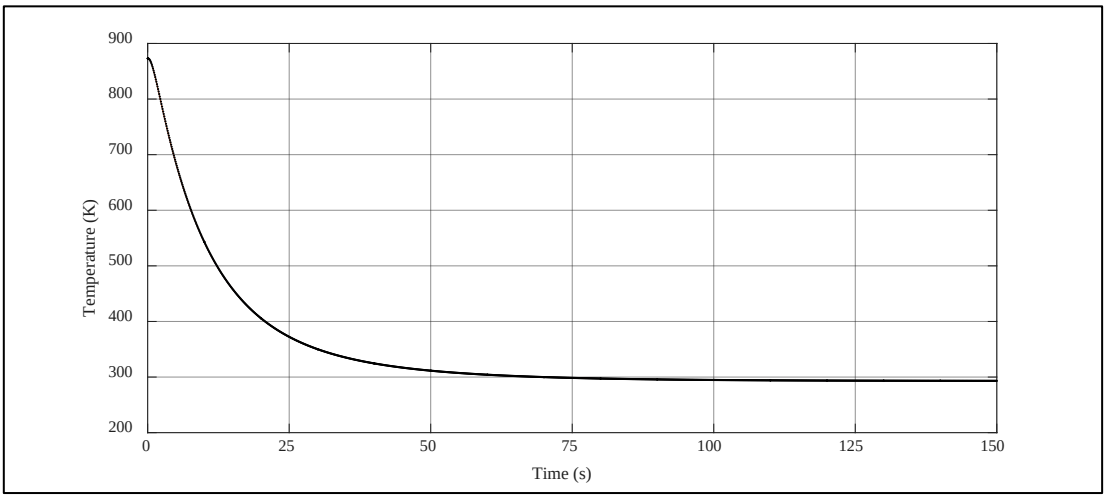

Figure 5.22 Temperature evolution of nodes 26301, 26310 and 26321 with k = 50.2 W/m·K, considering convection

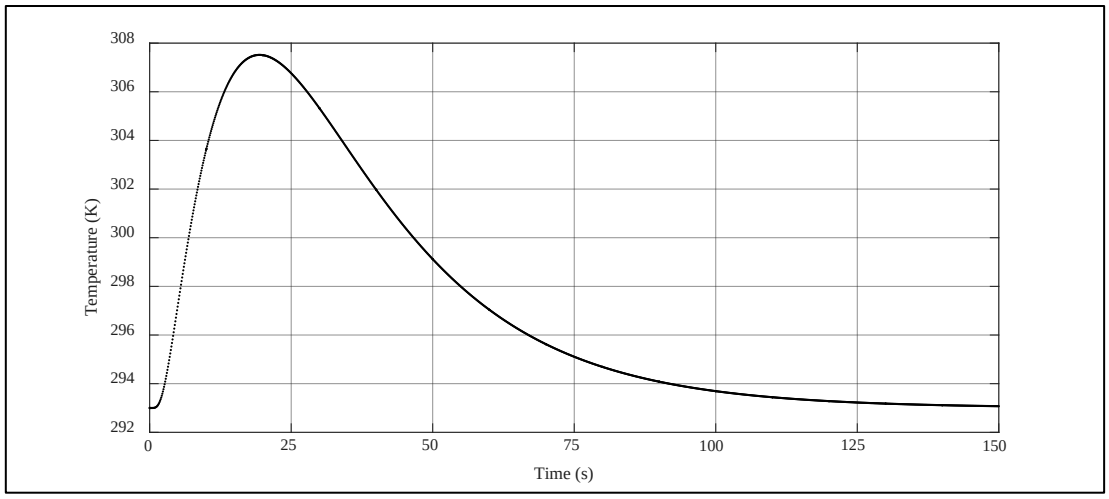

Figure 5.23 Temperature evolution of node 407585 with k = 50.2 W/m·K, considering convection

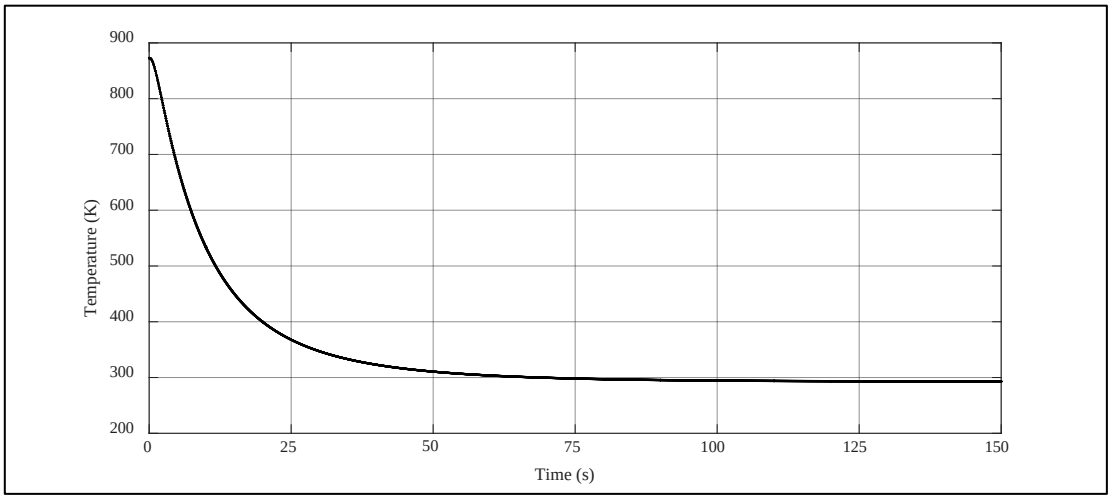

Figure 5.24 Temperature evolution of nodes 33801, 33805, 33810, 63910, 63906 and 63901 with k = 0.8 W/m·K, considering convection

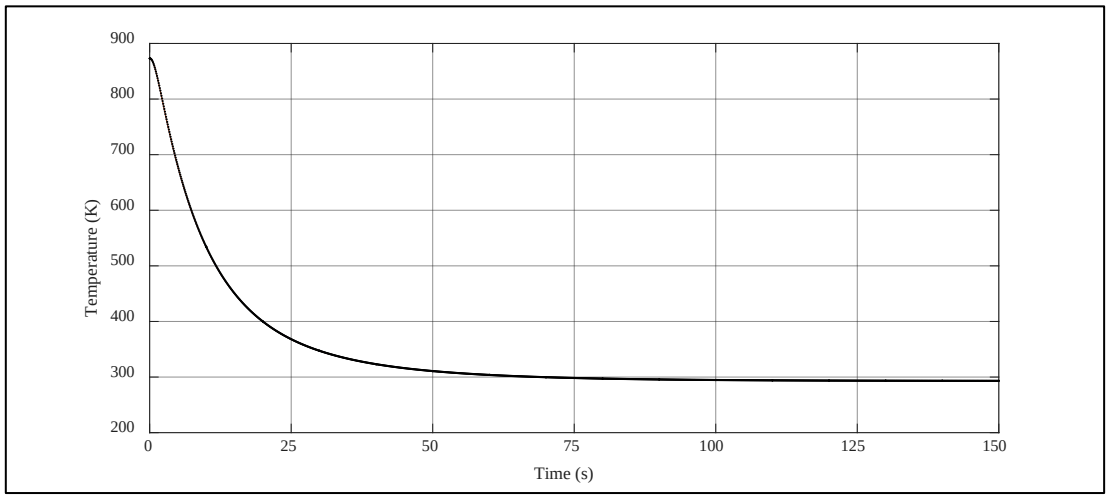

Figure 5.25 Temperature evolution of nodes 3801, 3810 and 3821 with k = 0.8 W/m·K, considering convection

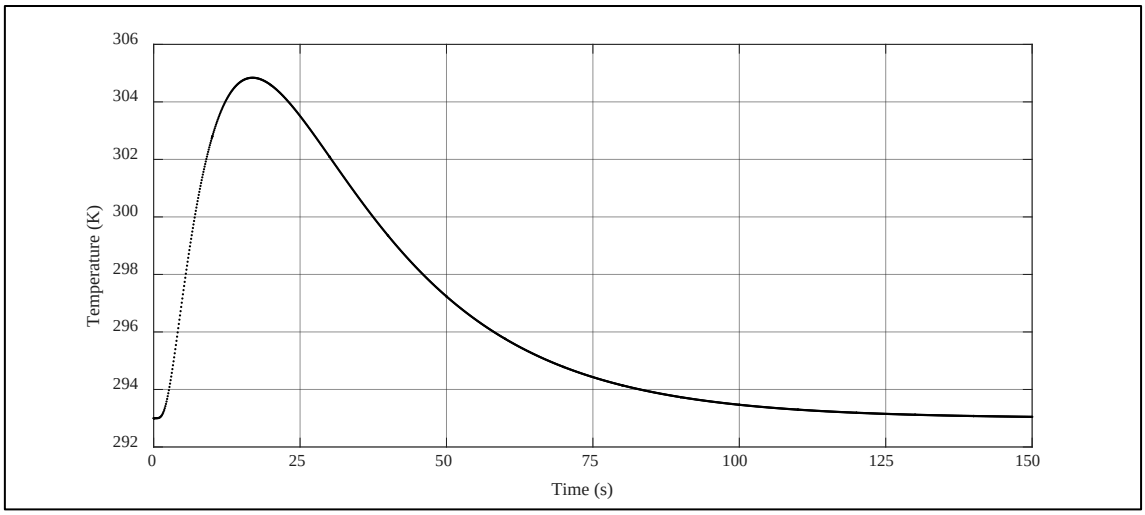

Figure 5.26 Temperature evolution of node 121259 with k = 0.8 W/m·K, considering convection

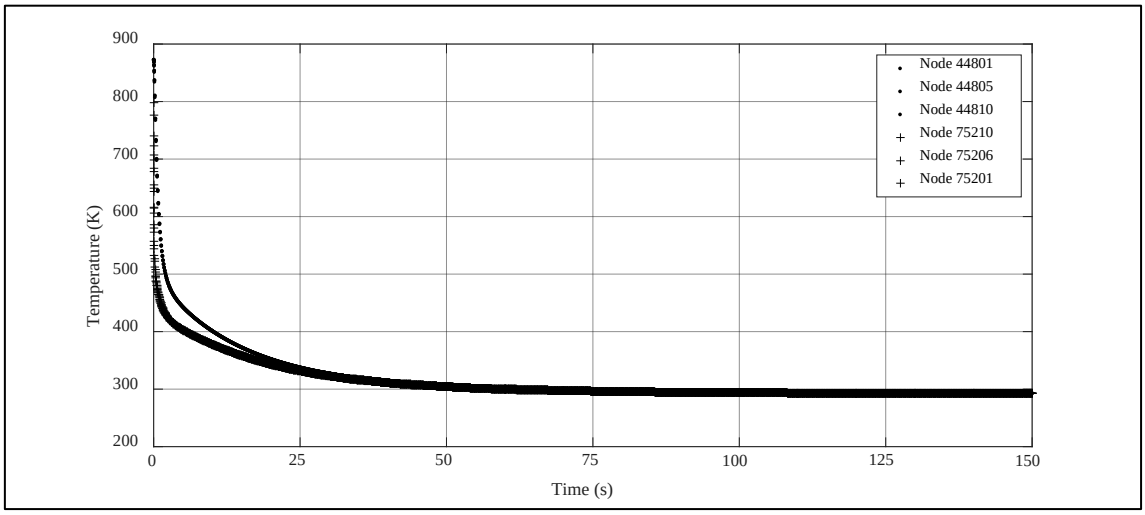

Figure 5.27 Temperature evolution of nodes 44801, 44805, 44810, 75210, 75206 and 75201 with k = 0.8 W/m·K, considering convection

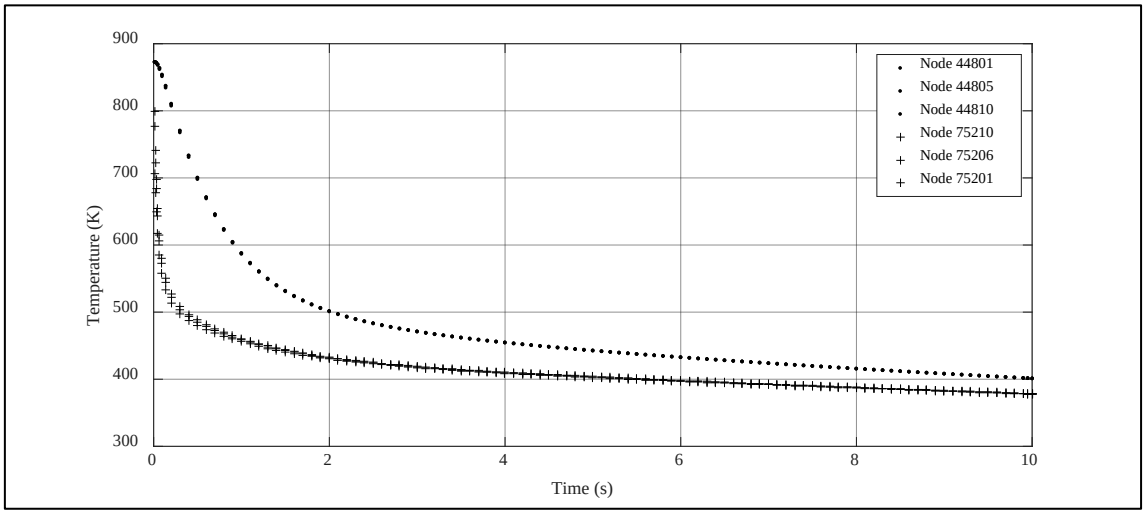

Figure 5.28 Zoom of figure 5.27

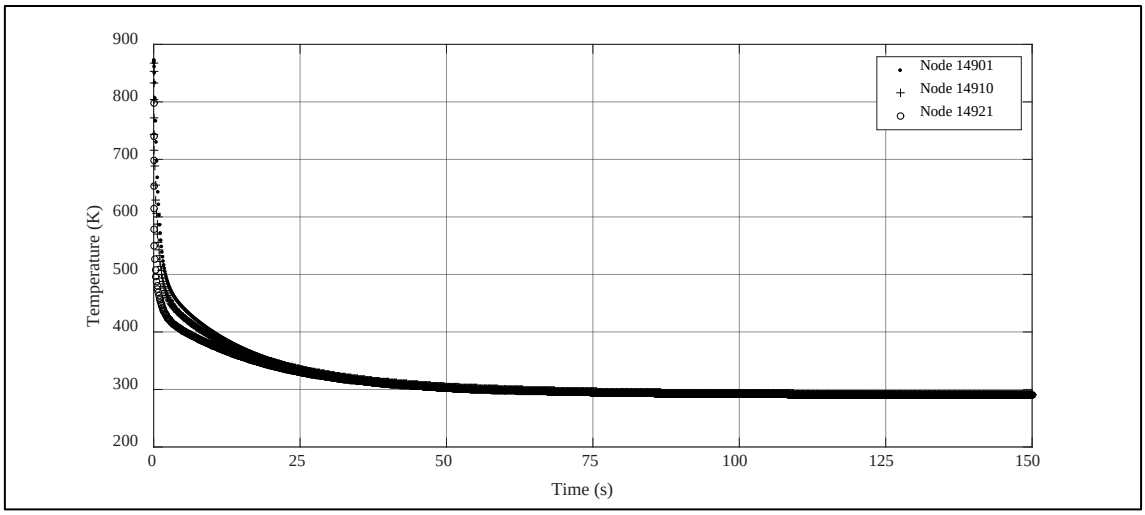

Figure 5.29 Temperature evolution of nodes 14901, 14910 and 14921 with k = 0.8 W/m·K, considering convection

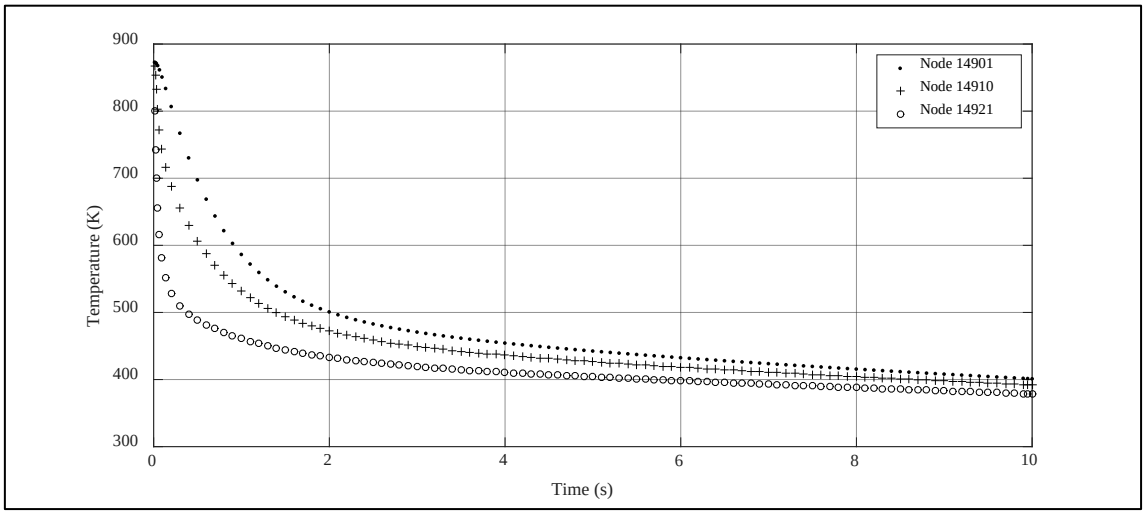

Figure 5.30 Zoom of figure 5.29

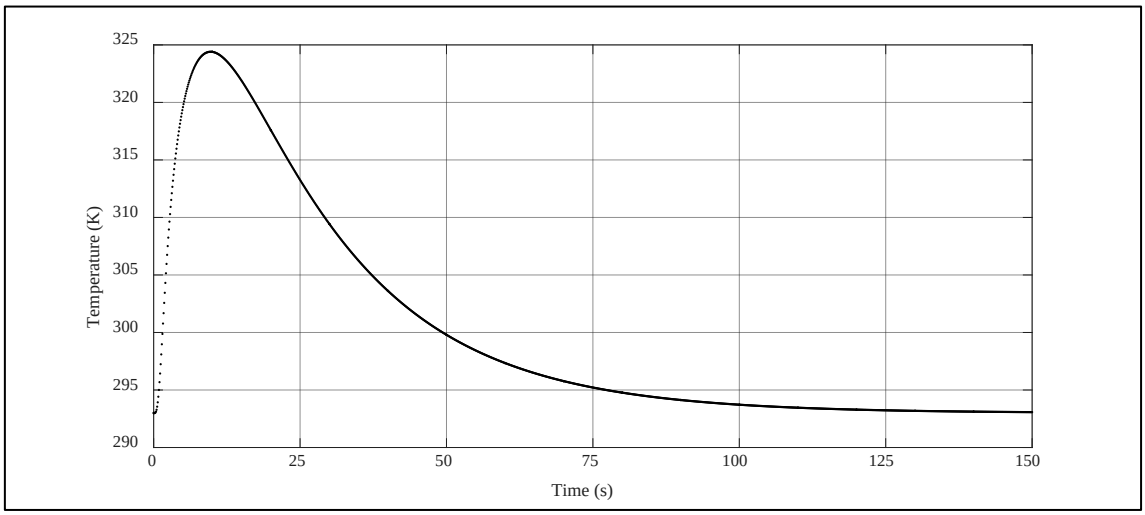

Figure 5.31 Temperature evolution of node 121354 with k = 0.8 W/m·K, considering convection

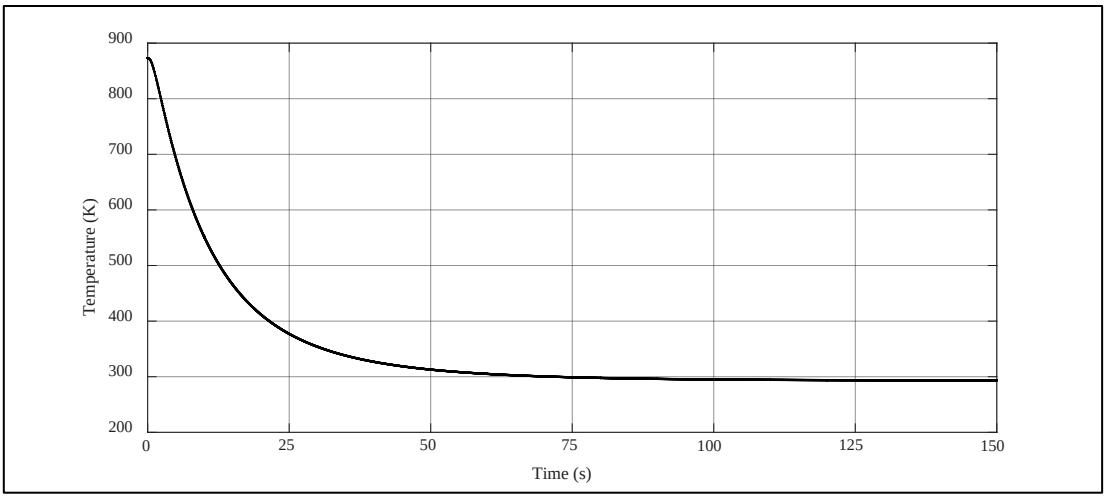

Figure 5.32 Temperature evolution of nodes 56101, 56105, 56110, 78910, 78906 and 78901 with k = 0.8 W/m·K, considering convection

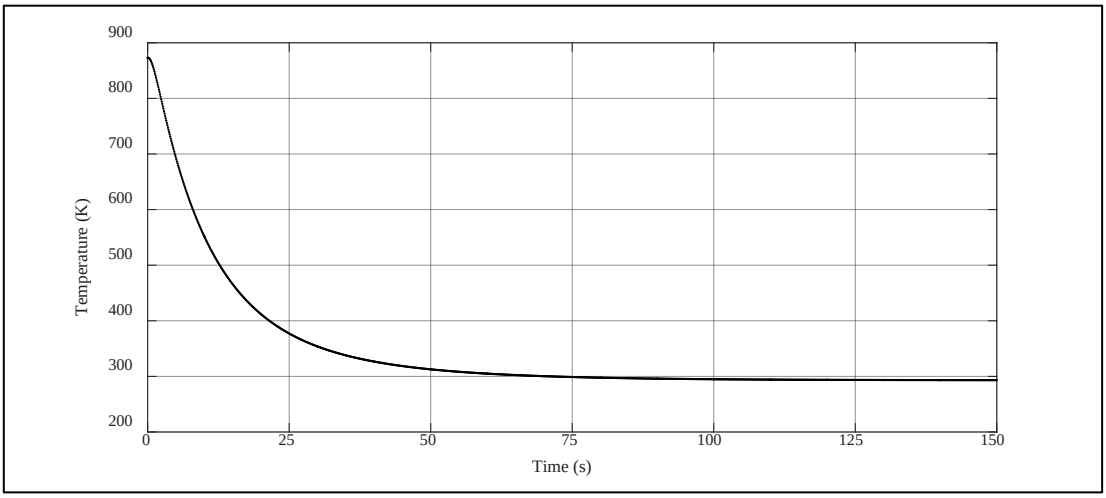

Figure 5.33 Temperature evolution of nodes 26301, 26310 and 26321 with k = 0.8 W/m·K, considering convection

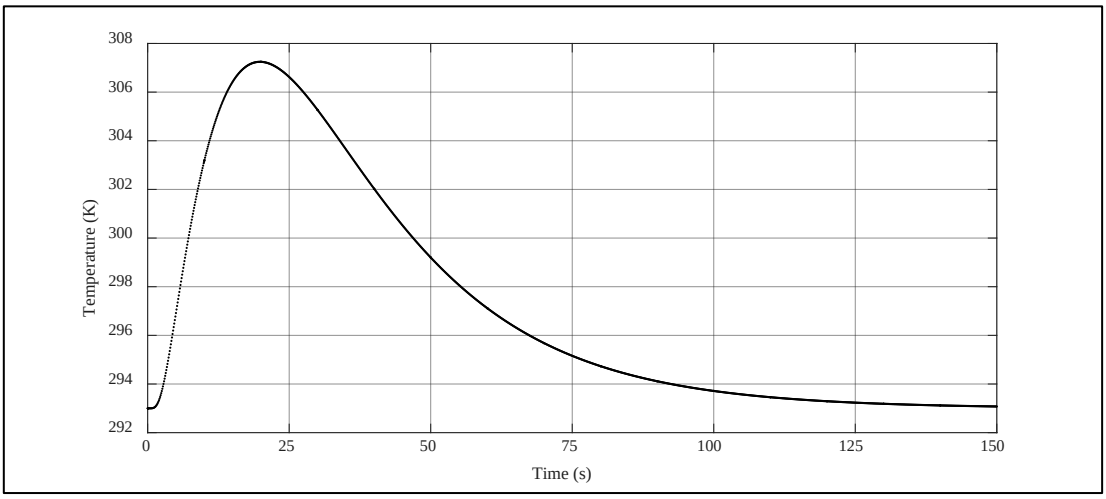

Figure 5.34 Temperature evolution of node 407585 with k = 0.8 W/m·K, considering convection

Fig. 5.35 shows the temperature difference between nodes 63906 and 33805 in the case of considering convection and interface of glass. At the beginning, the support is cold and the node 63906 transfers heat to the plate base. After approximately one second, the support heats up and the node 63906 is unable to transfer the heat in the same conditions. Approximately, at 2.5 s there is a temperature difference of 4.38 ºC.

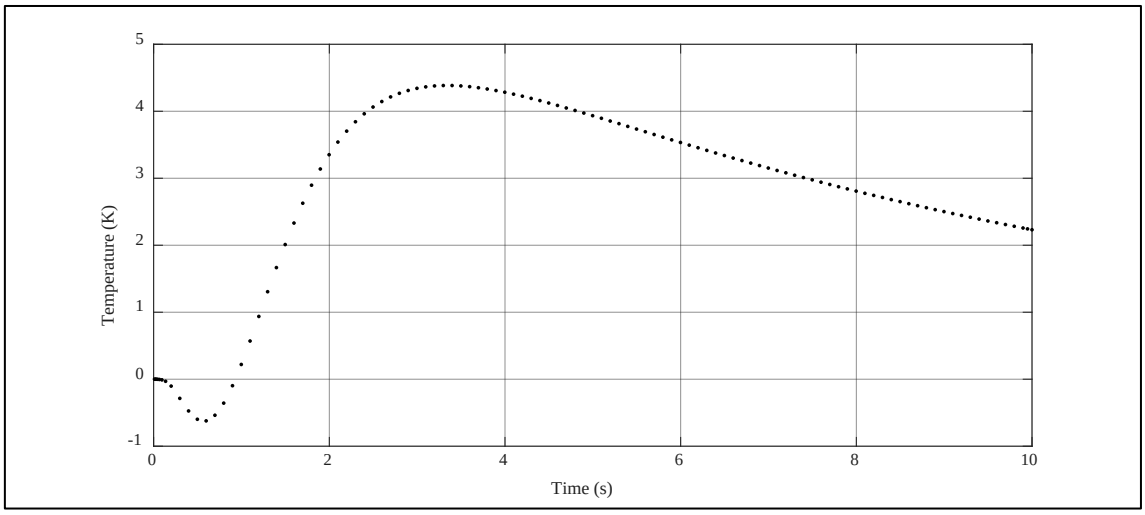

Figure 5.35 Temperature difference between nodes 63906 and 33805, considering convection and interface of glass

Fig. 5.36 shows the temperature difference between nodes 75206 and 44805 in the case of considering convection and interface of glass. At the beginning, the aluminium close to the support is colder than the upper aluminium layer. It is remarkable the difference of 292.6 K at 0.135 s.

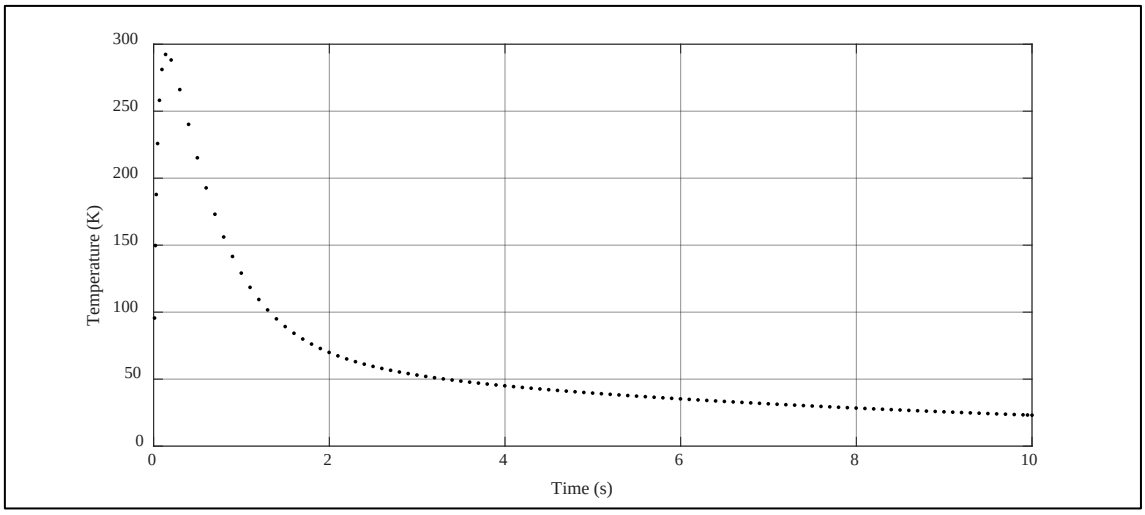

Figure 5.36 Temperature difference between nodes 75206 and 44805, considering convection and interface of glass

Now, it was realized the same simulations but with a film coefficient of 100 $W/m^2 \cdot K$, as it was described in chapter 4. The results of the thermal simulation with an interface conductivity equal to the steel one considering convection and without considering thermal radiation are shown in Figures 5.37 to 5.40 at 20 s, meanwhile Figures 5.41 to

5.44 show the results at the same time considering the conductivity in the interface equal to the glass one.

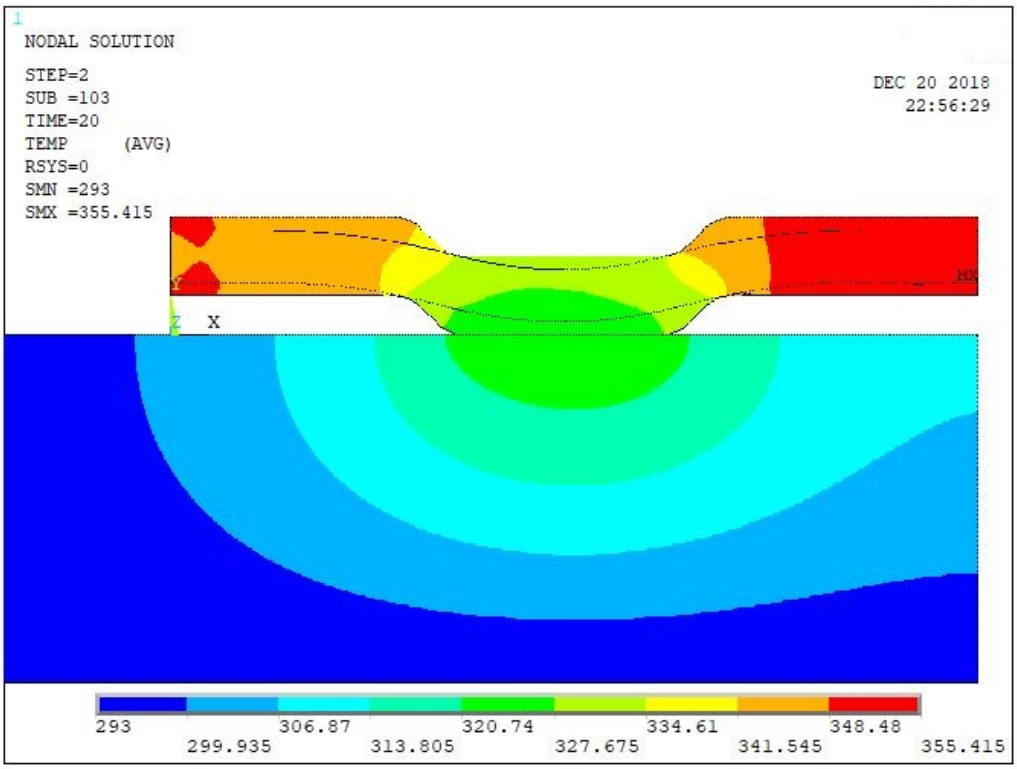

Figure 5.37 Temperature distribution at 20 s with an interface conductivity equal to the steel one, with k = 50.2 W/m·K and considering convection

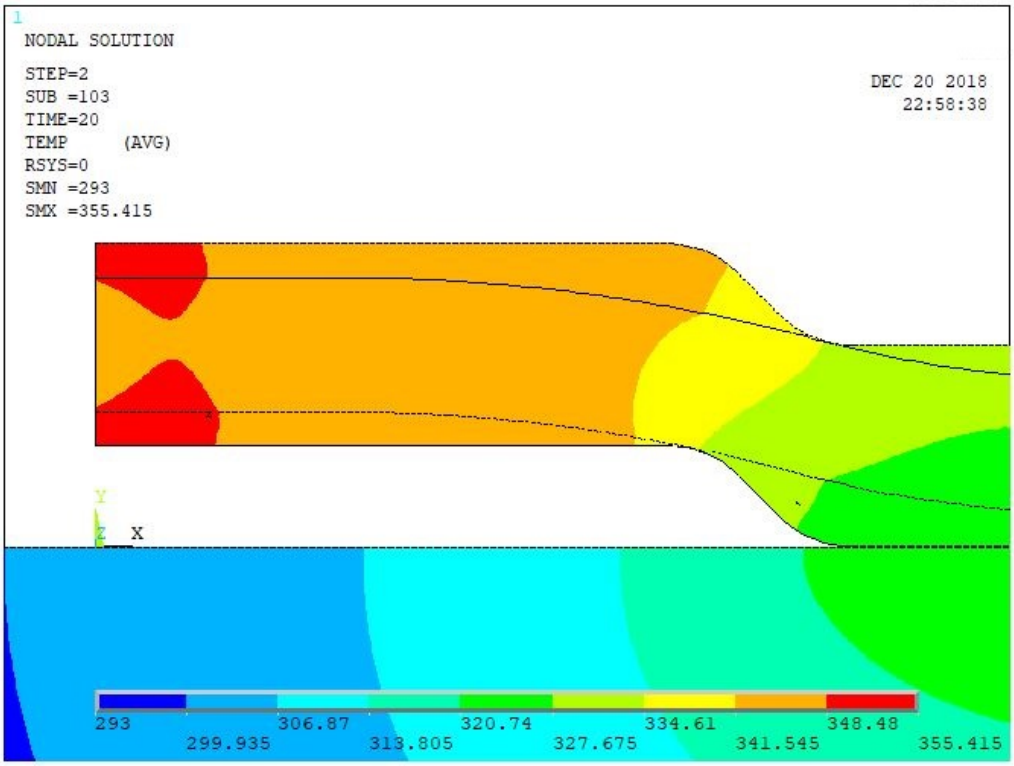

Figure 5.38 Temperature distribution at 20 s with an interface conductivity equal to the steel one, with k = 50.2 W/m·K and considering convection, left part of the plate

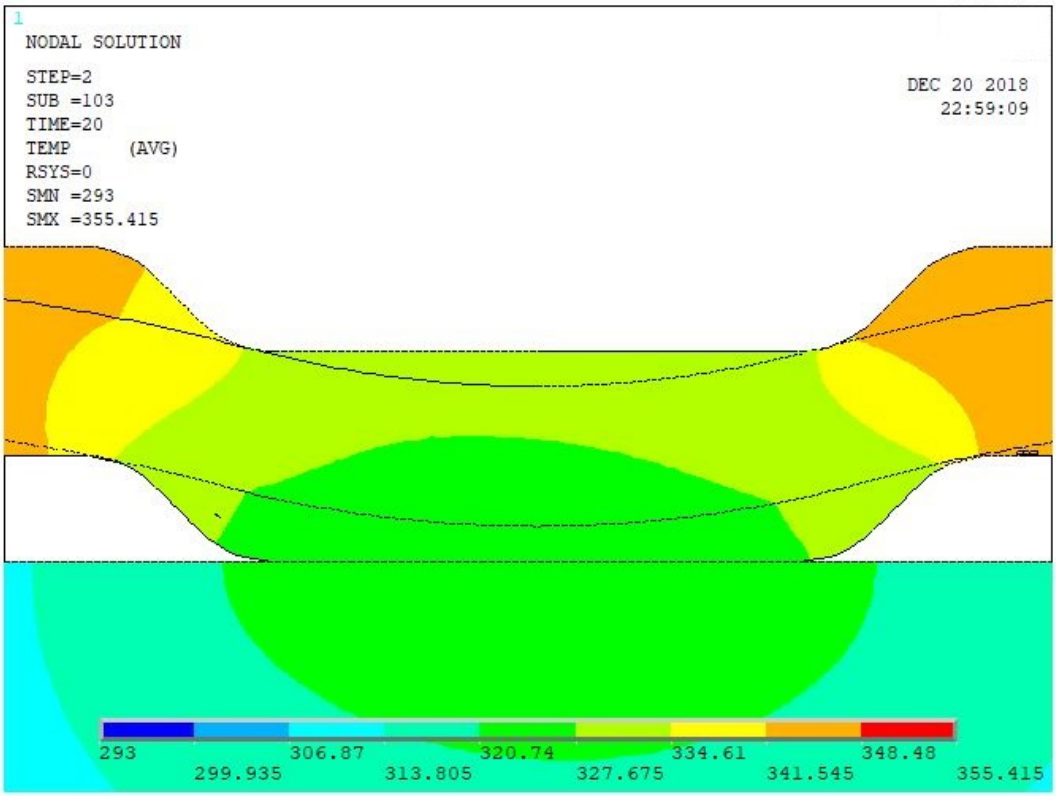

Figure 5.39 Temperature distribution at 20 s with an interface conductivity equal to the steel one, with k = 50.2 W/m·K and considering convection, centre of the plate

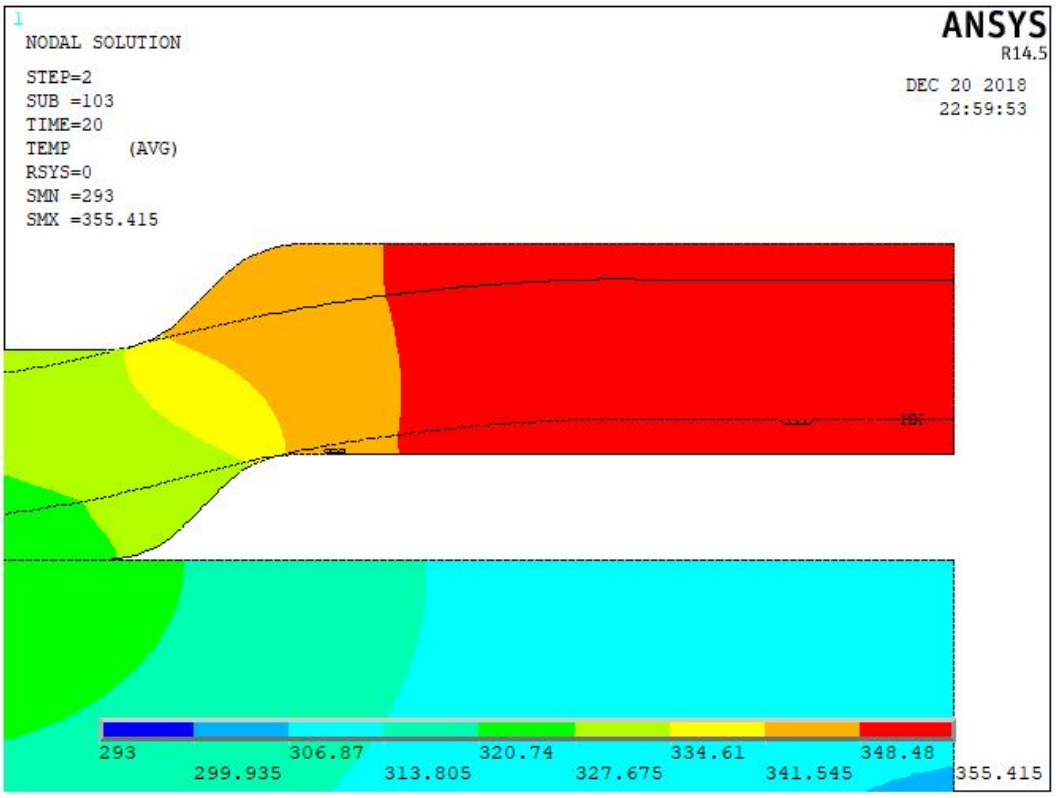

Figure 5.40 Temperature distribution at 20 s with an interface conductivity equal to the steel one, with k = 50.2 W/m·K and considering convection, right part of the plate

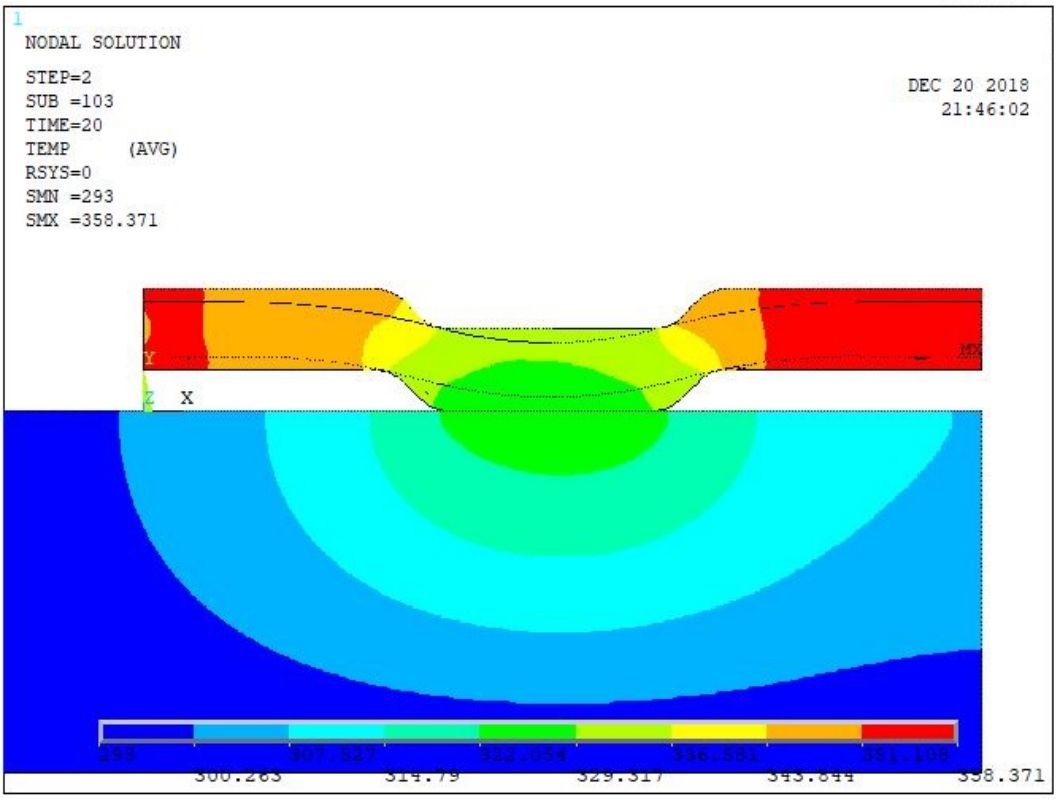

Figure 5.41 Temperature distribution at 20 s with an interface conductivity equal to the glass one, with k = 0.8 W/m·K and considering convection

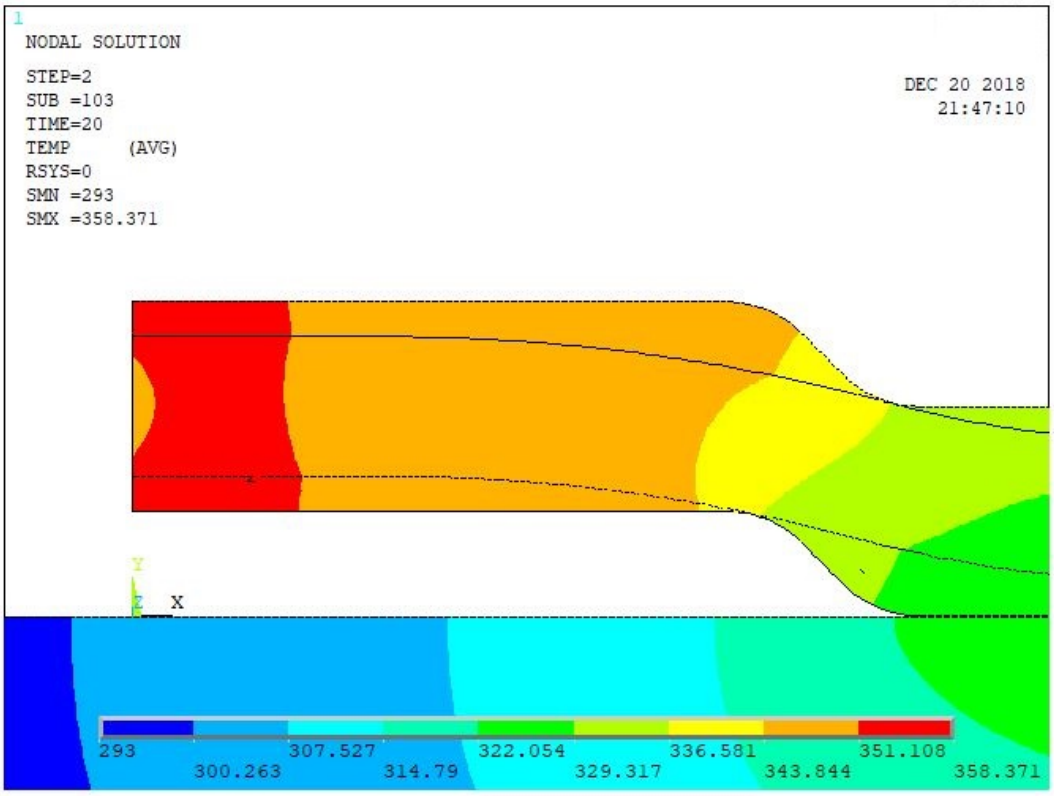

Figure 5.42 Temperature distribution at 20 s with an interface conductivity equal to the glass one, with k = 0.8 W/m·K and considering convection, left part of the plate

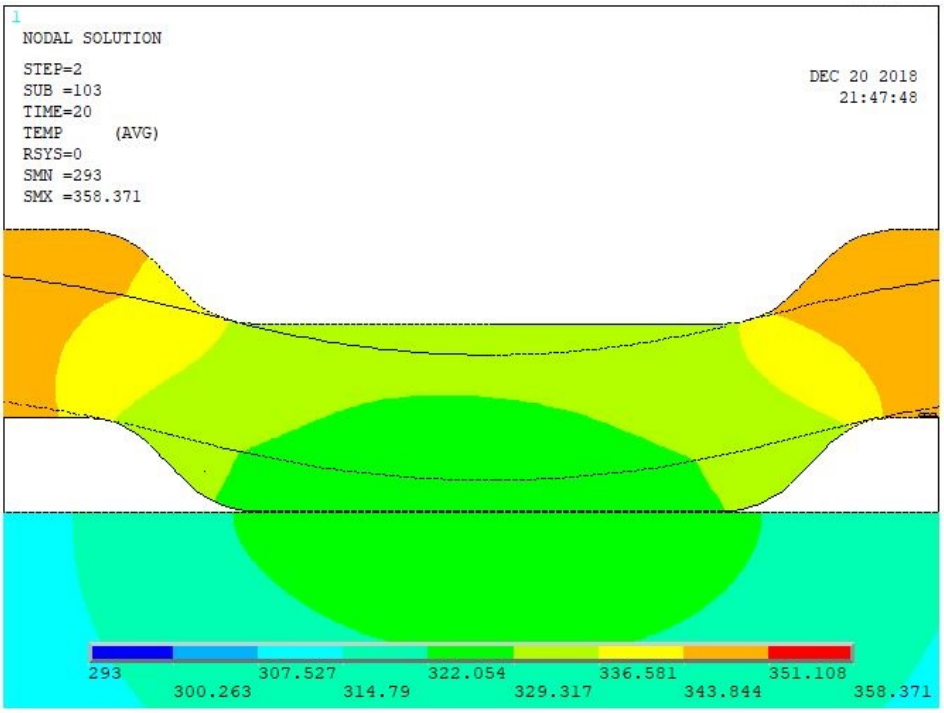

Figure 5.43 Temperature distribution at 20 s with an interface conductivity equal to the glass one, with k = 0.8 W/m·K and considering convection, centre of the plate

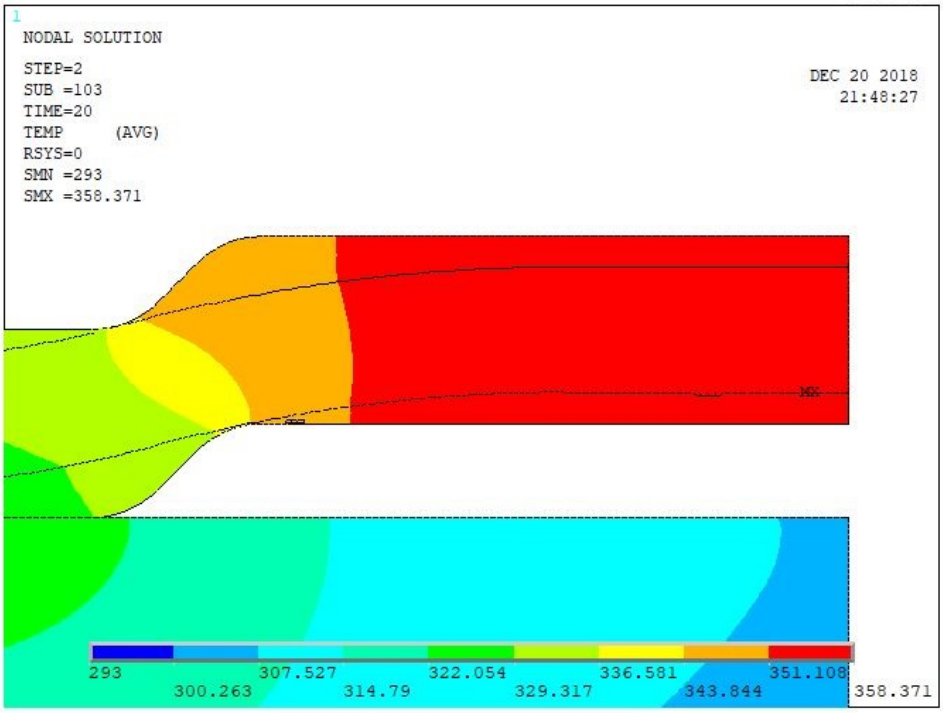

Figure 5.44 Temperature distribution at 20 s with an interface conductivity equal to the glass one, with k = 0.8 W/m·K and considering convection, right part of the plate

The results of the thermal simulation, evolution of the temperature, with interface conductivity equal to the steel one considering convection and without considering thermal radiation in the selected nodes, as shown in chapter 4, are shown in Figures 5.45 to 5.55, meanwhile Figures 5.56 to 5.66 show the results considering the conductivity in the interface equal to the glass one.

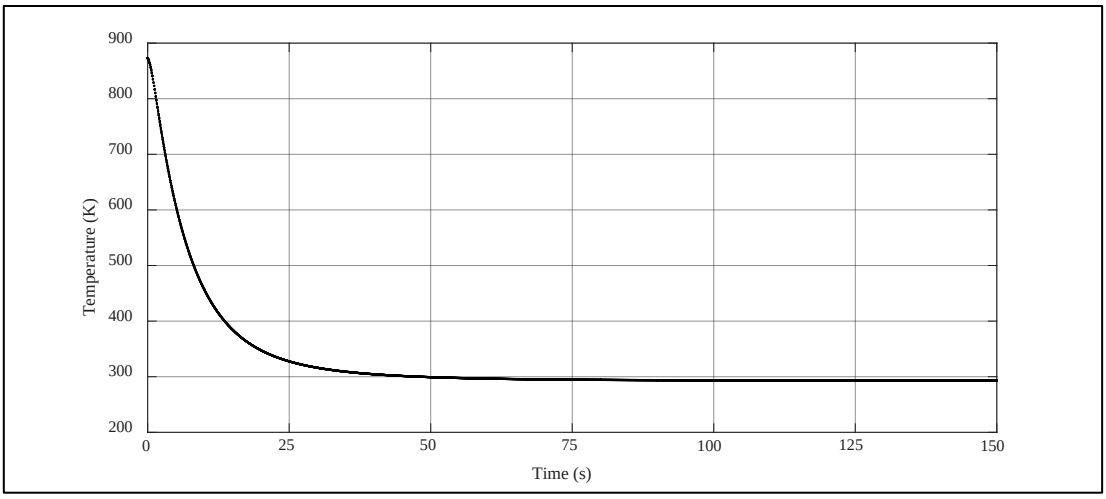

Figure 5.45 Temperature evolution of nodes 33801, 33805, 33810, 63910, 63906 and 63901 with k = 50.2 W/m·K, considering convection

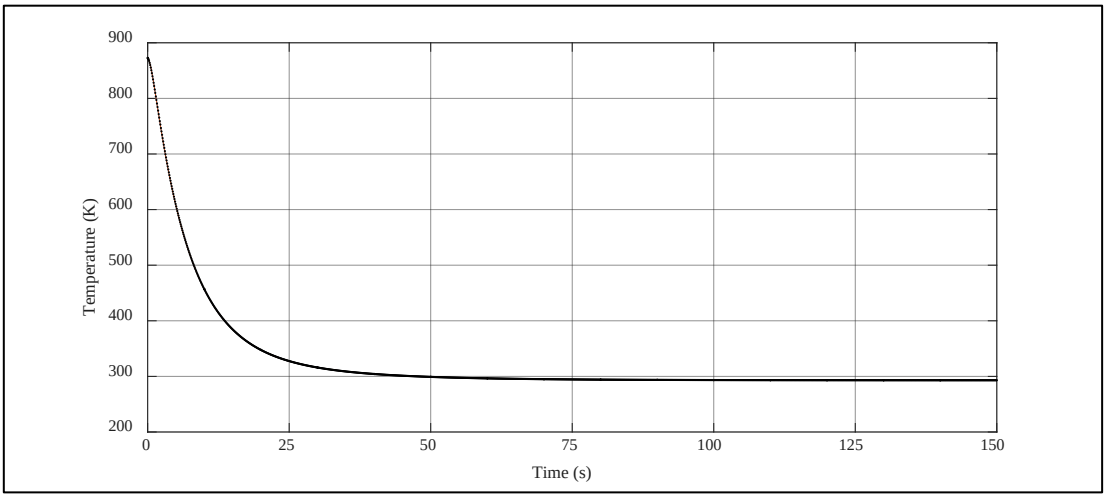

Figure 5.46 Temperature evolution of nodes 3801, 3810 and 3821 with k = 50.2 W/m·K, considering convection

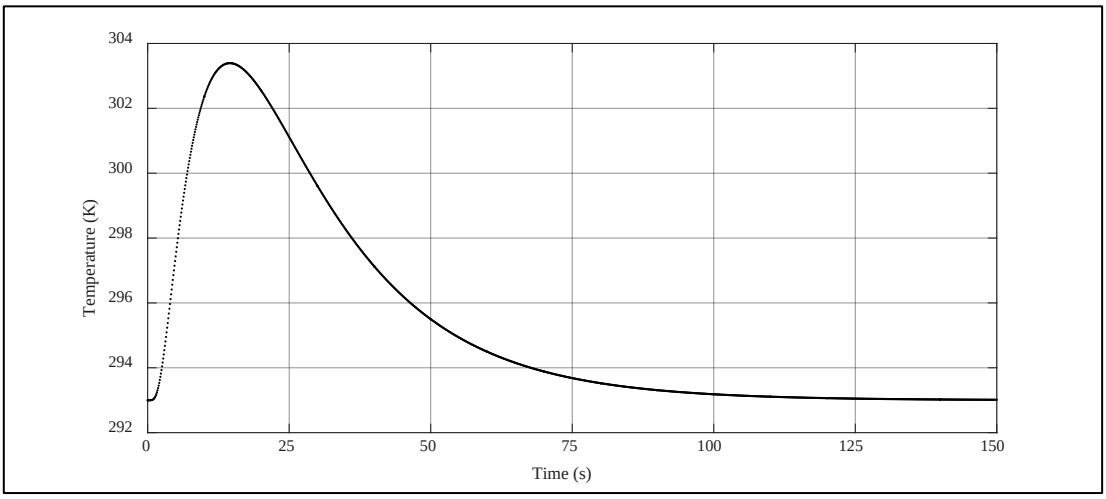

Figure 5.47 Temperature evolution of node 121259 with k = 50.2 W/m·K, considering convection

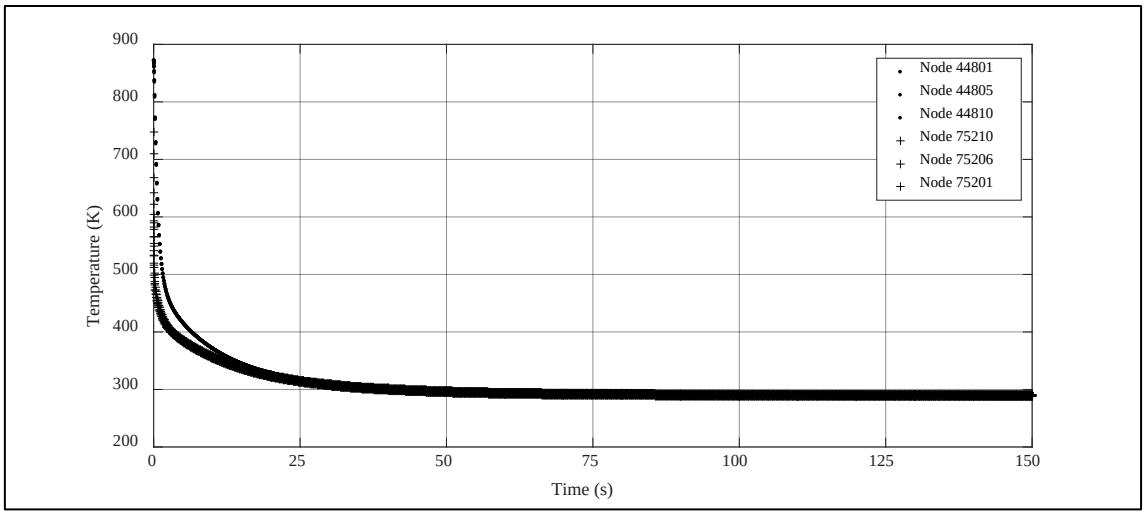

Figure 5.48 Temperature evolution of nodes 44801, 44805, 44810, 75210, 75206 and 75201 with k = 50.2 W/m·K, considering convection

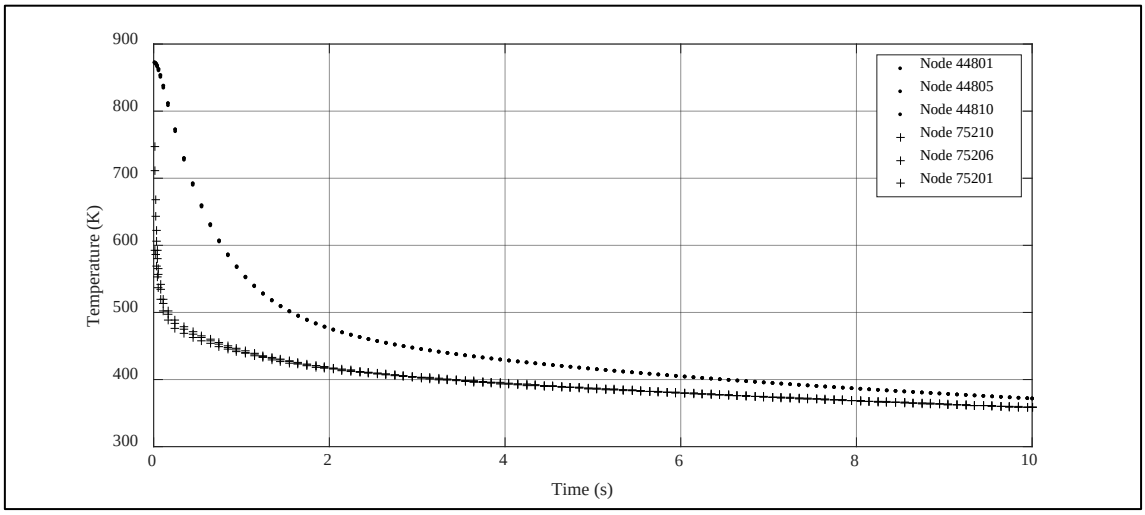

Figure 5.49 Zoom of figure 5.48

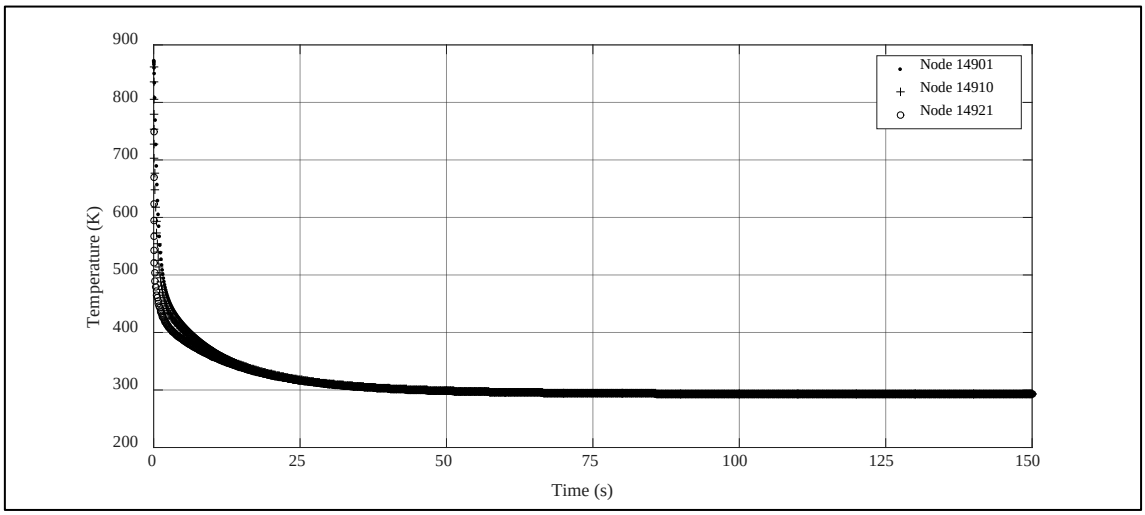

Figure 5.50 Temperature evolution of nodes 14901, 14910 and 14921 with k = 50.2 W/m·K, considering convection

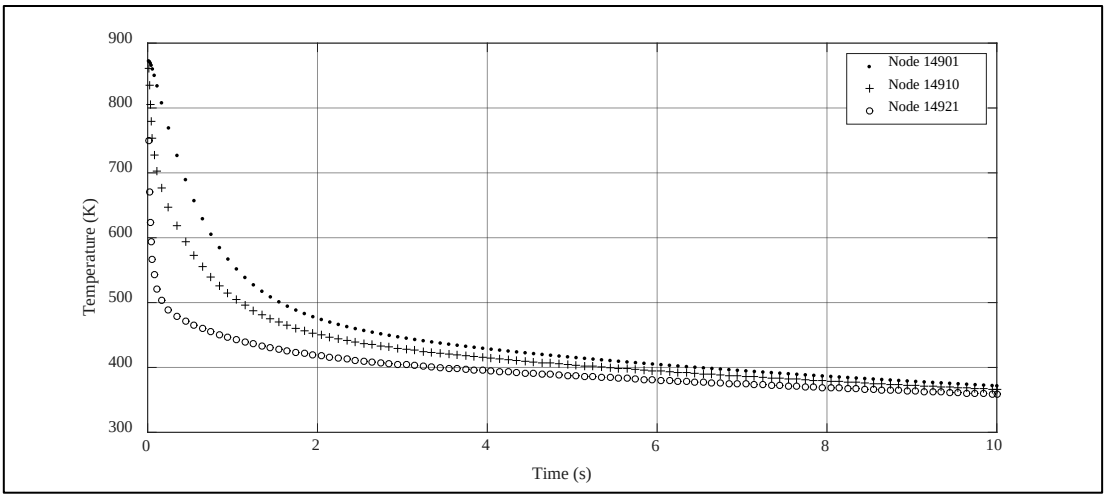

Figure 5.51 Zoom of figure 5.50

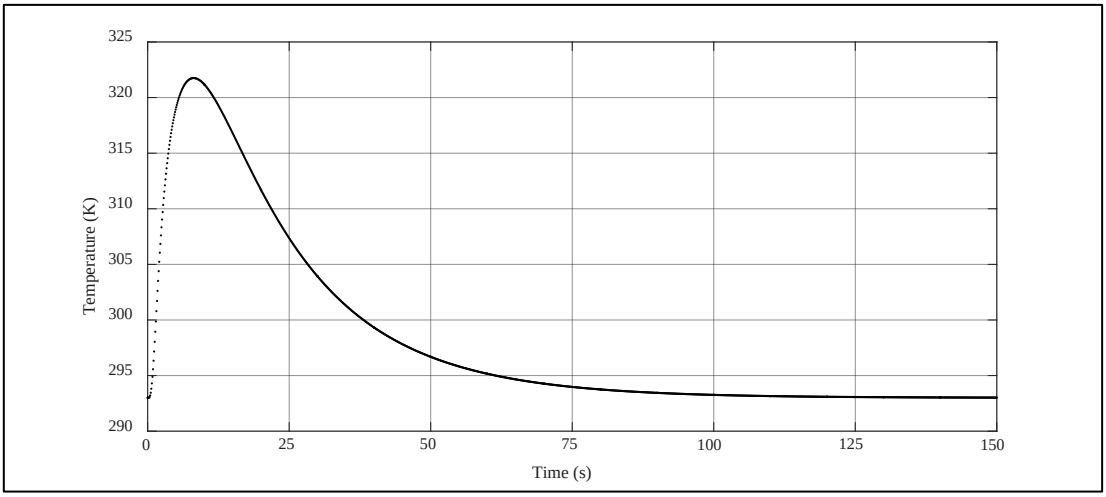

Figure 5.52 Temperature evolution of node 121354 with k = 50.2 W/m·K, considering convection

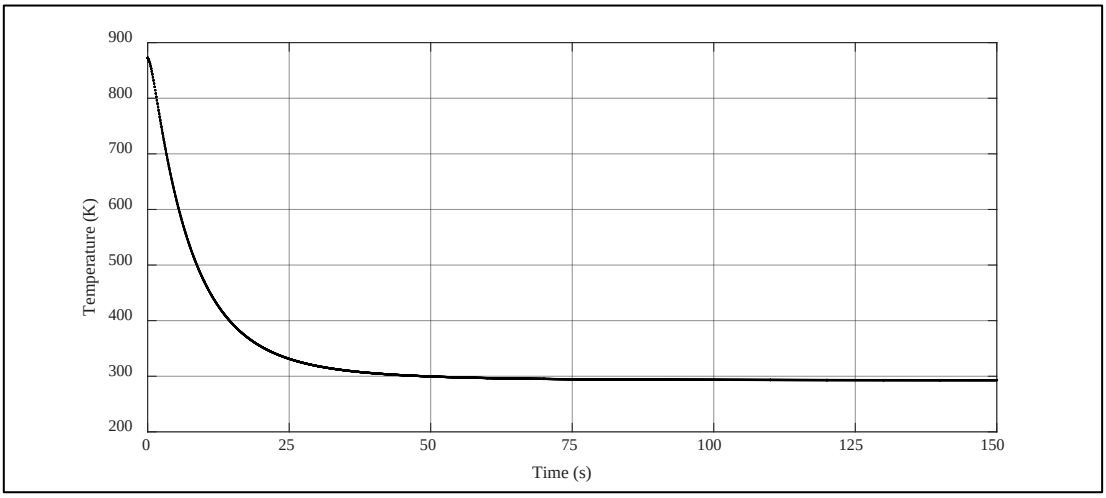

Figure 5.53 Temperature evolution of nodes 56101, 56105, 56110, 78910, 78906 and 78901 with k = 50.2 W/m·K, considering convection

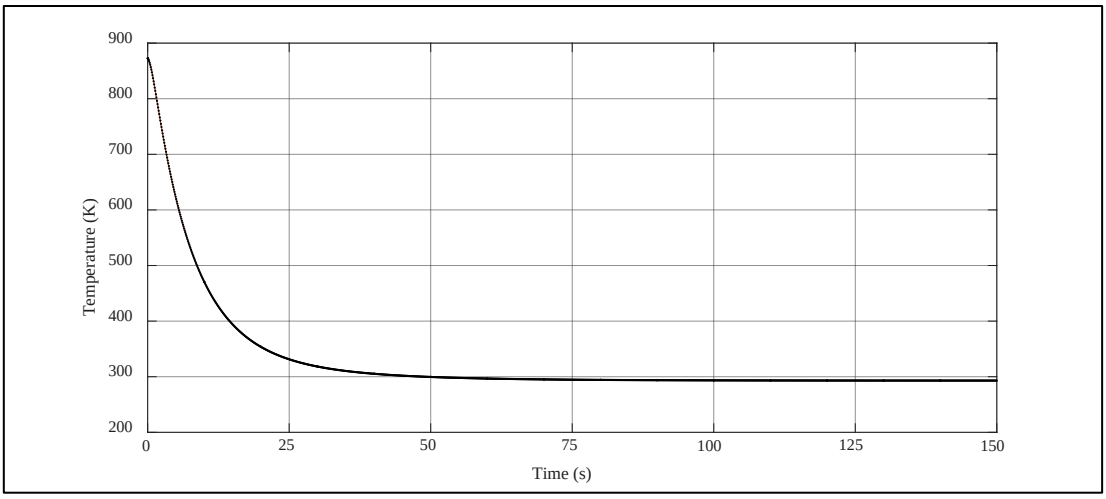

Figure 5.54 Temperature evolution of nodes 26301, 26310 and 26321 with k = 50.2 W/m·K, considering convection

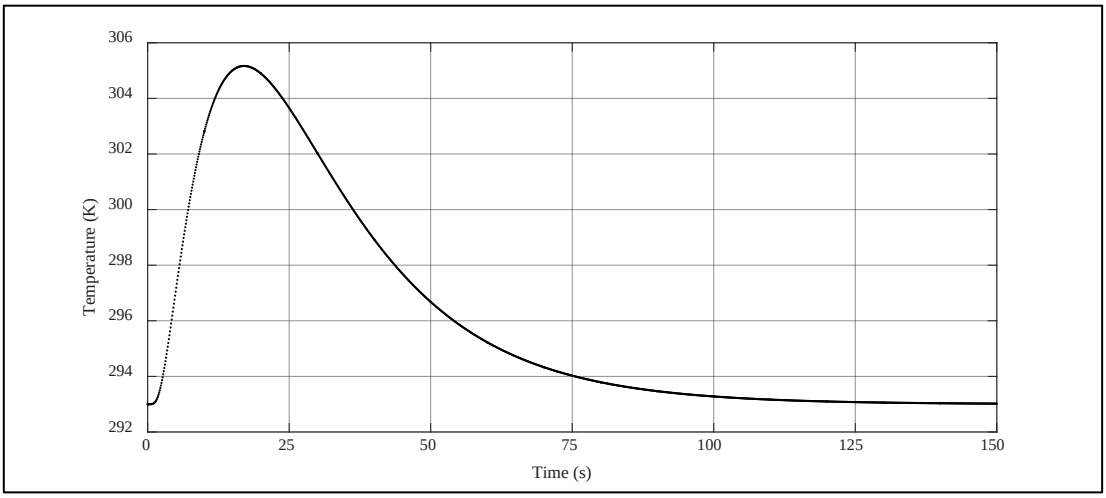

Figure 5.55 Temperature evolution of node 407585 with k = 50.2 W/m·K, considering convection

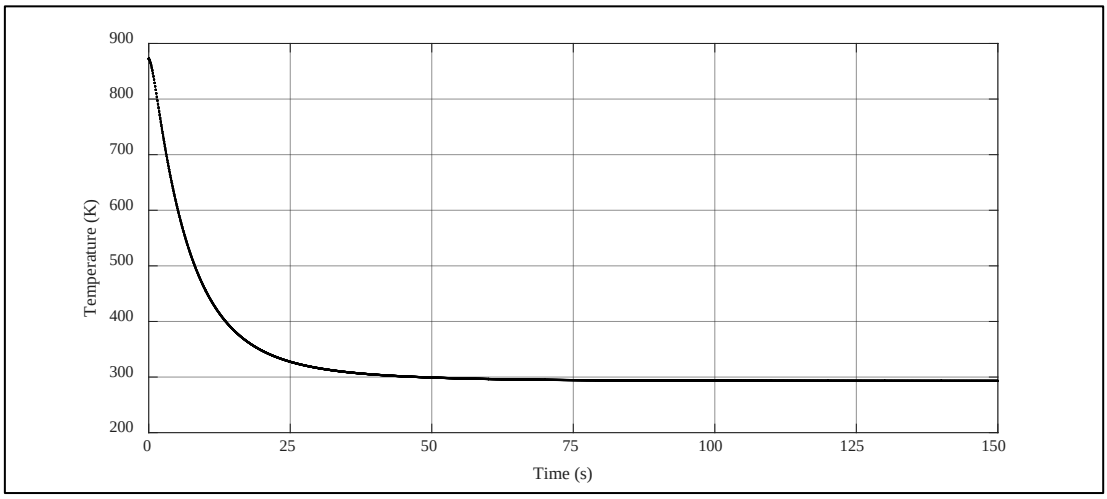

Figure 5.56 Temperature evolution of nodes 33801, 33805, 33810, 63910, 63906 and 63901 with k = 0.8 W/m·K, considering convection

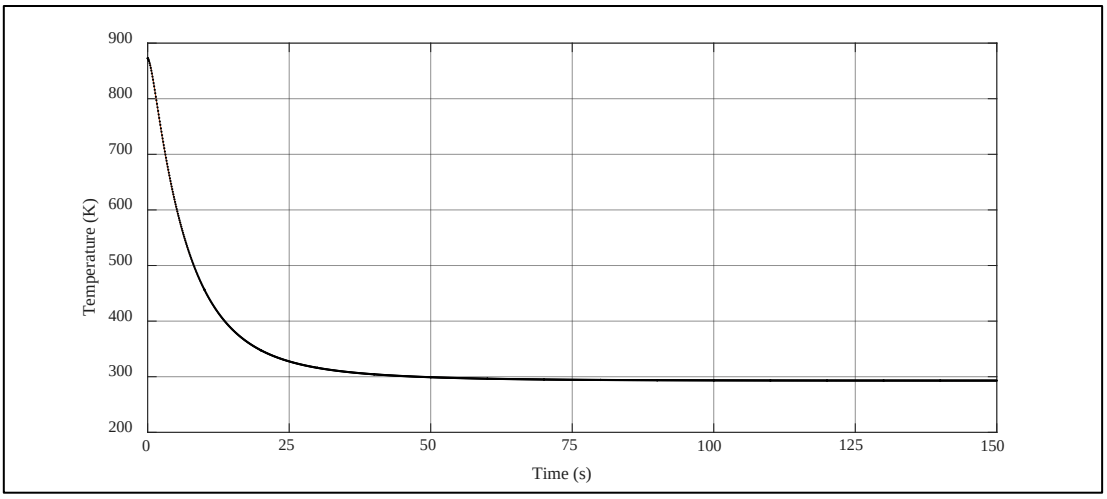

Figure 5.57 Temperature evolution of nodes 3801, 3810 and 3821 with k = 0.8 W/m·K, considering convection

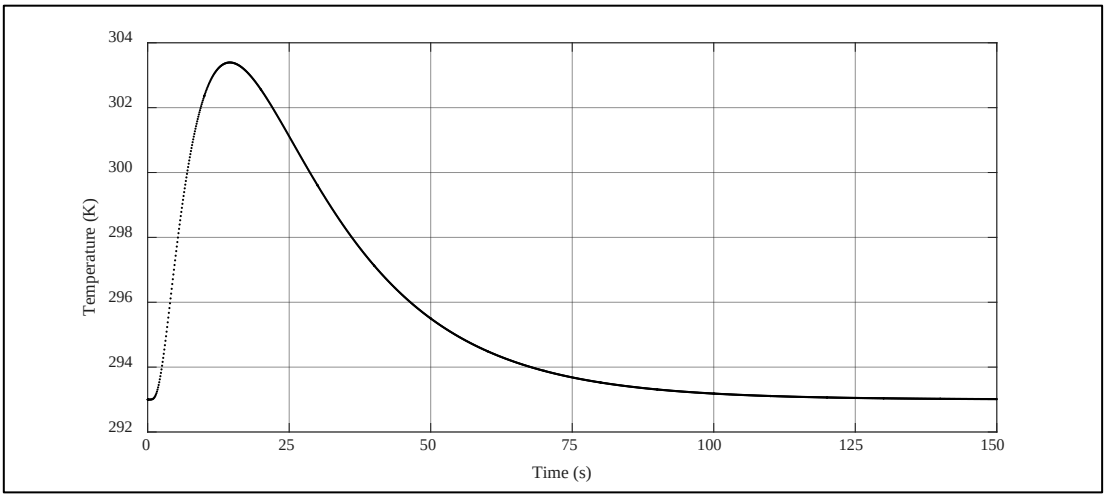

Figure 5.58 Temperature evolution of node 121259 with k = 0.8 W/m·K, considering convection

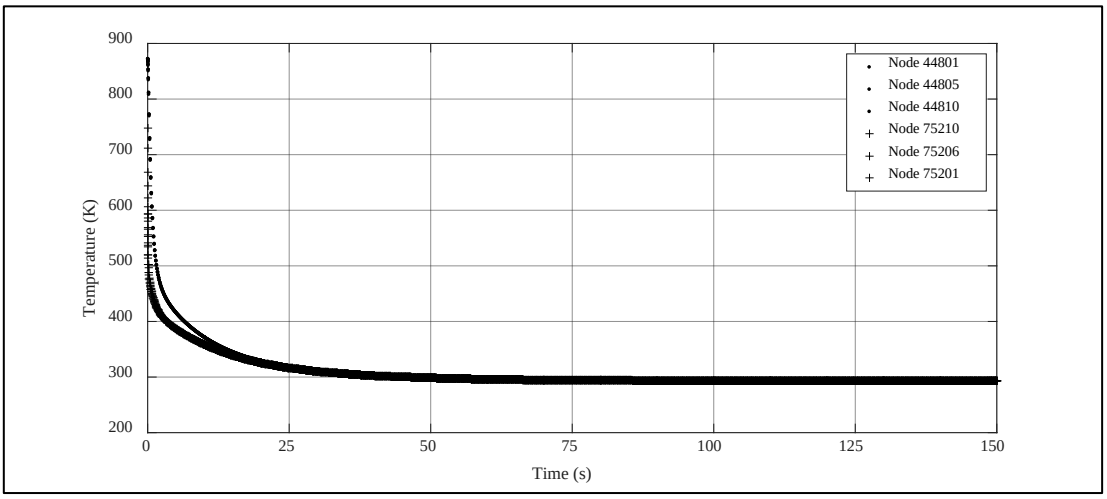

Figure 5.59 Temperature evolution of nodes 44801, 44805, 44810, 75210, 75206 and 75201 with k = 0.8 W/m·K, considering convection

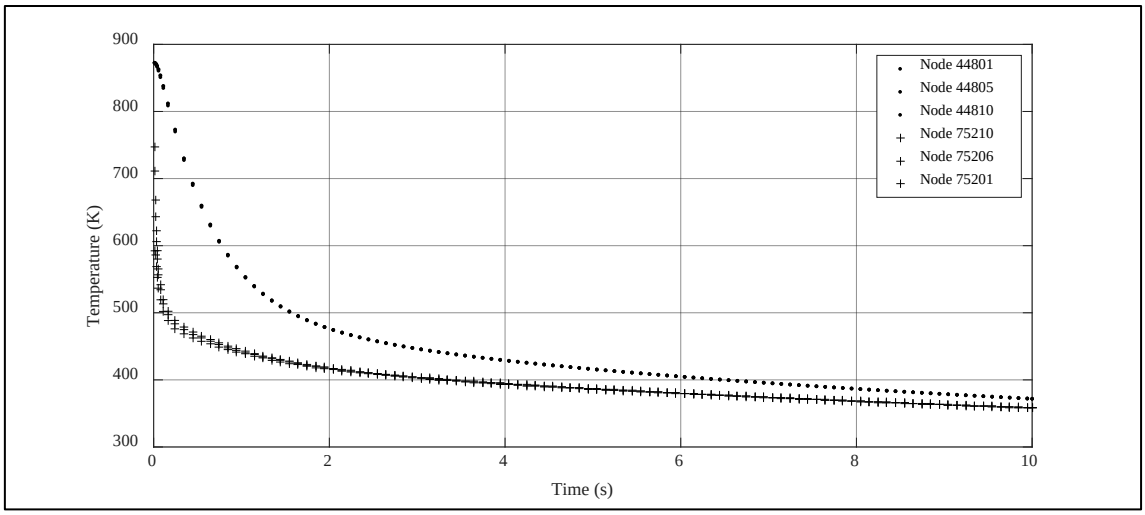

Figure 5.60 Zoom of figure 5.59

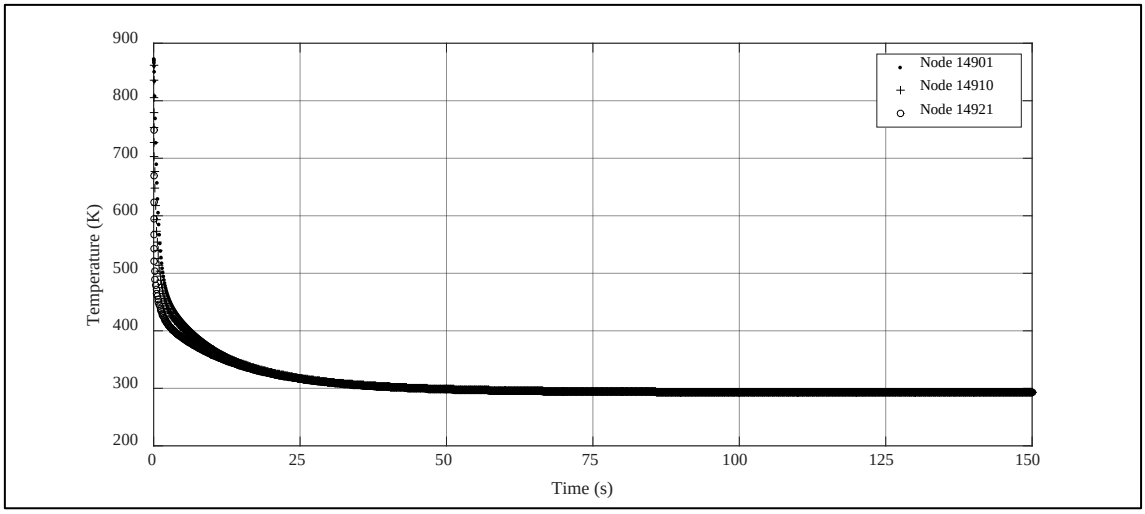

Figure 5.61 Temperature evolution of nodes 14901, 14910 and 14921 with k = 0.8 W/m·K, considering convection

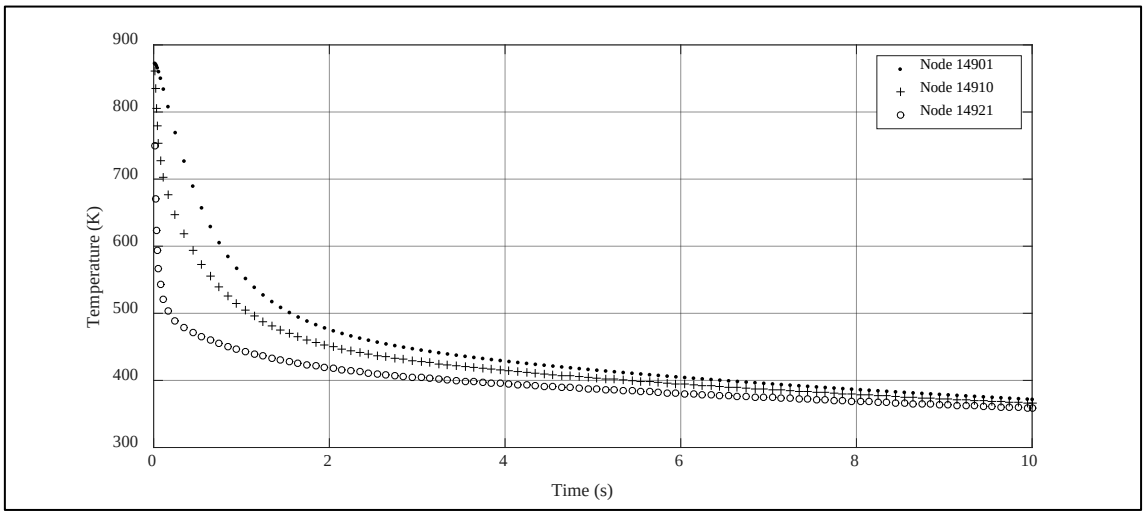

Figure 5.62 Zoom of figure 5.61

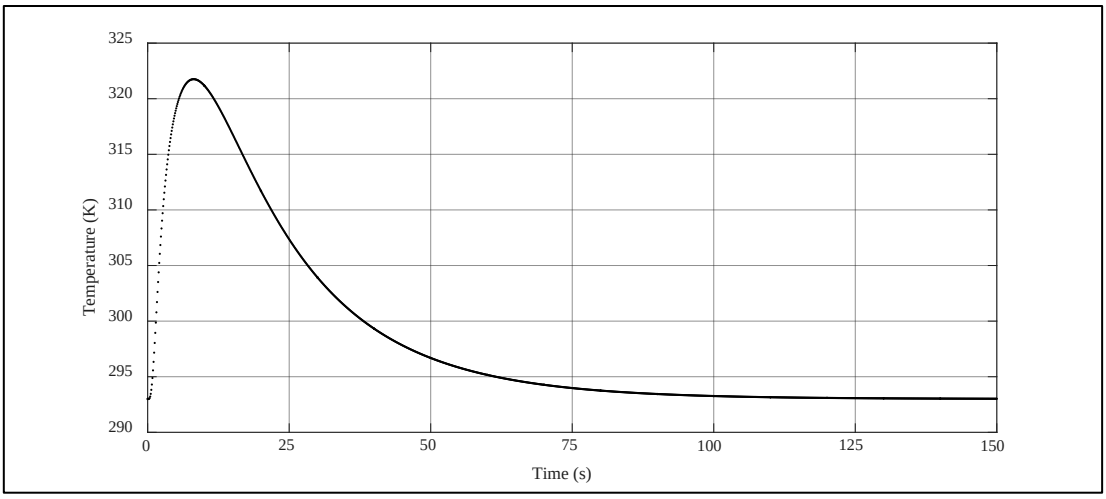

Figure 5.63 Temperature evolution of node 121354 with k = 0.8 W/m·K, considering convection

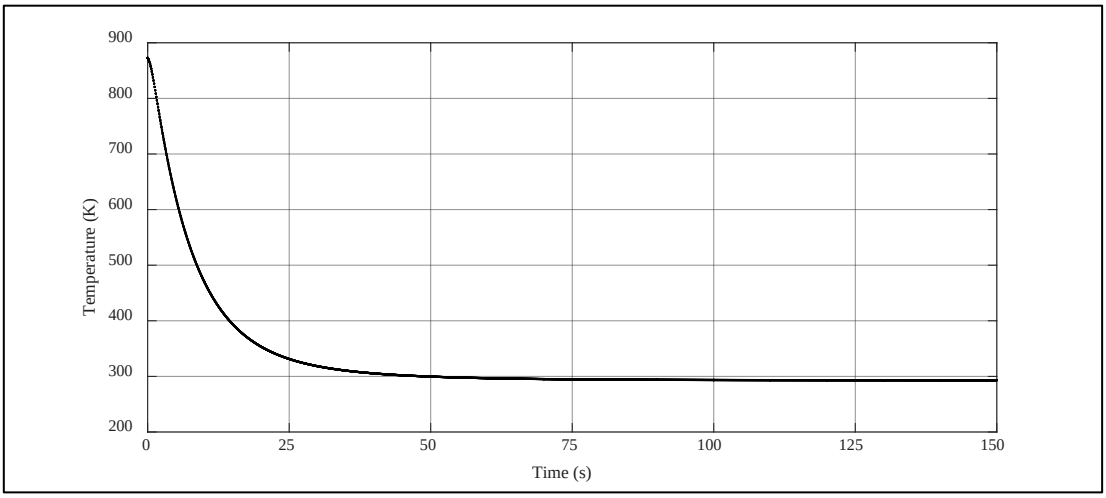

Figure 5.64 Temperature evolution of nodes 56101, 56105, 56110, 78910, 78906 and 78901 with k = 0.8 W/m·K, considering convection

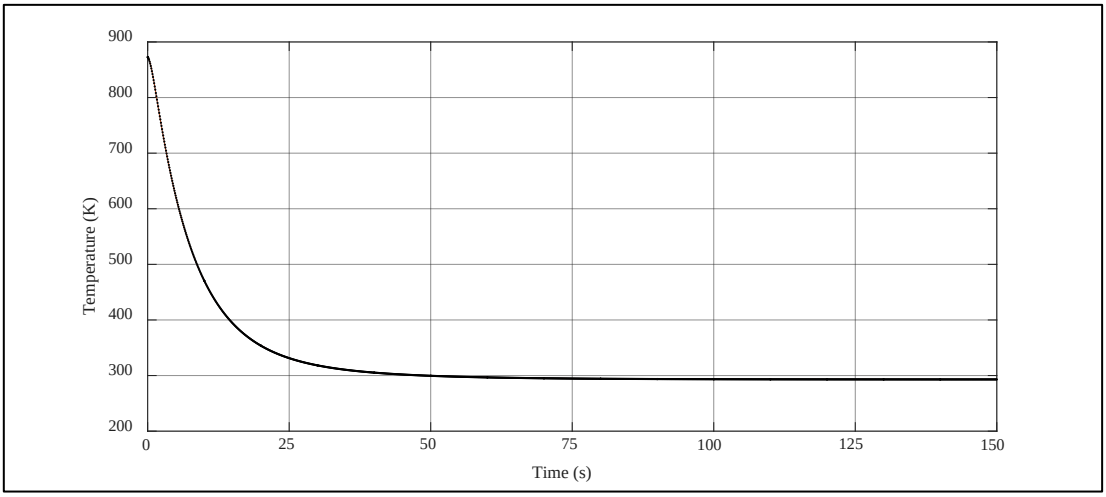

Figure 5.65 Temperature evolution of nodes 26301, 26310 and 26321 with k = 0.8 W/m·K, considering convection

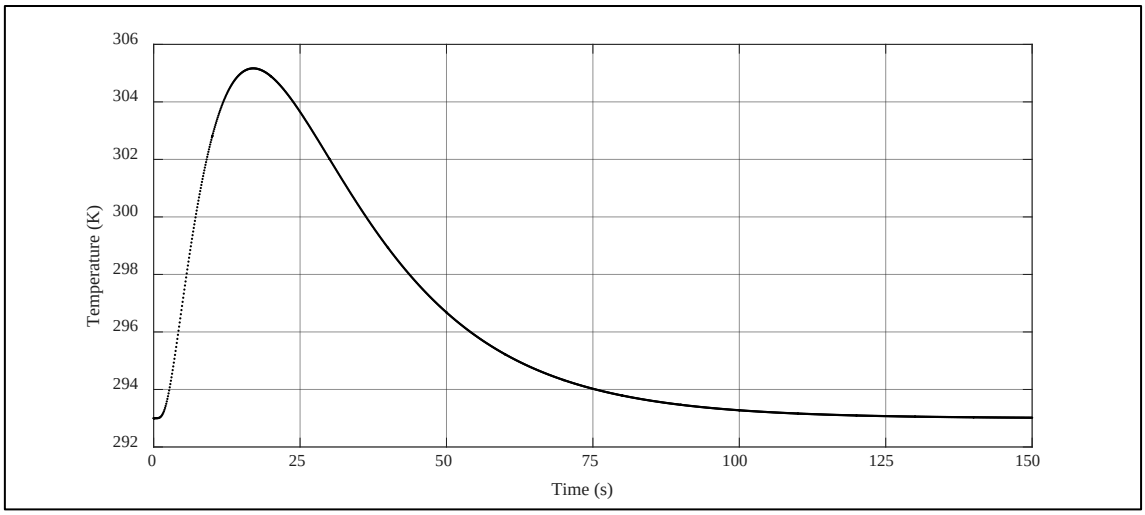

Figure 5.66 Temperature evolution of node 407585 with k = 0.8 W/m·K, considering convection

Fig. 5.67 shows the temperature difference between nodes 63906 and 33805 in the case of considering convection and interface of glass. At the beginning, the support is cold and the node 63906 transfers heat to the plate base. After approximately one second, the support heats up and the node 63906 is unable to transfer the heat in the same conditions. Approximately, at 2.5 s there is a temperature difference of 3.08 ºC.

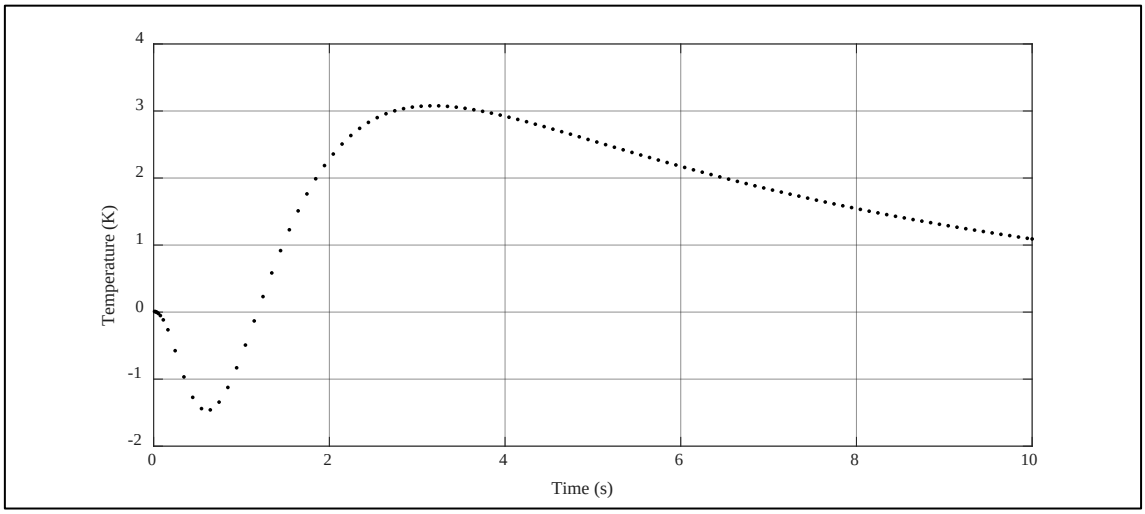

Figure 5.67 Temperature difference between nodes 63906 and 33805, considering convection and interface of glass

Fig. 5.68 shows the temperature difference between nodes 75206 and 44805 in the case of considering convection and interface of glass. At the beginning, the aluminium close to the support is colder than the upper aluminium layer. It is remarkable the difference of 323.8 K at 0.135 s.

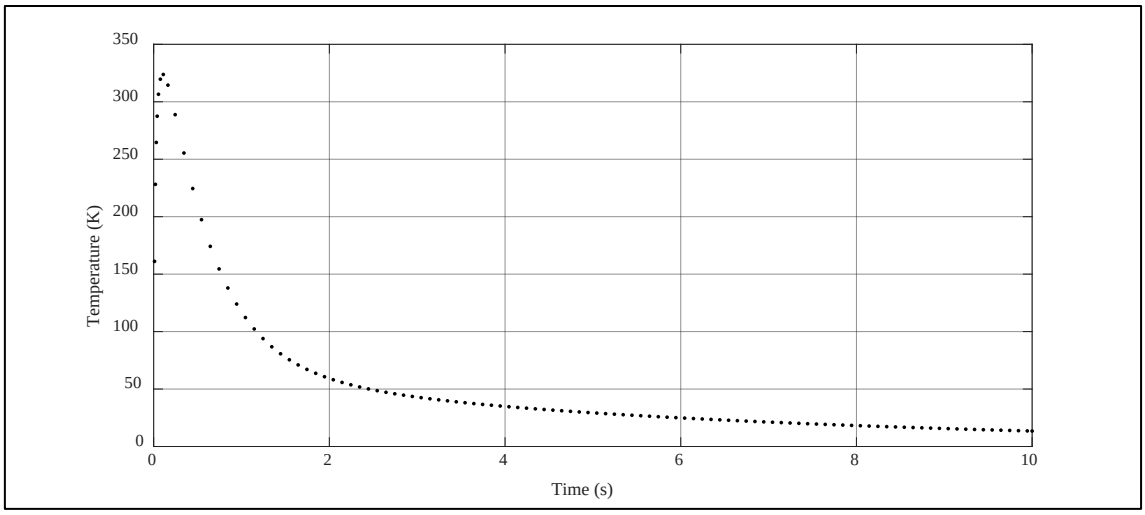

Figure 5.68 Temperature difference between nodes 75206 and 44805, considering convection and interface of glass

5.5 Thermal analysis of one thixoforged aluminium plate considering thermal radiation and without considering convection

The results of the thermal simulation with an interface conductivity equal to the glass one and with considering radiation are shown in Figures 5.69 to 5.72 at 20 s.

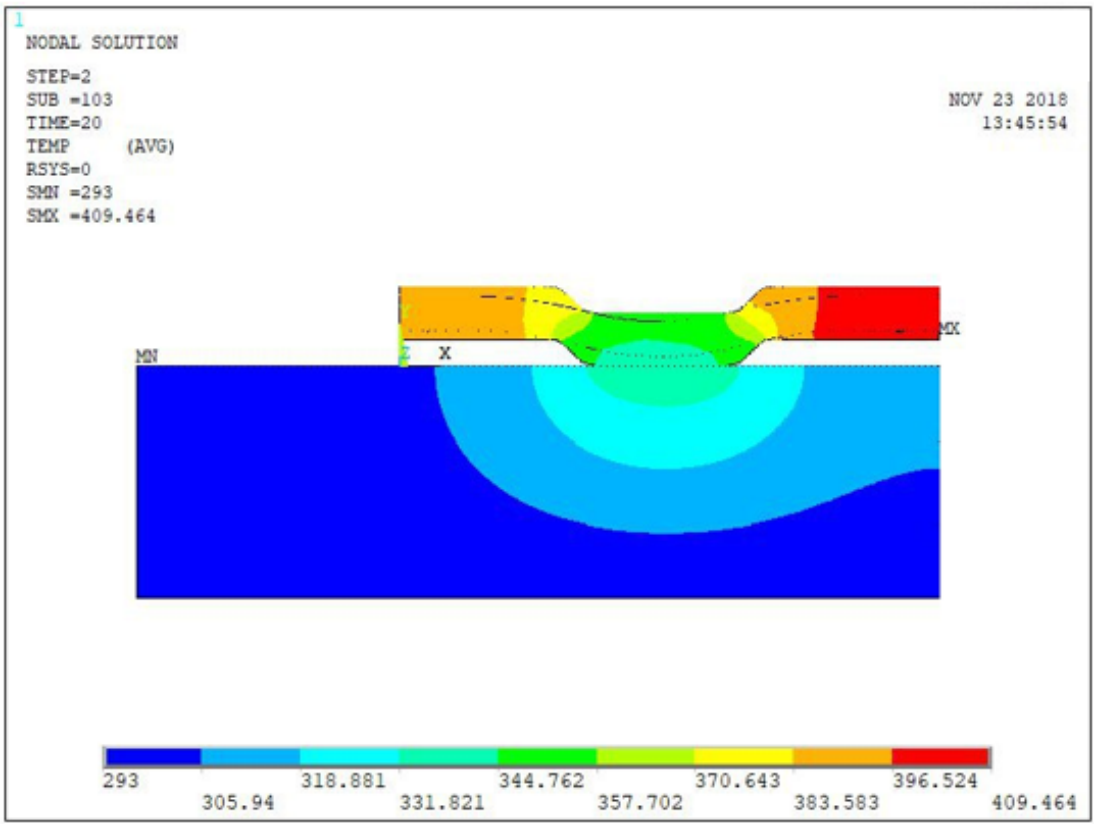

Figure 5.69 Temperature distribution at 20 s with an interface conductivity equal to the glass one, with k = 0.8 W/m·K, including thermal radiation

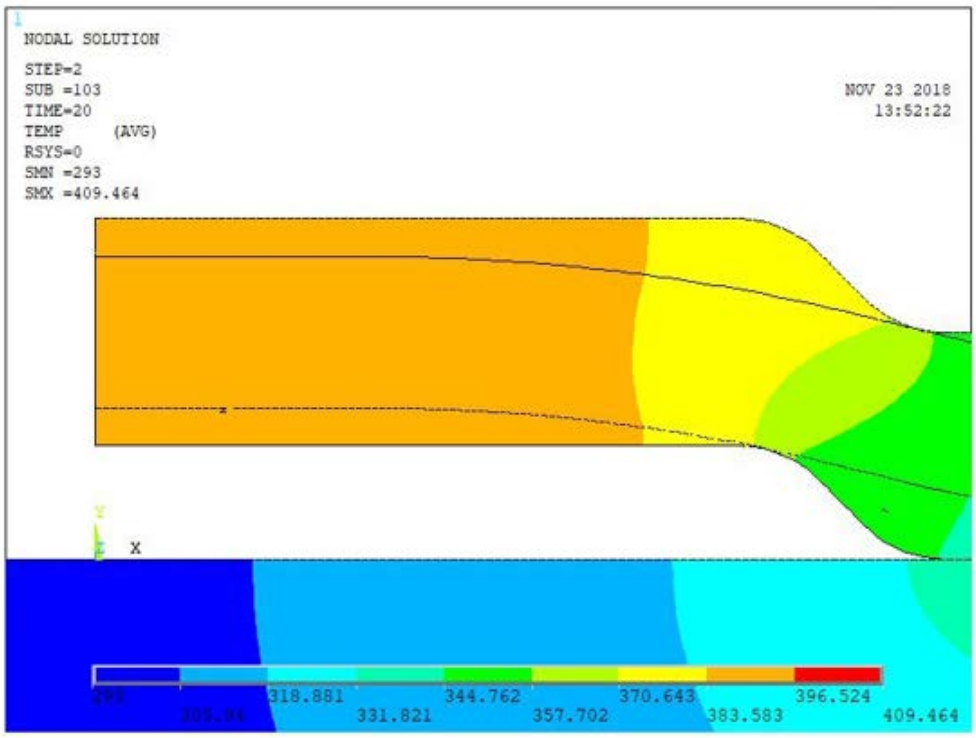

Figure 5.70 Temperature distribution at 20 s with an interface conductivity equal to the glass one, with k = 0.8 W/m·K, including thermal radiation, left part of the plate

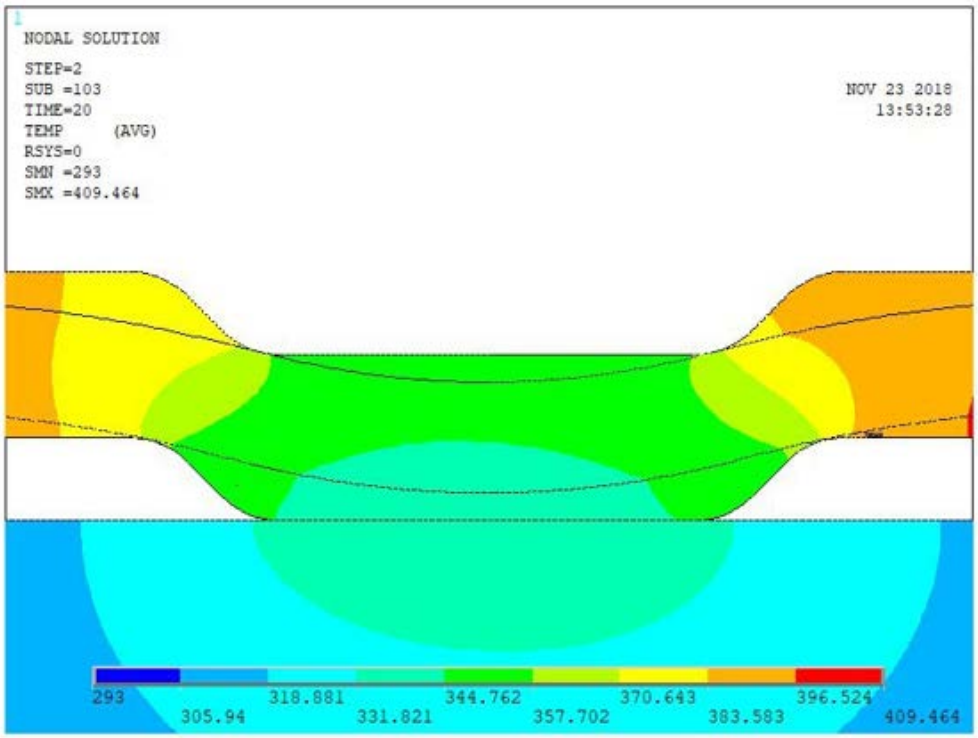

Figure 5.71 Temperature distribution at 20 s with an interface conductivity equal to the glass one, with k = 0.8 W/m·K, including thermal radiation, centre of the plate

The results of the thermal simulation, evolution of the temperature, with interface conductivity equal to the glass one and with considering thermal radiation in the selected nodes, as shown in chapter 4, are shown in Figures 5.73 to 5.83.

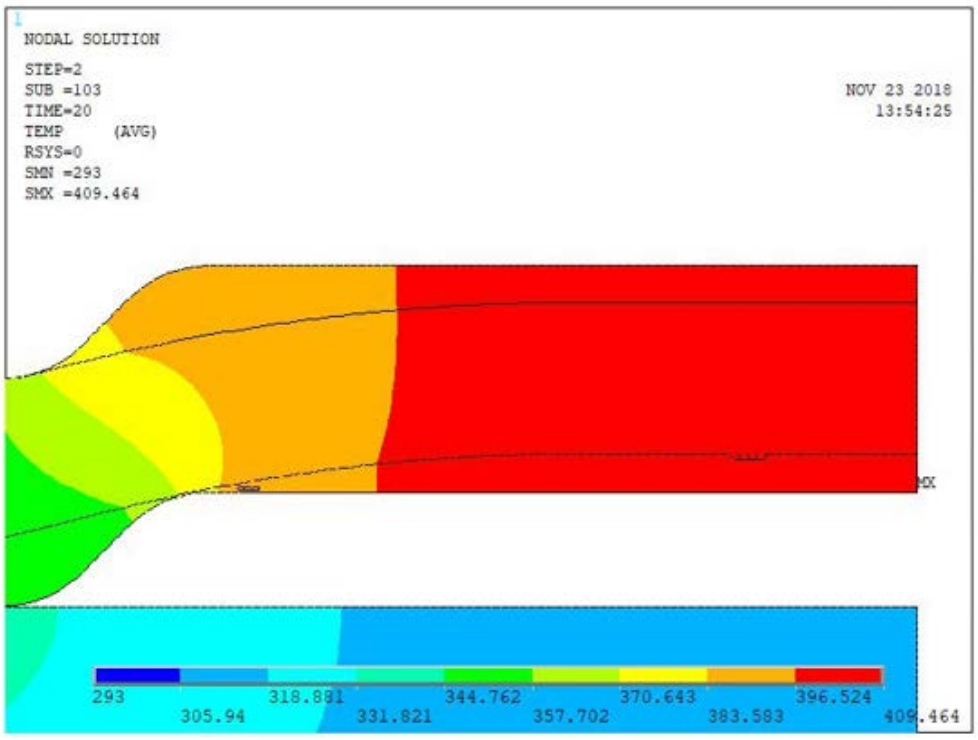

Figure 5.72 Temperature distribution at 20 s with an interface conductivity equal to the glass one, with k = 0.8 W/m·K, including thermal radiation, right part of the plate

Fig. 5.84 shows the temperature difference between nodes 63906 and 33805. As shown when we comment the Fig. 5.35, the node 63906 is chilling faster than the node 33805. When the support heats up, this node is chilling slower than the node 33805.

Fig. 5.85 shows the temperature difference between nodes 75206 and 44805. As shown when we comment the Fig. 5.36, at the beginning, the aluminium close to the support is colder than the upper aluminium layer. It is remarkable the difference of 286.8 K at 0.135 s, similar result as the calculation without thermal radiation.

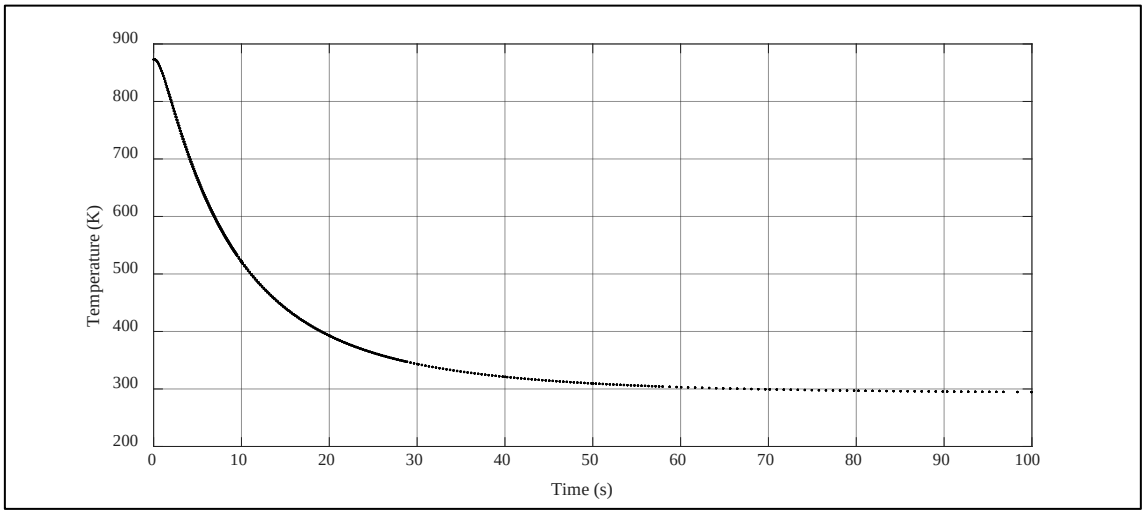

Figure 5.73 Temperature evolution of nodes 33801, 33805, 33810, 63910, 63906 and 63901 with k = 0.8 W/m·K, including thermal radiation

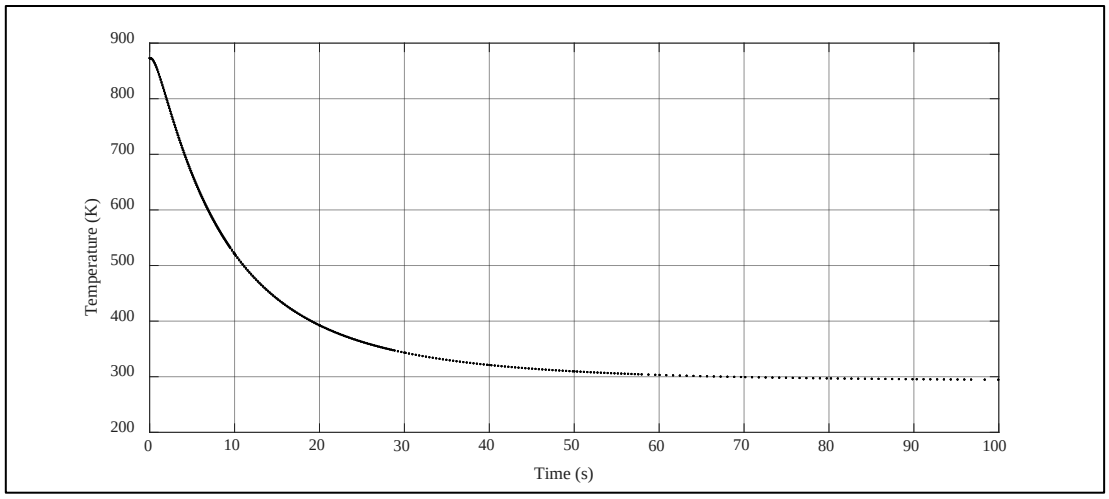

Figure 5.74 Temperature evolution of nodes 3801, 3810 and 3821 with k = 0.8 W/m·K, including thermal radiation

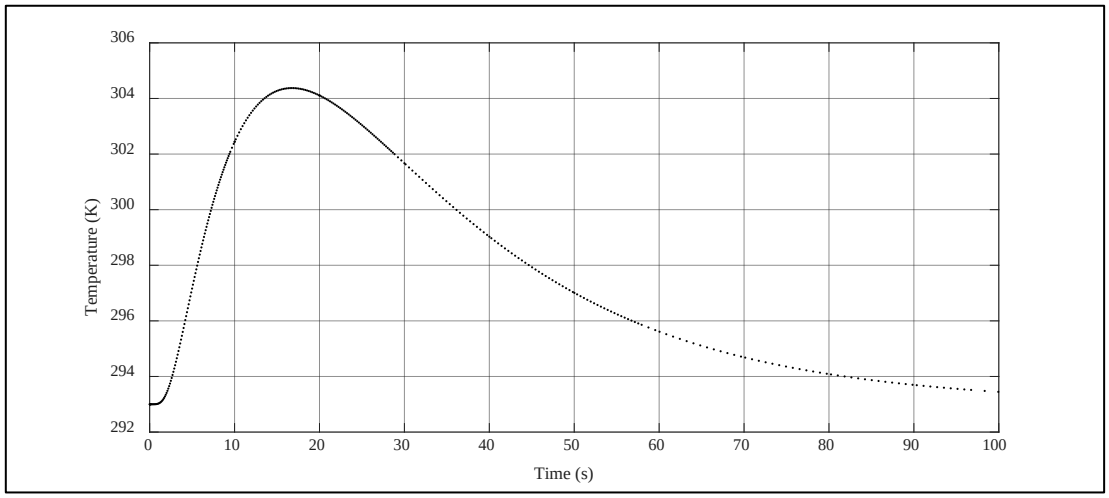

Figure 5.75 Temperature evolution of node 121259 with k = 0.8 W/m·K, including thermal radiation

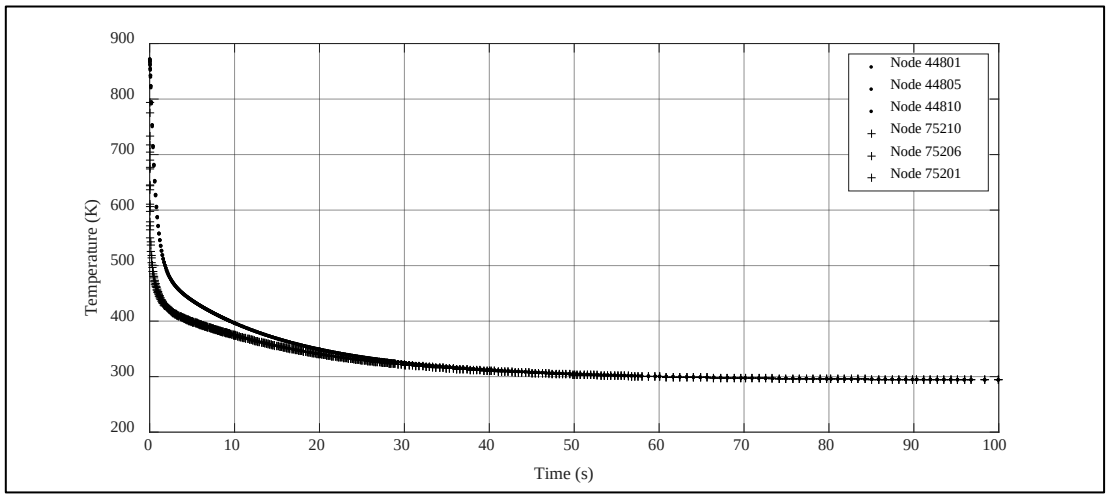

Figure 5.76 Temperature evolution of nodes 44801, 44805, 44810, 75210, 75206 and 75201 with k = 0.8 W/m·K, including thermal radiation

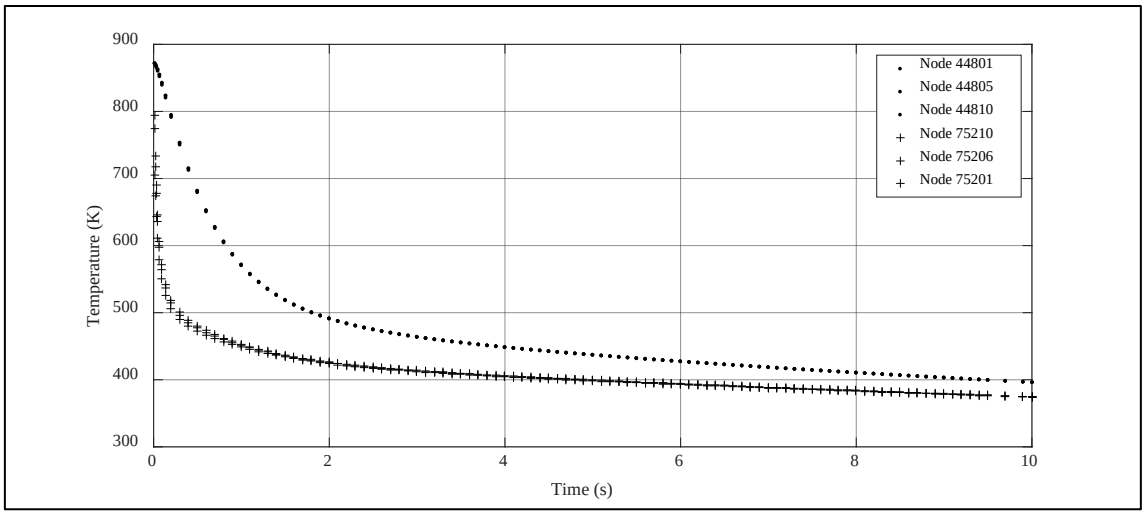

Figure 5.77 Zoom of figure 5.76

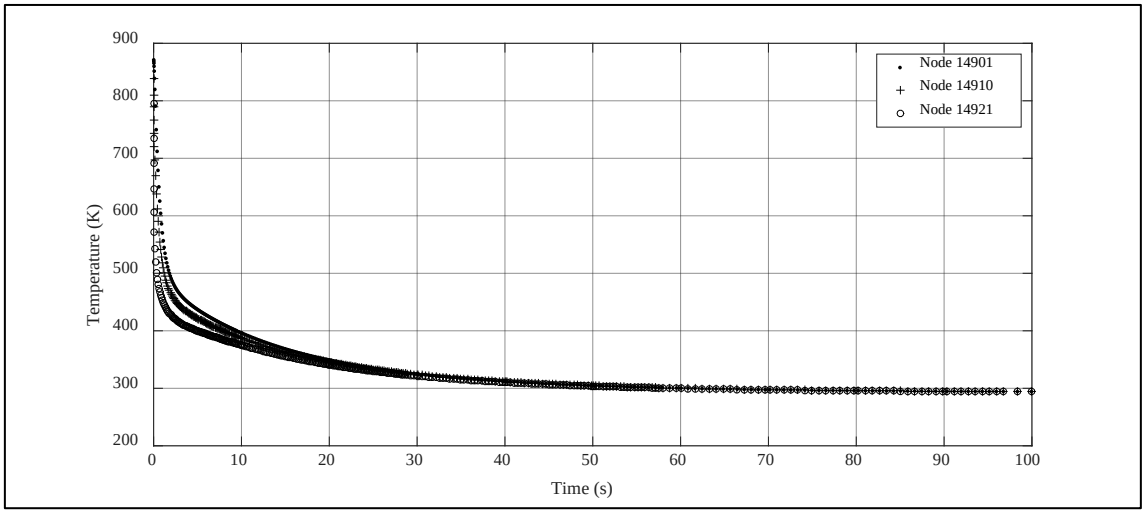

Figure 5.78 Temperature evolution of nodes 14901, 14910 and 14921 with k = 0.8 W/m·K, including thermal radiation

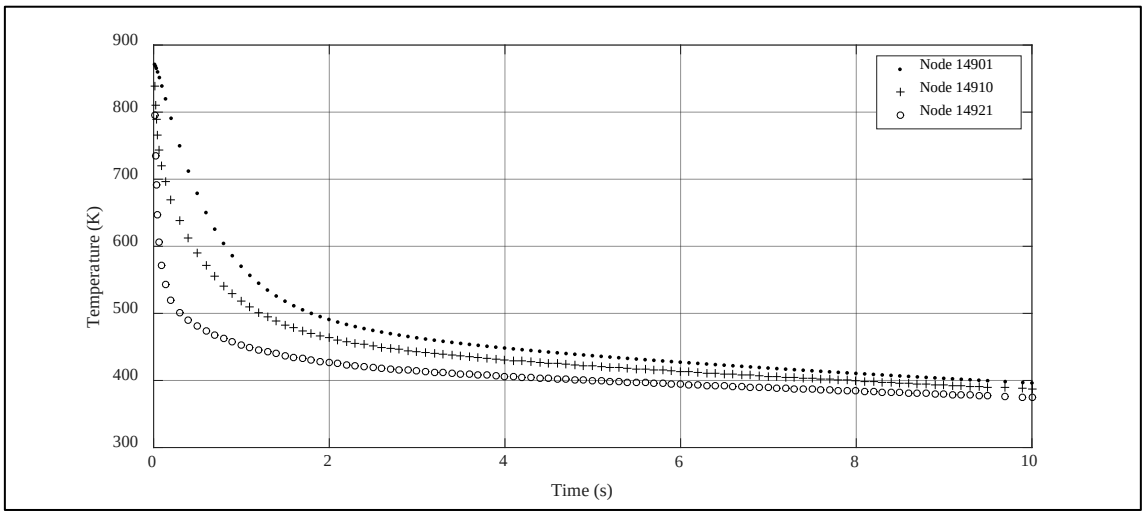

Figure 5.79 Zoom of figure 5.78

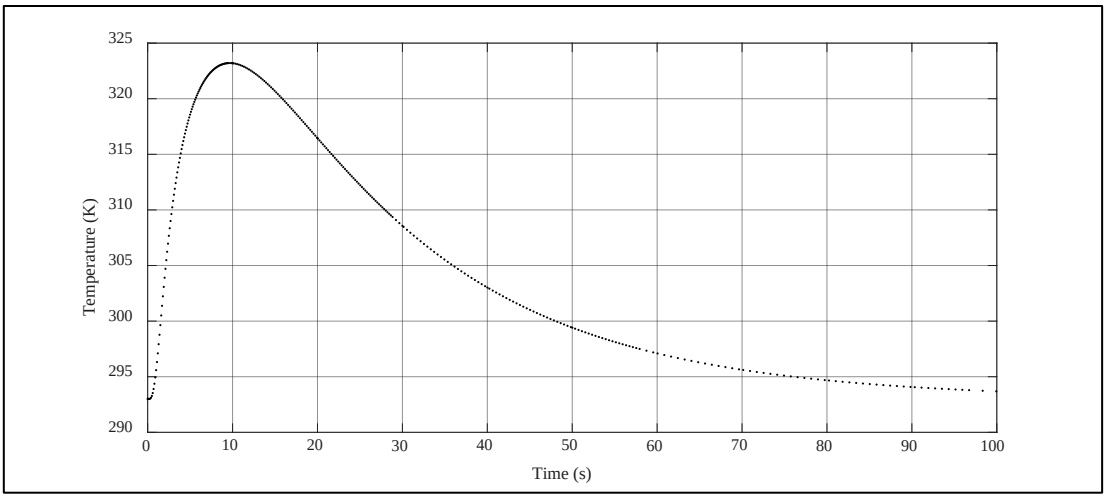

Figure 5.80 Temperature evolution of node 121354 with k = 0.8 W/m·K, including thermal radiation

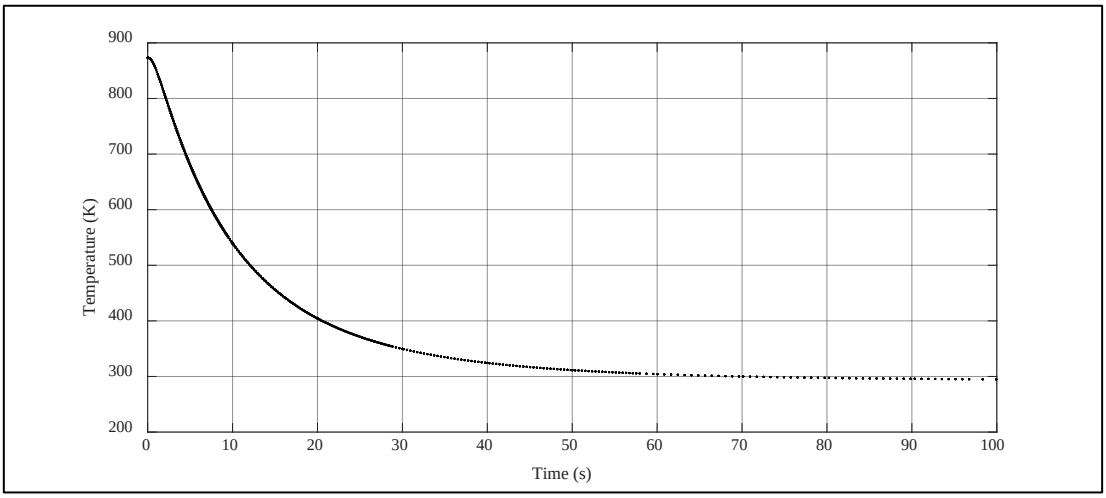

Figure 5.81 Temperature evolution of nodes 56101, 56105, 56110, 78910, 78906 and 78901 with k = 0.8 W/m·K, including thermal radiation

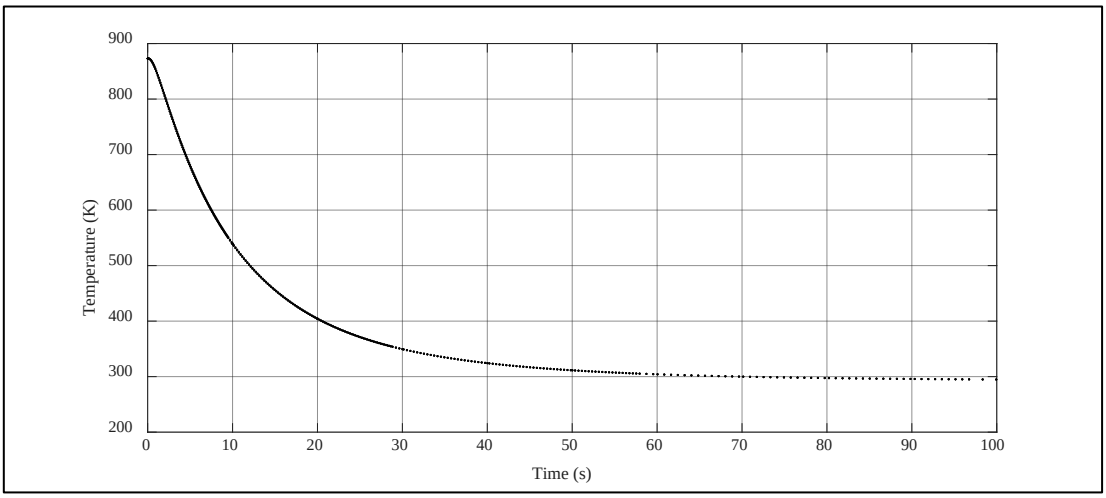

Figure 5.82 Temperature evolution of nodes 26301, 26310 and 26321 with k = 0.8 W/m·K, including thermal radiation

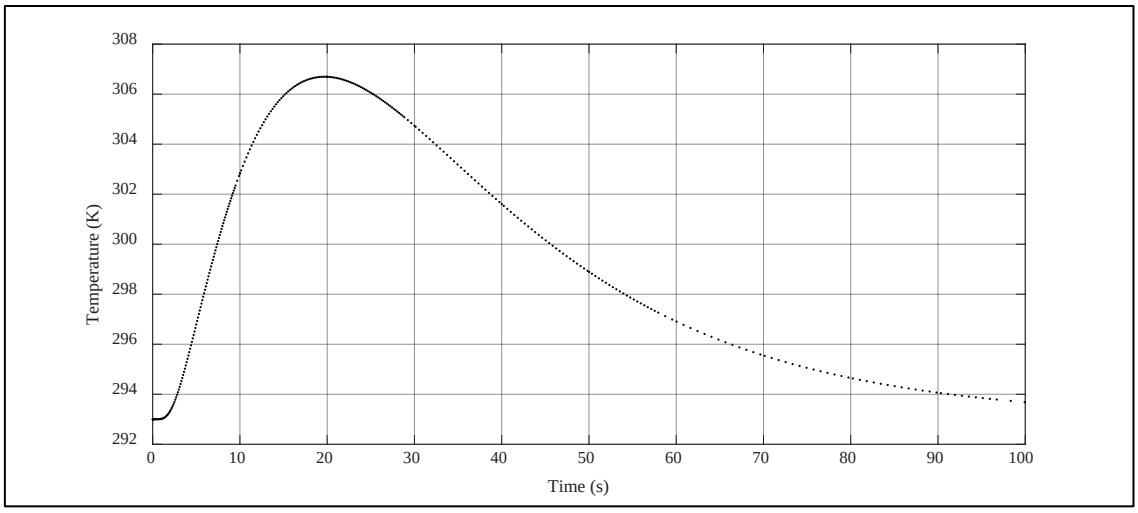

Figure 5.83 Temperature evolution of node 407585 with k = 0.8 W/m·K, including thermal radiation

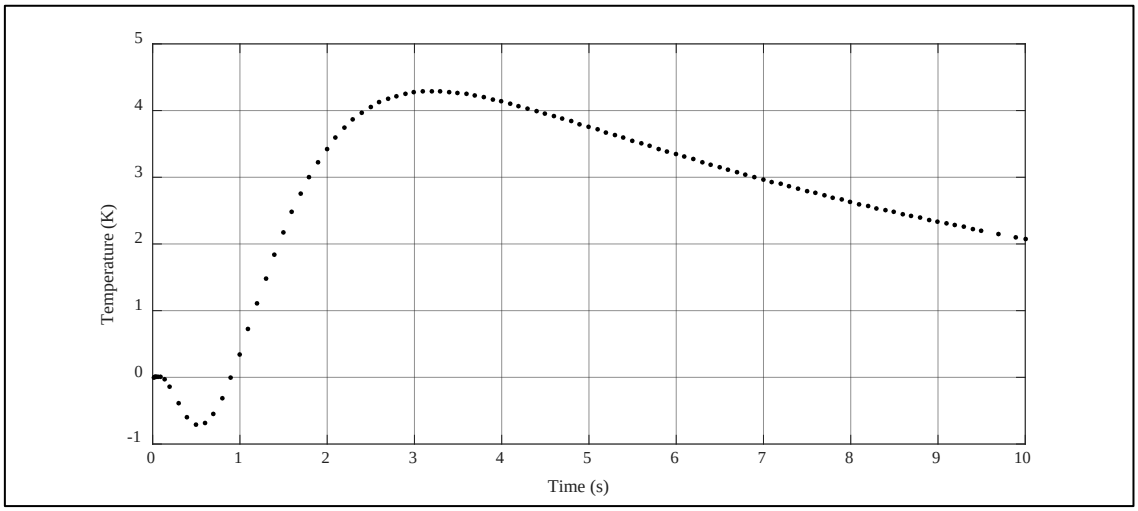

Figure 5.84 Temperature difference between nodes 63906 and 33805, including thermal radiation

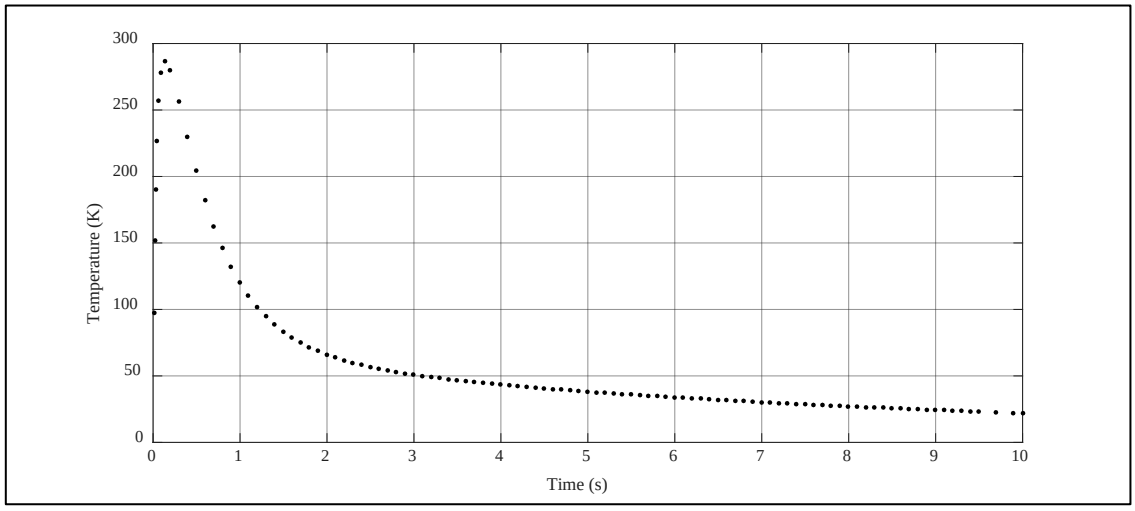

Figure 5.85 Temperature difference between nodes 75206 and 44805, including thermal radiation

Fig. 5.86 shows the chilling process including thermal radiation (top) and without including thermal radiation and a film coefficient of 10 $W/m^2 \cdot K$ (bottom). The two graphs correspond to the evolution temperature of the node 33805. Without considering radiation the temperatures of this node are higher than with radiation.

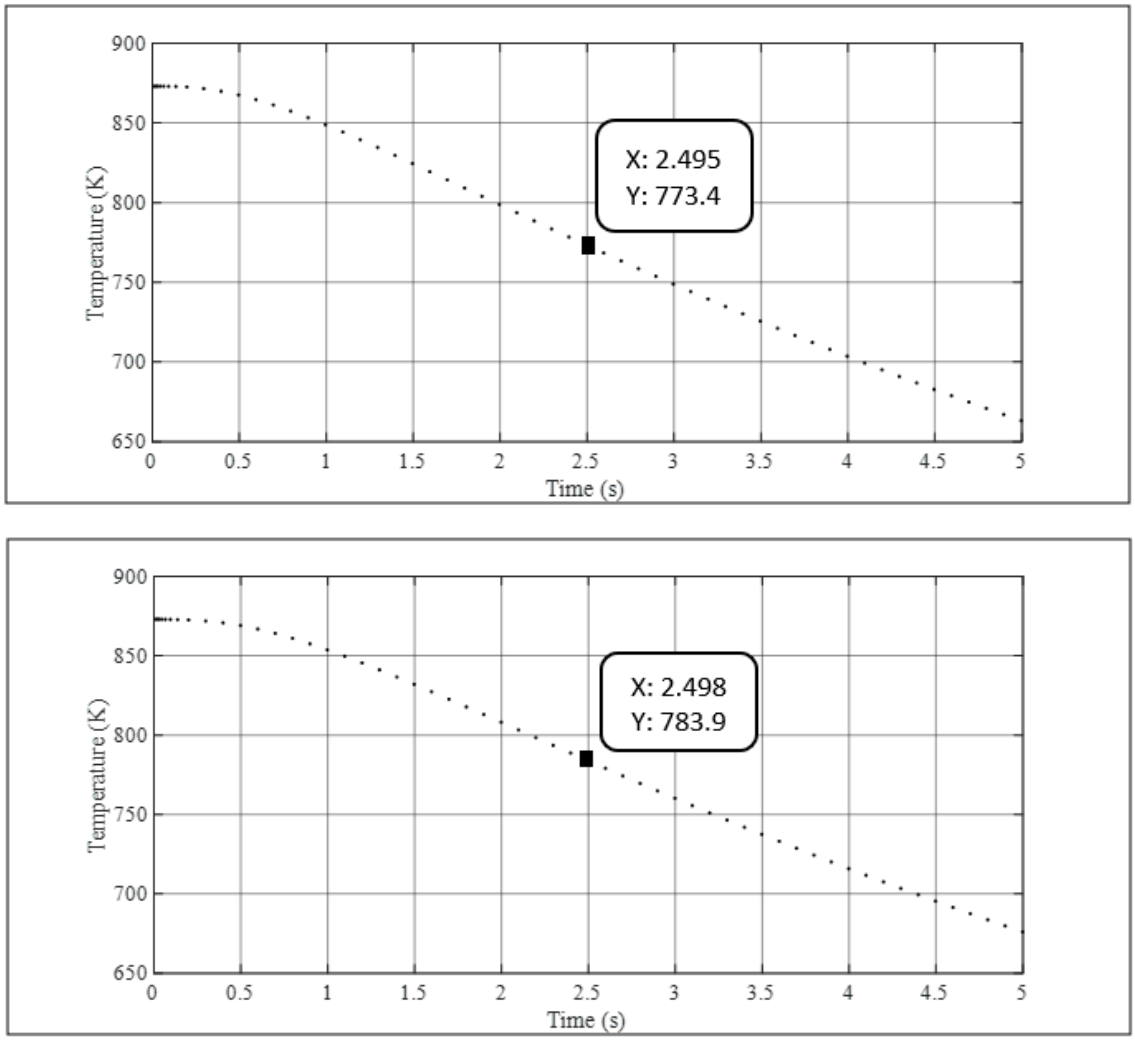

Figure 5.86 Comparison between the chilling process of the calculation including thermal radiation (top) and without including thermal radiation (bottom)

5.6 Thermal stress analysis of one thixoforged aluminium plate

Figures 5.87 to 5.94 show the stress field associated with the chilling process including radiation at 150 s in the X direction. Figures 5.95 to 5.98 show the stress field associated with the chilling process including radiation at 150 s in the Y direction. Figures 5.99 to 5.102 show the Von Mises stress associated with the chilling process including radiation at 150 s.

The results of the thermal stress simulation with interface conductivity equal to the glass one and considering radiation in the selected node, 34201, as shown in chapter 4, are shown in Figures 5.103 to 5.105.

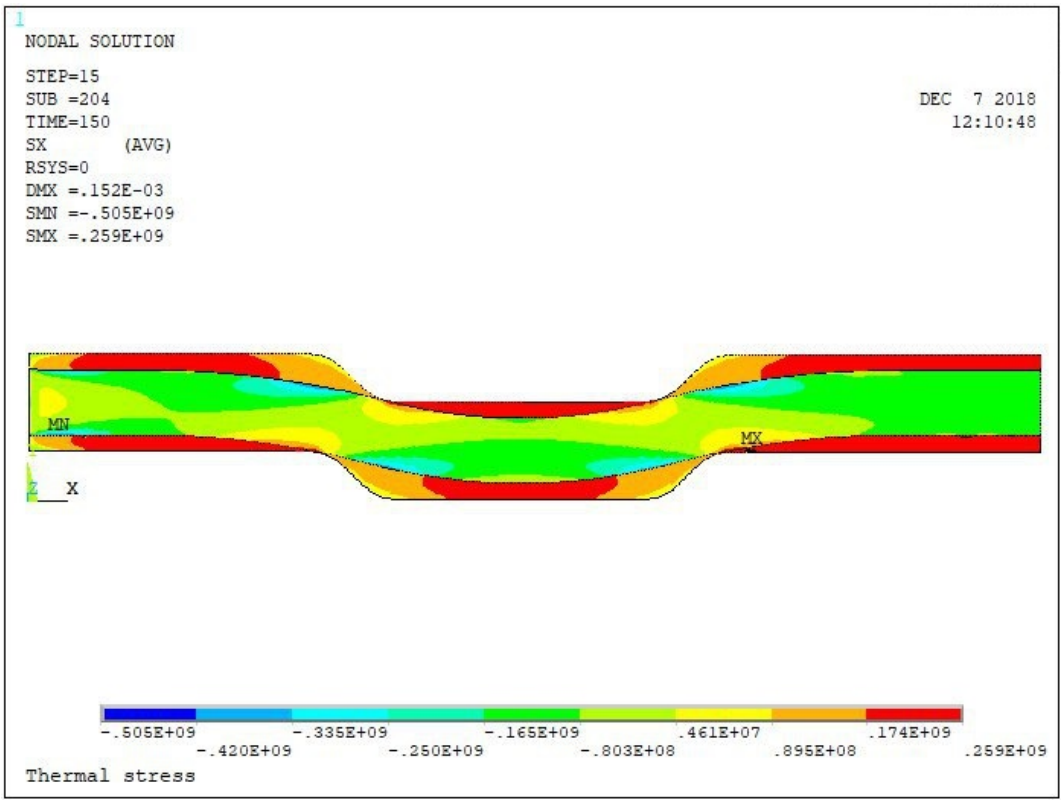

Figure 5.87 Thermal stress distribution, Sx, at 150 s considering radiation

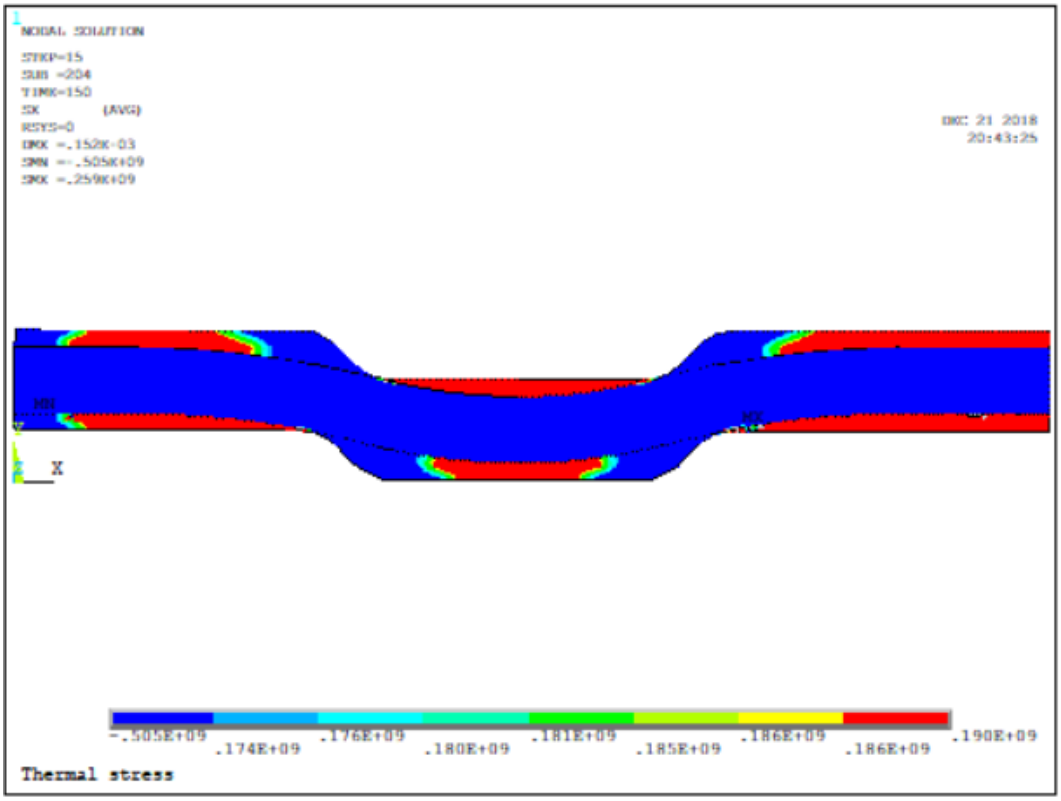

Figure 5.88 Change in the stress labels of Figure 5.87

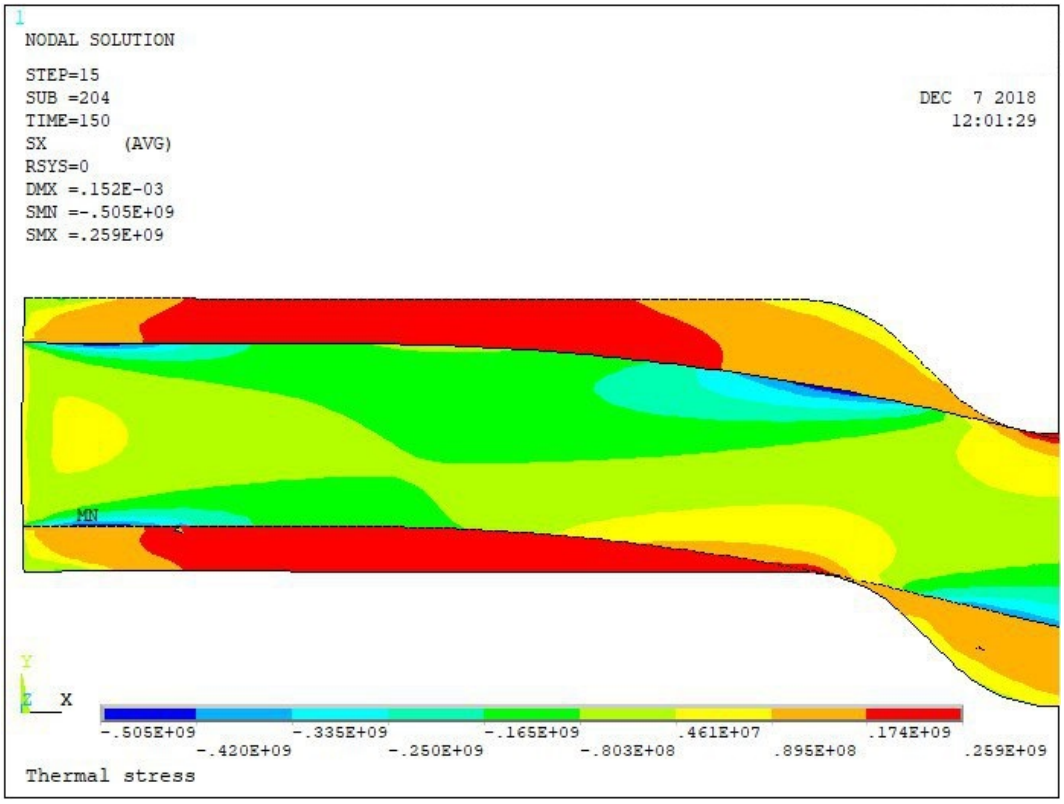

Figure 5.89 Thermal stress distribution, Sx, at 150 s considering radiation, left part of the plate

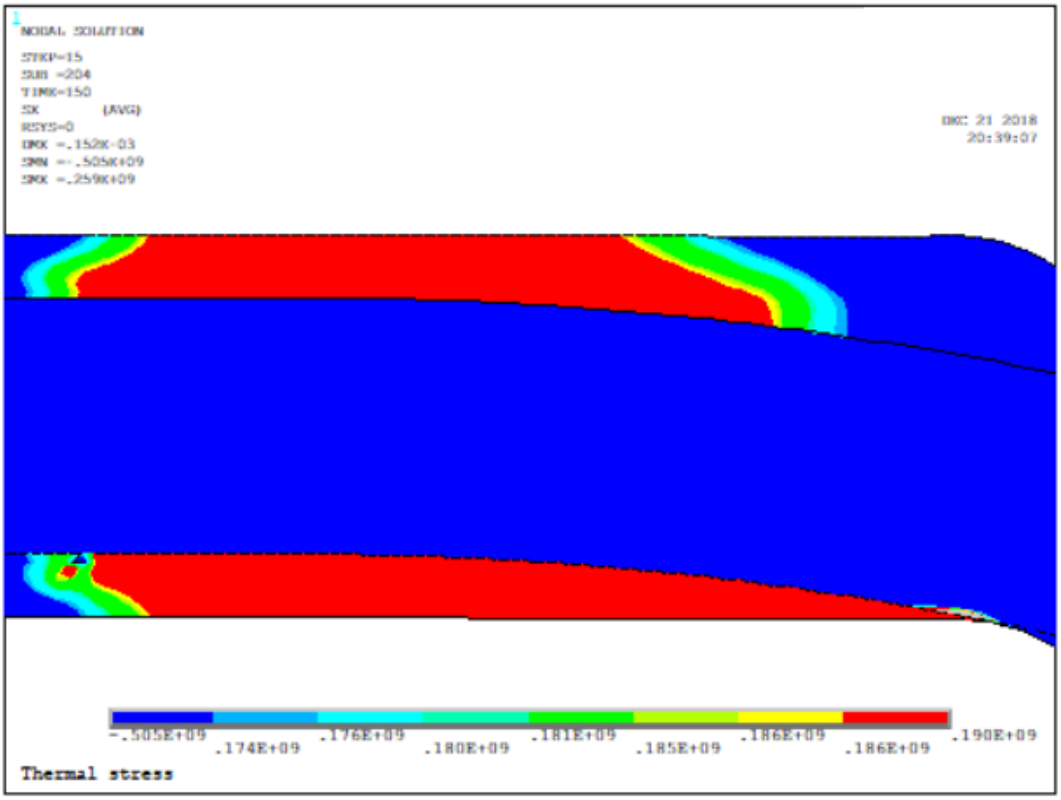

Figure 5.90 Change in the stress labels of Figure 5.89

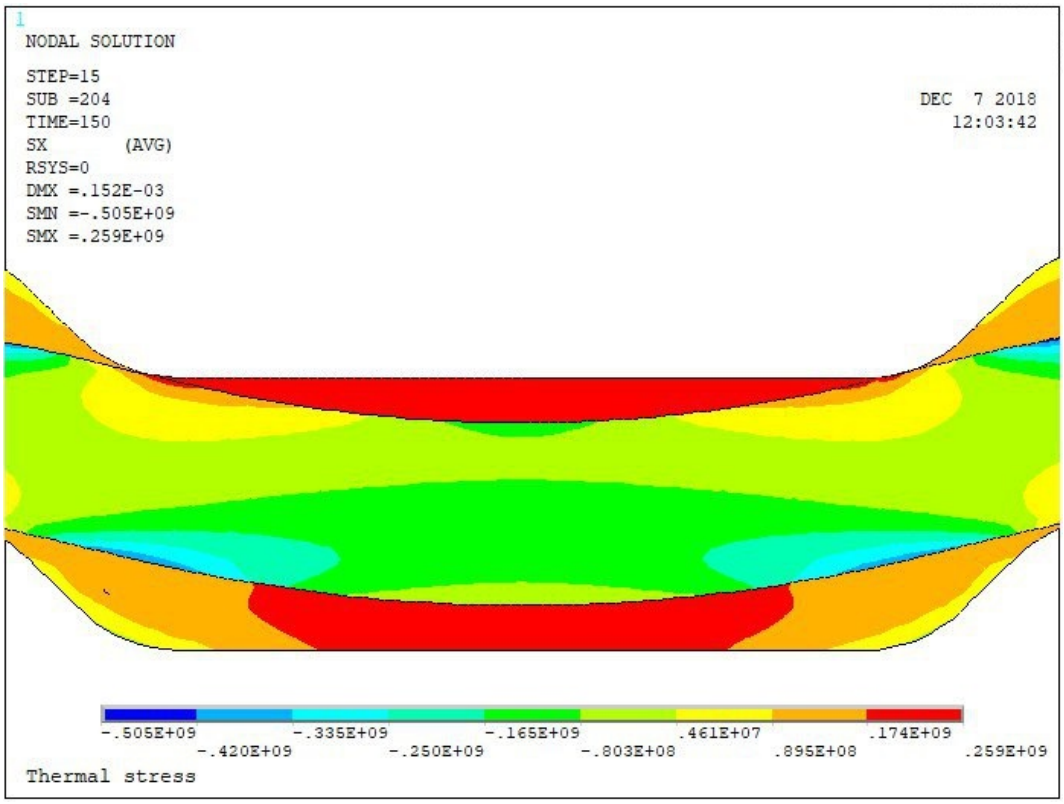

Figure 5.91 Thermal stress distribution, Sx, at 150 s considering radiation, centre of the plate

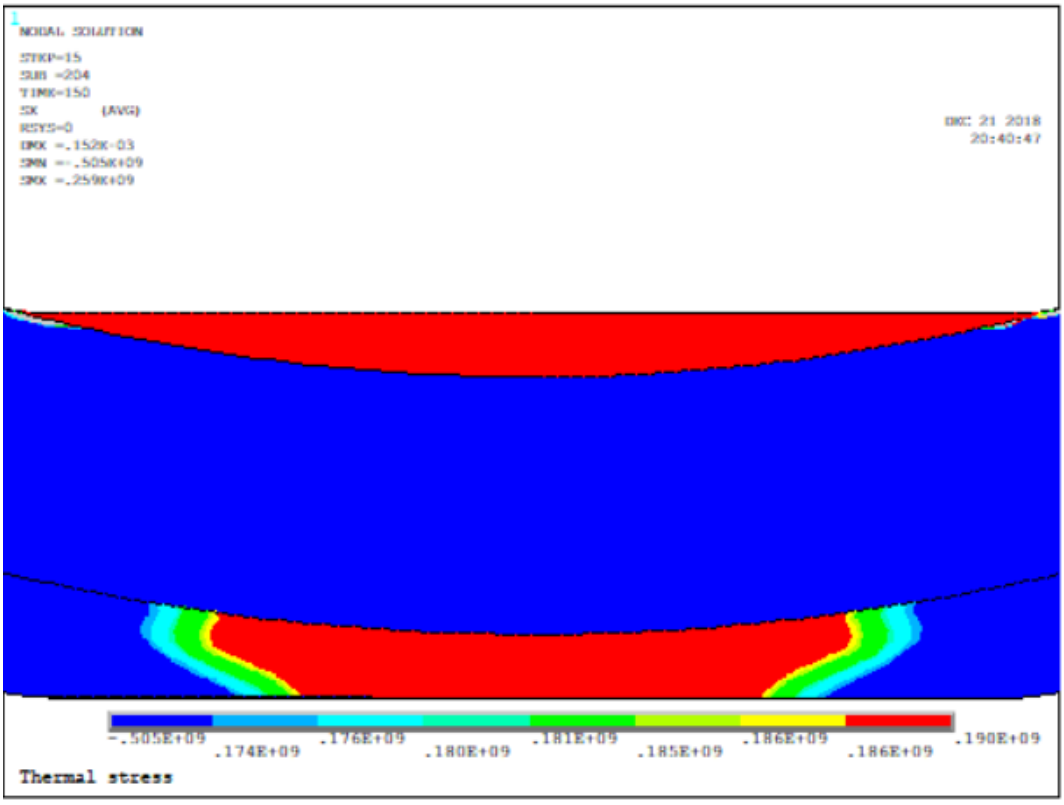

Figure 5.92 Change in the stress labels of Figure 5.91

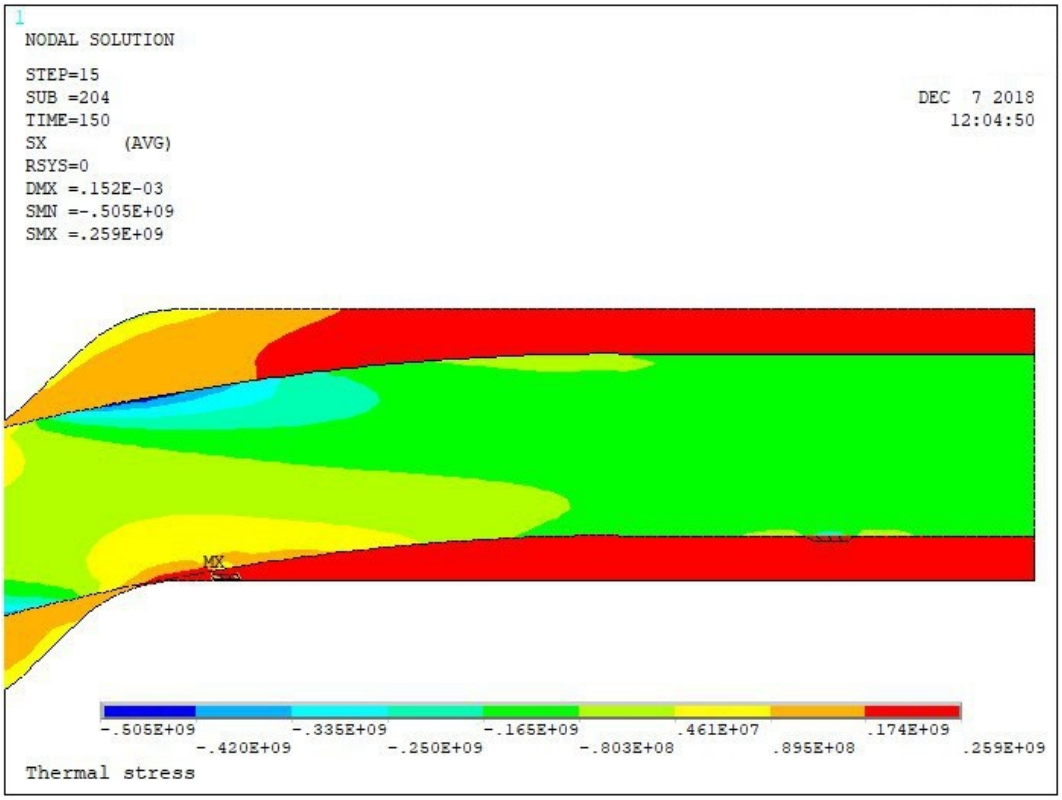

Figure 5.93 Thermal stress distribution, Sx, at 150 s considering radiation, right part of the plate

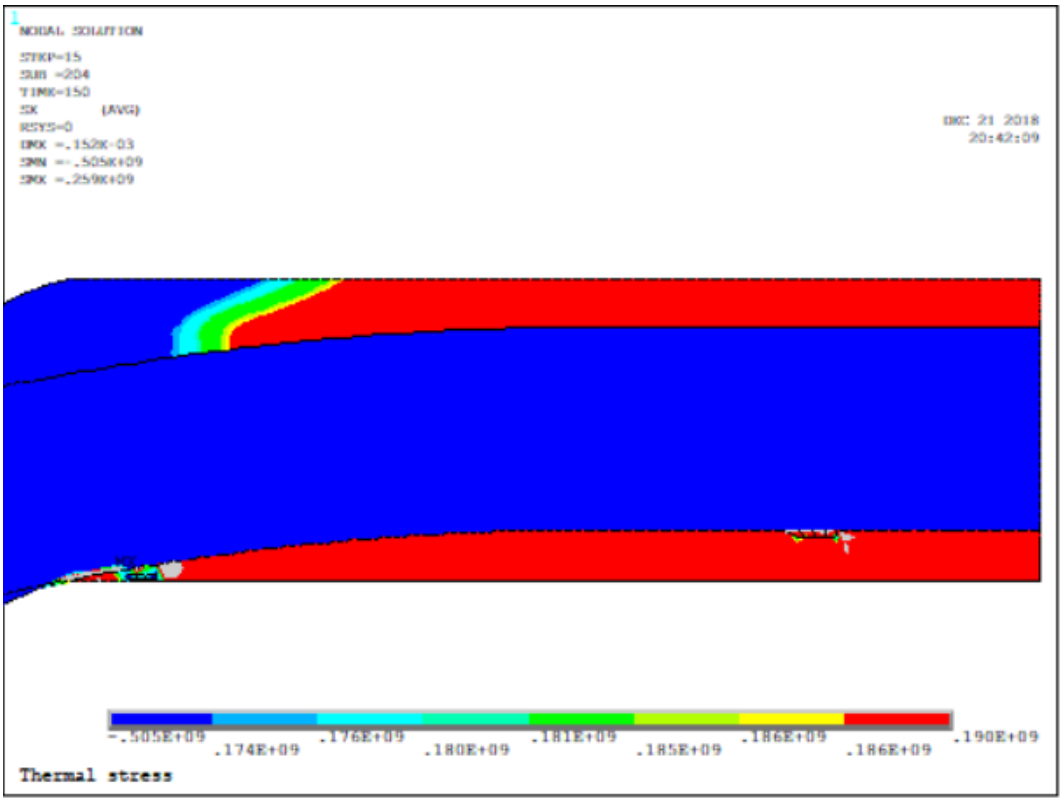

Figure 5.94 Change in the stress labels of Figure 5.93

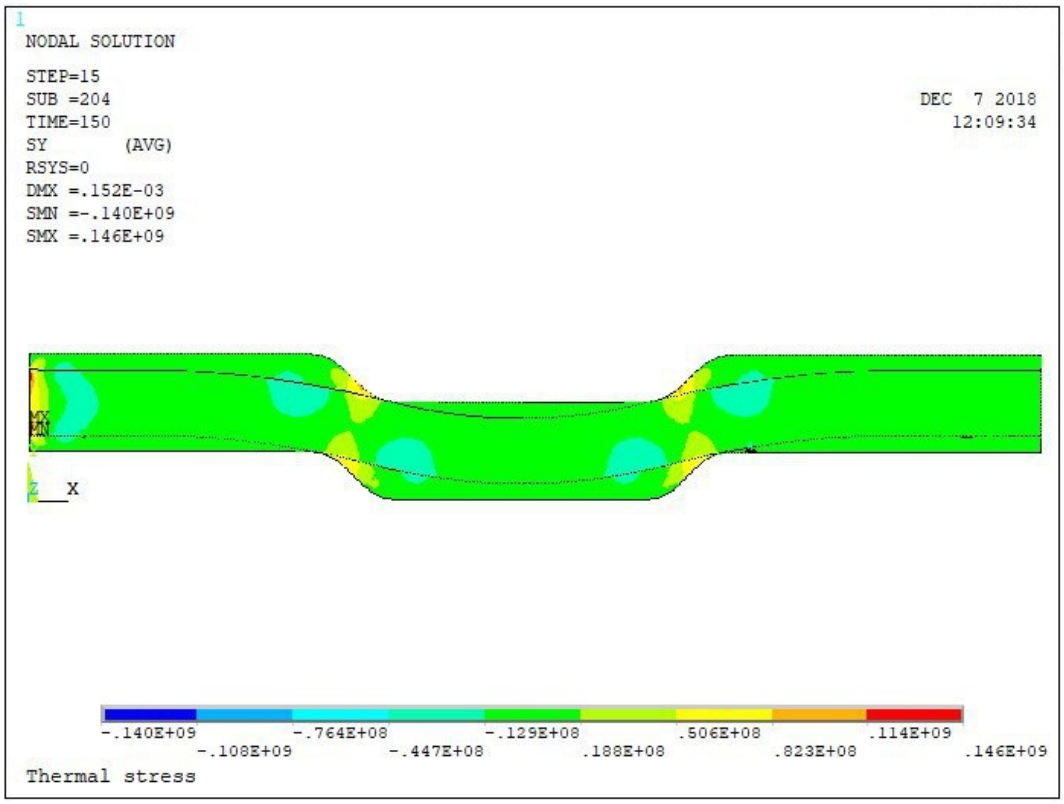

Figure 5.95 Thermal stress distribution, Sy, at 150 s considering radiation

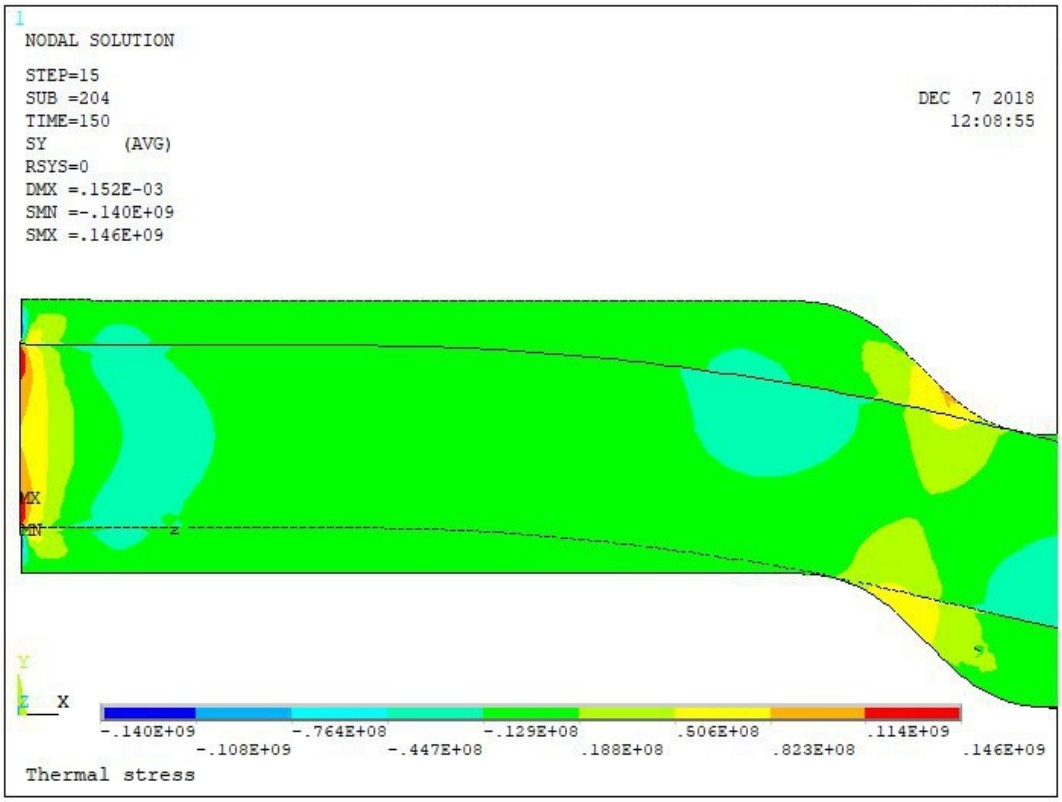

Figure 5.96 Thermal stress distribution, Sy, at 150 s considering radiation, left part of the plate

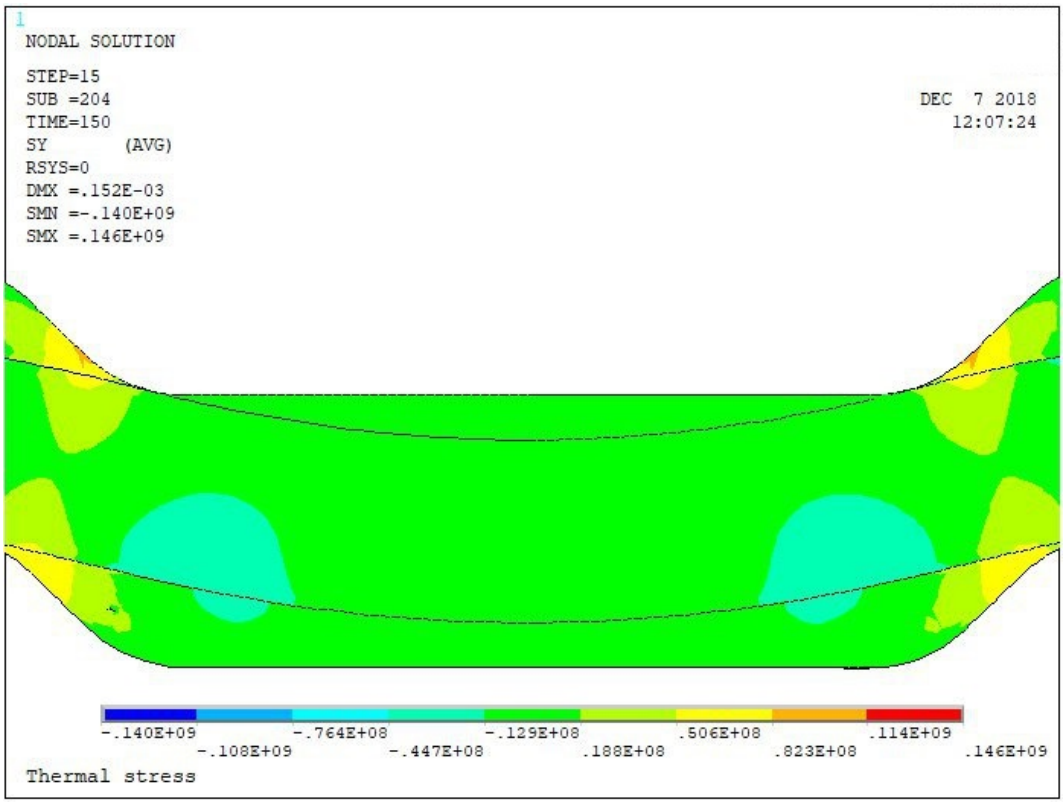

Figure 5.97 Thermal stress distribution, Sy, at 150 s considering radiation, centre of the plate

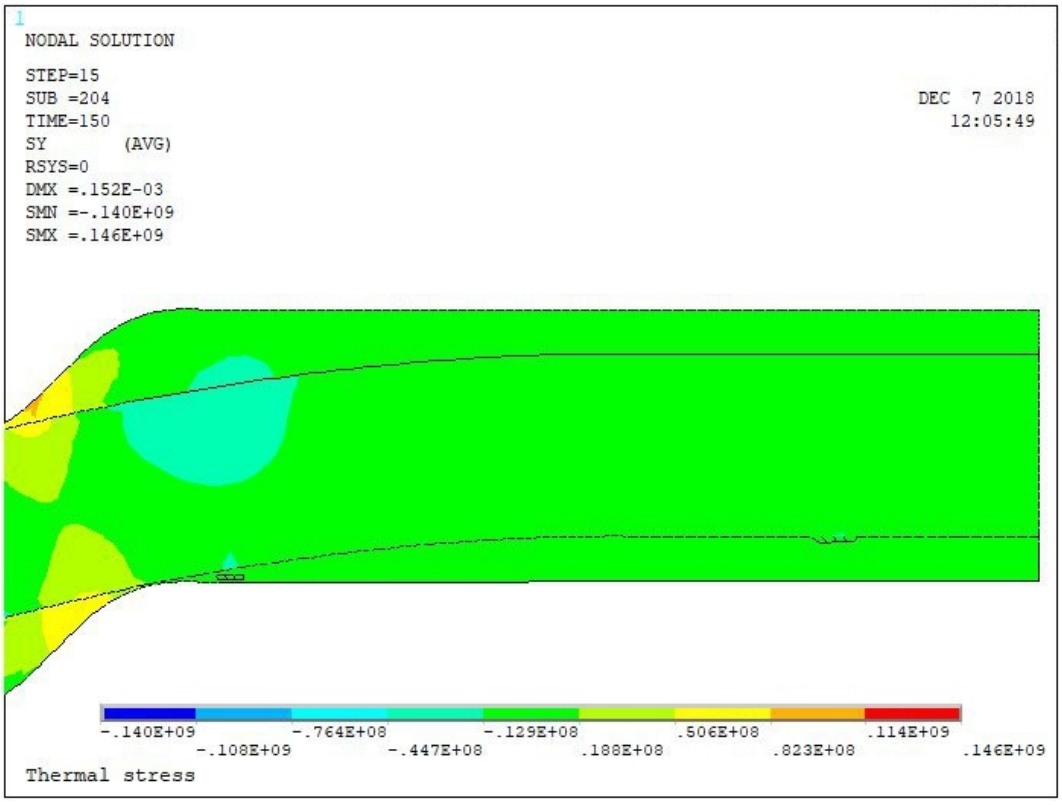

Figure 5.98 Thermal stress distribution, Sy, at 150 s considering radiation, right part of the plate

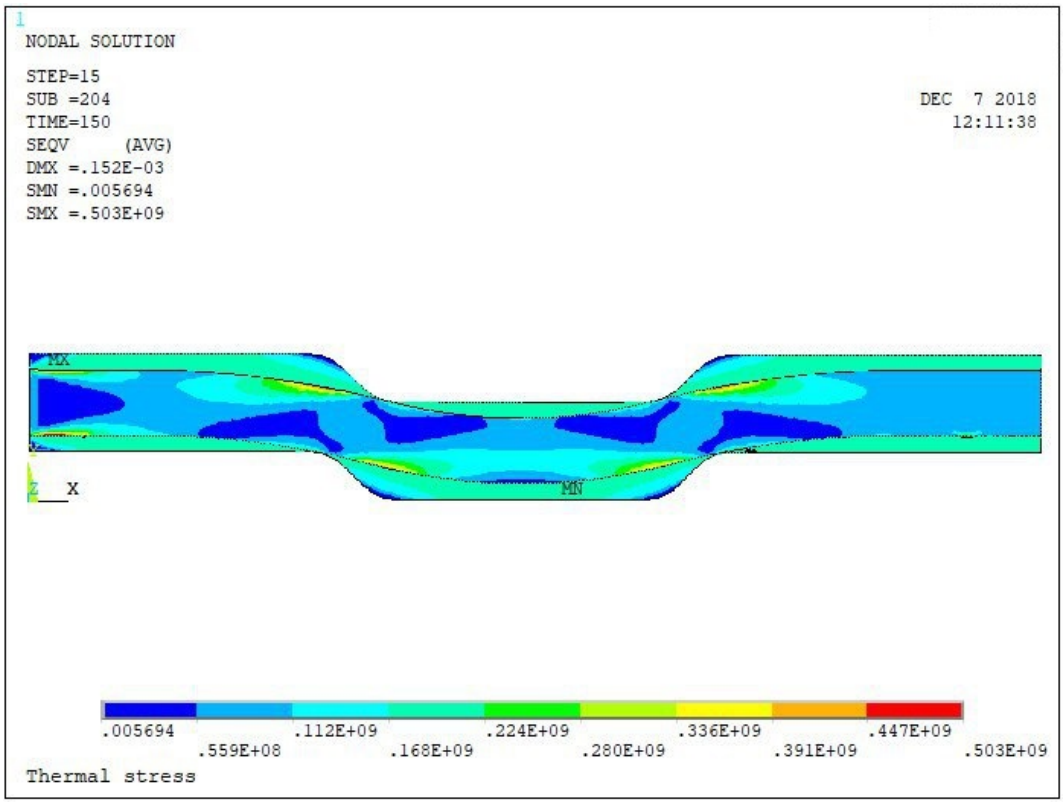

Figure 5.99 Von Mises stress, at 150 s considering radiation

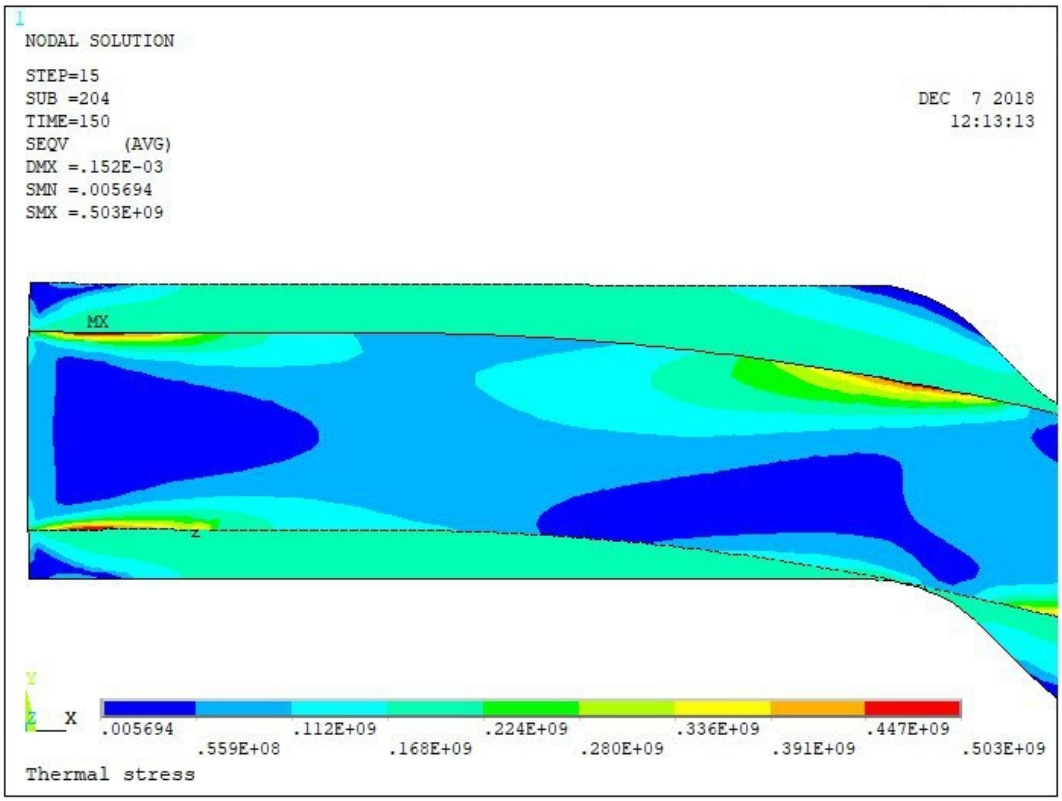

Figure 5.100 Von Mises stress, at 150 s considering radiation, left part of the plate

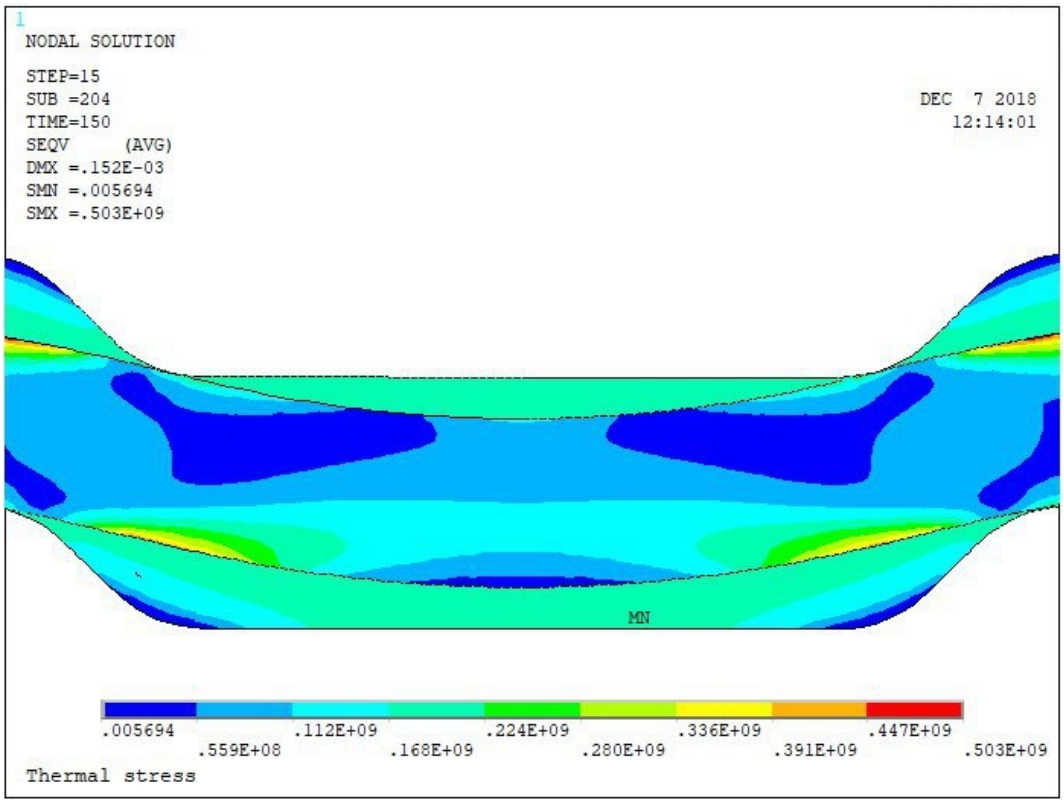

Figure 5.101 Von Mises stress, at 150 s considering radiation, centre of the plate

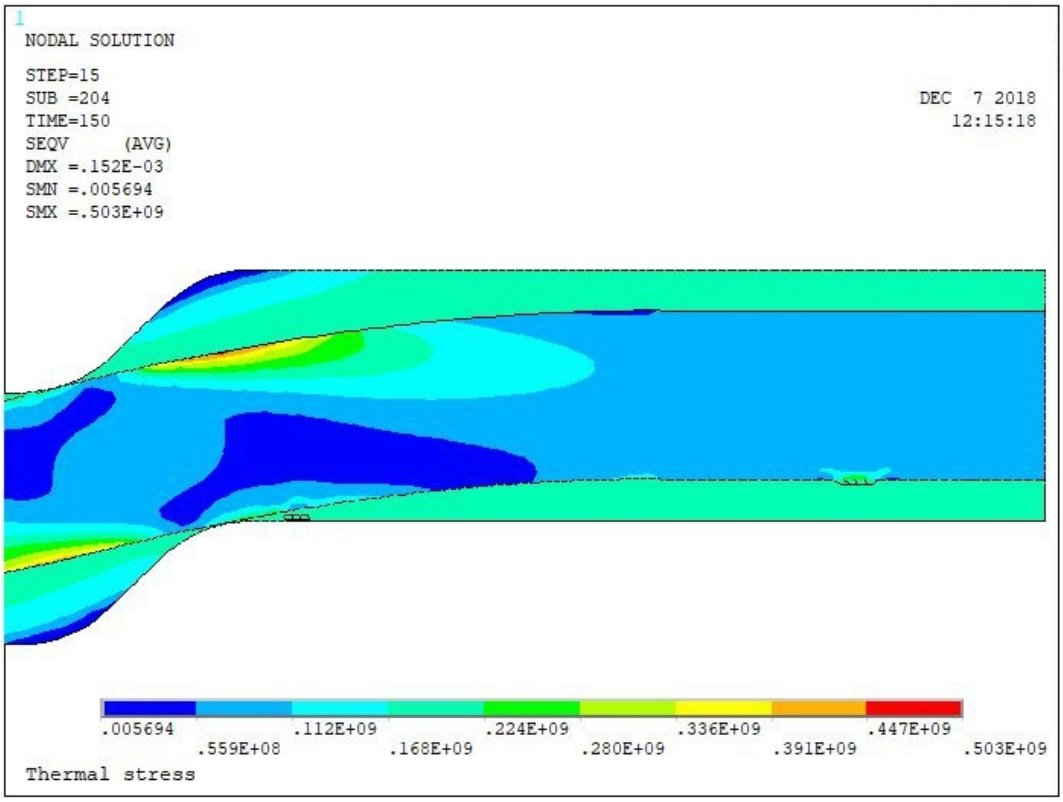

Figure 5.102 Von Mises stress, at 150 s considering radiation, right part of the plate

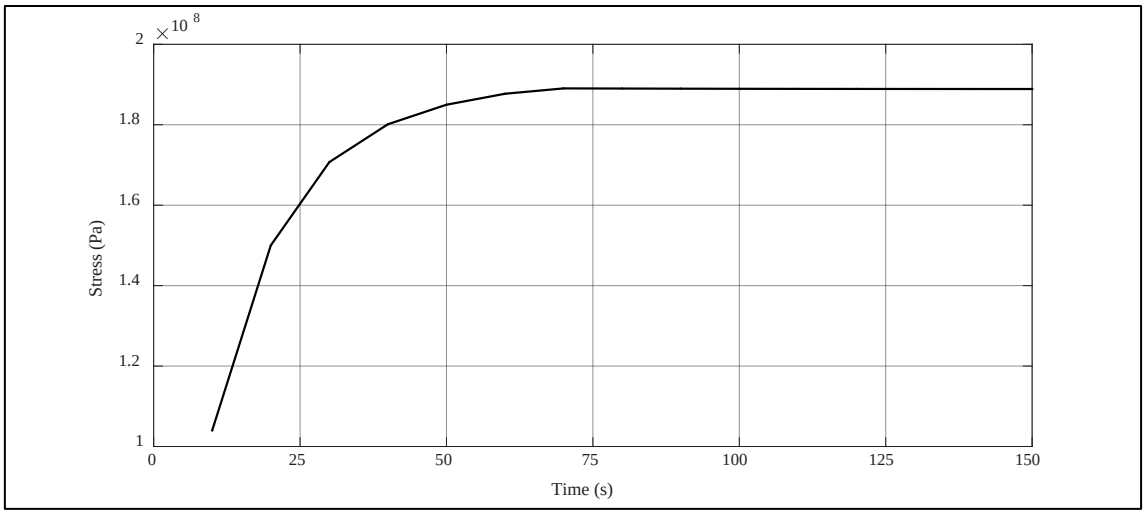

Figure 5.103 Thermal stress distribution, Sx, at 150 s considering radiation, node 34201

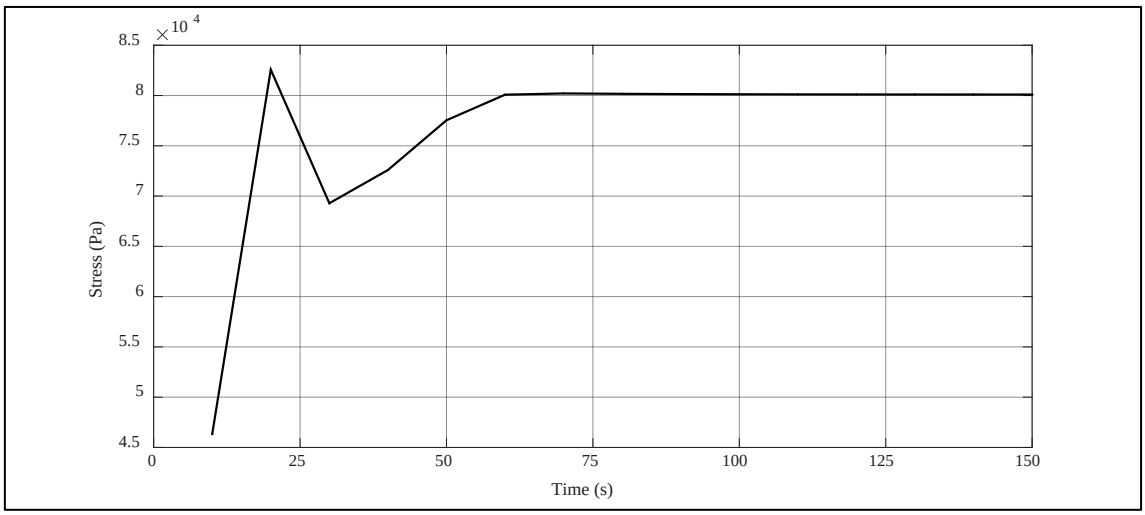

Figure 5.104 Thermal stress distribution, Sy, at 150 s considering radiation, node 34201

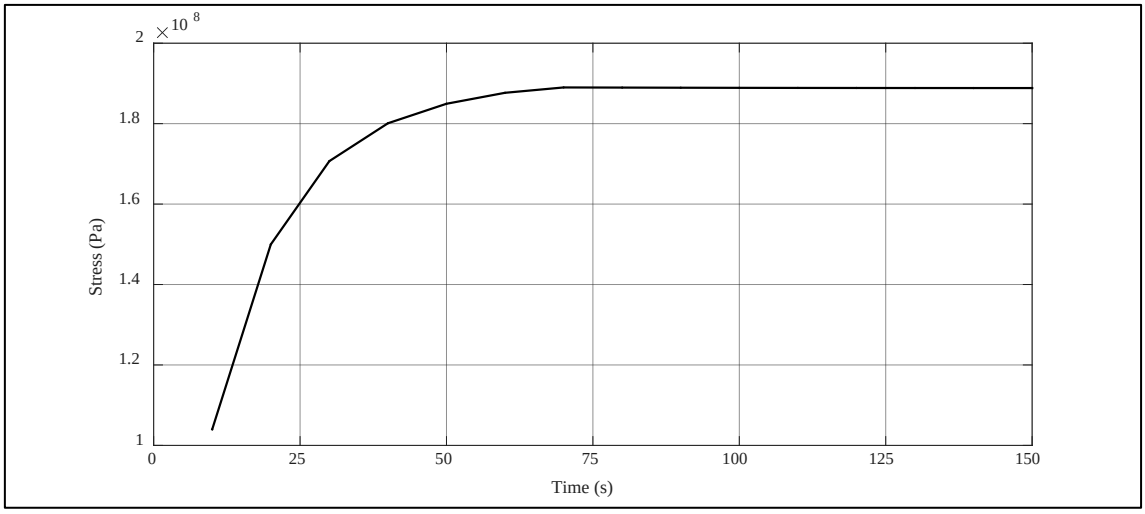

Figure 5.105 Von Mises stress, at 150 s considering radiation, node 34201

5.7 Manufacturing cost of a plate of MMC

The cost is divided in two section: pre-impregnated sheet (prepeg) and MMC plate.

5.7.1 Manufacturing cost of a prepeg

Information is available about the manufacturing of a pre-impregnated sheet of 800 mm x 600 mm (0.48 m^2). The cost calculation is broken down into the following sections:

a) Cost of the aluminium used in the coating of carbon fibre.

The carbon fibre fabric should be covered on both sides with aluminium wire of 5 g/m and a unitary cost of 13.276 €/kg.

First, the coating time will be calculated in minutes.

$$\text{Nº of coats/face} \cdot \text{Nº of faces} \cdot \text{Coating speed} =$$
$$= 6\ \text{coats/face} \cdot 2\ \text{faces} \cdot 45\ \text{s/face} = 540\ \text{s} = 9\ \text{min}$$

Then, this time can be converted into consumption of aluminium (Al) wire in meters.

$$\text{Wire feed speed} \cdot \text{Process time} = 3.9\ \text{m/min} \cdot 9\ \text{min} = 35.1\ \text{m of Al wire}$$

The cost of the aluminium is:

$$\text{Consumption of Al wire} \cdot \text{Linear density of aluminum} \cdot \text{Unit cost of aluminum} =$$
$$= 35.1\ \text{m} \cdot 5\ \text{g/m} \cdot 1\ \text{kg}/1000\ \text{g} \cdot 13.276\ €/\text{kg} = 2.33€ \approx 2.5€$$

Secondly, the cost of compressed air at 6 bar, provided by a compressor of 22 kW, will be calculated:

$$\text{Coating time} \cdot \text{Power} \cdot \text{Unit cost of energy consumed} =$$
$$= 9\ \text{min} \cdot 60\ \text{s}/1\ \text{min} \cdot 22\ \text{kW} \cdot 1\ \text{h}/3600\ \text{s} \cdot 0.15\ €/\text{kW} \cdot \text{h} = 0.5\ €$$

Thus, the total cost of the pre-impregnated coating is:

$$2.5\ € + 0.5\ € = 3\ €$$

b) Cost of the carbon fibre used in the manufacture of the composite material.

The carbon fibre has a surface density of 200 g/m^2 and a unit cost of 12 €/m^2.

The cost of carbon fibre with an area of 0.48 m^2 will be calculated:

$$\text{Pre} - \text{impregnated surface} \cdot \text{Unit cost} =$$
$$= 0.48\ \text{m}^2 \cdot 12\ €/\ \text{m}^2 = 5.76\ € \approx 6\ €$$

c) Amortization of equipment and wages of labour.

The cost of amortization of equipment and wages of labour will be calculated:

$$\text{Coating time} \cdot \text{Unit cost of amortization of equipment and wages of labour} =$$

$$= 9\ \text{min} \cdot 1\ \text{h}/60\ \text{min} \cdot 46\ €/\text{h} = 6.90\ € \approx 7\ €$$

The cost of amortization of equipment and wages of labour is an estimation.

From the previous sections we obtain a total cost of 16 € for a pre-impregnated sheet of 0.48 m^2. Therefore, a total cost per square meter of pre-impregnated sheet is obtained, 33.33 €.

5.7.2 Manufacturing cost of a MMC plate of 1 m^2 and 3 mm of thickness

The cost calculation is broken down into the following sections:

a) Cost of pre-impregnated sheets.

Since a plate of 1 m^2 and 3 mm thickness requires 6 sheets of pre-impregnated, the total cost of the plate is:

$$\text{Nº of pre} - \text{impregnated} \cdot \text{Unit cost of pre} - \text{impregnated} =$$

$$= 6 \text{ pre} - \text{impregnated} \cdot 33.33 \text{ €/pre} - \text{impregnated} = 199.98 \text{ €}$$

b) Cost of thixoforging.

Once the prepreg is developed, it must be linked by thixoforging. The heating is done by an infrared radiator with a power of 7.5 kW. It is necessary to establish the cost of the mould for the press per unit of plate manufactured, the additional aluminium for the manufacture of the plate, the consumed energy and the labour:

$$\text{Cost of the mould/Nº of plates manufactured} + \text{Aluminium for thixoforging} \cdot$$
$$\cdot \text{Unit cost of aluminium} + \text{Thixoforging time} \cdot \text{Power}$$
$$\cdot \text{Unit cost of energy consumed}$$
$$+ \text{Unit cost of amortization of equipment and wages of labour} =$$

$$= 20000 \text{ €/1000000 plates} + 3 \text{ kg} \cdot 13.276 \text{ €/kg} + 7 \text{ min} \cdot 60 \text{ s/1 min}$$
$$\cdot 7.5 \text{ kW} \cdot 1 \text{ h/3600 s} \cdot 0.15 \text{ €/kW} \cdot \text{h} + 10 \text{ min} \cdot 1 \text{ h/60 min}$$
$$\cdot 200 \text{ €/h} = 73.31 \text{ €}$$

It has been considered that the mould will be reused for the manufacture of 1000000 plates.

From the previous sections we obtain a total cost of 273.29 € for a plate of composite material made of carbon fibre and metal matrix.

The cost of a plate of 410 stainless steel plate with 3 mm thickness is: 1200-3500 US $/t. This offer comes from a retail supplier. Since the weight of a sheet of 1 m^2 is:

$$\text{Density} \cdot \text{Thickness} \cdot \text{Surface} =$$
$$= 7800 \text{ kg/m}^3 \cdot 3 \text{ mm} \cdot 1 \text{ m/1000 mm} \cdot 1 \text{ m}^2 = 23.4 \text{ kg}$$

Its cost is:

$$\text{Mass} \cdot \text{Unit cost} =$$

$$= 23.4 \text{ kg} \cdot [1.2 - 3.5] \text{ US \$/kg} = 28.08 - 81.90 \text{ US \$}$$

And its equivalent in euros is 24.24-70.06 €.

The plate of composite material has a cost between 3.9 and 11.27 times greater than that of equal size in steel. However, the weight of the composite plate is between 5.49 kg (considering negligible the proportion of aluminium and a density of carbon fibre of 1830 kg/m^3) and 8.37 kg (considering negligible the proportion of fibre of carbon and an aluminium density of 2790 kg/m^3). The steel plate has a weight between 3 and 4 times greater than that of equal size in composite material.

Now, we can calculate the thickness of a steel plate of equal strength. We will use tensile tests of the specimen shown in Figure 5.106.

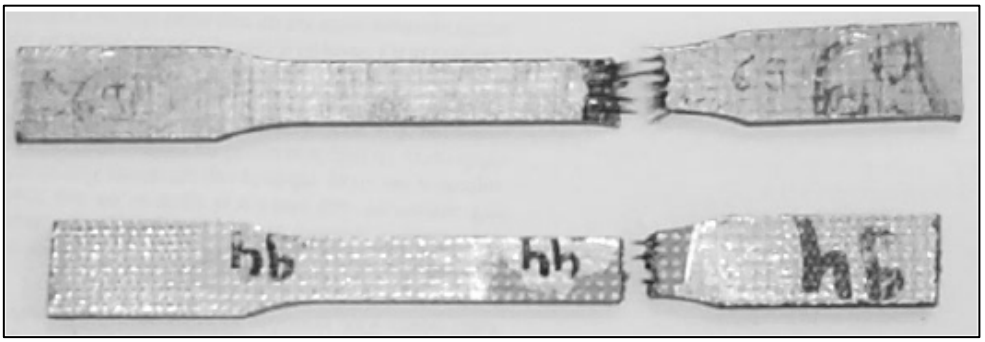

Figure 5.106 Test tube tested to traction

The result of the tests for this material yields a breaking stress of 800 MPa for unidirectional fibre, if the load is applied in the direction favourable to the fibre. If the fibre is bidirectional, the breaking stress is 500 MPa in the two perpendicular directions. Steel 410 has a breaking stress of 480 MPa, which means that the unidirectional composite material has a resistance 1.7 greater than steel, if we consider only unidirectional loads. If we consider bidirectional loads, we have similar resistances.

CONCLUSIONS

In this Master's Thesis, two models of Barbero have been analysed: one-eighth model of composite material with periodic microstructure and full model of RVE for a composite material with a periodic, hexagonal fibre array. Then, five thermal analysis of one thixoforged aluminium plate have been made. First, without considering radiation, with a convection characterized by a film coefficient of 10 $W/m^2 \cdot K$ and with an interface of steel. Secondly, the same case but with an interface of glass. Thirdly, without considering radiation, with a convection characterized by a film coefficient of 100 $W/m^2 \cdot K$ and with an interface of steel. Fourthly, the same case but with an interface of glass. Fifthly, considering only radiation and with an interface of glass. Furthermore, thermal stress analysis has been made using the results of the thermal analysis considering only radiation. Finally, manufacturing cost of a plate of MMC has been calculated.

On the models of Barbero have been made modifications that allow to use the programs considering different hypotheses of load or deformation.

The temperature of the support has an important effect on the temperatures developed, thus, on the tensions.

A comparison between convection and radiation heat transfer shows that the radiation is a little higher.

EXPRESSION OF THANKS

I want to express my appreciation to everyone who helped me to complete this work.

Firstly, I want to thank the Polytechnic University of Cartagena and his staff for their hospitality and the knowledge received.

I am also very grateful to all those professionals of the IFKB of Stuttgart University for their help in the introduction to the field of the Metal Matrix Composites (MMC) and Thixoforging process, especially to the Dr. Gadow, Dipl. Ing. Miguel Jiménez Martínez and Dr. Ing. Venancio Martínez García.

Finally, I express my sincere thanks to Dr. José Andrés Moreno Nicolás for allowing me to learn from his knowledge and pass me on his enthusiasm for the well-done work, furthermore, who has given me the guidance and help necessary to complete this work.

Enclosure A: Exercises

A.1 Transversely Isotropic Averaging

In this section, the elastic properties of a composite material reinforced with parallel cylindrical fibres randomly distributed in the cross-section are computed. The constituent properties are E_f = 241 GPa, ν_f = 0.2, E_m = 3.12 GPa, ν_m = 0.38, fibre volume fraction V_f = 0.4.

It is used the code PMMIE.m, which implements the periodic microstructure model (PMM) equations for the case of transversely isotropic fibres.

A.2 Transversely Isotropic stiffness tensor

In this section, E_1, E_2, ν_{12}, and ν_{23} for a unidirectional composite with isotropic fibres E_f = 241 GPa, ν_f = 0.2, and isotropic matrix E_m = 3.12 GPa, ν_m = 0.38 with fibre volume fraction V_f = 0.4 are computed. The fibre diameter is d_f = 7 μm, placed in a hexagonal array.

The dimensions a_2 and a_3 of the RVE, as shown in Fig. 1.13, are chosen to obtain V_f = 0.4 with a hexagonal array microstructure. The fibre volume and the total volume of the RVE are

$$v_f = 4 \cdot a_1 \cdot \pi \cdot \left(\frac{d_f}{2}\right)^2 ; v_t = (2a_1\ 2a_2\ 2a_3)$$

The ratio between both is the volume fraction. Therefore,

$$v_f = \pi \cdot \frac{\left(\frac{d_f}{2}\right)^2}{2 \cdot a_2 \cdot a_3} = 0.4$$

Additionally, the relation between a_2 and a_3 is established by the hexagonal array pattern

$$a_3 = a_2 \cdot \tan(60°)$$

These two relations yield a_2 and a_3, while the a_1 dimension can be chosen arbitrarily. In this case, the RVE dimensions are

$$a_1 = \frac{a_2}{4}; \quad a_2 = 5.2701\ \mu m; \quad a_3 = 9.1281\ \mu m$$

Since this RVE is symmetric, it is possible to model one-eighth of the RVE, as shown in Fig. 1.14. An ANSYS code is used to model one-eighth of the RVE.

The boundary conditions are defined in three load steps, which are then used to obtain the coefficients $C_{\alpha\beta}$ in columns one, two, and three. A unit strain is applied along each direction, each time. Eq. 1.19 is then used to obtain the stiffness coefficients.

Enclosure B: Mechanics of orthotropic materials

B.1 Strain and stress matrixes

A single lamina of fibre reinforced composite behaves as an orthotropic material. That is, the material has three mutually perpendicular planes of symmetry. The intersection of these three planes defines three axes, one of them coincides with the fibre direction, x'_1, and other with the thickness, x'_3 [Barbero, 2010].

If the gradients of the displacements are so small that products of partial derivatives of u_i are negligible with linear (first order) derivative terms, then the strain tensor ε_{ij} is given by

$$\varepsilon = \varepsilon_{ij} = \frac{1}{2}\left(u_{i,j} + u_{j,i}\right) \tag{B.1}$$

From the definition, Eq. B.1, strain is a second-order, symmetric tensor (i.e., $\varepsilon_{ij} = \varepsilon_{ji}$). In expanded form the strains are defined by

$$\begin{aligned}
\varepsilon_{11} &= \frac{\partial u_1}{\partial x_1} = \epsilon_1; \quad 2\cdot\varepsilon_{12} = 2\cdot\varepsilon_{21} = \left(\frac{\partial u_1}{\partial x_2} + \frac{\partial u_2}{\partial x_1}\right) = \gamma_6 = \epsilon_6 \\
\varepsilon_{22} &= \frac{\partial u_2}{\partial x_2} = \epsilon_2; \quad 2\cdot\varepsilon_{13} = 2\cdot\varepsilon_{31} = \left(\frac{\partial u_1}{\partial x_3} + \frac{\partial u_3}{\partial x_1}\right) = \gamma_5 = \epsilon_5 \\
\varepsilon_{33} &= \frac{\partial u_3}{\partial x_3} = \epsilon_3; \quad 2\cdot\varepsilon_{23} = 2\cdot\varepsilon_{32} = \left(\frac{\partial u_2}{\partial x_3} + \frac{\partial u_3}{\partial x_2}\right) = \gamma_4 = \epsilon_4
\end{aligned} \tag{B.2}$$

The engineering shear strain $\gamma_\alpha = 2\cdot\varepsilon_{ij}$, for $i \neq j$ is often used instead of the tensor shear strain. The strain tensor, being a second order tensor, can be displayed as a matrix [Beer et al., 2001]

$$[\varepsilon] = \begin{bmatrix} \varepsilon_{11} & \varepsilon_{12} & \varepsilon_{13} \\ \varepsilon_{12} & \varepsilon_{22} & \varepsilon_{23} \\ \varepsilon_{13} & \varepsilon_{23} & \varepsilon_{33} \end{bmatrix} = \begin{bmatrix} \epsilon_1 & \epsilon_6/2 & \epsilon_5/2 \\ \epsilon_6/2 & \epsilon_2 & \epsilon_4/2 \\ \epsilon_5/2 & \epsilon_4/2 & \epsilon_3 \end{bmatrix} \tag{B.3}$$

The stress tensor, being a second order tensor, can be displayed as a matrix, Figure B.1.

$$[\sigma] = \begin{bmatrix} \sigma_{11} & \sigma_{12} & \sigma_{13} \\ \sigma_{12} & \sigma_{22} & \sigma_{23} \\ \sigma_{13} & \sigma_{23} & \sigma_{33} \end{bmatrix} = \begin{bmatrix} \sigma_1 & \sigma_6 & \sigma_5 \\ \sigma_6 & \sigma_2 & \sigma_4 \\ \sigma_5 & \sigma_4 & \sigma_3 \end{bmatrix} \tag{B.4}$$

B.2 Equilibrium equations

When body forces are negligible, the expanded form of the equilibrium equations is:

$$\frac{\partial \sigma_{xx}}{\partial x} + \frac{\partial \sigma_{xy}}{\partial y} + \frac{\partial \sigma_{xz}}{\partial z} = 0$$

$$\frac{\partial \sigma_{xy}}{\partial x} + \frac{\partial \sigma_{yy}}{\partial y} + \frac{\partial \sigma_{yz}}{\partial z} = 0$$

$$\frac{\partial \sigma_{xz}}{\partial x} + \frac{\partial \sigma_{yz}}{\partial y} + \frac{\partial \sigma_{zz}}{\partial z} = 0 \tag{B.5}$$

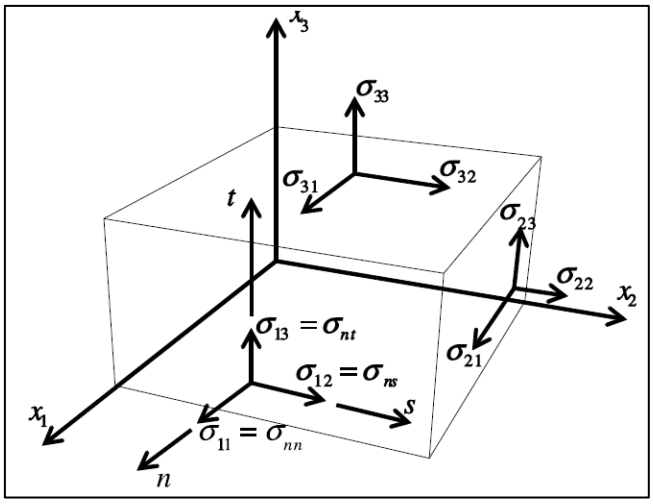

Figure B.1 Stress components

B.3 Transformation of constitutive equations

The constitutive equations that relate stress σ to strain ε are defined using tensor strains, as

$$\sigma' = C' \cdot \varepsilon \tag{B.6}$$

where it is used a coordinate transformation, Fig. B.2.

Therefore,

$$\{x'\} = [a] \cdot \{x\} \tag{B.7}$$

The stress tensor can be thought in matrix notation as

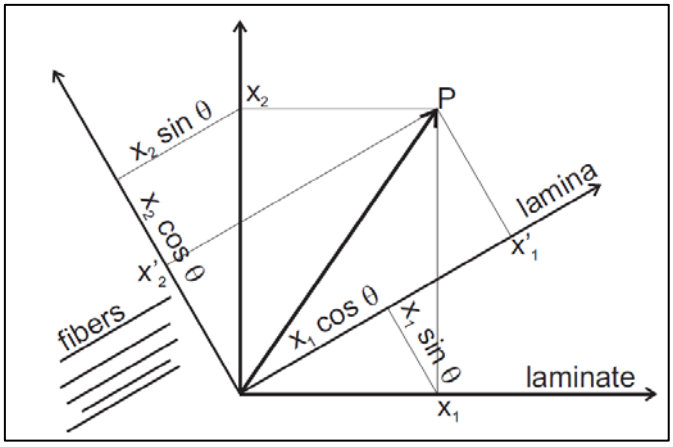

Figure B.2 Coordinate transformation

$$\{\sigma'\} = [a] \cdot \{\sigma\} \cdot [a]^T \tag{B.8}$$

The strain tensor transforms in the same way as the tensor stress.

$$[a] \cdot \{\sigma\} \cdot [a]^T = C' \cdot [a] \cdot \{\varepsilon\} \cdot [a]^T \tag{B.9}$$

Therefore,

$$\{\sigma\} = [C] \cdot \{\epsilon\} \tag{B.10}$$

$$[C] = [a]^T \cdot C' \cdot [a]$$

The constitutive equation for an anisotropic material is:

$$\begin{Bmatrix} \sigma_1 \\ \sigma_2 \\ \sigma_3 \\ \sigma_4 \\ \sigma_5 \\ \sigma_6 \end{Bmatrix} = \begin{bmatrix} C_{11} & C_{12} & C_{13} & C_{14} & C_{15} & C_{16} \\ C_{12} & C_{22} & C_{23} & C_{24} & C_{25} & C_{26} \\ C_{13} & C_{23} & C_{33} & C_{34} & C_{35} & C_{36} \\ C_{14} & C_{24} & C_{34} & C_{44} & C_{45} & C_{46} \\ C_{15} & C_{25} & C_{35} & C_{45} & C_{55} & C_{56} \\ C_{16} & C_{26} & C_{36} & C_{46} & C_{56} & C_{66} \end{bmatrix} \cdot \begin{Bmatrix} \epsilon_1 \\ \epsilon_2 \\ \epsilon_3 \\ \gamma_4 \\ \gamma_5 \\ \gamma_6 \end{Bmatrix} \tag{B.11}$$

For monoclinic material (only one plane of symmetry),

$$\begin{Bmatrix} \sigma_1 \\ \sigma_2 \\ \sigma_3 \\ \sigma_4 \\ \sigma_5 \\ \sigma_6 \end{Bmatrix} = \begin{bmatrix} C_{11} & C_{12} & C_{13} & 0 & 0 & C_{16} \\ C_{12} & C_{22} & C_{23} & 0 & 0 & C_{26} \\ C_{13} & C_{23} & C_{33} & 0 & 0 & C_{36} \\ 0 & 0 & 0 & C_{44} & C_{45} & 0 \\ 0 & 0 & 0 & C_{45} & C_{55} & 0 \\ C_{16} & C_{26} & C_{36} & 0 & 0 & C_{66} \end{bmatrix} \cdot \begin{Bmatrix} \epsilon_1 \\ \epsilon_2 \\ \epsilon_3 \\ \gamma_4 \\ \gamma_5 \\ \gamma_6 \end{Bmatrix} \tag{B.12}$$

For orthotropic material, Figure B.3,

$$\begin{Bmatrix} \sigma_1 \\ \sigma_2 \\ \sigma_3 \\ \sigma_4 \\ \sigma_5 \\ \sigma_6 \end{Bmatrix} = \begin{bmatrix} C_{11} & C_{12} & C_{13} & 0 & 0 & 0 \\ C_{12} & C_{22} & C_{23} & 0 & 0 & 0 \\ C_{13} & C_{23} & C_{33} & 0 & 0 & 0 \\ 0 & 0 & 0 & C_{44} & 0 & 0 \\ 0 & 0 & 0 & 0 & C_{55} & 0 \\ 0 & 0 & 0 & 0 & 0 & C_{66} \end{bmatrix} \cdot \begin{Bmatrix} \epsilon_1 \\ \epsilon_2 \\ \epsilon_3 \\ \gamma_4 \\ \gamma_5 \\ \gamma_6 \end{Bmatrix} \tag{B.13}$$

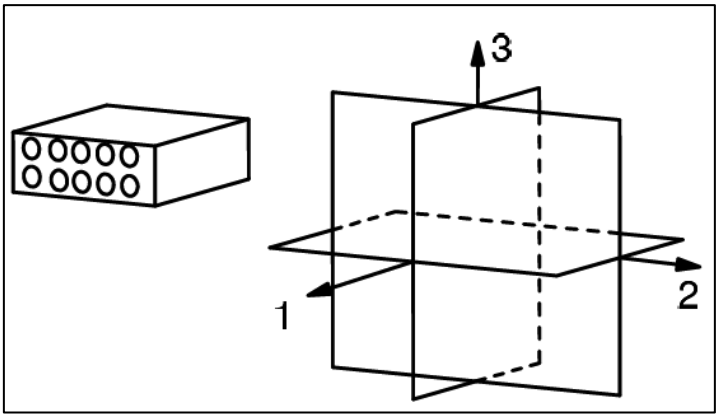

Figure B.3 Orthotropic material

For transversely isotropic material,

$$\begin{Bmatrix}\sigma_1\\ \sigma_2\\ \sigma_3\\ \sigma_4\\ \sigma_5\\ \sigma_6\end{Bmatrix} = \begin{bmatrix} C_{11} & C_{12} & C_{12} & 0 & 0 & 0 \\ C_{12} & C_{22} & C_{23} & 0 & 0 & 0 \\ C_{12} & C_{23} & C_{22} & 0 & 0 & 0 \\ 0 & 0 & 0 & (C_{22}-C_{23})/2 & 0 & 0 \\ 0 & 0 & 0 & 0 & C_{66} & 0 \\ 0 & 0 & 0 & 0 & 0 & C_{66} \end{bmatrix} \cdot \begin{Bmatrix}\epsilon_1\\ \epsilon_2\\ \epsilon_3\\ \gamma_4\\ \gamma_5\\ \gamma_6\end{Bmatrix} \tag{B.14}$$

For isotropic material,

$$\begin{Bmatrix}\sigma_1\\ \sigma_2\\ \sigma_3\\ \sigma_4\\ \sigma_5\\ \sigma_6\end{Bmatrix} = \begin{bmatrix} C_{11} & C_{12} & C_{12} & 0 & 0 & 0 \\ C_{12} & C_{11} & C_{12} & 0 & 0 & 0 \\ C_{12} & C_{12} & C_{11} & 0 & 0 & 0 \\ 0 & 0 & 0 & (C_{11}-C_{12})/2 & 0 & 0 \\ 0 & 0 & 0 & 0 & (C_{11}-C_{12})/2 & 0 \\ 0 & 0 & 0 & 0 & 0 & (C_{11}-C_{12})/2 \end{bmatrix} \cdot \begin{Bmatrix}\epsilon_1\\ \epsilon_2\\ \epsilon_3\\ \gamma_4\\ \gamma_5\\ \gamma_6\end{Bmatrix} \tag{B.15}$$

Enclosure C: Thermal radiation

C.1 Definitions in ANSYS

The following lines summarize the most interesting definitions:

- Enclosure: An open or closed enclosure in a radiation problem is a set of surfaces radiating to each other. Each open enclosure can have its own space temperature or space node which radiates to the ambient temperature. Each radiating surface has an emissivity and a direction of radiation assigned to it.
- View Factors (form factor or shape factor): To compute radiation exchange between any two surfaces, we calculate the fraction of the radiation leaving surface i which is intercepted by surface j. In ANSYS, we can calculate view factors using the hidden/non-hidden method for 2-D and 3-D problems or the Hemicube method for 3-D problems.
- Emissivity: Emissivity is a surface radiative property defined as the ratio of the radiation emitted by the surface to the radiation emitted by a black body at the same temperature. ANSYS restricts radiation exchange between surfaces to grey-diffuse surfaces. The word grey signifies that emissivity and absorptivity of the surface do not depend on wavelength (either can depend on temperature). The word diffuse signifies that emissivity and absorptivity do not depend on direction. For a grey diffuse surface, emissivity = absorptivity; emissivity + reflectivity = 1. Note that a black body surface has a unit emissivity.
- Temperature Offset: We can perform radiation calculations in absolute temperature units. If the model is defined in terms of degrees Fahrenheit or degrees Centigrade, we must specify a temperature offset. The temperature offset is 460° for the Fahrenheit system and 273° for the Centigrade system.
- Space Node: For an open enclosure problem, if the ambient is another body in the model, we can use the temperature of a space node to represent the free-space ambient temperature. A space node may be defined to absorb all energy not radiated to other elements. Any radiant energy not incident on any other part of the model will be directed to the space node.

C.2 Basics

The Stefan–Boltzmann law, also known as Stefan's law, states that the total energy radiated per unit surface area of a black body in unit time (known variously as the black-body irradiance, energy flux density, radiant flux, or the emissive power), $\dot{Q}$, is directly proportional to the fourth power of the black body's thermodynamic temperature.

A more general case is of a grey body, the one that doesn't absorb or emit the full amount of radiative flux. Instead, it radiates a portion of it, characterized by its emissivity, ε.

To find the total absolute power of energy radiated for an object we have to consider the surface area (A) and the Stefan–Boltzmann constant σ.

Figure C.1 shows an enclosure composed of N discrete surface areas.

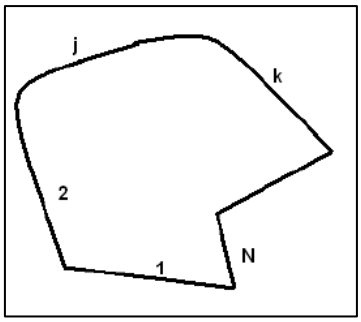

Figure C.1 Enclosure

Consider the kth inside surface area Ak of the enclosure shown in Fig. C.1. The quantities and are the rates of incoming and outgoing radiant energy per unit inside area, respectively. A heat balance for the surface area provides the relation:

$$\dot{Q_k} = \dot{q_k} \cdot A_k = (\dot{q_{0k}} - \dot{q_{ik}}) \cdot A_k \quad \text{(C.1)}$$

A_k = area of surface k.
$\dot{Q_k}$ = energy loss of surface k.

A second equation results from the fact that the energy flux leaving the surface is composed of emitted plus reflected energy. This gives:

$$\dot{q_{0k}} = \varepsilon_k \cdot \sigma \cdot T_k{}^4 + (1 - \varepsilon_k) \cdot \dot{q_{ik}} \quad \text{(C.2)}$$

σ = Stefan-Boltzmann constant.
T_k = absolute temperature of surface k.
ε_k = effective emissivity of surface k.

The incident energy is:

$$A_k \cdot \dot{q_{ik}} = A_1 \cdot \dot{q_{01}} \cdot F_{1k} + A_2 \cdot \dot{q_{02}} \cdot F_{2k} + \cdots A_k \cdot \dot{q_{0k}} \cdot F_{kk} + \cdots + A_N \cdot \dot{q_{0N}} \cdot F_{Nk} \quad \text{(C.3)}$$

F_{jk} = radiation view factors, 0 if i = k and planar surfaces.

If the kth surface is planar, $F_{kk} = 0$. From the configuration factor reciprocity relation:

$$A_1 \cdot F_{1k} = A_k \cdot F_{k1}, A_2 \cdot F_{2k} = A_k \cdot F_{k2}, \ldots, A_N \cdot F_{Nk} = A_N \cdot F_{kN} \quad \text{(C.4)}$$

Then Eq. C.3 can be written so the only area appearing is A_k, and eliminated:

$$\dot{q_{ik}} = \sum_{j=1}^{N} F_{kj} \cdot \dot{q_{0j}} \quad \text{(C.5)}$$

Then, from Eqs. C.1 and C.5:

$$\dot{q_k} = \dot{q_{0k}} - \dot{q_{ik}} = \dot{q_{0k}} - \sum_{j=1}^{N} F_{kj} \cdot \dot{q_{0j}} = \sum_{j=1}^{N} F_{kj} \cdot (\dot{q_{0k}} - \dot{q_{ij}}) \quad \text{(C.6)}$$

Provided that:

$$\sum_{j=1}^{N} F_{kj} = 1 \quad \text{(C.7)}$$

From Eq. C.2:

$$\dot{q}_{ik} = \frac{1}{1-\varepsilon_k} \cdot \dot{q}_{0k} - \frac{\varepsilon_k}{1-\varepsilon_k} \cdot \sigma \cdot T_k^{\,4} \tag{C.8}$$

And finally, from Eqs. C.1 and C.8:

$$\dot{q}_k = \dot{q}_{0k} - \dot{q}_{ik} = \frac{\varepsilon_k}{1-\varepsilon_k} \cdot (\sigma \cdot T_k^{\,4} - \dot{q}_{0k}) \tag{C.9}$$

Or:

$$\dot{q}_{0k} = \sigma \cdot T_k^{\,4} - \frac{1-\varepsilon_k}{\varepsilon_k} \dot{q}_k \tag{C.10}$$

Eq. C.10 is substituted into Eq. C.6.

$$\dot{q}_k = \sum_{j=1}^{N} F_{kj} \cdot \left[\sigma \cdot T_k^{\,4} - \frac{1-\varepsilon_k}{\varepsilon_k} \dot{q}_k - \sigma \cdot T_j^{\,4} + \frac{1-\varepsilon_j}{\varepsilon_j} \dot{q}_j\right] \tag{C.11}$$

On the other form:

$$\frac{\dot{q}_k}{\varepsilon_k} - \sum_{j=1}^{N} F_{kj} \cdot \frac{1-\varepsilon_j}{\varepsilon_j} \dot{q}_j = \sum_{j=1}^{N} F_{kj} \cdot \sigma \cdot \left(T_k^{\,4} - T_j^{\,4}\right) \tag{C.12}$$

Extending the Stefan-Boltzmann Law for a system of N enclosures, the energy balance for each surface in the enclosure for a grey diffuse body is given by the following equation, which relates the energy losses to the surface temperatures:

$$\sum_{j=1}^{N} \left(\frac{\delta_{kj}}{\varepsilon_j} - F_{kj} \cdot \frac{1-\varepsilon_j}{\varepsilon_j}\right) \cdot \frac{1}{A_j} \cdot \dot{Q}_j = \sum_{j=1}^{N} \left(\delta_{kj} - F_{kj}\right) \cdot \sigma \cdot T_j^{\,4} \tag{C.13}$$

δ_{kj} = Kronecker delta.

In mathematics, the Kronecker delta, is a function of two variables, usually integers, which is 1 if they are equal, and 0 otherwise.

For a system of two surfaces radiating to each other, Eq. C.13 can be simplified to give the heat transfer rate between surfaces i and j.

The heat flow transferred from Object i to Object j where the two objects see only a fraction of each other and nothing else is given by Eq. C.14.

$$\dot{Q}_{ij} = \frac{1}{\left(\frac{1-\varepsilon_i}{A_i \cdot \varepsilon_i} + \frac{1}{A_i \cdot F_{ij}} + \frac{1-\varepsilon_j}{A_j \cdot \varepsilon_j}\right)} \cdot \sigma \cdot \left(T_i^{\,4} - T_j^{\,4}\right) \tag{C.14}$$

This equation demonstrates the usage of but it represents a non-physical case since it would be impossible to position two finite objects such that they can see only a portion of each other and “nothing” else. On the contrary, the complementary view factor $(1 - F_{kj})$ cannot be neglected as radiation energy sent in those directions must be accounted for in the thermal bottom line.

A more realistic problem would consider the same two objects surrounded by a third surface that can absorb and readmit thermal radiation yet is non-conducting. In this manner, all thermal energy that is absorbed by this third surface will be readmitted, no

energy can be removed from the system through this surface. The equation which describes the heat flow from Object i to Object j for this arrangement is Eq. C.15.

$$\dot{Q}_1 = \frac{1}{\left(\frac{1-\varepsilon_i}{\varepsilon_i}+\frac{A_i+A_j-2\cdot A_i\cdot F_{ij}}{A_j-A_i\cdot\left(F_{ij}\right)^2}+\left(\frac{1-\varepsilon_j}{\varepsilon_j}\right)\cdot\frac{A_1}{A_2}\right)}\cdot A_i\cdot\sigma\cdot\left(T_i^{\,4}-T_j^{\,4}\right) \qquad (C.15)$$

If A_j is much greater than A_i, Eq. C.14 reduces to:

$$\dot{Q}_1 = A_i\cdot\varepsilon_i\cdot F_{ij}{}'\cdot\sigma\cdot\left(T_i^{\,4}-T_j^{\,4}\right) \qquad (C.16)$$

where:

$$F_{ij}{}' = \frac{F_{ij}}{F_{ij}\cdot(1-\varepsilon_i)+\varepsilon_i}$$

The view factor, F_{ij} is defined as the fraction of radiation leaving surface i which is intercepted by surface j. Hence:

$$F_{ij} = \frac{\text{radiation reaching surface j}}{\text{radiation leaving surface i}}$$

Figure C.2 shows two differential area elements.

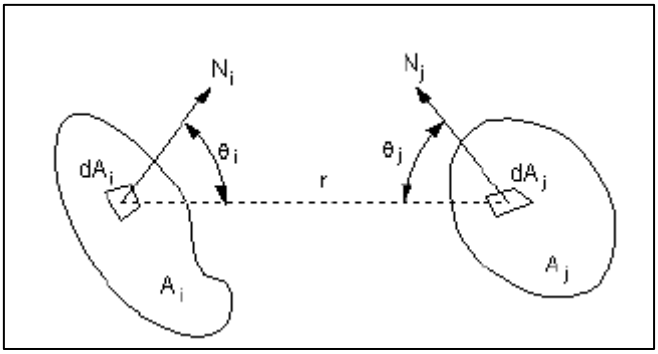

Figure C.2 Radiative interchange between two diffuse differential area elements

The total energy per unit time leaving dA_1 and incident on dA_2 is:

$$\dot{q}_1\cdot dA_1\cdot\cos\theta_1\cdot d\omega_1$$

Where $d\omega_1$ is the solid angle subtended by dA_2 when viewed from dA_1. The solid angle can be related to the projected area of dA_2 is:

$$r^2\cdot d\omega_1 = dA_2\cdot\cos\theta_2 \qquad (C.17)$$

Then, the total energy per unit time leaving and incident on dA_2 is:

$$\dot{q}_1 = \frac{dA_1\cdot\cos\theta_1\cdot dA_2\cdot\cos\theta_2}{r^2} \qquad (C.18)$$

On the other hand, the total energy per unit time leaving dA_1 is:

$$\dot{q}_1\cdot dA_1\cdot\pi$$

Where π is the solid angle for a hemisphere.

For the total surfaces:

$$F_{ij} = \frac{1}{A_i} \cdot \int_{Ai} \int_{Aj} \frac{\cos\theta_i \cdot \cos\theta_j}{\pi \cdot r^2} dA_j dA_i \qquad (C.19)$$

where:

A_i, A_j = area of surface i and surface j.
r = distance between differential surfaces i and j.
θ_i = angle between N_i and the radius line to surface dA_j.
θ_j = angle between N_j and the radius line to surface dA_i.
N_i, N_j = surface normal of dA_i and dA_j.

To calculate the form factor with ANSYS, a predetermined number of rays are projected from the viewing element to the hemisphere or semicircle. The form factor is the ratio of the number of rays incident on the projected surface to the number of rays emitted by the viewing element.

The view factor is used to parameterize the fraction of thermal power leaving object i and reaching object j. Specifically, this quantity is equal to:

$$\dot{Q}_{ij} = A_i \cdot F_{ij} \cdot \varepsilon_i \cdot \sigma \cdot T_i^4$$

Likewise, the fraction of thermal power leaving object j and reaching object I is given by:

$$\dot{Q}_{ji} = A_j \cdot F_{ji} \cdot \varepsilon_j \cdot \sigma \cdot T_j^4$$

The case of two blackbodies in thermal equilibrium can be used to derive the following reciprocity relationship for view factors:

$$A_i \cdot F_{ij} = A_j \cdot F_{ji}$$

Thus, once one knows F_{ij}, F_{ji} can be calculated immediately.

Radiation view factors can be analytically derived for simple geometries.

C.3 Procedures used in radiation matrix method

The non-hidden procedure calculates a view factor for every surface to every other surface whether the view is blocked by an element or not. In this procedure, the following equation is used and the integration is performed adaptively.

For a finite element discretized model, Eq. C.19 for the view factor F_{ij} between two surfaces i and j can be written as:

$$F_{ij} = \frac{1}{A_i} \cdot \sum_{p=1}^{m} \sum_{q=1}^{n} \left(\frac{\cos\theta_{jp} \cdot \cos\theta_{jq}}{\pi \cdot r^2} \right) \cdot A_{ip} \cdot A_{jp} \qquad (C.20)$$

where:

m = number of integration points on surface i.
n = number of integration points on surface j.

When the dimensionless distance between two viewing surfaces D, defined in Eq. C.21, is less than 0.1, the accuracy of computed view factors is known to be poor.

$$D = \frac{d_{min}}{\sqrt{A_{max}}} \tag{C.21}$$

where:

d_{min} = minimum distance between the viewing surfaces A_1 and A_2.
A_{max} = max (A_1, A_2).

Thus, the order of surface integration is adaptively increased from order one to higher orders as the value of D falls below 8. The area integration is changed to contour integration when D becomes less than 0.5 to maintain the accuracy. The contour integration order is adaptively increased as D approaches zero.

Figure C.3 shows case where non-hidden method is necessary.

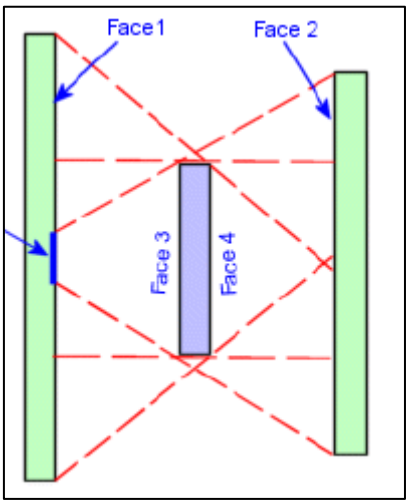

Figure C.3 Blocked surface, the middle area of face 1 (blue line) is totally blocked against radiation from face 2

The hidden procedure is a simplified method which uses Eq. C.19 and assumes that all the variables are constant, so that the equation becomes:

$$F_{ij} = \frac{A_j}{\pi \cdot r^2} \cdot \cos\theta_i \cdot \cos\theta_j \tag{C.22}$$

The hidden procedure numerically calculates the view factor in the following conceptual manner. The hidden-line algorithm is first used to determine which surfaces are visible to every other surface. Then, each radiating, or “viewing”, surface (i) is enclosed with a hemisphere of unit radius. This hemisphere is oriented in a local coordinate system ($x' y' z'$), whose centre is at the centroid of the surface with the z axis normal to the surface, the x axis is from node i to node j, and the y axis orthogonal to the other axes. The receiving, or “viewed”, surface (j) is projected onto the hemisphere exactly as it would appear to an observer on surface i.

As shown in Fig. C.4, the projected area is defined by first extending a line from the centre of the hemisphere to each node defining the surface or element. That node is then projected to the point where the line intersects the hemisphere and transformed into the local system x' y' z'.

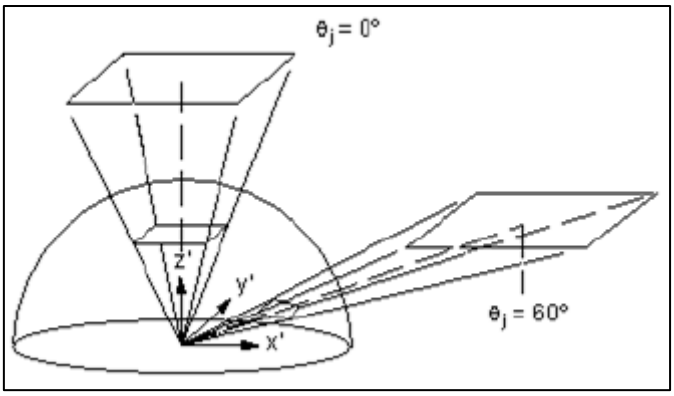

Figure C.4 Receiving surface projection

The view factor, F_{ij}, is determined by counting the number of rays striking the projected surface j and dividing by the total number of rays (N_r) emitted by surface i. This method may violate the radiation reciprocity rule, that is, $A_i \cdot F_{i-j} \neq A_j \cdot F_{j-i}$.

C.4 Hemicube method

The hemicube method is based upon Nusselt's hemisphere analogy. Nusselt's analogy shows that any surface, which covers the same area on the hemisphere, has the same view factor. From this it is evident that any intermediate surface geometry can be used without changing the value of the view factors. In the hemicube method, instead of projecting onto a sphere, an imaginary cube is constructed around the centre of the receiving patch. A patch in a finite element model corresponds to an element face of a radiating surface in an enclosure. The environment is transformed to set the centre of the patch at the origin with the normal to the patch coinciding with the positive Z axis. In this orientation, the imaginary cube is the upper half of the surface of a cube, the lower half being below the 'horizon' of the patch. One full face is facing in the Z direction and four half faces are facing in the +X, -X, +Y, and -Y directions. These faces are divided into square 'pixels' at a given resolution, and the environment is then projected onto the five planar surfaces.

Figure C.5: "The Hemicube" shows the hemicube discretized over a receiving patch from the environment.

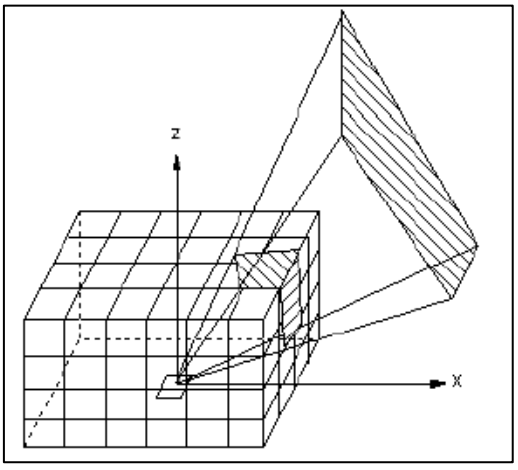

Figure C.5 The hemicube

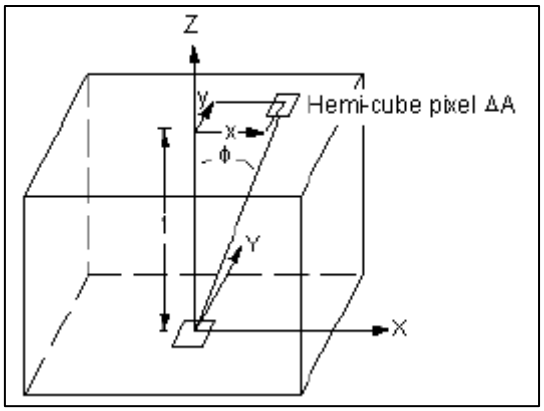

Figure C.6 Derivation of delta-view factors for hemicube method

The contribution of each pixel on the cube's surface to the form-factor value varies and is dependent on the pixel location and orientation as shown in Fig. C.6. A specific delta form-factor value for each pixel on the cube is found from modified form of Eq. C.19 for the differential area to differential area form-factor. If two patches project on the same pixel on the cube, a depth determination is made as to which patch is seen in that particular direction by comparing distances to each patch and selecting the nearer one. After determining which patch (j) is visible at each pixel on the hemicube, a summation of the delta form-factors for each pixel occupied by patch (j) determines the form-factor from patch (i) at the centre of the cube to patch (j). This summation is performed for each patch (j) and a complete row of N form-factors is found.

At this point the hemicube is positioned around the centre of another patch and the process is repeated for each patch in the environment. The result is a complete set of form-factors for complex environments containing occluded surfaces. The overall view factor for each surface on the hemicube is given by:

$$F_{ij} = \sum_{n=1}^{N} \Delta F_n = \frac{\cos \Phi_i \cdot \cos \Phi_j}{\pi \cdot r^2} \cdot \Delta A_J \qquad \text{(C.23)}$$

where:

N = number of pixels.
ΔF = delta-view factor for each pixel.

The hemicube resolution determines the accuracy of the view factor calculation and the speed at which they are calculated using the hemicube method.

Enclosure D: Mesh

D.1 SOLID 186

SOLID186, Figure D.1, is a higher order 3-D 20-node solid element that exhibits quadratic displacement behaviour. Each node has three degrees of freedom per node: translations in the nodal x, y, and z directions. The element supports plasticity, hyperelasticity, creep, stress stiffening, large deflection, and large strain capabilities. It also has mixed formulation capability for simulating deformations of nearly incompressible elastoplastic materials, and fully incompressible hyperelastic materials**.**

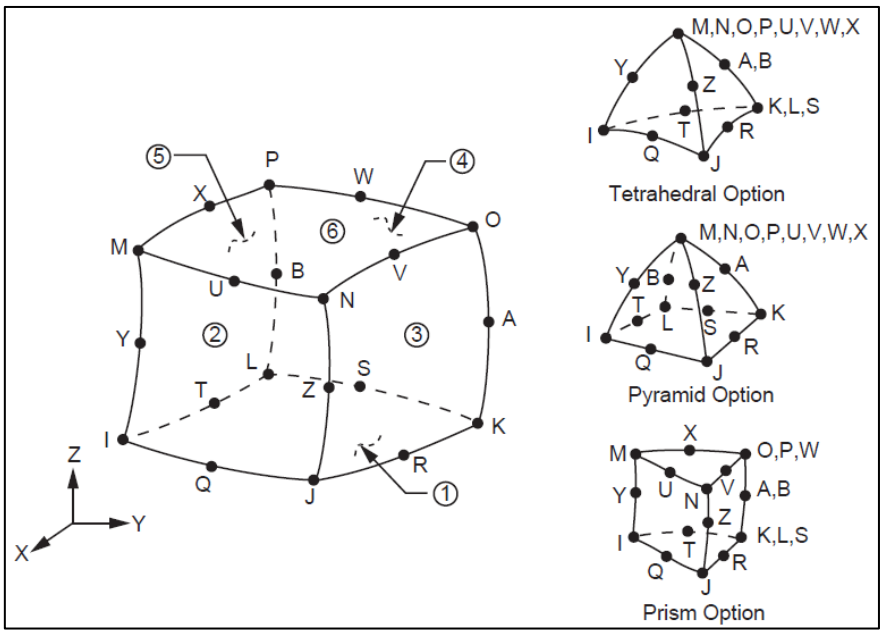

Figure D.1 SOLID186 Homogeneous structural solid geometry [ANSYS]

D.2 PLANE 55

PLANE55 can be used as a plane element with a 2-D thermal conduction capability. The element has four nodes with a single degree of freedom, temperature, at each node, Figure D.2. The line between nodes J and I is face 1, between nodes K and J is face 2, between nodes L and K is face 3, between nodes I and L is face 4.

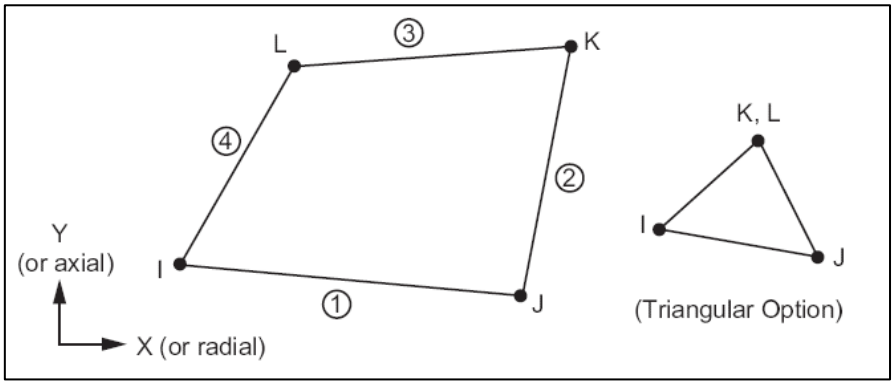

Figure D.2 PLANE55 geometry [ANSYS]

The element is applicable to a 2-D, steady-state or transient thermal analysis. If the model containing the temperature element is also to be analysed structurally, the element should be replaced by an equivalent structural element (such as PLANE182).

Convection or heat flux (but not both) and radiation may be input as surface loads at the element faces as shown by the circled numbers on Fig. D.2.

D.3 PLANE 182

PLANE182 is used for 2-D modelling of solid structures, Figure D.3. The element can be used as either a plane element or an axisymmetric element. The element has plasticity, hyperelasticity, stress stiffening, large deflection, and large strain capabilities.

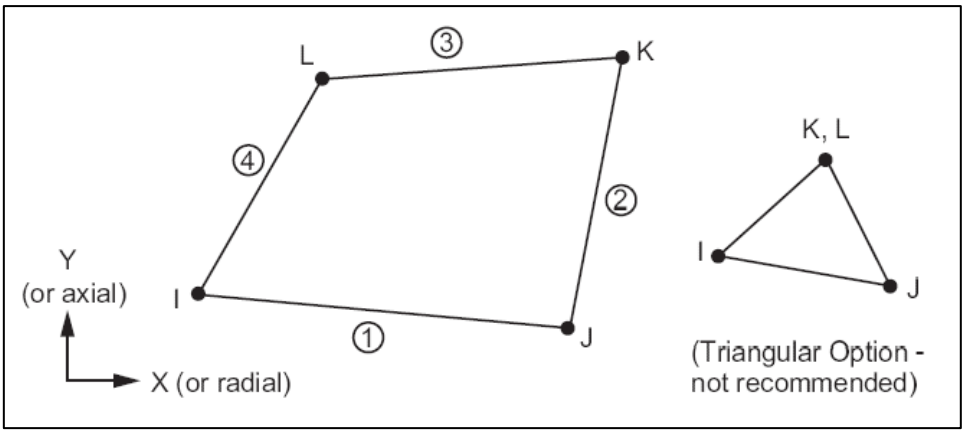

Figure D.3 PLANE182 geometry

The command KEYOPT(3) equal to 5 is used to enable generalized plane strain.

Enclosure E: ANSYS command

E.1 List of useful command

ASEL,Type,Item,Comp,VMIN,VMAX,VINC,KSWP
Type
Label identifying the type of select:
S - Select a new set (default).
A - Additionally select a set and extend the current set.
Item
Label identifying data.
Comp
Component of the item.
VMIN
Minimum value of item range.
VMAX
Maximum value of item range.
VINC
Value increment within range.
KSWP
Specifies whether only areas are to be selected:
0 - Select areas only.
1 - Select areas, as well as key points, lines, nodes, and elements associated with selected areas. Valid only with Type = S.

CE,NEQN,CONST,NODE1,Lab1,C1,NODE2,Lab2,C2,NODE3,Lab3,C3
NEQN
Set equation reference number.
n - Arbitrary set number.
HIGH - The highest defined constraint equation number. This option is especially useful when adding nodes to an existing set.
NEXT - The highest defined constraint equation number plus one. This option automatically numbers coupled sets so that existing sets are not modified.
CONST
Constant term of equation.
NODE1
Node for first term of equation. If -NODE1, this term is deleted from the equation.
Lab1
Degree of freedom label for first term of equation.
Structural labels: UX, UY, or UZ (displacements); ROTX, ROTY, or ROTZ (rotations, in radians).
Thermal labels: TEMP, TBOT, TE2, TE3, . . ., TTOP (temperature).
C1
Coefficient for first node term of equation. If zero, this term is ignored.
NODE2, Lab2, C2
Node, label, and coefficient for second term.
NODE3, Lab3, C3
Node, label, and coefficient for third term.

$$\text{Constant} = \sum_{I=1}^{N} (\text{Coefficient}(I) \cdot U(I))$$

The following example is a set of two constraint equations, each containing three terms:

0.0 = 3.0* (1 UX) + 3.0* (4 UX) + (-2.0)* (4 ROTY)
CE,1,0,1,UX,3,4,UX,3,4,ROTY,-2

2.0 = 6.0* (2 UX) + 10.0* (4 UY) + 1.0* (3 UZ)
CE,2,2,2,UX,6,4,UY,10,3,UZ,1

CEDELE,NEQN1,NEQN2,NINC,Nsel
NEQN1, NEQN2, NINC
Delete constraint equations from NEQN1 to NEQN2 in steps of NINC. If NEQN1 = ALL, NEQN2 and NINC will be ignored all constraint equations will be deleted.
Nsel
Additional node selection control.

CM,Cname,Entity
Cname
An alphanumeric name used to identify this component.
Entity
Label identifying the type of geometry items to be grouped:
NODE - Nodes.

CMSEL,Type,Name,Entity
Type
Label identifying the type of select:
S - Select a new set.
R - Reselect a set from the current set.
A - Additionally select a set and extend the current set.
U - Unselect a set from the current set.
Name
Name of component or assembly whose items are to be selected.
Entity
If Name is blank, then the following entity types can be specified:
NODE - Select the node components only.

CNVTOL,Lab,VALUE,TOLER,NORM,MINREF
Lab
Valid convergence labels.
F - Force Convergence.
VALUE
Typical reference value for the above label for this analysis. If negative, and if this convergence label was previously specified explicitly, then convergence based on this label is removed. (A negative VALUE will not remove a default convergence label.) Defaults to the maximum of a program calculated reference or MINREF. For degrees of freedom, the reference is based upon the selected NORM and the current total DOF value. For forcing quantities, the reference is based upon the selected NORM and the applied loads.

TOLER
When SOLCONTROL,ON, tolerance about VALUE defaults to 0.005 for force. When SOLCONTROL,OFF, the defaults are 0.001 for force.
NORM
Specifies norm selection:
2 - L2 norm.
1 - L1 norm.
0 - Infinite norm.
MINREF
The minimum value allowed for the program calculated reference value.
Negative - No minimum is enforced.
Blank - Defaults to 0.01 for force convergence and 0.0 otherwise.
When SOLCONTROL,OFF, defaults to 1.0 for force convergence.

CUTCONTROL,Lab,VALUE,Option
Lab
Specifies the criteria for causing a cutback. Possible arguments are:
PLSLIMIT - Maximum equivalent plastic strain allowed within a time-step (substep). If the calculated value exceeds the VALUE, the program performs a cutback (bisection).

D,Node,Lab,VALUE,VALUE2,NEND,NINC,Lab2,Lab3,Lab4,Lab5,Lab6
Node
Node at which constraint is to be specified. If ALL, NEND and NINC are ignored and constraints are applied to all selected nodes. A component name may also be substituted for Node.
Lab
Valid degree-of-freedom label. If ALL, use all appropriate labels.
Structural labels: UX, UY, or UZ (displacements); ROTX, ROTY, or ROTZ (rotations); WARP (warping).
Thermal labels: TEMP, TBOT, TE2, TE3, . . ., TTOP (temperature).
For structural static and transient analyses, translational and rotational velocities are also valid loads.
Use these labels: VELX, VELY, VELZ (translational velocities); OMGX, OMGY, OMGZ (rotational velocities).
For structural analyses, HDSP (hydrostatic pressure) is also valid. However, HDSP is not included when Lab = ALL.
For structural transient analyses, the following acceleration loads are also valid: ACCX, ACCY, ACCZ (translational accelerations); DMGX, DMGY, DMGZ (rotational accelerations). The velocity and acceleration loads are not included when Lab = ALL.
The degrees of freedom are not included when Lab = ALL. To constrain all cross-section degrees of freedom, specify Lab = SECT.
Value
Degree-of-freedom value or table name reference for tabular boundary conditions. To specify a table, enclose the table name in percent (%) signs (for example, D,Node,TEMP,%tabname%). Use the *DIM command to define a table.
VALUE2
Second degree-of-freedom value (if any).

NEND, NINC
Specifies the same values of constraint at the range of nodes from Node to NEND, in steps of NINC.
Lab2, Lab3, Lab4, Lab5, Lab6
Additional degree-of-freedom labels.

ESEL,Type,Item,Comp,VMIN,VMAX,VINC,KABS
Type
Label identifying the type of select:
S - Select a new set (default).
A - Additionally select a set and extend the current set.
ALL - Restore the full set.
Item
Label identifying data:
ELEM - Element number.
MAT - Material number.
VMIN
Minimum value of item range.
VMAX
Maximum value of item range.

ET,ITYPE,Ename,KOP1,KOP2,KOP3,KOP4,KOP5,KOP6,INOPR
ITYPE
Arbitrary local element type number.
Ename
Element name, PLANE55.
KOP1, KOP2, KOP3, . . . , KOP6
KEYOPT values. KEYOPT(1), procedure to evaluate film coefficient, 1 for evaluate at element surface temperature, TS. KEYOPT(3), element behaviour, 0 for Plane.

ETABLE,Lab,Item,Comp,Option
Lab
Any unique user defined label for use in subsequent commands and output headings. If the same as a previous user label, this result item will be included under the same label. Up to 200 different labels may be defined. Defaults to an eight character label formed by concatenating the first four characters of the Item and Comp labels. For example, if item is defined by S and the comp by X, the lab is defined by SX.
Item
Label identifying the item.
S - Stress.
VOLU - Element volume. Based on unit thickness for 2-D plane elements (unless the thickness option is used) and on the full 360 degrees for 2-D axisymmetric elements.
Comp
Component of the item.
X, Y, Z, XY, YZ, XZ for S item.
Option
Option for storing element table data:
MIN - Store minimum element nodal value of the specified item component.
MAX - Store maximum element nodal value of the specified item component.
AVG - Store averaged element centroid value of the specified item component (default).

ETCHG,Cnv
Cnv
Converts the element types to the corresponding type. Valid labels are:

TTS - Thermal to Structural.
STT - Structural to Thermal.
ETS - Electrostatic to Structural.
ETT - Electrical to Thermal.

FILL,NODE1,NODE2,NFILL,NSTRT,NINC,ITIME,INC,SPACE
NODE1, NODE2
NODE1, first node of nodes set to be filled in. NODE2, last node of nodes set to be filled in.
NFILL
Nodes between NODE1 and NODE2.
NINC
Addition of this increment to each of the remaining filled-in node numbers. Defaults to the integer result of (NODE2-NODE1) / (NFILL + 1).
ITIME, INC
Fill-in operation a total of ITIMEs, incrementing NODE1, NODE2 and NSTRT by INC each time after the first.

***GET**,Par,Entity,ENTNUM,Item1,IT1NUM,Item2,IT2NUM
Par
The name of the resulting parameter.
Entity
Entity keyword:

NODE.
SSUM.

ENTNUM
The number or label for the entity. In some cases, a zero (or blank) ENTNUM represents all entities of the set. N represents node number.
Item1
The name of a particular item for the given entity.

ITEM – used with SSUM.

IT1NUM
The number (or label) for the specified Item1 (if any). Some Item1 labels do not require an IT1NUM value.
Item2, IT2NUM
A second set of item labels and numbers to further qualify the item for which data are to be retrieved. Most items do not require this level of information.

***if**,i,ne,1,then
Command in Fortran. It means if $i \neq 1$ then.

LDREAD,Lab,LSTEP,SBSTEP,TIME,KIMG,Fname,Ext,--
Lab
Valid load label:

TEMP - Temperatures from a thermal analysis are applied as body force nodal loads (BF) in a structural analysis, an explicit dynamic analysis, or other type of analysis. When used in conjunction with KIMG=1 and KIMG=2, temperatures can be applied to a subsequent thermal analysis as nodal loads (D) or initial conditions (IC), respectively.

LSTEP
Load step number of the data set to be read. If LAST, ignore SBSTEP and TIME and read the last data set.
SBSTEP
Substep number (within LSTEP). If zero (or blank), LSTEP represents the last substep of the load step.
TIME
Time-point identifying the data set to be read. Used only if both LSTEP and SBSTEP are zero (or blank).
If TIME is between two solution time points on the results file, a linear interpolation is done between the two data sets. If TIME is beyond the last time point on the file, use the last time point.
KIMG
When used with the TEMP label, KIMG indicates how temperatures are to be applied. In an explicit dynamic analysis, KIMG = 0 is the only valid option for applying temperature loads.

0 - Apply temperatures as body loads (BF).
1 - Apply temperatures as nodal loads (D).
2 - Apply temperatures as initial conditions (IC).

Fname
File name and directory path. An unspecified directory path defaults to the working directory.
The file name defaults to Jobname.
Ext
Filename extension. The extension defaults to RST if Fname is blank.
--
Unused field.

MP,Lab,MAT,C0,C1,C2,C3,C4
Lab
Valid material property label:

ALPX - Secant coefficients of thermal expansion (also ALPY, ALPZ).
C - Specific heat.
DENS - Mass density.
EMIS - Emissivity.
EX - Elastic moduli (also EY, EZ).
GXY - Shear moduli (also GYZ, GXZ).
HF - Convection or film coefficient.
KXX - Thermal conductivities (also KYY, KZZ).
NUXY - Minor Poisson's ratios (also NUYZ, NUXZ) (NUXY = νyx).

MAT
Material reference number to be associated with the elements.
C0,C1,C2,C3,C4
Property = $C0 + C1 \cdot T + C2 \cdot T^2 + C3 \cdot T^3 + C4 \cdot T^4$

MPDATA,Lab,MAT,SLOC,C1,C2,C3,C4,C5,C6
Lab
Valid property label:

ALPX - Secant coefficients of thermal expansion (also ALPY, ALPZ).
C - Specific heat.
DENS - Mass density.

EMIS - Emissivity.
EX - Elastic moduli (also EY, EZ).
GXY - Shear moduli (also GYZ, GXZ).
HF - Convection or film coefficient.
KXX - Thermal conductivities (also KYY, KZZ).
NUXY - Minor Poisson's ratios (also NUYZ, NUXZ) (NUXY = νyx).

MAT
Material reference number to be associated with the elements.
SLOC
Starting location in table for generating data.
If 1 - Data input in the C1 field is the first constant in the table.
If 7 - Data input in the C1 field is the seventh constant in the table, etc.
C1, C2, C3, . . . , C6
Property data values assigned to six locations starting with SLOC.
If a value is already in this location, it is redefined.
A blank (or zero) value for C1 - The previous value in SLOC is reset to zero.
A value of zero can only be assigned by C1.
Blank (or zero) values for C2 to C6 leave the corresponding previous values unchanged.

MPTEMP,SLOC,T1,T2,T3,T4,T5,T6
SLOC
Starting location in table for entering temperatures.
1 - Data input in the T1 field applies to the first constant in the table.
7 - Data input in the T1 field applies to the seventh constant in the table, etc.
T1, T2, T3, . . . , T6
Temperatures assigned to six locations starting with SLOC.
If a value is already in this location, it will be redefined.
A blank (or zero) value for T1 resets the previous value in SLOC to zero.
A value of zero can only be assigned by T1.
Blank (or zero) values for T2 to T6 leave the corresponding previous values unchanged.

NGEN,ITIME,INC,NODE1,NODE2,NINC,DX,DY,DZ,SPACE
ITIME
Generation operation of a total of ITIME times.
INC
Increment of all nodes in the given pattern by INC each time after the first.
NODE1
Generation of nodes from the pattern of nodes beginning with NODE1.
DX
Node location increments in the active coordinate system.

NSEL,Type,Item,Comp,VMIN,VMAX,VINC,KABS
Type
Label identifying the type of select:
S - Select a new set (default).
A - Additionally select a set and extend the current set.
ALL - Restore the full set.
Item
NODE.

VMIN
Minimum value of item range.
VMAX
Maximum value of item range.

RADOPT,--,FLUXTOL,SOLVER,MAXITER,TOLER,OVERRLEX,--,--,--,--,
MAXFLUXITER
--
Unused field.
FLUXTOL
Convergence tolerance for radiation flux. This value is a relative tolerance.
The radiation flux norm for FLUXTOL is expressed as:

$$\frac{\sqrt{\sum_{j=1}^{N_{surf}}(Q^{i+1}-Q^{i})^2}}{\sqrt{\sum_{j=1}^{N_{surf}}(Q^{i+1})^2}}$$

where i is the pass or iteration number and j is the surface facet for radiation.
SOLVER
Choice of solver for radiosity calculation:
0 - Gauss-Seidel iterative solver (default).
1 - Direct solver.
2 - Jacobi solver.
MAXITER
Maximum number of iterations for Gauss-Seidel iterative or Jacobi solver.
TOLER
Convergence tolerance for Gauss-Seidel iterative or Jacobi solver. This value is an absolute tolerance.
OVERRLEX
Over-relaxation factor applied to Gauss-Seidel iterative or Jacobi solver.
--, --, --, --
Unused fields.
MAXFLUXITER
Maximum number of flux iterations to be performed according to the specified solver type:
0 - If the FULL solver is specified, convergence criteria are monitored and iterations are performed until convergence occurs. If the QUASI solver is specified, convergence criteria are ignored and one iteration is performed. This value is the default.
1, 2, 3, ...N - If the FULL solver is specified, convergence criteria are monitored and iterations are performed until convergence occurs, or until the specified number of iterations has been completed, whichever comes first. If the QUASI solver is specified, convergence criteria are ignored and the specified number of iterations are completed.

SF,Nlist,Lab,VALUE,VALUE2
Nlist
Nodes defining the surface upon which the load is to be applied. If ALL, all selected nodes [NSEL] are used.
Lab
CONV for convection.

RDSF for surface-to-surface radiation.
VALUE
If Lab = CONV, VALUE is typically the film coefficient.
If Lab = RDSF, VALUE is the emissivity value.
VALUE2
If Lab = CONV, VALUE2 is typically the bulk temperature.
If Lab = RDSF, VALUE2 is the enclosure number. Radiation will occur between surfaces flagged with the same enclosure numbers. If the enclosure is open, radiation will also occur to ambient. If VALUE2 is negative radiation direction is reversed and will occur inside the element for the flagged radiation surfaces.

SMULT,LabR,Lab1,Lab2,FACT1,FACT2
LabR
Label assigned to results.
Lab1
First labelled result item in operation.
Lab2
Second labelled result item in operation.
FACT1
Scale factor applied to Lab1. A blank or '0' entry defaults to 1.0.
FACT2
Scale factor applied to Lab2. A blank or '0' entry defaults to 1.0.
LabR = (FACT1·Lab1)·(FACT2·Lab2)

SPCTEMP,ENCL,TEMP
Defines a free-space ambient temperature for radiation using the Radiosity method.
ENCL
Radiating surface enclosure number.
TEMP
Temperature of free-space in the reference temperature system.
TB,Lab,MAT,NTEMP,NPTS,TBOPT,EOSOPT,FuncName
Lab
Material model data table type:

PLASTIC - Nonlinear plasticity with stress-vs.-plastic strain data.
MISO - Multilinear isotropic hardening using von Mises or Hill plasticity.
MKIN - Multilinear kinematic hardening using von Mises or Hill plasticity.

MAT
Material reference number.
NTEMP
The number of temperatures for which data will be provided (if applicable). Temperatures are specified via the TBTEMP command.
NPTS
For most labels where NPTS is defined, the number of data points to be specified for a given temperature. Data points are defined via the TBDATA or TBPT commands.

TBPT,Oper,X1,X2,X3, ...,XN
Oper
Operation to perform:

DEFI - Defines a new data point. The point is inserted into the table in ascending order of X1. If a point already exists with the same X1 value, it is replaced.
DELE - Deletes an existing point. The X1 value must match the X1 value of the point to be deleted (XN is ignored).

X1, X2, ..., XN
The N components of the point. N depends on the type of data table. Except for TB,EXPE all other TB Tables support only 2 components.

TBTEMP,TEMP,KMOD
TEMP
Temperature value.
KMOD
If blank - TEMP defines a new temperature.
If an integer - 1 to NTEMP (from the TB command), modify that previously defined temperature to the TEMP value, unless TEMP is blank, then that previously defined temperature is reactivated. Use TBLIST to list temperatures and data. The next TBDATA or TBPT commands also add or change the data at this temperature.
If CRIT (and TEMP is blank) - The next TBDATA values are failure-criteria keys.
If STRAIN (and TEMP is blank) - The next TBDATA values are strains as described for the MKIN property option.

V2DOPT,GEOM,NDIV,HIDOPT,NZONE
GEOM
Choice of geometry:
0 - Planar (default).
1 – Axisymmetric.
NDIV
Number of divisions for axisymmetric geometry (that is, the number of circumferential segments).
HIDOPT
Viewing option:
0 - Hidden (default).
1 - Non-hidden.
NZONE
Number of zones (that is, the number of rays emanating from a surface) for view factor calculation.

VFOPT,Opt,Filename,Ext,Dir,Filetype,Fileformat
Opt
View factor option:
NEW - Calculate view factors and write them to a file.
OFF - Do not recalculate view factors it they already exist in the database, otherwise calculate compute them.
READ - Read view factors from a binary file. For subsequent SOLVE commands, switch to the default option (OFF).
NONE - Do not write view factors to a file.
Fname
File name for view factor matrix.
Ext
Filename extension for view factor matrix.
Dir
Directory path for view factor matrix.
Filetype
View factor file type:
BINA - Binary (default).
ASCI - ASCII.

Fileformat
Format for the specified Filetype:

Binary files (Filetype = BINA):

0 - No compression. (View factor file size may be very large.)

1 - Zeroes are compressed out. (Useful for large models to reduce the view factor file size.)

ASCII files (Filetype = ASCI):

0 - 10F7.4 (low precision, lower accuracy).

1 - 7F11.8 (high precision, higher accuracy).

The **function node(x,y,z)** provides the node number with x, y, z-coordinates.
The function nx(N) provides the x-coordinate of the node number N. Analogous response is obtained using ny and nz.

The **function ndnext(neg_node)** provides next selected node having a node number greater than neg_node.

E.2 Frequent asked questions (FAQ)

- Procedure to read results by Load Step Number, Figure E.1:

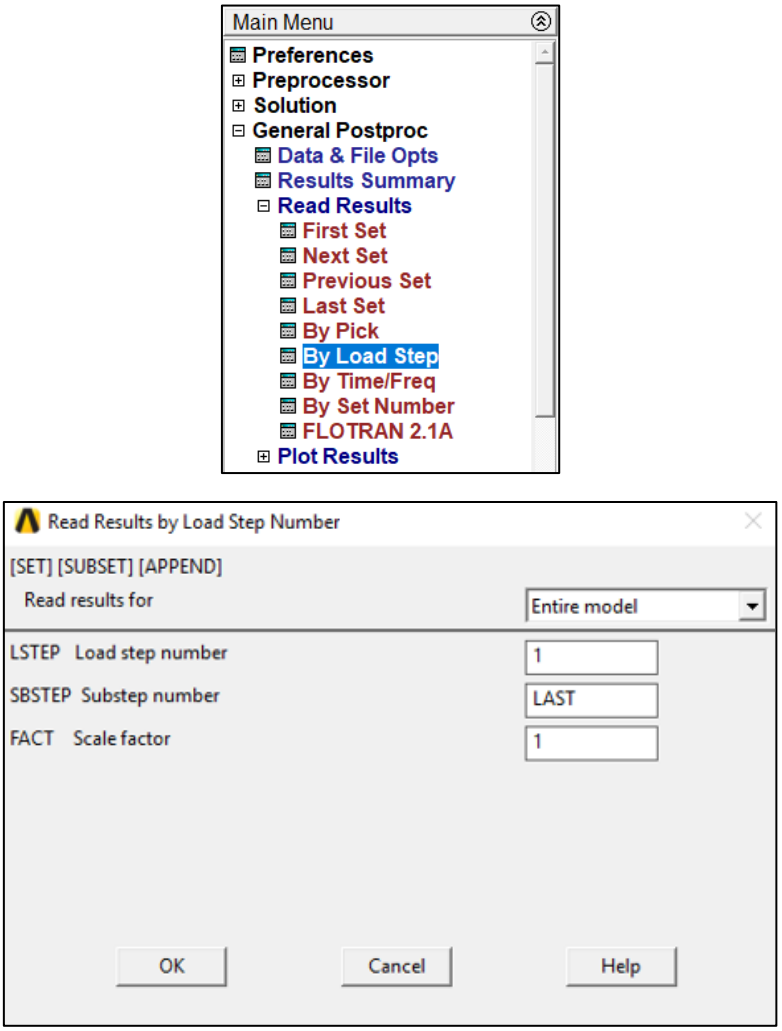

Figure E.1 Procedure to read results

- Procedure to select stress value label, Figure E.2:

In order to change the stress values label, the following path must be followed:

PlotCtrls>Style>Contours>Non-uniform Contours…

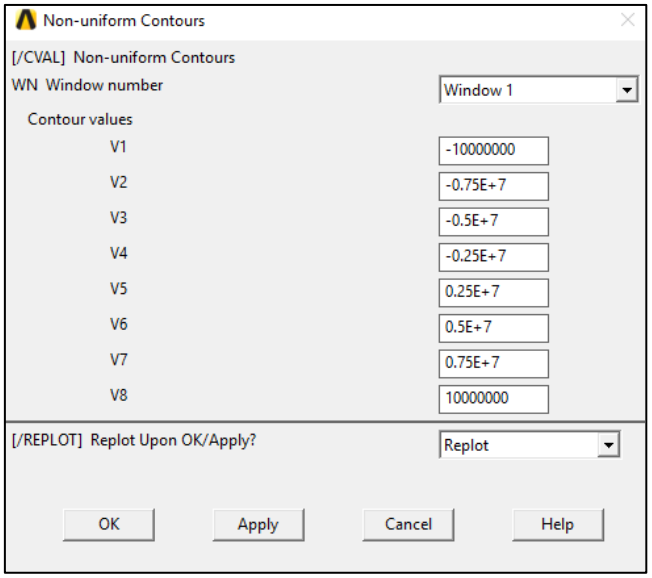

Figure E.2 Procedure to read results